HAL
open science

Secondary injection fluidic thrust vectoring of an axisymmetric supersonic nozzle

Vladeta Zmijanovic

To cite this version:

Vladeta Zmijanovic. Secondary injection fluidic thrust vectoring of an axisymmetric supersonic nozzle. Other. Université d'Orléans, 2013. English. NNT : 2013ORLE2010 . tel-00872072

HAL Id: tel-00872072

https://theses.hal.science/tel-00872072

Submitted on 11 Oct 2013

HAL is a multi-disciplinary open access archive for the deposit and dissemination of scientific research documents, whether they are published or not. The documents may come from teaching and research institutions in France or abroad, or from public or private research centers.

L'archive ouverte pluridisciplinaire **HAL**, est destinée au dépôt et à la diffusion de documents scientifiques de niveau recherche, publiés ou non, émanant des établissements d'enseignement et de recherche français ou étrangers, des laboratoires publics ou privés.

UNIVERSITÉ D'ORLÉANS

ÉCOLE DOCTORALE

Energie - Matériaux - Sciences de la Terre et de l'Univers

Institut de Combustion Aérothermique Réactivité et Environnement

CNRS Orléans

THÈSE présentée par :

Vladeta ZMIJANOVIC

soutenue le : **16 avril 2013.**

pour obtenir le grade de : **Docteur de l'Université d'Orléans**

Discipline/ Spécialité : PHYSIQUE/ Aérothermodynamique

Vectorisation fluidique de la poussée d'une tuyère axisymétrique supersonique par injection secondaire

Secondary injection fluidic thrust vectoring of an axisymmetric supersonic nozzle

THÈSE dirigée par :

Amer CHPOUN	Professeur, Université d'Evry Val d'Essonne

RAPPORTEURS :

Pascal BAUER	Professeur, Université de Poitiers (ENSMA)
David ZEITOUN	Professeur, Université de Provence Aix-Marseille

---

JURY:

Konstantinos KONTIS	Professeur, Université de Manchester, Royaume-Uni
Pascal BAUER	Professeur, Université de Poitiers (ENSMA)
David ZEITOUN	Professeur, Université de Provence Aix-Marseille
Amer CHPOUN	Professeur, Université d'Evry Val d'Essonne
Iskender GOKALP	Directeur de recherche, ICARE, *(codirecteur de thèse)*
Mohamed SELLAM	Maître de Conférences, Université d'Evry Val d'Essonne
Luc LEGER	Maître de Conférences, IUT d'Université d'Orléans
Sandrine PALERM	Ingénieur, CNES (DLA)

Acknowledgements

This thesis work was made possible by collaboration and support between CNES and CNRS. The work was conducted in ICARE (Institut de Combustion, Aérothermique, Réactivité et Environnement) (UPR 3021) of CNRS DCLPC in Orléans. I would like to acknowledge and express my gratitude to all persons who directly and indirectly took part in this PhD thesis project.
I am grateful to Professor Amer Chpoun for proposing and directing this interesting topic together with Sandrine Palerm and Jean Oswald from CNES. I would also like to express my gratitude to Dr. Mohamed Sellam for assistance during experiments, proofreading the thesis manuscript and help with french translations. I am thanking to Dr. Luc Leger for assistance during the multi-species experiments and for help with force-balance design and construction together with Jerome Joseph. I would also like to thank to Dr. Eric Depussay for support.

Especially, I'm greatly appreciating Dr. Viviana Lago for all the help, advices and assistance during my work and all conducted experiments together with Nicolas Gouillon. Special big thank and all my gratitude I am expressing to Dr. Dmitry Davidenko who provided me essential directions, explanations and assistance with the nozzle design, performance and hot-gas analysis.
I would also like to mention and thank to all ICARE personnel with director Dr. Iskender Gokalp for great four years spent with them; Among them, Dr. Ivan Fedioun for explanations and fruitful discussion about the problem matter, and all building-A colleagues: Kathe, Mehmet, Dennis, Sedina and others.

I'm also appreciating time and effort of the thesis reporters and jury members; prof. Bauer, prof. Zeitoun and prof. Kontis, as well as their valuable remarks. Together with people from CNES I need to mention appreciable and fruitful assistance from Bertin Technologies and its finest Laurent Lequette, Pierre Steinfeld and Gilles Bouré.
Going back in history, I need to acknowledge the importance of my previous studies and express my gratitude to professors at Ecole Polytechnique and at Faculty of Mechanical Engineering at Belgrade University who have had a huge influence on my present scientific work.

Finally, I must acknowledge the support of my family during my eduction and work, as well as great love, support and patience of my loving Tijana.

Secondary Injection Fluidic Thrust Vectoring of an Axisymmetric Supersonic Nozzle

Abstract

Transverse injection into the divergent section of an axisymmetric convergent-divergent propulsive nozzle is investigated for the fluidic thrust vectoring effects. Secondary injection thrust vector control represents a promising alternative to the conventional mechanically driven thrust vectoring due to simplicity and significant mass reduction. Investigation on the large number of cases and aspects was conducted in the framework of CNES *Perseus* program.

Five experimental test nozzle models are designed, built and equipped with the diagnostic tools. Full scale experimental and numerical investigation was preceded by the theoretic/analytical approach. Number of identified parameters is extensively analyzed and presented in this study. Experiments were supported by numerical simulations and further enhanced by additional nozzle models, cases and analysis parameters.

Pertinent side force and pitch vector angle of 5 to 9° were achievable with the mass-flow-rate ratio of 5 to 8%. Investigation aspects as the main nozzle geometrical characteristics, position of the injector and secondary to primary flow conditions are found to dominantly influence thrust vectoring capabilities. Further improvements are achieved by optimizing the geometric parameters of the secondary injector nozzle, as the angle of injection, shape of the secondary nozzle and by use of the multiport injection. Multispecies and hot-gas analysis identified influencing physical properties and demonstrated that fluidic thrust vectoring system preserves a solid performance using the combustion products injections.

Vectorisation fluidique de la poussée d'une tuyère axisymétrique supersonique par injection secondaire

Résumé

La vectorisation de la poussée d'une tuyère propulsive supersonique axisymétrique est étudiée par le biais d'une injection fluidique transversale dans sa partie divergente. Cette étude menée dans le cadre du programme *PERSEUS* du CNES a été motivée par la recherche d'une solution alternative, de conception simple et pouvant conduire à une réduction significative de masse comparée au pilotage conventionnel de la poussée par actionneurs mécaniques.
Pour cela, cinq modèles de tuyères ont été conçus, réalisés et équipés d'outils de diagnostic. Un travail basé sur des approches théorique et analytique a précédé une étude extensive, numérique et expérimentale, pour l'analyse des performances de ce concept. Un certain nombre de paramètres clés du problème ont été identifiés et leurs influences sur les performances du concept ont été analysées et présentées dans cette étude. Les résultats expérimentaux ont été confortés par des simulations numériques qui ont permis en outre d'analyser d'autres paramètres thermomécaniques.
L'analyse des résultats montre que pour certaines configurations optimales, des angles de déviation pertinents de 5 à 9° peuvent être obtenus pour des taux d'injections modérés de 5 à 8%. Les paramètres tels que le profil de la tuyère principale, la position de l'injecteur, les conditions d'injection des flux secondaire et principal ont une influence prépondérante sur le potentiel de vectorisation du concept. Le système peut être rendu davantage performant en optimisant les paramètres géométriques de l'injecteur secondaire comme l'angle d'injection, la

forme de l'injecteur et l'utilisation de l'injection "multiport". L'analyse numérique étendue aux écoulements chauds multi-espèces, plus proches des applications réelles, a montré que la vectorisation fluidique reste très performante lors de l'injection de produits de combustion dans le divergent.

Contents

Contents vii

List of Figures xi

Nomenclature xxv

1 General Introduction 1

1.1 Study context 6

1.2 Document organization 7

2 Methodology and analytical approach in SITVC investigation 9

2.1 Fundamentals of supersonic cross-flow interaction field 9

2.1.1 Two-dimensional case and previous works synthesis 11

2.1.2 Three-dimensional case and previous works synthesis . . . 13

2.2 Transverse injection into a supersonic nozzle 15

2.2.1 Secondary injection in a two-dimensional planar C-D nozzle 16

2.2.2 SITVC in a supersonic rocket nozzle 19

2.3 Axisymmetric convergent-divergent nozzle design and performance 22

2.3.1 Calculation of the forces acting on an axisymmetric C-D nozzle 25

2.3.2 Design of an axisymmetric C-D nozzle contour 27

2.4 Definition of analysis and performance parameters 30

2.5 Analytical modeling of the SITVC in an axisymmetric C-D nozzle 33

3 Experimental approach and test environment 39

3.1 Test facility 39

3.2 Qualitative flow analysis 42
3.3 Quantitative diagnostics 44
3.3.1 Parietal pressures 45
3.3.2 Force balance 46
3.4 Experimental test nozzle models 48

4 Numerical simulations test environment 51
4.1 Introduction to CFD approach and numerical environment 51
4.1.1 Numerical environment 53
4.2 Governing equations and turbulence modeling 53
4.2.1 Governing equations 55
4.2.2 Turbulence modeling 57
4.2.3 Fluid models 60
4.3 Numerical grid and boundary conditions 61
4.3.1 Near wall meshing 64
4.4 Numerical testing approach 66

5 Analysis of primary characteristics of SITVC axisymmetric nozzle 71
5.1 Introduction 71
5.2 Secondary injection port position 72
5.2.1 Qualitative flow analysis 72
5.2.2 Quantitative measurements 79
5.2.3 Injector position observations and remarks 89
5.3 Design characteristics and types of the primary nozzle 90
5.3.1 Primary nozzle sizing and SITVC 92
5.3.2 Supersonic rocket nozzle types 101
5.3.3 Remarks on primary nozzle design effect 108
5.4 Interaction flowfield & primary and secondary flow conditions . . 110
5.4.1 Secondary flow conditions 114
5.4.2 Primary flow conditions 124
5.5 Conclusion remarks 132

6 Properties of pneumatic actuator nozzle and secondary injection types 135

6.1 Introduction 135

6.2 Secondary nozzle geometry 136

6.2.1 Characterization of $\theta = 30°$ slot shaped secondary injection case 138

6.2.2 Quantitative pressure and forces measurements 142

6.3 Secondary nozzle attitude angle 146

6.3.1 Characterization of 20° upstream inclined SITVC conical nozzle 147

6.3.2 Upstream inclined secondary injection thrust vector control performance analysis 150

6.4 Secondary nozzle types and configurations 158

6.4.1 Convergent-Divergent secondary nozzle type 158

6.4.2 Multiport injection pneumatic actuator 161

6.4.2.1 Meridionally grouped multiport SITVC 163

6.4.2.2 Radially grouped multiport SITVC 165

6.5 Concluding remarks 169

7 Gas properties effect, multispecies and hot-gas analysis 171

7.1 Basic introduction to gas properties analysis 171

7.2 Model of species physical properties 172

7.3 Bi-species SITVC results discussion 178

7.3.1 Qualitative flow analysis of bi-specie injection case 178

7.3.2 Quantified diagnostics via pressures, forces and performance data 182

7.4 Introduction to hot-gases analysis 186

7.5 Thermochemical equilibrium calculations of reactions in combustion chamber 186

7.6 1D & axisymmetric nozzle calculations 189

7.7 SITVC nozzle 3D hot-gases simulations 194

7.8 Conclusion remarks 199

Conclusions and perspectives **201**

References **207**

Appdx A - Design of an axisymmetric CD nozzle contour **217**

A.1 Method of characteristics 217

A.2 Selection of TIC nozzle and boundary-layer correction 222

Appdx B - Force data acquisition **227**

B.1 Static calibration and sensor data treatment 228

B.2 Flow meter and force measuring 234

Appdx C - Version Française **237**

C.1 Introduction générale 237

C.2 Chapitre 2 243

C.3 Chapitre 3 244

C.4 Chapitre 4 245

C.5 Chapitre 5 246

C.6 Chapitre 6 251

C.7 Chapitre 7 253

C.8 Conclusions 254

List of Figures

1.1 Roots and early examples of aircraft TVC systems 1
1.2 TVC enabled super-manoeuvrability of MiG-29 OVT 2
1.3 Examples of mechanically driven space launcher TVC systems . . 3
1.4 Schemes of counter flow and throat shifting methods 4
1.5 ICBM Minuteman-II LGM-30F second stage engine with SITVC . 5

2.1 Scheme of 2D case of the slot injection on a flat plate and wall-pressure distribution estimation 10
2.2 Scheme of blunt-body model 12
2.3 Scheme of 3D case of the circular sonic injection on a flat plate into supersonic flow 14
2.4 Scheme of blunt-body model 17
2.5 Simplified scheme of SITVC in an axisymmetric C-D nozzle . . . 18
2.6 Scheme of the linearized model for fluid injection analysis 19
2.7 Pressure sensitive color oil photographs of nozzle-wall shock interface 21
2.8 Scheme of Method of characteristics procedure 27
2.9 Simplified scheme of the transverse injection into the supersonic cross-flow 34
2.10 Scheme of the separation alongside nozzle wall 37

3.1 Wind-tunnel test sections hall of FAST platform in CNRS-ICARE 39
3.2 Scheme of the wind-tunnel EDITH operation-cycle 40
3.3 EDITH test section acquisition site 41
3.4 Scheme of the designed and installed Z-schlieren 43
3.5 CAD designed pressure measurement map 44

3.6 CAD design of axial pressure probes locations 45
3.7 TIC-i0.88 nozzle with installed parietal pressure tools 46
3.8 Nozzle-chamber on the force-balance system 47
3.9 Experimental test nozzles 48
3.10 TIC profile BL correction 49
3.11 Secondary injection convergent nozzles 50

4.1 Normal circular cross section of the divergent TIC nozzle domain 62
4.2 Computational domain with listed boundary conditions 63
4.3 Injection port profiles at the nozzle wall 64
4.4 BL at injection port zone of the divergent section TIC nozzle symmetry 65
4.5 $y+$ at 360° TIC nozzle section 3D grid for 3 levels of mesh quality 66
4.6 Numerical computations process algorithm 66
4.7 Pressure coefficient at the wall of symmetry plane for the given grid sequences 68
4.8 Pressure coefficient the wall of symmetry plane for the 3 turbulence models 69

5.1 Schlieren images of conical test nozzle with injection at $x_j/l_n = 0.7$ 73
5.2 Schlieren images of conical test nozzle with 2nd injection at $x_j/l_n = 0.9$ 73
5.3 Image processing tool deflected flow angle measurement 74
5.4 Shock polar for 2.8 $Mach$ in the hodograph plane 75
5.5 $x_j/l_n = 0.7$ case 3D flowfield with iso-Mach contours 76
5.6 2D scheme of the 2nd injection nozzle wall zone portion 77
5.7 $x_j/l_n = 0.9$ case 3D flowfield with iso-Mach contours 77
5.8 Combined shock polar diagrams of the regular and Mach wall-reflection for an incident oblique shock wave at $M1 = 2.6$ in polar plane 78
5.9 CAD draft with the Kulite® probes housings distribution for Nozzle C-i $x_j/l_n = 0.9$ 79
5.10 $x_j/l_n = 0.7$ case symmetry plane 80

5.11 Skin friction distribution for 2 experimental/numerical test cases $x_j/l_n = 0.7$ and $x_j/l_n = 0.9$ 81
5.12 C_f^* recentralized to the auxiliary coordinate system at injection point and non-dimensionalized by d_j 82
5.13 Skin friction distributions, recentralized to the auxiliary coordinate system 83
5.14 Penetration height versus injection position 84
5.15 Experimental temporal raw data acquisition history 84
5.16 Kulite probes temporal data acquisition history 85
5.17 Wall-pressure data at the symmetry wall injection side recentralized to the auxiliary coordinate system at injection point and non-dimensionalized by d_j 86
5.18 Wall-pressure profiles at selected nozzle meridians, detection of the separation line 87
5.19 Vectoring and force amplification factors vs. non-dimensional injection position 89
5.20 Limit deflection angle φ_{Dmax} and corresponding Mach angle for range of upstream incident M1 values 91
5.21 Pressure contour plots for inviscid numerically simulated cases of $\alpha = 5.8°$ SITVC conical nozzles, $[Pa]$ 92
5.22 Mach number plots for different SITVC test nozzle models 94
5.23 Entropy and turbulent production contour plots for Mach 3 TIC $x_j/l_n = 0.88$ nozzle 96
5.24 Skin friction in symmetry plane of TIC $Mach$ 3 nozzle and different 2nd injection positions 97
5.25 Skin friction in symmetry plane of TIC $Mach$ 5 nozzle and different 2nd injection positions 97
5.26 Vectoring and specific impulse amplification factor versus different injector positions of TIC test nozzles 99
5.27 $Mach$ number plot in nozzle symmetry plane 101
5.28 $Mach$ number plot in TOC nozzle symmetry plane 102
5.29 $Mach$ number plot,streams and characteristic shock zones in nozzle symmetry plane 103

5.30 Shock polar diagram for triple point at approximated planar shock interaction of core flow M1=6.7 and $\varphi_D = 25°$ 104
5.31 Wall-pressure profiles for different Mach 5 rocket nozzle types . . 105
5.32 Mach number plots of the *Mach* 5 APG nozzle in the symmetry plane 106
5.33 Wall-pressure profiles for *Mach* 5 nozzles with transverse secondary sonic injection at injection side of the symmetry plane 106
5.34 Pressure contours and mach number plot for cross-section slices of APG nozzle 107
5.35 xy-plane view of TIC $x_j/l_n = 0.88$ SITVC nozzle schlieren visualization at NPR=37.5, SPR=1 111
5.36 xz-plane view of TIC $x_j/l_n = 0.88$ SITVC nozzle schlieren visualization at NPR=37.5, SPR=1 112
5.37 3D numerical schlieren of the TIC test nozzle 113
5.38 TIC x_j/l_n nozzle model *Mach* number plot and pressure level contour lines 113
5.39 Wall pressure distribution at injection side of a symmetry plane for NPR=37.5 and range of SPR 115
5.40 Analytical wall-pressure distribution at injection side of a symmetry plane for NPR=37.5 and range of SPR 116
5.41 Wall pressure distribution at meridional positions around nozzle axis for NPR=37.5 and SPR=1 117
5.42 Wall pressure distribution at meridional positions around nozzle axis for NPR=37.5 and SPR=0.833 118
5.43 Vectoring pitch angle versus mass-flow-rate ratio obtained from numerical and experimental results and from selected analytical models 121
5.44 Vectoring and specific impulse amplification factor vs mass-flow-rate ratio 122
5.45 Non-dimensionalized injectant mach disk height with related mass-flow-rates 123
5.46 Numerical and experimental schlieren photos for SPR=1 and series of overexpansion NPRs 125

5.47 Mach number plot and pressure stream contours for SPR=1 and series of overexpansion NPRs 126
5.48 3D iso-surfaces for NPR=10, SPR=1 127
5.49 Wall-pressure profiles for constant SPR=1 and series of overexpansion NPRs of TIC-i.$x_j/l_n = 0.882$ nozzle 129
5.50 Performance data plotted versus NPR for TIC-i.$x_j/l_n = 0.882$ nozzle, $SPR = 1$ 131

6.1 Definition of the slot contour on the divergent section of the TIC nozzle 136
6.2 Static pressure distributions for SITVC slot configurations at $NPR = 8.26$ and $SPR = 1$ by Wing 137
6.3 Numerical pressure contours of separation and affected zones with slot SITVC nozzle at $NPR = 37.5, SPR = 1$ conditions 138
6.4 Wall-pressure plots for different injection port geometries of SITVC TIC nozzle at $f_m = 0.08,\ SPR = 1,\ NPR = 37.5$ conditions . . . 139
6.5 Wall-pressure plots with separation line of SITVC TIC nozzle at $f_m = 0.08,\ SPR = 1,\ NPR = 37.5$ conditions 139
6.6 Wall-pressure profiles for slot and circular SITVC nozzle at $NPR = 37.5, f_m = 0.08, SPR = 1$ conditions 140
6.7 Schlieren photographs of SITVC TIC nozzle with slot shaped port at $f_m = 0.08,\ SPR = 1,\ NPR = 37.5$ conditions 141
6.8 Top view schlieren photographs of SITVC TIC nozzle with slot shaped port at $f_m = 0.08,\ SPR = 1,\ NPR = 37.5$ conditions . . 141
6.9 Wall-pressure plot with Mach number iso-surfaces for slot SITVC nozzle at $NPR = 37.5, f_m = 0.08, SPR = 1$ conditions 142
6.10 Meridians of TIC-slot nozzle at which the experimental and numerical data was probed 143
6.11 Experimental and numerical pressure data at 0° meridian, at $NPR = 37.5, SPR = 1$ 144
6.12 Experimental and numerical pressure data for range of meridian positions, at $NPR = 37.5, SPR = 1$ 145

6.13 Schlieren photographs of SITVC C-a.09 nozzle with inclined circular injection at $SPR = 1,\ NPR = 37.5$ conditions 147
6.14 Wall-pressure contours and flow iso-mach surfaces for 20° inclined circular injection of C-a.0.9 nozzle at $SPR = 1,\ NPR = 37.5$ conditions 148
6.15 Pressure and Mach number plots of SITVC C-a.09 nozzle with inclined circular injection 149
6.16 Wall-pressure and separation delineation along wall of conical $Mach3$ nozzle with injection at $x_j/l_n = 0.9$ 150
6.17 Wall-pressure profiles of $x_j/l_n = 0.9$ SITVC conical nozzles and various inclination angles, φ 151
6.18 Wall-pressure and separation delineation along wall of TIC nozzle with upstream inclined injection 152
6.19 Contour plots of TIC nozzle with $\varphi = 60°$ upstream inclined injection at $x_j/l_n = 0.88$, $SPR = 1$, $NPR = 37.5$ 152
6.20 Pressure profiles of wall and injection port in symmetry plane for $x_j/l_n = 0.88$ SITVC TIC nozzle 153
6.21 Interaction - wall side force temporal evolution for $x_j/l_n = 0.88$ SITVC TIC nozzle and 2 inclination cases 153
6.22 $k-\varepsilon$ Turbulence kinetic energy and dissipation in symmetry plane of the TIC nozzle $\varphi = 60°$ inclined injection case 155
6.23 Performance coefficients versus inclination angles, *blue - conical nozzle, red - TIC nozzle* 156
6.24 Mach iso-surfaces with turbulence-kinetic-energy evolution contours of the TIC nozzle $\varphi = 30°$ inclined slot injection case, $NPR = 37.5, SPR = 1$ 157
6.25 Performance coefficients versus inclination angles of circular and lot SITVC TOC nozzle case at, $SPR = 1, NPR = 37.5$ 157
6.26 Mach number plot and contours in symmetry plane of TIC nozzle with supersonic secondary transverse injection 159
6.27 Pressure profiles in symmetry plane of TIC nozzle with sonic and supersonic secondary transverse injection cases at $SPR = 1, NPR = 37.5$ 160

6.28 Iso-surfaces of secondary plateau pressure adapted supersonic M=2 injection into a TIC nozzle at $x_j/l_n = 0.88, SPR = 1, NPR = 37.5$ 160
6.29 Side force components produced by sonic and supersonic secondary transverse injection cases into primary TIC nozzle at $x_j/l_n = 0.88, SPR = 1, NPR = 37.5$ 162
6.30 Meridionally grouped multiport SITVC, wall separation and interface zones 163
6.31 Meridionally grouped multiport SITVC, entropy plots depicting separation interaction evolution and dissipation, $[J/K]$ 164
6.32 Meridionally grouped multiport SITVC, 3D Mach number plots . 165
6.33 Mach number plot at yz planes from the injection section towards the exit 166
6.34 Radially grouped multiport SITVC, wall separation and interface zones 167
6.35 Radially extracted entropy plots with leading iso-surface and velocity vector streamlines 167
6.36 Wall pressure profiles for single and multiport radially and meridionally grouped injection into primary TIC nozzle at $x_j/l_n = 0.7, SPR = 1, NPR = 450$ 168

7.1 $C_p(T)$ for $60 - 500K$ temperature range of components and air mixture 173
7.2 $\mu_M(T)$ for $60 - 500K$ temperature range of injectant species and air mixture 174
7.3 $C_p(T)$ for Argon with curve fitting polynomial functions 174
7.4 Bi-color schlieren images of secondary gas transverse injection into primary nozzle supersonic air flow at $NPR = 37.5, SPR = 1$ . . . 179
7.5 Massic fractions surfaces of SITVC TIC nozzle at $x_j/l_n = 0.88$, $SPR = 1$, $NPR = 37.5$ 180
7.6 Sidewise $y-direction$ velocity contour plots at $y/y_e = 0.565, 0.913, 0.783$ extracted (xz) slices of SITVC TIC nozzle 181
7.7 Mach contour plots in symmetry plane of SITVC TIC nozzle at $x_j/l_n = 0.88$, $f_m = 0.076$, $NPR = 37.5$ 181

7.8 Wall-pressure profiles at injection side of symmetry of different secondary injectants into main air flow at fixed $SPR = 1$ and $NPR = 37.5$ 182
7.9 Wall-pressure profiles at injection side of symmetry of different secondary injectants into main air flow at fixed $f_m = 0.076$ and $NPR = 37.5$ 183
7.10 Vectoring amplification versus γM_g product ratio of injectant in the main flow 185
7.11 Specific impulse amplification versus γM_g product ratio of injectant in the main flow 185
7.12 Scheme of rocket combustion chamber cross sections 187
7.13 1D thermochem. equilibrium computations temperature and thrust force 190
7.14 $C_2H_5OH - lO_X$ 1D Specific impulse profile 192
7.15 $C_2H_5OH - lO_X$ Thrust force and temperature profiles 192
7.16 $H_2 - lO_X$ Specific impulse and temperature profiles 192
7.17 $C_2H_5OH - lO_X$ 2D-axi viscous CPS_C temperature plot 193
7.18 $C_2H_5OH - lO_X$ 2D-axi viscous CPS_C temperature evolution at the axis and wall 194
7.19 $C_2H_5 - OH - lO_X$, 3D entropy and temperature evolutions in SITVC TIC nozzle 195
7.20 Wall-pressure profiles in symmetry plane for hot and cold $C_2H_5OH - lO_X$ case and monospecie cold air case in SITVC TIC nozzle at $NPR = 37.5$, $SPR = 1$, $x_j/l_n = 0.88, P_0 = 300kPa$ 196
7.21 Skin friction in symmetry plane for hot $C_2H_5OH - lO_X$ case and cold air case in SITVC TIC nozzle at $NPR = 37.5$, $SPR = 1$, $x_j/l_n = 0.88, P_0 = 300kPa$ 197
7.22 Numerical wall-pressure data of 2 fuel-oxidant cases in symmetry plane in SITVC TIC nozzle at $x_j/l_n = 0.88, NPR = 37.5, SPR = 1$ 197

A.1 Sauer sonic line approximation 218
A.2 Illustration of initial-value line 220
A.3 Model for determining the curvature κ at the narrowest cross-section 221

A.4 Profiles at the nozzle throat section 222
A.5 Velocity and energy profiles at the nozzle exit 223
A.6 MoC calculated ideal nozzle Mach plot and truncation sequences . 224
A.7 Integration scheme for max pressure force of calculated profiles . . 224

B.1 CATIA V5 CAD view of the balance system assembly 227
B.2 HBM S2M linearity and reversibility 228
B.3 HBM S2M directions and creep 229
B.4 Mounted nozzle chamber system on the force balance system and measuring axes 229
B.5 Calibration using pulley supports 230
B.6 Examples of static load signal test raw data 230
B.7 Examples of convergence of averaged values curve 231
B.8 Examples of calibration using series of small weights 232
B.9 Temporal evolution of x-transducers measurement at $0.25Hz$ and 182 samples for 139.4N of static load, with drift and deviation . . 233
B.10 Examples of repeatability test for y-axis force transducers under $5.14N$ of static load 233
B.11 Temporal evolution of chamber pressure along with the axial force 235
B.12 EL-FLOW mass-flow meter 235
B.13 Functional scheme of the thermal mass flow sensor by Bronkhorst® 236

C.1 247
C.2 247
C.3 248
C.4 249
C.5 250
C.6 251
C.7 254

Nomenclature

Roman Symbols

A	surface area
a	speed of sound
c	speed of sound
C_d	discharge coefficient
C_F	force coefficient
C_f	coefficient of friction
C_M	moment coefficient
C_p	specific heat under constant pressure
c_P	coefficient of pressure
C_V	specific heat under constant volume
C_{AF}	force amplification factor
C_{AI}	global amplification factor
C_{AV}	vectoring amplification factor
$\vec{D}$	dynalpy
d_n	normal distance to the wall

NOMENCLATURE

F	force
f_m	$f_m = \dot{m}_j/\dot{m}$ secondary to primary mass-flow-rate ratio
h	enthalpy
h_j	Mach disk or penetration height
I_{sp}^r	weightless state specific impulse
k	turbulence energy production rate
l_n	nozzle length
M	Mach number
M_g	Molar mass
$\vec{P}$	contact or pressure forces
P	total pressure
p	pressure
P_k	Production term for turbulence energy
Pr	Prandtl number
S	surface
$\vec{R}$	resultant force
R_g	specific gas constant
Re	Reynolds number
Sc	Schmidt number
T	temperature
u	flow velocity
V	volume

v	velocity in y direction
w	velocity in z direction
x	axial flow direction
y	vertical(side) direction
z	lateral direction

Greek Symbols

α	angle between profile tangent and main axis
β	$k-\varepsilon$ dissipation proportionality coefficient
δ	vector pitch angle
δ_{BL}	boundary-layer thickness
ε	turbulence dissipation rate
$\overline{\phi}$	averaged value
ϕ'	fluctuating value
φ	inclination angle from axis normal
φ_D	flow deflection angle
γ	ratio of specific heats
κ	half conic angle
λ	thermal conductivity
μ	molecular, dynamic viscosity
μ_t	viscosity of turbulence
ν	kinematic viscosity
ρ	density of fluid

σ	A/A_c expansion ratio
σ_M	Mach angle
$\bar{\tau}_{ij}$	Reynolds stress
τ	shear stress
τ_w	wall-shear-stress
θ	central arc angle
ω	specific dissipation rate
χ	molar fraction

Subscripts

$*$	vacuum
0	inlet or initial values
c	critical chocked flow section, throat
e	condition at nozzle exit plane
I	interface
j	secondary injection
q	overall quantity
S	isentropic condition
w	conditions at the wall

Other Symbols

$\mathcal{D}$	diffusivity coefficient
$\dot{m}$	mass flow rate
$\Re$	universal gas constant

$y+$ non-dimensional wall distance

Acronyms

$1D$ one-dimensional

$2D$ two-dimensional

$3D$ three-dimensional

APG adverse pressure gradient

BL boundary-layer

$C-D$ convergent-divergent

CFD computational fluid dynamics

DES detached eddy simulation

FTV fluidic thrust vectoring

LDV laser doppler velocimeter

LES large eddy simulation

LIF laser induced fluorescence

MoC Method of Characteristics

NPR nozzle pressure ratio

$SITVC$ secondary injection thrust vector control

SPR secondary pressure ratio

SVC shock vector control

Chapter 1

General Introduction

Nozzle thrust vector control (TVC) represents a necessity for any aerospace vehicle operating in the upper layers of the atmosphere or in the space environment where there is no aerodynamic response of the medium that can be used to manoeuvre the vehicle. There is a number of different ways to apply the thrust vector control to the aerospace vehicle. Conventionally used methods rely on the mechanically or electromechanically driven TVC systems. Mechanical systems utilise hydraulic actuators to achieve gimbal nozzle vectoring, rotate aircraft nozzle petals or completely move/rotate engine nacelles.

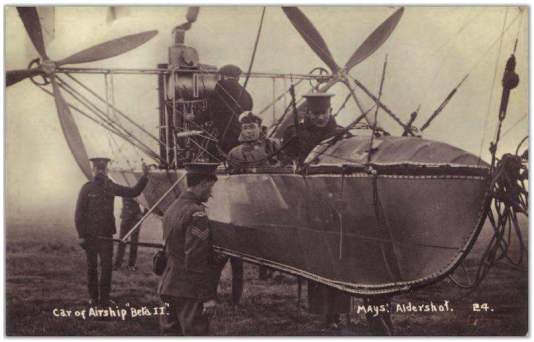

(a) Airship with moving propellers

(b) Tiltrotor aircraft V-22 Osprey

Figure 1.1: Roots and early examples of aircraft TVC systems

Thrust vector control roots may be traced to the early concepts, even before the invention of the engine powered airplane in 1903. and its development should be considered together with the evolution of the aviation and aerospace technol-

ogy. The first TVC operated aircrafts may be identified in the pre-World War 1 flown airships as *Delta* from 1908 in Figure 1.1a which was fitted with the swiveling propellers gondola. Since then, a number of features evolved related to the TVC as the changeable angle of attack propeller blades, the movable propeller engine, the invention and evolution of a helicopter and various alternations of the airplane-helicopter technologies like tiltrotor aircraft in Figure 1.1b. These systems proved as reliable and efficient and they are in the use by a vast number of the conventional aircrafts today. Turbofan, turbojet, ramjet and rocket engines use a nozzle as an end element of the propulsion cycle to deliver the thrust and therefore a TVC is reasonably implemented at the nozzle element. Mechanical TVC systems with the hydraulic actuators are used on the number of military jet aircrafts to enhance maneuverability, survivability and shorten take-off & landing (STOL) or to conduct vertical take-off landing (VTOL). There is a large number of the early examples as the Dassault Mirage IIIV and Balzac V or the famous Hawker-Siddeley Harrier which used a highly manoeuvrable thrust vectored Rolls-Royce Pegasus engine able of VTOL. Advanced fourth generation fighter jets as MiG-29 OVT use a multiaxis TVC which controls each petal of the exit nozzle section enabling the nozzle to change its area ratio and move the exhausting jet up to 90° in any direction, Figure 1.2. TVC along with the fly by wire technology represents one of the basic requirements for the 5th and eventual 6th generation of the fighter jets.

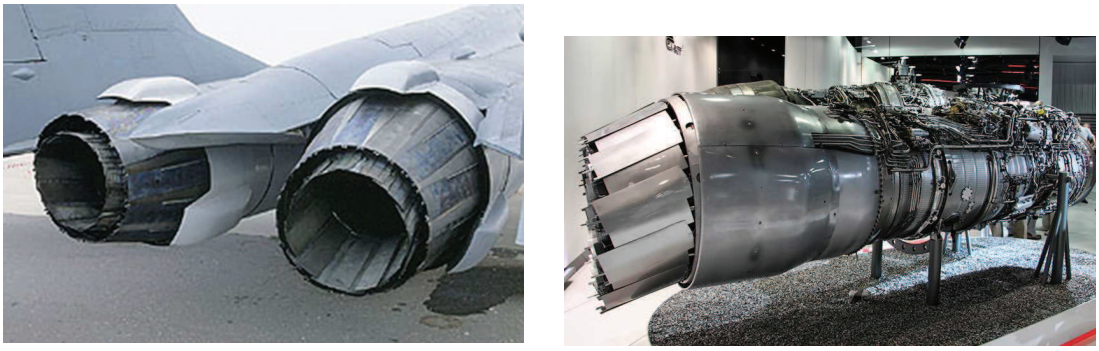

(a) MiG-29 OVT TVC nozzles (b) MiG-29 OVT's RD-133 TVC engine

Figure 1.2: TVC enabled super-manoeuvrability of MiG-29 OVT

The rocket nozzles usually use a hydraulic actuated gimbal in order to move

the whole nozzle with the combustion chamber. The flow throughout the nozzle remains axisymmetric while the nozzle axis alters the attitude towards the vehicle axis. This kind of the TVC system is conventionally used on the Ariane space launchers depicted in Figure 1.3a, JAXA H-IIB launcher, space shuttle main engines (SSMEs) and number of launcher and ballistic missiles rocket engines. One derivation of this system is to use a cluster of smaller nozzles which require less power to move and which may have faster dynamic response. The examples are Soyuz-TMA launcher depicted in Figure 1.3b, and planetary landers as the late NASA-MLS *Curiosity* Mars lander. In order to facilitate and improve vectoring system several alterations of mechanical TVC have been designed and used. Derived form Ariane 5 EAP project the new ESA Vega launcher uses electromechanically driven actuator pairs on the first three stages to control the vehicle attitude. By eliminating the previous robust hydraulic mechanical TVC, new system gain on reduced mass and a fewer percent faster dynamic response. One alternative used on the very light surface-to-air missiles or air-to-air missiles is use of mechanical deflectors which can be mounted on the nozzle exit creating a solid obstacle for the oncoming supersonic flow and therefore deflecting the jet.

(a) Ariane 5 Vulcain2 engine mounted on the support frame, gimbal and hydraulic actuators

(b) Main and auxiliary TVC nozzles of Soyuz TMA

Figure 1.3: Examples of mechanically driven space launcher TVC systems

Alternative to the mechanically driven TVC system can be found in the use of fluidic means for thrust vectoring. By the use of fluidic thrust vector control (FTV) it is possible to completely eschew mechanical and electromechanically driven hydraulic actuators and benefit from the substantially large mass reduction, simplicity of the system and a significant increase in the dynamic response, Riebe[1]. FTV, analyzed also in this study, considers the fixed nozzle geometry and use of the fluidic injection to divert the nozzle jet. There are several different concepts of the fluidic thrust vectoring which may be divided into the three major groups: the shock vector control by secondary fluid injection, the throat shifting method and counter and co-flow method. However, all three concepts utilize an asymmetric adverse pressure gradient which is generated by the secondary flow in the main jet.

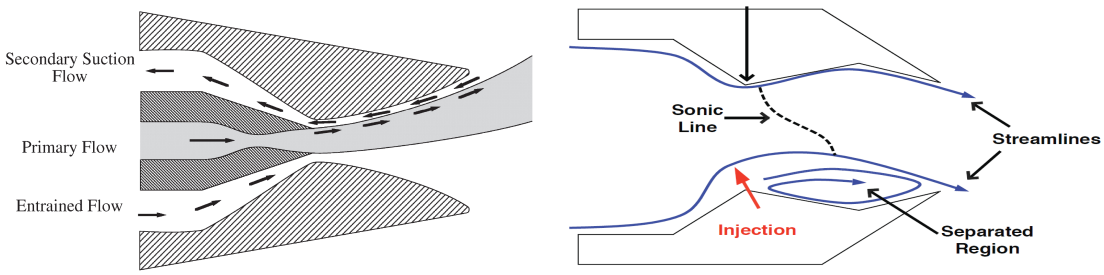

(a) Scheme of counter flow fluidic thrust vectoring

(b) Scheme of sonic line skewing for dual throat nozzle

Figure 1.4: Schemes of counter flow and throat shifting methods by Flamm[2]

Counter and co-flow method incorporates a secondary external channel or collar parallel to the nozzle wall, illustrated in Figure 1.4a. By this it is possible to create a counter flow suction on one side or co-flow injection generating an asymmetry in the main flow. The positive effects of this method was very good thrust ratio between non-vectoring and vectoring mode and relatively high deflection angles especially for the low supersonic flow velocities. Major drawbacks of this system are complex double nozzle geometry and therefore increase in size and mass and dangerous flow attachment due to Coanda's effect to the collar walls which are inevitable in certain flow regimes. Related to the counter flow method, the Coanda's effect co-flow injection showed possible thrust vectoring effects and it is investigated as a combined method with the shock vector control,

Deere[3]. Throat shifting method or skewing of a sonic line implies using of a forced asymmetric injection at the throat region of a convergent-divergent nozzle by which secondary air stream creates a new skewed aerodynamic minimum area. By shifting the throat location from the geometric minimum area to the new aerodynamic minimum size the flow turning occurs in the subsonic region. Subsonic flow turning minimize the thrust loses maintaining the relatively satisfying thrust vectoring effects for the low nozzle pressure ratios (NPR). For the higher NPR throat shifting method becomes inefficient in terms of delivered side force and inflicts instable supersonic flow. This method is also previewed by some researchers as an additional or combined method with the shock vector control for the multiaxis vectoring.

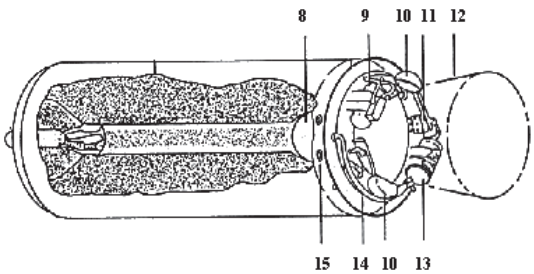

(a) Draft isometric view of the LGM-30 Minuteman2 second stage: 8-Nozzle throat; 9-TVC gas generator; 10-Injector control unit; 11-Injector ports (x4); 12-Nozzle exit cone; 13-Roll control gas generator; 14-Injectant tank; 15-Roll control nozzle (x4)

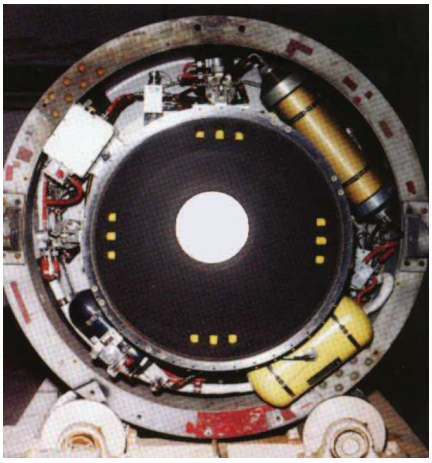

(b) Frontal image of Minuteman2 second stage engine

Figure 1.5: ICBM Minuteman-II LGM-30F second stage engine with SITVC

Thrust vector control by a secondary fluid injection represents a group of concepts where the secondary flow is transversely injected into the divergent section of a supersonic nozzle in order to deflect the main flow and to generate useful side force. Unlike the theoretical and experimental concepts mentioned above, SITVC is the method which was successfully used at several operating aerospace

vehicles. The investigation on this concept began in the early 1960s and it was very quickly implemented for the solid propellent rockets. As there were difficulties to gimbal solid propellent rocket engine due to position of the solid grain and the combustion chamber, an alternative was found in the secondary gas or liquid injection TVC using the additional tanks. The SITVC system was successfully incorporated in the land-based intercontinental ballistic missile (ICBM) beginning with LGM-30F *Minuteman-II* in Figure 1.5 and in the first submarine-launched ballistic missiles (SLBM) as UGM-27C *Polaris A3* and its successor UGM-73 *Poseidon*. With the operational use of contemporary liquid rocket engine SLBM *Trident* type, SITVC was discarded for the mechanically driven hydraulic TVC. However, evolution of the hybrid rocket engines in the past decades and their planned use on the new commercial space launchers and commercial tourist space planes has renewed rising interest in the SITVC and more attention has been paid to it over the past few years. For example, SPG Inc. a rocket engine supplier of the *SpaceX* incorporates SITVC system on its hybrid rockets using the fluid which is already stored in LOx tank, Simurda *et al.*[4] and Karabeyoglu *et al.*[5].

1.1 Study context

The promising FTV potentials in the large mass reduction, simplicity, effectiveness and responsiveness are especially inline with the needs of the small satellite "micro/nanosat" launcher as the one intended by the CNES *Perseus* program, Hingre *et al.*[6], Bec *et al.*[7]. The current PhD study is conducted in the framework of the CNES *Perseus* macro-project *Apteros* which is aimed at the development of the innovative and immature solutions for the advanced propulsion systems. Secondary injection thrust vector control of an axisymmetric supersonic nozzle as a context of this work is extensively elaborated covering the wide range of investigation aspects. This method of fluidic thrust vectoring is selected as a straightforward and relatively proved but not yet completely matured concept particularly for the aimed small space launcher without additional tanks and pressurization. Therefore, the study was conducted with starting premises to keep secondary pressure ratio close to the unity value, $SPR = 1$ and to keep secondary to primary mass-flow-rate ratio at the low-moderate level close or a bit above 5%

$f_m = \dot{m}_j/\dot{m}_0 \approx 0.05$.
Transverse injection at the divergent section of an axisymmetric supersonic nozzle generates a very complex flowfield and side effects. This complex flowfield involves the strong adverse pressure gradients, asymmetric supersonic flow separation inside the nozzle, shock generation, interaction and reflection, strong vortex dominated zones and vortex induced downstream mixing. These effects are coupled with the side effects of the nozzle wall bounded internal supersonic flow, irregular ambient conditions and properties of the primary and secondary injectants. To cover a number of fluid mechanics and aerothermodynamics rising problems, a thorough study is conducted comprising of the three major investigation approaches: theoretical/analytical study, and at fully extent experimental and numerical investigations. While experiments provide data about the flow, they often lack the possibility of having a direct and detailed insight into the physics of the flow field. The combined research methods therefore appear as a logical choice considering complexity of the problem and number of the investigation points. All aspects of the study are subjected to all three investigation approaches. Experimental results were paired with the numerical data and analyzed for isolated and coupled effects on the SITVC system. Experimental and numerical investigations are conducted in CNRS *Institute for Combustion Aerothermodynamics Reactivity & Environment* on the test platform which was developed during this study.

1.2 Document organization

The thesis manuscript is organized as follows.

Chapter 2 elaborates theoretical two-dimensional and three-dimensional cases of transverse injection at the flat plate and consequently in two-dimensional and axisymmetric three-dimensional nozzles. This is followed by the presentation of the axisymmetric C-D nozzle design governing equations and performance criteria. Last section of this chapter covers analytical approach and built analytic mathematical model for evaluation of the axisymmetric nozzle SITVC.

Chapter 3 presents experimental facility and experimental methods used in this study. Its sections cover the test bench description, qualitative methods,

quantitative flow and forces diagnostics and nozzle test models description.

Chapter 4 describes CFD approach and numerical test environment. Numerical models are presented and defined together with numerical grid design and mesh quality check.

Chapters 5, 6 and 7 are organized as an independent results discussion chapters with own introductory section on the beginning and conclusion at the end.

Chapter 5 describes the major influential aspects as the primary nozzle geometry, point of injection, mass-flow-rate ratio and flow regimes.

Chapter 6 deals with additional optimization points as the geometrical shape of the injector nozzle, the secondary injection angle and multiport fluidic thrust vectoring.

Chapter 7 elaborates gas properties effect on the SITVC and presents experimental and numerical results of the multispecies injection tests. This is further complemented by the multispecies analysis with combusted hot-gas numerical investigation on SITVC axisymmetric nozzle.

General conclusions and remarks for the future work are given at the end of this manuscript.

Chapter 2

Methodology and analytical approach in SITVC investigation

2.1 Fundamentals of supersonic cross-flow interaction field

The supersonic cross-flowfield induced by sonic transverse injection into an oncoming supersonic flow represents a problematic which is apparent in numerous aerospace engineering applications. These applications may range from the supersonic combustion process by a transverse sonic injection in a combustion chamber of the scram-jet engines to the hypersonic vehicle reaction control jets and various fluidic thrust vectoring applications.
The secondary flow injected through the sonic throat into the supersonic cross-flow acts as an obstacle and constitutes a source of the flow momentum change. As a response to the secondary jet obstruction, a strong bow shock wave is formed in the main flow separating the main supersonic flow from the injectant. Consequential to the bow shock, an adverse pressure gradient is generated, which upstream of the secondary injection port separates the main flow boundary layer. From the incipient detachment point originates a weaker separation shock with a milder slope towards the nozzle axis, that formes an interface between the wall and the separated main flow. In general, the separation distance depends on the penetration height of the injectant and the type and size of the main flow

boundary layer. The separated flow region is dominated by a recirculation vorticity zone, illustrated in Figure 2.1. Namely, in the upstream separated region, recirculation involves two counter-rotating vortices; the primary upstream vortex (PUV) close to the separation point that effectively governs the pressure rise till the plateau pressure value and the secondary upstream vortex (SUV) closer to the injection port and responsible for the pressure peak due to a sudden secondary jet expansion and separation-bow shock interaction. Secondary flow, injected through the sonic throat, is highly under-expanded and thus the expansion fan forms at the orifice with a Mach disk on the end of compression sequence. Downstream of the secondary injection port, a low pressure zone aft of the injector creates a suction which pulls the secondary jet plume towards the wall. Consequently, wake vortices shedding takes place at the wall boundary downstream of the injector and trailing vortices appear ahead of the secondary plume, which are mainly responsible for the effective turbulent mixing downstream.

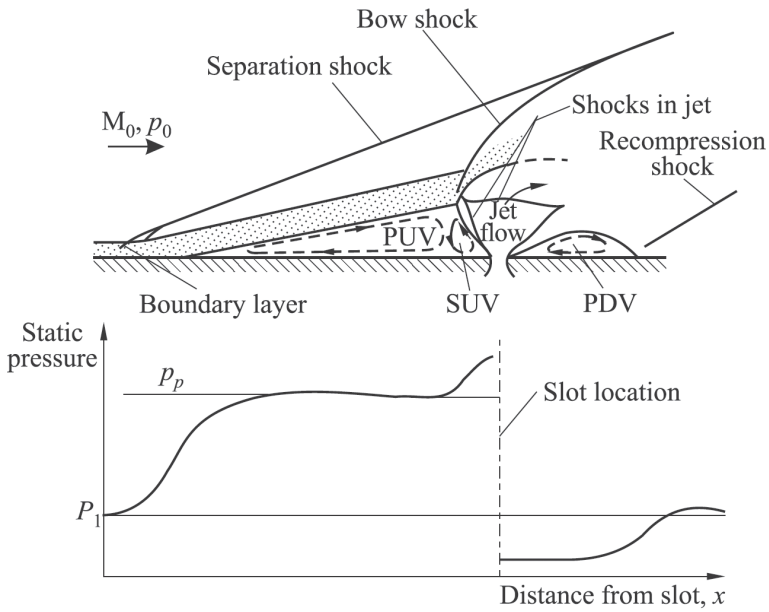

Figure 2.1: Scheme of 2D case of the slot injection on a flat plate and wall-pressure distribution estimation after Spaid and Zukoski [8]

Two fundamental cases may be naturally considered in a fundamental supersonic cross-flow interactions investigation. Sonic injection through the span-wise slot on a flat plate into the supersonic cross-flow is regarded as a two-dimensional case

where lateral movements and effects are neglected. Analogically, a sonic injection through the circular throat on a flat plate represents a basic three-dimensional case with distinctive effects in the axial, radial and lateral direction.

2.1.1 Two-dimensional case and previous works synthesis

More detailed investigations on the wall-bounded supersonic cross-flows emerged in 1960s primarily to comply the requirements of supersonic mixing and combustion applications but also for the purposes of fluidic thrust vectoring systems evaluation. Number of engineering design observations were gathered and investigated from the point of a basic two-dimensional (2D) case by several research teams as; Spaid and Zukoski at Caltech JPL[9] [10], Schetz and Billig at John Hopkins APL[11] [12] [13], Thompson, Hoffman and Guhse at Purdue JPC[14] [15] and in France by Allegre, Dupuichs and Devillers at CNRS-ICARE, previously laboratoire d'Aerothermique[16] [17] [18]. The topic was also extensively investigated by Russian researchers, as referred Avduevskii *et al.*[19].

Secondary transverse injectant plume, from the slot at a flat plate, rapidly and widely expands in the main flow with its windward side directly exposed to the formed bow shock. After generation and bending around the transverse injectant plume nose, the bow shock interacts with the weaker separation shock and continues through the main flow in a form of an oblique shock wave. On the injectant frontal edge the bow shock increasing the pressure while at at the leeward side low pressure zone aft of injector creates a suction that pulls secondary jet towards the plate. These actions fold and deform the shape of a secondary plume into the form of a concave body. Zukoski and Spaid[20] predicted that transverse slot injection therefore will obstruct the main supersonic flow in a quite similar way as a forward facing step which was investigated by Zukoski[21]. With an assumption that there is no mixing between the main and the secondary flows for a reasonable time and length they have developed the *blunt-body model* where the frontal surface of a blunt-body is modeled as a quarter cylinder continuing into the flat surface step as described in Spaid *et al.*[10]. Using this model and by applying force and momentum balance on the blunt body interface it was possible to derive and calculate penetration height of the transverse injectant as

a determining characteristic for the upstream separation and downstream mixing distances. For the better estimation, this procedure was coupled with the viscosity nature of the main flow boundary layer, reported in Spaid and Zukoski[8]. Generally, two coefficients were used for separation distance estimation which depends on the turbulent or laminar nature of the boundary layer. The shorter, turbulent boundary-layer separation was proved as being an invariant of the Reynolds number value as reported in Spaid[9]. Schetz and Billig[11] alike Devillers[17] paid further attention to the vortex generation in a supersonic cross-flow as it represents the main transport mechanism involved in separation region recirculation and in development of the downstream mixing zone. Evaluation of the forces exerted on a flat plate was reported by Broadwell[22] with the considered injectant configurations as liquid and gases, reactive and non-reactive. From the mentioned investigation, two empirical approaches were proposed; When the source is concentrated at the point, an idealization of the gas injection and corresponding *blast-wave theory* analysis are acceptable. Alternatively, the *linearized theory*[23] is found eligible when the source is distributed.

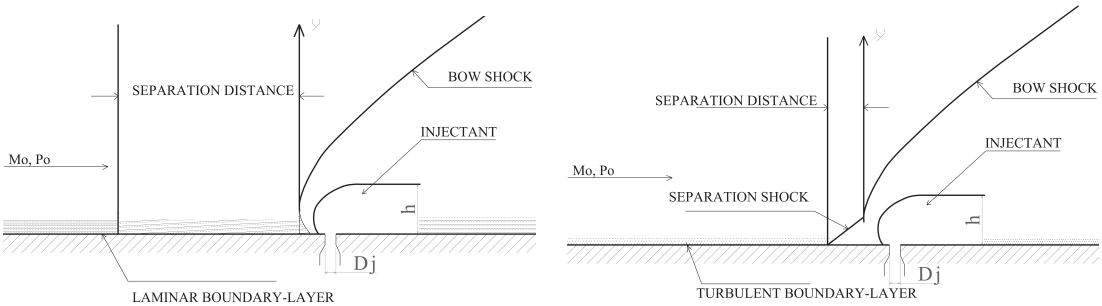

(a) Injection into laminar supersonic flow (b) Injection into turbulent supersonic flow

Figure 2.2: Scheme of blunt-body model by Spaid *et al.*[10]

With an evolution of the numerical methods and computational power, the computational fluid dynamics (CFD) approach became relevant during the past decades for the supersonic cross-flow analysis. Efforts on modeling and incorporating $k-\varepsilon$ turbulent stress model in viscous analysis by Chenault and Beran[24] were followed by experimental validation in the same study and previously in Papamoschou and Hubbard[25][26]. Analogously, Erdem and Kontis[27] elaborated and validated $k-\omega$ model with RANS solver on the Spaid *et al.*[10] experimental investigation.

Further attention was paid to the theoretical basis for numerical modelling of the vortex generation, transport mechanisms and mixing layers as in reported works by Delery and Dussauge[28] and Dussauge *et al.*[29]. Importance of the shock wave boundary-layer interactions was emphasized in these works pointing to the need of further analysis aimed in flow control mechanism. Late development of the advanced numerical methods as the large and detached eddy simulation (LES) and (DES) for the supersonic combustion purposes introduced these models to the supersonic cross-flows 2D problem as in Schetz *et al.*[30].

2.1.2 Three-dimensional case and previous works synthesis

Alike 2D nature of a slot injection case, a circular transverse sonic injection at the flat plate into a supersonic cross-flow is a purely three-dimensional case where flow effects propagate in all three spatial directions. After the incipient separation point and formation of a separation region, the counter-rotating vortices develop in a recirculation zone, propagating in the jet symmetry plane but also in the lateral span-wise direction. Initial vortices then merge into a horseshoe shaped vortical zone which wraps around injection port and effectively increases pressure in the affected zone of a flat plate. At the injection port a largely under-expanded secondary flow expands suddenly through the Prandtl-Meyer fan emerging at the edge of injection port and it is naturally surrounded by the barrel shock wave. Occurrence of the secondary jet expansion barrel shock in a supersonic cross-flow appears differently than the one in a quiescent medium. Namely, the shape of a secondary plume involves two prominent features; the barrel shock indentation due to a reflection on the flat plate and the inner shock reflection caused by the folding of the barrel shock windward side into itself. The strong expansion sequence ends with the Mach disk and a subsonic region behind it. Further downstream, the trailing cross-flow vortex pairs responsible for effective mixing appear with a maximum upwash velocity in the jet symmetry plane. At the flat plate aft of the injector, wake vortex shedding takes place. The bow shock follows the concave shape of a secondary jet plume and propagates in a vertical plane and laterally span-wise, forming a 3D shell around the secondary plume and the separation zone from the main supersonic flow, before mixing initiates on the

leeward side.

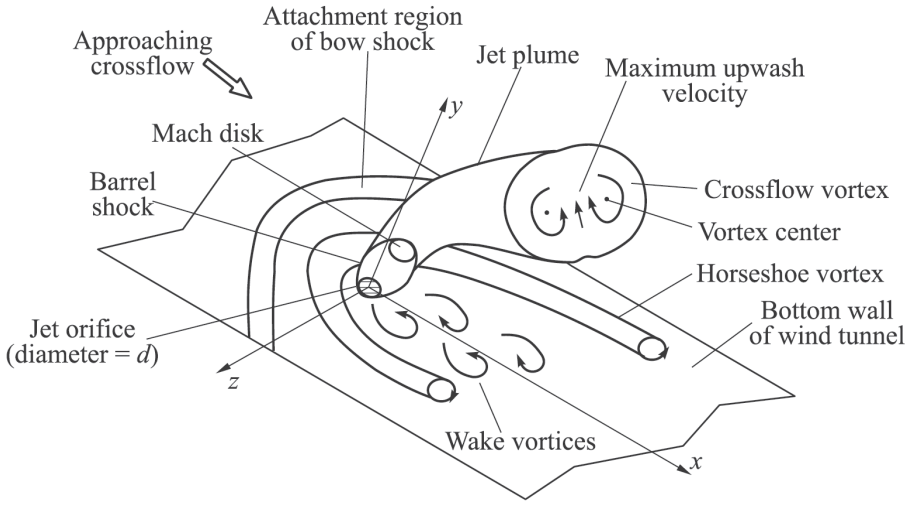

Figure 2.3: Scheme of 3D case of the circular sonic injection on a flat plate into supersonic flow after Santiago and Dutton[31]

Analogues to the mentioned 2D case which was first to be modeled analytically and then also present in the first numerical attempts, the 3D case represents a more challenging case to solve considering a three-dimensional nature of the turbulent shock waves boundary-layer interactions and mixing layers in the supersonic flow. The full numerical modeling was preceded by a fundamental investigation of a circular injection on the flat plate as for example in Broadwell and Breidenthal[32]. In the mentioned work authors were concentrated on description the transverse jet in a moving flow medium with an emphasis on the vortex formation, which govern dissipation and diffusion primarily present in mixing processes. Recirculation Γ of the vortices was defined via the transverse velocity of a jet and vortex core separation distance. The study on the vortex structure was then broadened by Haven and Kurosaka[33] who used a similar experimental setup but with considered compressible jet sources to describe the kidney and anti-kidney trailing vortex formation responsible for mixing initialization. Recirculation zones and vortex formation by a transverse sonic gas injection into supersonic flow and secondary jet structure was reported in Viti, Neel, and Schetz[34] where they tried to improve and in more detail explain the analytical model and jet penetration

studies reported previously in Schetz and Billig[11] and Billig *et al.*[13]. In the mentioned work[34], authors identified six primary vortices: the main separation horseshoe vortex, an upper trailing vortex, two trailing vortices aft of the bow shock and additional two trailing vortices that interact and form an unique rotational zone. The under-expanded transverse injectant recompress via barrel shock with a concave indentation of the barrel shock lee side and folding of the windward side due to an inner reflection line. Combined effect of the concave indentation in the leeward side of the barrel shock and the lower trailing vortices are found to generate a low pressure region aft of the injector.
Similarly to the early investigations, jet penetration experiments were performed by Hefner and Sterrett[35], Avduevskii *et al.*[19] and Vlagov *et al.*[36] in which jet location and penetration height were characterized in terms of the relative specific impulse of the jet, the injection angle and shape of the injectant nozzle. In the experimental work reported by Santiago and Dutton[31] two-component LDV was used to determine the three velocity components and five kinematic Reynolds stresses where maximum upwash velocity was found in-between the trailing cross-flow vortex pair. This study was followed afterwards by Chenault *et al.*[37] with a numerical attempt to model, simulate and analyze a detailed vortical structure. Used $k - \varepsilon$ turbulence model with RANS solver, reportedly, predicted very well the location and the size of the structures with also reported minor inconsistency in the turbulence intensity levels.

2.2 Transverse injection into a supersonic nozzle

The secondary transverse injection in a supersonic nozzle affects the bounded jet flowfield in a slightly different way than an open shear supersonic cross-flow on a flat plate. Namely, the generated structures largely affect the nozzle flow by eliminating the flow symmetry generating the boundary-layer separation, vorticity zone interactions and possible bow shock - nozzle interactions. In the reverse direction, the nozzle flow affects developing cross-flow structures and the secondary injectant plume by deforming these flow structures which results in a shock reflection inside the secondary plume. Analogously to the fundamental investigations, the two main supersonic nozzle cases may be distinguished;

a two-dimensional or planar convergent-divergent (2D C-D) nozzle, usually used in experimental configurations and at some advanced fighter jet engines and a three-dimensional axisymmetric convergent-divergent rocket nozzle.

2.2.1 Secondary injection in a two-dimensional planar C-D nozzle

The case of a secondary injection into a 2D supersonic nozzle has been extensively investigated for the fundamental flow physics effects and for the thrust vectoring purposes in some recent publications as in[38] [39] [40] [3] [38], as well as in the past decades[41]. Transverse injection into a 2D C-D nozzle exhibits the similar effects as 2D case of a slot injection at the flat plate. Separation inside the nozzle and a bow shock which correspondingly propagates in a free stream flow as an oblique shock, affects the main nozzle flow by diverting it through the shock wave. Additional effects may occur with an eventual occurrence of a shock reflection from the opposite wall side or flow reattachment downstream of the injector. Thrust loss due to a pressure change through the main shock was found rather small as the investigations were based on the lower Mach number nozzles intended for fighter jet engines as in Deere[42] and Mangin[38]. At higher NPRs, pressure loss affects the nozzle flow and significant effects on vectoring performances were reported. Multiport injection investigated for several interrelated positions of the injectors, was found somewhat more efficient for certain NPR values below 4 but without clear relation between the NPR value and inter-distance of secondary ports in Waithe and Deere[40]. With an increase of NPR the multiport injection was reported inefficient comparing to the single port injection of the same secondary mass flow rate.

Comparing the secondary injection pressure and the effects related to the separation and nozzle pressure loss, Mangin[38] reported that optimal effects are assumingly reached with a secondary injection adapted to the plateau pressure of a separation zone. Under that flow regime no expansion fan would occur at injector windward edge relieving the effect of separation zone on the penetrating secondary plume. In the lower Mach number nozzles this was possible to achieve by optimizing the size of the injector and position at the nozzle divergent

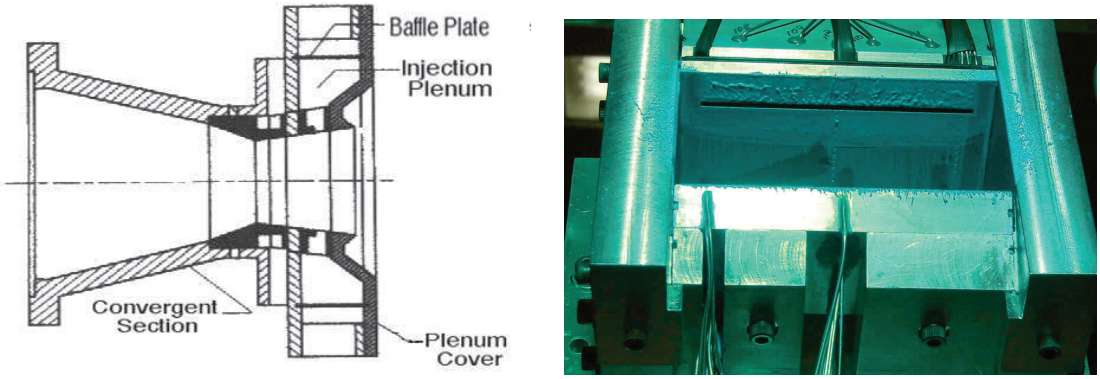

(a) Draft view of 2D C-D SVC nozzle (b) View of slot injection wall side

Figure 2.4: Experimental 2D C-D test nozzle for SVC by Waithe and Deere[40]

section. As reported in Mangin *et al.*[43] and Wing[41], position of the injector effect was limited and it was related to the adaptable flow regime. With an increase of NPR, injector position closer to the nozzle exit was found more efficient with the positive influence of the upstream inclined injection as well. Mangin[38] reported increase in the flow deflection with an upstream inclination till values of 60 degrees from the normal position. Nevertheless, completely parallel counter or Coanda's effect co-flow injection was found inefficient comparing to the slot transverse injection for the thrust vector control in a 2D C-D nozzle as denoted in Wing[41], while Flamm[44] reported an efficiency increase by this FTV method if the jet attachment is additionally regulated. The SVC in 2D C-D nozzle performed relatively more efficiently for smaller than higher NPRs. However, a smaller decrease in performances appear with injector positions allowing the shock impingement and reflection depending on a secondary pressure ratio (SPR). Considering that the throat skewing method yielded lower vectoring performances but higher non-vectoring to vectoring thrust ratios as in Wing[45] and Mangin[38], Deere *et al.*[46] proposed combination of the SVC and sonic throat skewing method to asses favorable effects of the both methods. However, SVC was found generally more viable vectoring type to be used for eventual implementation for fighter jet engines due to the system simplicity and avoiding potentially dangerous unsteadiness inside the throat skewed nozzle. Secondary injection in a 2D C-D nozzle, suitable for an experimental investigation, enables direct isolation of the fluid dynamics problem features and because of visual access it was

appropriate for investigation using the numerous flow visualization techniques as: shadowgraph, PIV and pressure color paint found in Mangin[38] and Jaunet[39]. Describing the secondary injection problem in 2D C-D nozzle with the velocity profiles according to Mangin[38] investigation, Jaunet[39] developed an approach using PIV technique and proper orthogonal decomposition (POD) to perform instability analysis of 2D C-D nozzle SVC problem. Small but positive side force was obtained and positive effects of injection close to exit and upstream inclination were also confirmed. The nozzle wall modification for thrust vectoring in this study generated a specific shock pattern that in correlation with an acoustic wave in the subsonic region generated a two-dimensional transverse jet flapping motion. Dynamic study performed on this flapping motion via proper orthogonal decomposition pointed to the aeroacoustic screech instability related problem but it was shown that modes of vectored and non-vector regime are very similar without significant impact. Additionally, laser Doppler velocimetry in the wake of actuator quantified the impact on mixing layer. Generally, studies on 2D nozzles indicated a good perspective for the SVC implementation on the new jet engines with meritorious effects of increasing dynamic response and maneuverability. However, some limitations in the performance not completely fulfilling demands of manufacturers, while the side effects of flow asymmetry and aero acoustic problems need to be further optimized.

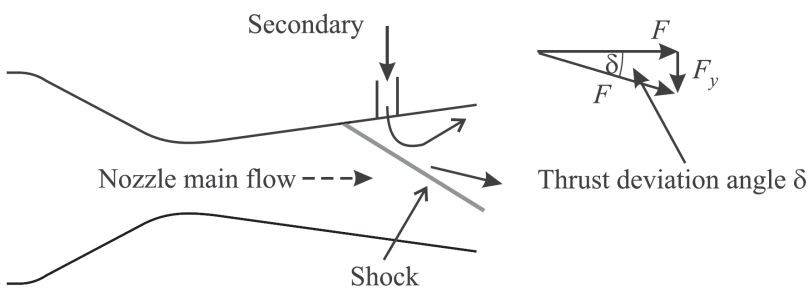

Figure 2.5: Simplified scheme of SITVC in an axisymmetric C-D nozzle

2.2.2 SITVC in a supersonic rocket nozzle

Engineering attempts to use secondary injection thrust vector control in a rocket C-D nozzle preceded 2D nozzles investigations. In these early studies empirical and theoretical-analytical methods were used in order to assess the positive and negative effects of a secondary injection in the divergent section of a rocket nozzle. The flow in an axisymmetric nozzle differs from the 2D case mainly by the flow structures development in the axial, vertical and lateral directions and because of pronounced nozzle wall effects. Early works as Broadwell[22] who evaluated force exerted on the wall adjacent to the injection port and Thompson *et al.*[14] which proposed evaluation parameters, tried to bridge a 2D injection problem to the axisymmetric nozzle case. Number of theoretical models that emerged from the fundamental supersonic cross-flow investigations as the blast wave theory, or already mentioned Zukoski and Spaid blunt body analytical model were adapted for the rocket nozzle SITVC. They were used to evaluate the performances and to identify determining characteristics as the separation distance and penetration height. Walker *et al.*[47] and in Walker and Shandor[23] proposed an adapted linearized model of fluid injection for thrust vector control.

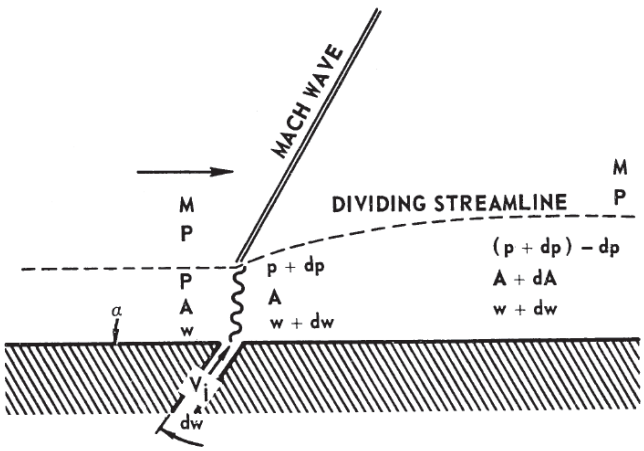

Figure 2.6: Scheme of the linearized model for fluid injection analysis by Walker and Shandor[23]

The mentioned model applied to the supersonic conical nozzle also considered and incorporated intrinsic gas properties which allowed SITVC theoretical analysis with different injectant gases. This model proved as very well posed in number of

followed investigations and theoretical models evaluation studies, as in Guhse[15] and Masuya *et al.*[48]. Since the first experimental investigations such as McAuley and Pavli[49], the researchers tried to analyze the different injection types and geometrical parameters in order to investigate optimal methods for engineering use. Different types of FTV as SITVC, wall-parallel counter and co-flow, slanted tube, throat skewing, dual throat, slot and multiport injection have been investigated and reported in works of Riebe[1], Nielson *et al.*[50], Woodberry and Zeamer[51], Flamm[2], Wing and Giuliano[52] and Hozaki *et al.*[53]. Evaluating the amplification factor, which was defined as the ratio of the effective specific impulse of secondary stream to the specific impulse of undisturbed primary flow, McAuley and Pavli[49] found that radial and upstream inclined secondary injection exhibit a substantially higher amplification factor than the tangential, slanted tube and throat skewing methods which have overall poor FTV performances. Comparing the position with a single and a multiport injection, it was found that multiport injection has optimal FTV values at position of 80% of main nozzle expansion while single injection side force was higher with position closer to the nozzle exit. In this study overall FTV performances was up to 10% higher for the single than for the multiport injection. Similarly to this and study of Guhse[15], Nielson *et al.*[50] investigated number of radial and parallel multiport arrangements in the rocket nozzle. The single port injection exhibited a higher effectiveness in all the arrangements and tests presented and reported in the study. Aim of the several studies was also to examine the injection angle effect on the SITVC system. In all of them, an angular injection relative to the nozzle axis and upstream inclined proved as the most efficient with some different conclusions about the optimal use. Riebe[1] evaluated range of injection angles in relation to linearity, vector system assembly and frequency response. Upstream angle value of 22.5^o was found optimal considering the force augmentation and fixed flow conditions. Experimental investigation of the large range of injection angles at one optimally selected secondary injection port position was conducted by Nielson *et al.*[54]. Similarly to the McAuley and Pavli[49] and Riebe[1], Nielson *et al.*[54] reported a gradual augmentation of the side force with an upstream injection inclination increase. For their Mach 2 nozzle, a breakdown angle of 48.5^o was detected after which, a rapid deterioration in performance was observed. Ana-

logues to the increase of side force with an upstream inclined injection, there is a corresponding decrease in an axial thrust augmentation. On the other hand, downstream oriented injection decreases side force and vectoring but increases the axial thrust. Considering these points and optimal vectoring system Woodberry and Zeamer[51] proposed a variable orifice injectors which could be positioned according to the need and flight regime. For the fixed injection, Woodberry and Zeamer[51] found upstream oriented angular injection of 25° as the optimal one using the inert liquid injectants.

(a) $f_m = 0.03$ small separation zone and downstream flow reattachment

(b) $f_m = 0.07$ larger separation, no reattachment

Figure 2.7: Pressure sensitive color oil photographs of nozzle-wall shock interface by Newton and Spaid[55]

Naturally, the most dominant characteristics in aerodynamic forces evaluation, for the predefined injectants, was the secondary mass-flow-rate. For the sonic secondary injection, critical mass-flow-rate is defined as function of the injectant total pressure and temperature, molar mass, γ and the secondary injection port area. Number of investigations considered amplification factor with the different secondary injection mass-flow-rate configurations. The side force almost linearly increases with the increase of a secondary mass flow $\dot{m}_j$. Nevertheless, it is denoted that performance decreases if the mass flow rate is increased by enlarging injection port as reported in Guhse[56], Guhse and Thompson[57], Hozaki

et al.[53], Newton and Spaid[55], Walker *et al.*[47], Nielson *et al.*[58], Woodberry and Zeamer[51], Viti *et al.*[59] and Ko and Yoon[60]. This amplification decay is related to the interaction of flows and higher momentum of higher pressure gas that play the major role in diverting the main jet and augmenting the injectant natural reactive force. The other effect of the secondary injection position comes from the lower static pressure at the nozzle stations closer to the exit enabling the higher injection reactive force (dynalpy flux) and thus an increased penetration or accommodation height. Nielson *et al.*[58] also denoted that the reduction of the side force will occur when the trace of the shock on the nozzle wall crosses the center-line of the nozzle. The effects of the affected nozzle flow in different cross-sections are also captured using the laser induced fluorescence method in New and Tay[61]. Concerning the optimal mass flow rate injection, Wing and Giuliano[52] investigated a geometrical shape of the injector as the circular, ring and slot injection and its effect on the performances. The ring injection was disregarded in mentioned investigation as it proved to be inefficient, while the slot injection for certain applications showed increase in the side force and overall performances. Wing and Giuliano[52] concluded that geometrical shape of injector overall has just a minor effect on the FTV system performances. Finally with an evolution of the numerical methods in the last decades, number of investigations based on the numerical simulations as Ko and Yoon[60] or Maarouf[62] examined SITVC problem and possible optimization techniques.

2.3 Axisymmetric convergent-divergent nozzle design and performance

Supersonic convergent-divergent propulsive nozzle as an end-element of the propulsion cycle of any rocket engine enables the expansion of propellents from subsonic state in the combustion chamber to the supersonic flow regime at the nozzle exit plane. The task of accelerating and efficiently exhausting combusted and reactive gases according to the delivered thrust is the main objective of the propulsion system design. Imposing the nozzle inlet stagnation properties (p_0, T_0) together with the geometric characteristics of the nozzle throat area A_c and nozzle expansion ra-

tio it is possible to calculate other quantities using the theory of one-dimensional nozzle flows. The one-dimensional theory assumes that the flow properties are constant across the section A normal to the nozzle axis. Since the flow in the real nozzle is of two-dimensional character, or in complicated cases three-dimensional, these assumptions represents only raw approximation. However, 1D flow theory often provides reliable approximation at the preliminary design stage. Compressible nozzle flow theory is a fundamental matter of any relevant gas dynamics literature as Liepmann and Roshko[63]. In the current study, used and derived theories at predesign stage originate mainly from Delery[64], where they are elaborated in more detail.

According to the presented 1D theory, the fluid is assumed as a non-viscous and the flow permanent, while the nozzle is approximated to ensure an isentropic expansion from the initial conditions (p_0, T_0) to the conditions in the exit plane $(p_e, T_e, \rho_e ...)$ Considering these assumptions, the expansion can be represented in the Mollier (S, h)diagram available in Delery[64]. In the context of 1D hypothesis the flow is governed by the continuity equation 2.1, Euler equation of motion 2.2 and energy equation 2.3.[1]

$$continuity: \quad \frac{d\rho}{\rho} + \frac{du}{u} + \frac{dA}{A} = 0 \tag{2.1}$$

$$Euler: \quad u \cdot du + \frac{dp}{p} = 0 \tag{2.2}$$

$$energy: \quad h + \frac{u^2}{2} = h_0 = const \tag{2.3}$$

Substituting the values in above first two equation, under the isentropic flow assumption, results in:

[1]all the notations are explained in the nomenclature section

$$\frac{du}{u}\left[1-\frac{u^2}{(dp/d\rho)}\right]+\frac{dA}{A}=0 \tag{2.4}$$

$$c^2=(\frac{\partial p}{\partial \rho})_S=\frac{dp}{d\rho} \tag{2.5}$$

and finally resulting in fundamental $Hugoniot$ equation 2.7 that characterize continues, steady, inviscid, divariant and non-reacting supersonic flow.

$$\frac{du}{u}\left(1-\frac{u^2}{(c^2)}\right)+\frac{dA}{A}=0 \tag{2.6}$$

$$\frac{du}{u}\left(1-M^2\right)+\frac{dA}{A}=0 \tag{2.7}$$

These equations need to be supplemented by a thermodynamic relation. Supposing a perfectly calorical gas, energy equation may be written as;

$$C_pT+\frac{u^2}{2}=C_pT_0=const \tag{2.8}$$

$$\Rightarrow\ u^2+2C_pT=const, 2C_pT=\frac{2}{\gamma-1}c^2 \tag{2.9}$$

$$u^2+\frac{2}{\gamma-1}c^2=const \tag{2.10}$$

with resulting $Saint-Venant$ equation 2.10. According to the Mollier (s,h) gas thermodynamic distribution it is possible to calculate flow properties for each nozzle section, $A(x)$. With the known critical section area A_c and perfectly calorical gas assumptions it is possible to deduce properties relation in any nozzle cross section according to the fundamental, $Saint-Venant$ and $Hugoniot$ equations.

$$\frac{T}{T_0} = \left(1 + \frac{\gamma - 1}{2} M^2\right)^{-1} \tag{2.11}$$

$$\frac{p}{p_0} = \left(1 + \frac{\gamma - 1}{2} M^2\right)^{-\frac{\gamma}{\gamma-1}} \tag{2.12}$$

$$\frac{\rho}{\rho_0} = \left(1 + \frac{\gamma - 1}{2} M^2\right)^{-\frac{1}{\gamma-1}} \tag{2.13}$$

$$\frac{A}{A_c} = \frac{1}{M}\left[\left(\frac{2}{\gamma+1}\right)\left(1 + \frac{\gamma - 1}{2} M^2\right)\right]^{\frac{\gamma+1}{2(\gamma-1)}} \tag{2.14}$$

$$u = \sqrt{2(h_0 - h)} \xrightarrow{h=0, vaccum} u_* = \sqrt{2h_0} = \sqrt{\frac{2}{\gamma - 1}} c_0 \tag{2.15}$$

In one-dimensional theory under the steady state assumption, a nozzle mass flow rate can be calculated using the continuity equation for critical (throat) nozzle section $\bar{\dot{m}}_q$, 2.16. Calculated ideal critical mass flow rate should be then corrected with the discharge coefficient C_d representing a mass flow deviation from the ideal case according to the gas properties, type of boundary layer and shape of the throat.

$$\bar{\dot{m}}_q = \frac{C^*(\gamma)}{\sqrt{C_p T_0}} p_0 A_c, \quad where: \tag{2.16}$$

$$C^*(\gamma) = \frac{\gamma}{\sqrt{\gamma - 1}} \left(\frac{\gamma + 1}{2}\right)^{-\frac{\gamma+1}{2(\gamma-1)}}, \dot{m}_q = C_d \bar{\dot{m}}_q \tag{2.17}$$

2.3.1 Calculation of the forces acting on an axisymmetric C-D nozzle

With an assumption that the fluid does not have weight and the motion is steady it is possible to define the balance between the momentum flux forces of the fluid

and the tension vector $\vec{P}$ that represents the contact forces exerted by the fluid on a close surface (S).

$$\iint_{(S)} \left[\vec{P} + (\rho\vec{u}.\vec{n})\,\vec{u}\right] dS = 0, \quad or: \tag{2.18}$$

$$\iint_{(S)} \vec{D} dS = 0, \vec{D} = \vec{P} + (\rho\vec{u}.\vec{n})\,\vec{u} \tag{2.19}$$

With dynalpy, $\vec{D}$, defined as an integrant of the force balance relation, it is directly deductable that flux of the dynalpy vector through the closed surface is zero. Applied to the nozzle case where forces acting on the external side of the nozzle wall (S_2) (drag) with momentum flux term in that case set to zero, it is possible to derive dynalpy flux relations as:

$$\vec{R} = -\left[\iint_{(S_1)} \vec{D} dS + \iint_{(S_2)} \vec{D} dS\right] \tag{2.20}$$

$$\iint_{(S_1)} \vec{D} dS = -\iint_{(S_2)} \vec{P} dS = -\vec{R} \tag{2.21}$$

where it is possible to arrive to conclusion that a resultant of aerodynamic forces is equal to the opposite flux of the dynalpy vector through a surrounding surface. Applied to the 1D theoretical nozzle for ideal case when caption drag is zero, or nozzle vacuum operation it is possible to define intrinsic or vacuum thrust as:

$$F_e^* = -\left(\iint_{(S_e)} \vec{D} dS\right) \cdot \vec{x} = \iint_{(A_e)} \left[\vec{P} + (\rho\vec{u}.\vec{n})\,\vec{u}\right] dS \tag{2.22}$$

For the nozzle atmospheric operation, the caption drag exists and it may be considered as a tension vector or ambient pressure force acting on the nozzle surface. Applied to the 1D nozzle flow pressure forces on the external surface cancel each other due to axisymmetric shape leaving only the pressure force actin on a exit section. The conventional or gross nozzle thrust is then defined as a force opposite to the resultant in the nozzle exit section.

$$F_e^* = \iint_{(A_e)} \left[\vec{P} + (\rho\vec{u}.\vec{n})\,\vec{u}\right] dS - \iint_{(A_I)} \vec{P} dS \tag{2.23}$$

$$\xrightarrow{1Dsolution} F_{ex} = [\rho_e u_e^2 + (p_e - p_a)]A_e \tag{2.24}$$

In this PhD study, reactive thrust force is evaluated at the exit section of the main axisymmetric supersonic nozzle models and at the injection port on the divergent nozzle section in the y direction. Surface integrals of the pressure and viscous forces on the nozzle walls are then calculated for the side force evaluation.

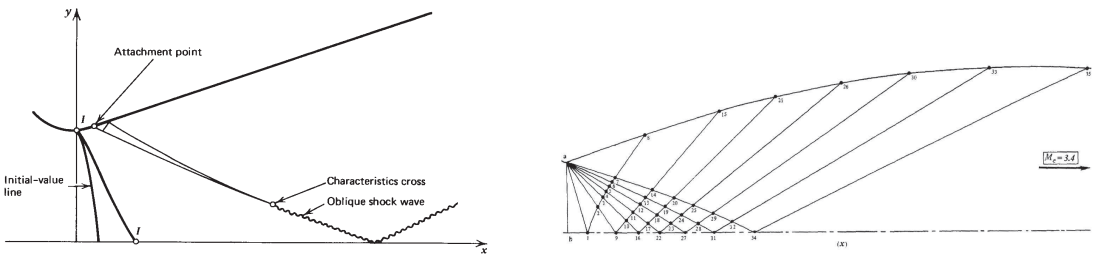

(a) Initial-value sonic line and conical profile and characteristic compression waves

(b) Ideal contour profile characteristics

Figure 2.8: Scheme of Method of characteristics procedure by Zucrow and Hoffman[65]

2.3.2 Design of an axisymmetric C-D nozzle contour

Four axisymmetric C-D nozzle types are considered in this study. Analytical, experimental and numerical analyses were based on the referent conical and truncated-ideal-contour (TIC) Mach 3 nozzles. Additionally, for comparison and results discussion Rao thrust-optimized-contour (TOC) and Rao adverse-pressure-gradient (APG) nozzles are numerically simulated for the referent SITVC case and compared in the Chapter 5.

1. *Conical C-D nozzle*

   The conical C-D nozzle of Mach 3.01 is designed as a subscale model to the nozzle intended for the *Perseus* launcher and according to the wind-tunnel

design requirements and limitations. Basic nozzle parameters are given in the Table 2.1.

Table 2.1: Conical C-D nozzle design parameters

Parameters	Values
throat radius	$r_{th} = 9.89 \cdot 10^{-3} m$
divergent section length	$L = 10.11 r_{th} = 100 \cdot 10^{-3} m$
expansion ratio	$\sigma = A_e/A_{th} = 4.09$
half conical angle	$\kappa = 5.8^o$
conical loss factor	$\frac{1+\cos\kappa}{2} = 0.9974$
exit Mach number	$M_e = 3.$
designed nozzle pressure ratio	$NPR_D = 37$

Conical nozzle with the small half-conic angle was selected providing a very low loss factor averaged to 0.9977 of the ideal nozzle thrust.

2. *Truncated-Ideal-Contour axisymmetric C-D nozzle*

   To design a TIC nozzle, calculation of an ideal profile based on the three-dimensional method of characteristics was used as it may be found in Zucrow and Hoffman[65]. As the initialization values, stagnation pressure and temperature of $p_0 = 300kPa$ and $T_0 = 247K$ were used according to the wind-tunnel conditions. The throat curvature was aimed to be very smooth and continual with the subsonic and supersonic curvature radii equal to the 3 times throat radius $r_{csub} = r_{csup} = 3 \cdot r_{th}$. Therefore, it was acceptable to calculate sonic line according to the Sauer's method[65] which was the initialization point for the method of characteristic calculation, with potential velocity as the marching characteristic. Final ideal contour nozzle is calculated until the completely parallel uniform flow at the nozzle exit and vacuum conditions. The calculated ideal profile is then truncated at the section where $p_e = 8kPa$ according to the wind-tunnel design conditions which also corresponded to the optimal thrust. As the method of characteristics is an ideal inviscid method, 2D axisymmetric numerical RANS calculations are performed with the $Spalart-Alamaras$, $k-\epsilon$ and $k-\omega$ turbulence model in order to identify boundary layer size. Final TIC contour is corrected for these values.

Table 2.2: TIC C-D nozzle design parameters

Parameters	Values
throat radius	$r_{th} = 10 \cdot 10^{-3} m$
divergent section length	$L = 6.8 r_{th} = 68 \cdot 10^{-3} m$
expansion ratio	$\sigma = A_e/A_{th} = 4.87$
exit Mach number	$M_e = 3.03$
designed nozzle pressure ratio	$NPR_D = 37.5$

Design of the nozzle and method of characteristics are explained in Appendix 7.8 in more details.

3. *Optimized nozzle contours*

   Two Rao optimization methods are used to design and numerically test and compare eventual use of optimized nozzle contour with the SITVC system. These nozzles were not experimentally verified and tested in the current study. However, the selected nozzle cases have been experimentally tested in other facilities; TOC at LEA Poitiers as in Deck[66] and APG nozzle has been investigated for SITVC use and reported in Hozaki *et al.*[53].

   Thrust optimization implies the shortening of the nozzle length and increasing the thrust ratio according to Rao[67]. Thrust or weighted optimized characteristic calculations produces a nozzle contour which unlike the ideal de Laval contour, allows appearance of the internal shock. Namely, after the small supersonic portion throat curvature radius the nozzle contour evolves with a steep gradient that the nozzle flow expansion cannot follow ideally. This results in the inflection point in the divergent section close to the throat at which an internal shock emerges separating the high momentum kernel flow from the lower momentum peripheral flow.

   Finally, for the SITVC and fluidic thrust vectoring methods that utilize adverse pressure gradient, Rao[68] proposed a design of the nozzle that would have pressure profile favorable for the adverse pressure gradient but without loosing the basic nozzle performances. This nozzle type is designed according to Rao $24° - 2$ Mach 5 nozzle and further investigated numerically with details given in Chapter 5.

Table 2.3: TOC axisymmetric C-D nozzle design parameters

Parameters	Values
throat radius	$r_{th} = 10 \cdot 10^{-3} m$
divergent section length	$L = 15 r_{th} = 15.075 \cdot 10^{-3} m$
expansion ratio	$\sigma = A_e / A_{th} = 30.25$
exit Mach number	$M_e = 5.2$
designed nozzle pressure ratio	$NPR = 600$

2.4 Definition of analysis and performance parameters

To measure and quantify observed nozzle interaction flowfield the analysis parameters are defined. They are derived to faithfully represent numerical and experimental information data, to analyze and compare them. Some of the parameters are fundamental and common in compressible fluid dynamics analysis while there are also specifically derived parameters in order to best describe secondary injection fluidic thrust vectoring case. All further discussed analysis parameters are defined in this section.
One of the fundamental fluid dynamics quantity is the free stream dynamic pressure defined as:

$$q_n = \frac{1}{2} \rho_\infty u_\infty \tag{2.25}$$

The free stream parameters in this study are taken for the nozzle exit. However, the nozzle models used in this study are not ideal de Laval nozzles with uniform velocity profile on the exit but with the variable one. In accordance with this free stream values are defined for the exit portion that was between 0.6 and 0.8 of the exit radius with the pressure conditions matching ambient and designed (adaptation) ones. Therefore, the q-dependent coefficient values should be regarded as a normalized coefficient. Free stream conditions are denoted in the Chapter 3.

Basic aerodynamics coefficient is the coefficient of pressure which for compressible supersonic flow is slightly modified to account the compressibility and can be defined according to Delery[64]:

$$c_P = \frac{2}{\gamma \cdot M_\infty^2}\left(\frac{p}{p_\infty} - 1\right) \tag{2.26}$$

The other nondimensionalized pressure value that can be used is the pressure nondimensionalized by the referent total chamber pressure P_0 which was kept constant in this study. $c_P^* = (p/P_0)$
Additionally, in evaluating the pressure and separation zone the skin friction coefficient C_f can be defined.

$$C_f = \frac{\tau_w}{q_n}, \text{or here alternatively: } C_f^* = \frac{\tau_w}{P_0} \tag{2.27}$$

where the wall-shear-stress is:

$$\tau_w = \mu\left(\frac{\partial u_{tan}}{\partial d_n}\right)_{d_n=0} \tag{2.28}$$

with u_{tan} and d_n representing the velocity parallel to the wall and the normal distance to the first cell. Since the nozzle wall is not flat but highly deviated, at each computation point geometric transformation needs to be performed to evaluate the wall shear stress. By denoting the wall and the first cell value with an index w and *1* simplified transformation is written as:

$$\tan\alpha = \frac{y_{w(i+1)} - y_{w(i)}}{x_{w(i+1)} - x_{w(i)}} \text{ and } yl_1 = y_{w(i)} - y_{1(i)}$$

$$d_n = \sqrt{\frac{(y_{w(i)} - y_{1(i)})^2}{1 + (\frac{y_{w(i+1)} - y_{w(i)}}{x_{w(i+1)} - x_{w(i)}})^2}} \tag{2.29}$$

By defining the minimal normal distance it is possible then to evaluate a modulus of the wall shear stress form the non-dimensional wall distance for a wall-bounded flow which can be defined in the following way:

$$y+ = \sqrt{\frac{\|\tau_w\|}{\rho}}\frac{\rho}{\mu}d_n \tag{2.30}$$

The global force exerted on the nozzle wall can be defined as a surface integral

of the pressure and viscous forces acting on the wall as:

$$F_w = q \cdot \oint \oint c_P dS - \oint \oint \tau_w dS \tag{2.31}$$

Similarly, moment created by this force around the z-axis, for the coordinate system placed at the throat center, can be defined as:

$$M_{wz} = q \cdot \oint \oint c_P \cdot x dS - \oint \oint \tau_w \cdot x dS \tag{2.32}$$

The wall force coefficient is then:

$$C_{Fw} = \frac{F_w}{Dp_0} \tag{2.33}$$

Where, Dp_0 is the dynalpy flux of the primary jet. One can note that such a defined force and coefficients does not consider contributions of the primary and secondary jet momentums.

Secondary injection performance parameters:
To quantify global effects of the secondary injection in the supersonic nozzle several additional parameters are defined. The vectoring or peaching angle δ is defined as:

$$\delta = \arctan\left[\frac{F_y}{F_x}\right] = \tan^{-1}\left[\frac{\sum f_Y + \sum(\dot{m}u)_y}{\sum f_X + \sum(\dot{m}u)_x}\right] \tag{2.34}$$

representing the ratio of the pressure forces and the momentum fluxes in y and x directions. However, this parameter needs to be coupled with the performance coefficients in order to correctly evaluate contributions of the secondary injection. Previously simple defined vectoring and global amplification factors by Riebe[1], McAuley and Pavli[49] and Guhse[15] representing "the ratio of the effective impulse of the secondary stream to the undisturbed specific impulse of the primary stream" are slightly modified to correspond better to the previously defined vectoring angle. Therefore, the vectoring and global amplification factors are:

$$C_{AV} = \frac{\arctan \frac{F_y}{F_x}}{\left(\frac{\dot{m}_j}{\dot{m}}\right) \cdot 100} \tag{2.35}$$

$$C_{AI} = \frac{I^*_{sp}}{I_{sp0}} = \frac{\frac{\sqrt{F_x^2+F_y^2}}{\dot{m}_0+\dot{m}_j}}{\frac{F_0}{\dot{m}_0}} \tag{2.36}$$

and related force amplification coefficient:

$$C_{AF} = \frac{\sqrt{F_x^2 + F_y^2}}{F_0} \tag{2.37}$$

Above-defined performance criteria is presented in the graphs and tables with corresponding non-dimensionalized units as NPR, SPR mass-flow-rate ratios, pressure ratios (p/P_0), pressure coefficient c_P and the non-dimensionalized space coordinates (x/l_n, x/D_j) and the temporal scales.

2.5 Analytical modeling of the SITVC in an axisymmetric C-D nozzle [1]

The analytical blunt body model by Spaid and Zukoski constitutes a basis of an adopted model used to solve equations for penetration height and separation distance. Criteria proposed by the different authors as in Billig *et al.*[13], Schetz and Billig[11] and Green[70] are used to complement the blunt body model expressions for an axisymmetric conical nozzle case, as in Maarouf[62]. The separation point and penetration height parameter may be evaluated from the momentum equations and pressure relations of the selected free shock separation (FSS) criteria. The 2D scheme of the transverse injection blunt body model is depicted in Figure 2.9. The penetration height h is found from the momentum balance applied to the control volume in the x direction. Control volume depicted in Figure 2.9 defines the interface between the wall and the main and injected flow in the symmetry plane. The balance relation implies that net pressure force, or

[1] Some of the presented work is adapted in:
Sellam, Chpoun, Zmijanovic, and Lago[69], *Int. J. Aerodynamics* **2** 2,3,4 (2012)

drag, acting on the control volume boundary surface is equal to the momentum of fluid leaving the domain. As proposed by Spaid and Zukoski the approximation of this interface is modelled as a quarter sphere of radius h followed by the half open cylinder.

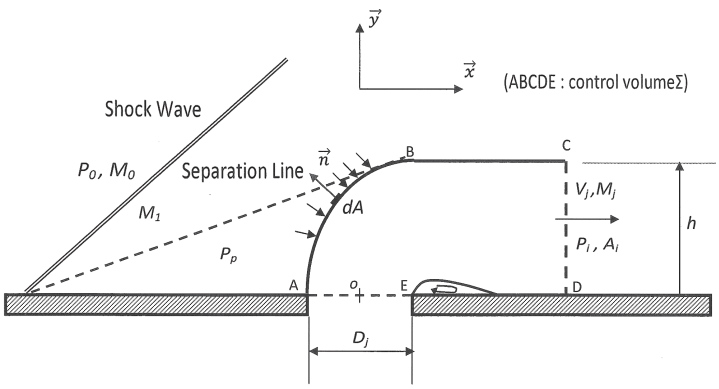

Figure 2.9: Simplified scheme of the transverse injection into the supersonic cross-flow

It is possible to decompose the balance equation of pressure forces that act on the control volume boundary with the momentum rate. Momentum rate through $\overline{ABC}$ boundary is zero as no mass exchange is assumed between primary and secondary jets.

$$\int_{\Sigma} \rho \overrightarrow{U}\,\overrightarrow{U}\,\overrightarrow{n}\,dA = \int_{\Sigma} -p\overrightarrow{n}\,dA \tag{2.38}$$

$$\int\limits_{AB} -p\overrightarrow{n}\,dA + \int\limits_{CD} -p\overrightarrow{x}\,dA = \int\limits_{CD} \rho \overrightarrow{U}\,\overrightarrow{U}\,\overrightarrow{x}\,dA \tag{2.39}$$

The net force acting on the control volume in x-direction may be separated on pressure force acting on the upwind section of the interface $\int_{AB} -p\overrightarrow{n}\,dA = F_{x1}\overrightarrow{x}$ and the forces at the exit of control volume, $\int_{CD} -p\overrightarrow{x}\,dA = F_{x2}\overrightarrow{x}$. While along $\overline{CD}$ boundary $\overrightarrow{U} = u\overrightarrow{x}$, then

$$\sum F_x = \int\limits_{CD} \rho u^2 ds = F_{x1} + F_{x2} \tag{2.40}$$

where, F_{x1} or drag is defined as an integral of the pressure force over the spherical

surface, approximated by the Newtonian law:

$$F_{x1} = \int_A dF_{x1} = \int_0^{\frac{\pi}{2}} p \cos\theta dA \tag{2.41}$$

solved for the radius h this integration gives:

$$F_{x1} = \frac{\pi h^2}{2}\left(p_0 + \frac{1}{2}q_0 C_{pmax}\right) \tag{2.42}$$

Where, C_{pmax} is the pressure coefficient corresponding to the the maximum angle θ, $\pi/2$, between the incident pressure force direction and the normal to the wall. It can be also represented in relation to the total pressure P_{01} behind a normal shock standing in the main flow which is characterized by the values of pressure p_0, Mach number M_0 and dynamic pressure q_0 before the separation.

$$C_{pmax} = \frac{P_{01} - p_0}{\frac{1}{2}\rho_0 u_0^2} \tag{2.43}$$

$$\frac{P_{01}}{P_0} = \left[\frac{(\gamma+1)^2 M_0^2}{4\gamma M_0^2 - 2(\gamma-1)}\right]^{\gamma/(\gamma-1)} \left[\frac{1-\gamma+2\gamma M_0^2}{\gamma+1}\right] \tag{2.44}$$

F_{x2} represents x-component of the resultant force acting at the exit of the control volume interface. The exit section is defined as a semi-circular cross-section with an area A_i and with a corresponding exit section pressure p_i which may be equalized to the ambient pressure for the adapted regime conditions.

$$F_{x2} = -p_i A_i = -p_i \frac{\pi}{2} h^2 \tag{2.45}$$

This leads to the expression of the x-component net force:

$$\sum F_x = \pi h \left(\frac{p_0 - p_i}{2} + \frac{1}{4}q_0 C_{pmax}\right) \tag{2.46}$$

Interior of the control volume interface is defined by the secondary injectant. Basic 1D isentropic flow relations give the momentum expression for the sonically injected transverse secondary flow:

$$\int \rho v^2 ds = \dot{m}_j V_j \tag{2.47}$$

where, $\dot{m}_j$ denotes the mass flow rate of the injectant and V_j flow velocity. Further isentropic transformations give:

$$\dot{m}_j V_j = 2C_d A_j \gamma_j P_{0j} \left(\frac{2}{\gamma_j - 1}\right)^{\frac{1}{\gamma_j - 1}} \cdot \left[\frac{1}{\gamma_j^2 - 1}\left(1 - \left(\frac{p_j}{P_{0j}}\right)^{\frac{\gamma_j - 1}{\gamma_j}}\right)\right]^{\frac{1}{2}} \tag{2.48}$$

where, C_d is a discharge coefficient and A_j represents area of the injector defined by its diameter D_j. Pressure terms represent a total pressure of the secondary jet, P_{0j} and pressure at the exit of control volume, p_j . Finally, by replacing corresponding terms in the Eq. 2.40 it is possible to derive an expression for the penetration height h_j.

$$h_j = D_j \sqrt{\frac{C_d \gamma_j P_{0j} \left(\frac{2}{\gamma_j - 1}\right)^{\frac{1}{\gamma_j - 1}} \sqrt{\frac{1}{\gamma_j^2 - 1}\left(1 - \left(\frac{p_j}{P_{0j}}\right)^{\frac{\gamma_j - 1}{\gamma_j}}\right)}}{(p_0 - p_i) + \frac{q_0 C_{pmax}}{2}}} \tag{2.49}$$

Two empirical FSS criteria, adapted to conical nozzles, are considered in analytical assay to determine unknown pressure variables. The Schilling[71] criterion based on the cold flow experiments conducted with a conical and a truncated ideal nozzle gives the pressure relation for supersonic nozzle free separation as:

$$\frac{p_{sep}}{P_0} = k_1 \left(\frac{P_0}{p_a}\right)^{k_2} \tag{2.50}$$

where, $k_1 = 0.541$ and $k_2 = -0.136$ denote empirically found coefficients for conical CD nozzles and where P_0, p_{sep} and p_a denote respectively stagnation pressure of the oncoming flow ahead of the separation, the wall pressure of the incipient separation point and ambient pressure at the nozzle exit. This relation can be paired with the FSS criterion by Green[70] which gives the Mach number ratio through the separation shock. The M_0 denotes Mach number of an oncoming supersonic flow before the separation and M_1 Mach number behind the shock.

$$\frac{M_1}{M_0} = 0.78 \tag{2.51}$$

The plateau pressure rise in the separated region is evaluated correspondingly to

the derived Schilling[71] criterion for conical 20° half-angle CD nozzles and for $\gamma = 1.2$ as a function of an increasing Mach number:

$$\frac{P_0}{p_p} = 0.582 \left(1 + \frac{\gamma - 1}{2} M_0^2\right)^{-0.1197 \frac{\gamma}{\gamma - 1}} \tag{2.52}$$

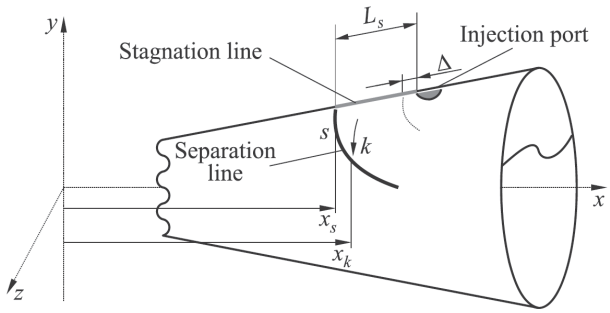

Figure 2.10: Scheme of the separation alongside nozzle wall

The separated region in the nozzle needs to be delineated in order to correctly approximate side force effect on the nozzle wall, Figure 2.10. Separation line, delimiting the separation area upstream of the injector along the nozzle wall is determined considering the Billig theoretical model built for the estimation of a detached shock wave which forms around spherical and cylindrical nosed bodies Billig[12]. The calculation of this line according to Billig[12], necessitates as an input, the value of separation distance l_s upstream of the injection port along the stagnation line. The separation distance is evaluated after solving the penetration height of the fluidic obstacle analogues to Zukoski[21]. In this iterative process, constant plateau pressure deduced from a separation criterion is applied along the l_s while the pressure gradient is iterated for the area between l_s and separation line along the nozzle wall. This gradient varies at each iteration point x_k from the plateau pressure p_p to the pressure of an isentropic undisturbed nozzle flow, while at the abscissa $P(x_k)$ follows a power law distribution.

Chapter 3

Experimental approach and test environment

3.1 Test facility

The experiments were performed at the CNRS-ICARE FAST platform (*Facilities for Aerothermodynamics & Supersonic Technologies*) on the test bench which has been built, equipped and arranged around the supersonic/hypersonic test facility EDITH by acknowledged authors of this study.

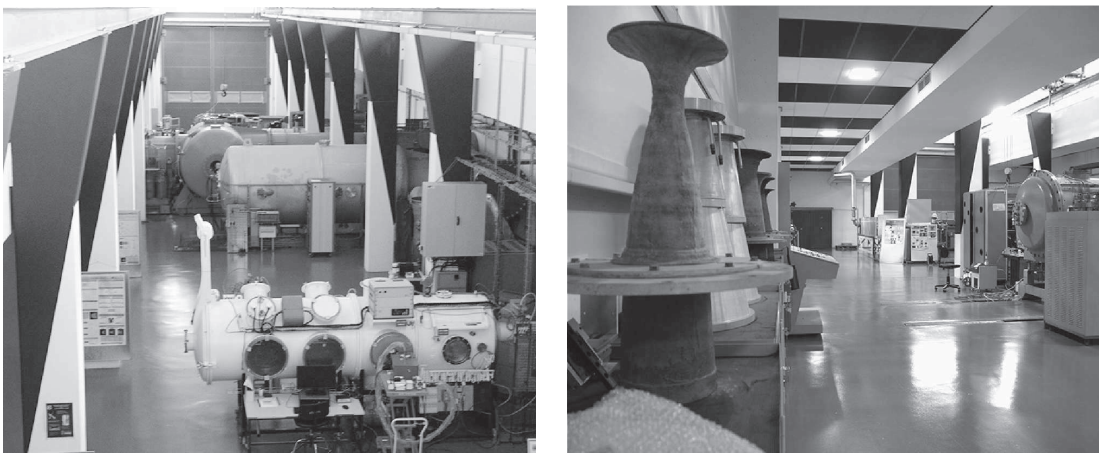

Figure 3.1: Wind-tunnel test sections hall of FAST platform in CNRS-ICARE

EDITH, previously a continuous-operation Mach 5 wind-tunnel (SH2) is newly

set as a blow-down type wind-tunnel accommodated for a nozzle test-bench. The atmospheric air is collected, dried and cleaned from the oil and particles before it is compressed till $30MPa$ and stored in $320l$ reservoir. Dried and oil-free compressed air in *Bauer Mini Verticus3* compressor is then supplied via $8mm$ diameter pipeline to the pressure regulation station and after the main valve to the radial flow splitter. From there, six $10mm$ radially distributed tubes are feeding a stilling chamber with $300kPa$ cold dry air. Stilling chamber and supersonic nozzle are mounted on the force balance, which is described hereafter. The ensemble is placed in the test section of the EDITH wind-tunnel which is depressurized via two primary $345kW$ $MPR^{®}$ pumps inherited from the previous (SH2) setup. Butterfly type valve before the collector maintains and controls the test-section pressure. The operation arrangement is also illustrated in Figure 3.2.

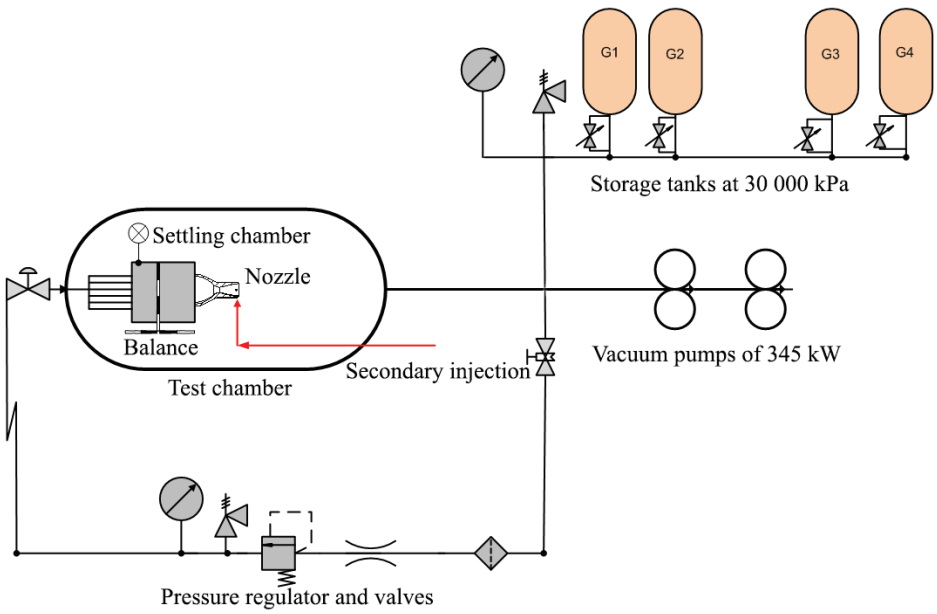

Figure 3.2: Scheme of the wind-tunnel EDITH operation-cycle

To introduce a secondary flow into the nozzle, a secondary settling chamber was built with a convergent type nozzle connected to the divergent section of the main axisymmetric C-D nozzle. Depending on a injectant case, the compressed air or compressed gas bottles were connected via secondary pressure regulator and secondary flow splitter. The gas is then supplied via four radially distributed tubes to the secondary chamber.

Table 3.1: Operation cycle of EDITH

Wind-tunnel section	Design parameters
compressor & reservoir	$p_{reservoir} = 30000kPa$, $V_{reservoir} = 320l$
pressure regulator & flow splitter	$p_{regulated} = 1200kPa$, $6 \times 10mm$ tubes
stilling chamber	$D_{chamber} = 160mm, L_{chamber} = 200mm$
secondary stilling chamber	$D_{chamber} = 60mm, L_{chamber} = 80mm$
test section	$D_{test} = 1200mm, L_{test} = 1700mm$
MPR® pumps	$Pw_{pump} = 345kW$

Total pressures and temperatures were measured at all flow regulated points and in the both stilling chambers and in the test section. Thermocouples of type-K are nominally calibrated to the value range of $3.7 - 1643.3K$ with the precision of 0.1K, while the *Baumer TED6* pressure transducers in the stilling chambers were measuring in the range of 100 to $600kPa$ with the precision of $1kPa$ and in the test section of 0 to $100kPa$ with the precision of $0.1kPa$. The mass-flow-rate of the secondary flow was initially measured via *Bronkhorst*® Fw-700 flow meter with the temperature and pressure measurements at the flow meter section.

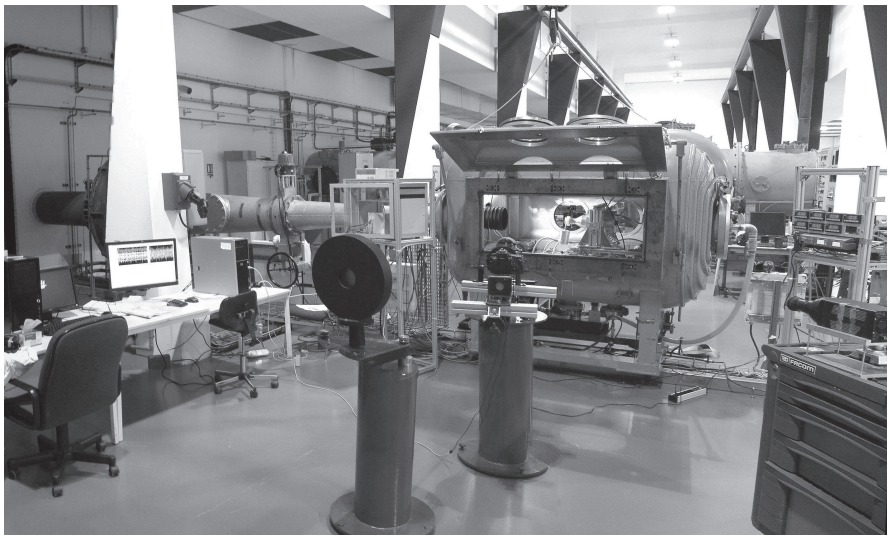

Figure 3.3: EDITH test section acquisition site

The cold flow tests were performed with no preheating of the main or the secondary flow. However, test section elements and supply pipelines were not ther-

Table 3.2: EDITH setup aerodynamic conditions

Stagnation conditions	Ambient and free stream conditions
$P_0 = 300kPa$	$p_a = 8kPa$
$T_0 = 260 \div 243K$	$T_a = 290K$
$\rho_0 = 4.26kg/m^3$	$\rho_a = 0.098kg/m^3$
$NPR_D = 37$	$U_e = 574.73m/s$
$A_{th}/A_e = 0.236$	$\rho_e = 0.3142kg/m^3$
	$M_e = 3$
	$R_e/m = 2.7729 \cdot 10^7/m$

moisolated allowing the thermoconduction on the walls. This has resulted in a total temperature variation with steady decay during the test from $260K$ to $243K$. Aforementioned total temperature range yields a static temperature at the exit section of Mach 3 nozzles between $94K$ and $87K$. These values are still above the air incipient boiling point found at $T_b = 78.6K$ and even with the range at below $T_c = 132.6K$ pressure range were significantly below the critical pressure of $p_c = 3.771MPa$. More detail elaboration of the flow conditions and gas specie properties is given in Chapter 7

The main flow total pressure of $P_0 = 300kPa$ was maintained for a considerable test time of $\sim 96s$, which was sufficient regarding the pressures and forces data acquisition.

3.2 Qualitative flow analysis

The flow visualization was used to qualitatively analyze and identify the flow structures that form at the nozzle exit. Monochromatic and color Z-schlieren techniques were used depending on the case, the gas properties and the aimed effect. Primary constructed, the monochromatic Z-schlieren comprises of a halogen light source (Lamp GHD) illuminating through a slit and a lens under $8deg$ incident a $300mm$ diameter parabolic (telescopic) mirror. Parabolic mirror reflects a parallel collimated light beam through the photographic quality glass windows of the wind-tunnel test section to the identical mirror on the opposite side. From the decollimating parabolic mirror, light is reflected via planar mirror and at the

focal point a sharp razor edge is placed. The amount of cut light is regulated via a fine adjuster, cutting approximately half of the light, Figure 3.4. As a distorted beam focuses imperfectly, the razor edge cuts half of the focused light revealing and emphasizing the density gradient affected light rays. Behind the cutter on the same photographic mounting rail a collecting lens was set to project the light image directly onto the camera sensor. The *Canon*® EOS 60D was used as a primary camera, while the *Princeton Intruments*® PI-MAX 2 was a secondary camera able to perform fast acquisitions.

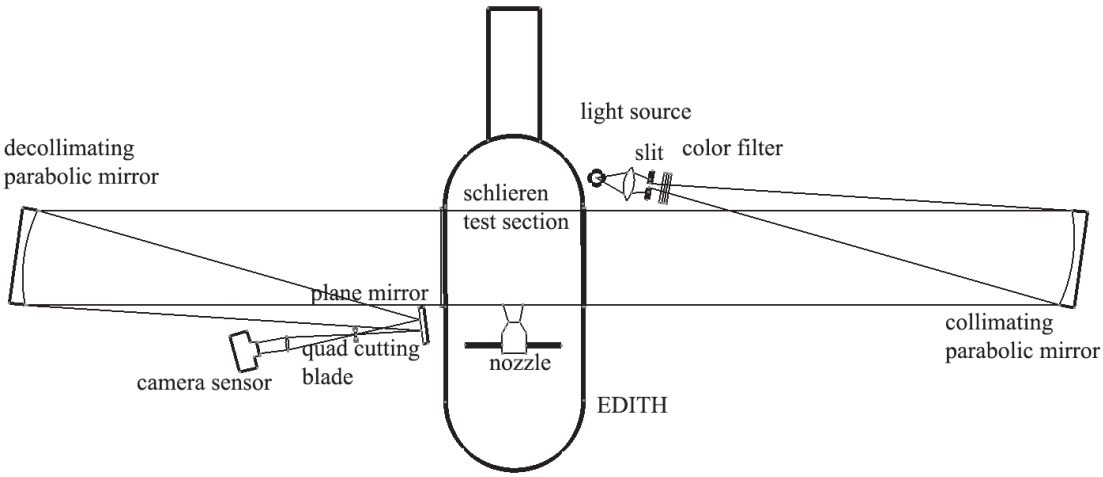

Figure 3.4: Scheme of the designed and installed Z-schlieren

For the different gas injection experiments, a color schlieren was used as well. Bi-color schlieren was set by adding the bi-color filter after the slit focusing the light and two parallel cutters on the opposite side at the focal point.

The camera was connected to the acquisition computer and controlled via the WinView software. The temporal image acquisition was synchronized with the *LabView*® software in order to compare with the quantitative data. The images have been post-treated via *Matlab*® Image Processing Toolbox for the quasi-quantitative measurements of the exit Mach number using the sharp cone in front of the exit flow or for the angular value of the observed flow deflection.

3.3 Quantitative diagnostics

The initial quasi-quantitative analysis of the schlieren images was coupled with the analytical and the initially obtained numerical results in order to plan and to design diagnostic tools deployment. The diagnostics consisted of the three major groups of measurements; 1. primary, secondary and ambient stagnation values, 2. parietal pressure measurements and 3. force balance measurements.

Stagnation pressures and temperatures were measured with calibrated *Baumer* TED6 pressure transducers and type-K thermocouples. Initially, stagnation pressure at the exit was measured via Pitot tube placed in the center of the exhausted supersonic jet in order to compare the values with the cone shock angles measurements of the nozzle exit Mach number. Additionally, on the secondary flow supply line a flow meter was placed to monitor the secondary injection mass flow rate.

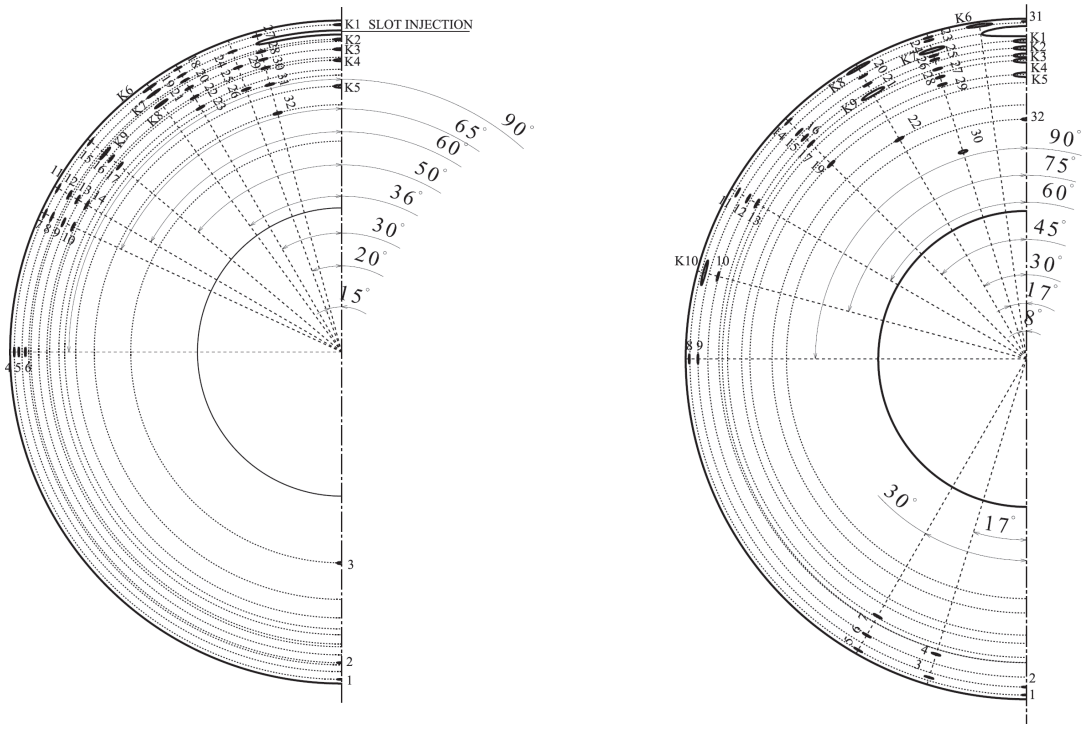

(a) TIC nozzle with transverse rectangular slot injection

(b) TIC nozzle with transverse circular sonic injection

Figure 3.5: CAD designed pressure measurement map

3.3.1 Parietal pressures

Two types of the parietal pressure measurements were designed and used on the test nozzle models, a miniature pressure transducer probes and pressure taps. At the injection side of the nozzle symmetry plane fast pressure transducers *Kulite*® XCQ-062 were used to capture separation and eventual unsteady behaviour in the separation zone. Furthermore, they were also used at the lateral limits of the horseshoe vortex zone and side of the injection port. Additionally, pressure taps were connected to the *Scanivalve*® ZOC-22B miniature pressure scanner placed under the tests nozzles and via amplifier to the computer. Program in G language (LabView) was written to register and to translate voltages to pressure values as a raw data under $8kHz$ sample rate and as a 2000 sample chunks averaged data every $0.25s$.

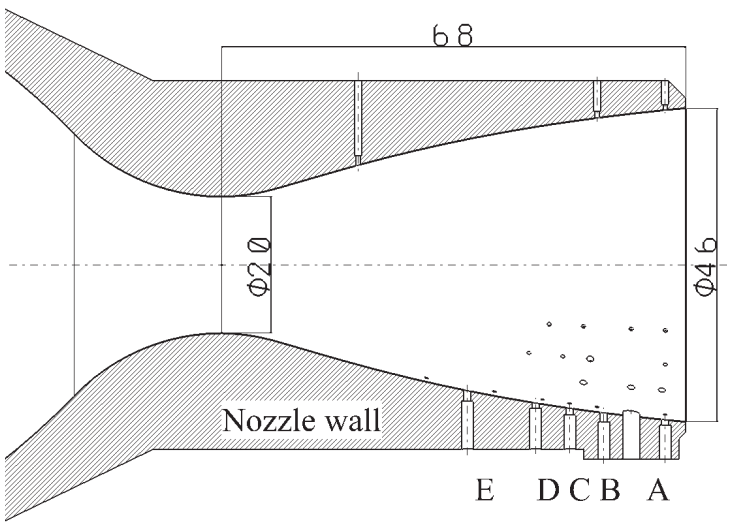

Figure 3.6: CAD design of axial pressure probes locations

In order to capture effects at the nozzle wall, pressure taps and pressure transducers were positioned along the nozzle wall meridians. According to the analytical and numerical results, these meridian lines are found at $13deg$, $20deg$, 30, $36deg$, 45, $60deg$, $75deg$ and $90deg$ schematically depicted in Figure 3.5. In the axial and lateral directions, pressure probes are distributed in the manner to have a satisfactory resolution is the affected separated and vortex zones while fewer probes placed in an unaffected nozzle portion may be superimposed for sufficient number

of measurement points. *Kulite*® pressure probes for circular injection TIC noz-

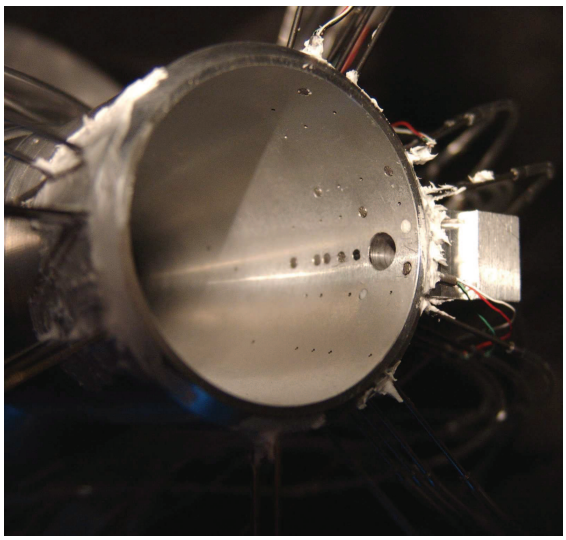

Figure 3.7: TIC-i0.88 nozzle with installed parietal pressure tools

zle were flush mounted. This way of mounting enables high frequency pressure acquisition. However, due to a very high Reynolds number, $Re/m \sim 2.8 \cdot 10^7/m$ turbulence generated oscillations were beyond the probing bias. Additionally, flush-mounted flat head cylindrical probes on the curved and variable angle nozzle wall generate the small flow disturbances. Therefore, for other nozzle case, the probes were pocket-mounted which provided a slower static pressure conditions measurements but without disturbances due to a probe insertion and with the smoother and more consistent averaged values.

3.3.2 Force balance

To measure aerodynamic forces acting on the nozzle, a force balance is designed and constructed. The constructed force balance was measuring the global force components in all three spatial directions. It consists of the two frames assembled in a way to allow independent movement in spatial directions. Such a force-balance design provides a force components measurement that doesn't necessitate determination of the center of thrust. Frames were connected to each other and to the force transducers via constructed system using a slide bearing. The used

$Bosh - Rexroth^{®}$ frictionless slide bearings provided very low friction support for axial and radial loads with nominal friction coefficient in the range of $\mu_s = 0.001 - 0.002$. The moving frames are connected to the one side of the $HBM^{®}$ S2M force transducers while the other side of the force-transducers was attached to the static frame fixed to the test section support.

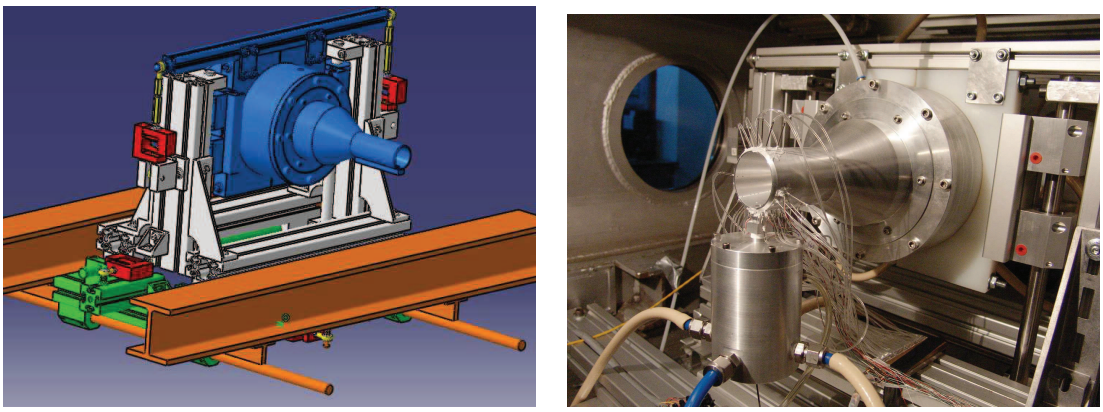

(a) CATIA V5 assembly design of the force balance

(b) TIC nozzle fully equipped and mounted on the force balance

Figure 3.8: Nozzle-chamber on the force-balance system

Two types of $HBM^{®}$ S2M force transducers were used, with the nominal range of $0-200N$ and of $0-20N$. Since the system was preloaded with the mass of test model that was $\sim 13.6kg$ in y direction, two symmetrically placed $HBM^{®}$ S2-200 transducers were used to support the mass and to provide a low friction ratio measurement. In the non-preloaded axial x direction one $HBM^{®}$ S2-200 force transducers is used for the force measurements which were maximally reaching up to $157N$. In the lateral, z direction, a $HBM^{®}$ S2-20 transducer is used to measure the eventual asymmetric loads on the nozzle lateral sides.

The $HBM^{®}$ S2M is a S-shaped force transducer that uses a strain gauge technology to measure force induced dilatations and it can provide force data with the accuracy of 0.02 related to the full range of the transducer. $HBM^{®}$ S2-200 factory calibration yields a total error of $0.58N$ for $150N$ of measured force, $0.56N$ for $20N$ of measured force and $0.66N$ for $5N$ of measured force. The force transducers are connected to the $HBM^{®}$ RM4220 amplifiers increasing the voltage signal before the $NI^{®}$ SCXI-1140 fast acquisition cards. Considering the

complexity of the force balance system, a laboratory calibration was conducted on the separate elements and with a fully mounted test system.
The y side force which was ranging around $20N$ was measured with an absolute error of $\pm 0.764N$ while the axial thrust force in x direction was measured with one transducers had an absolute error of $\pm 1.176N$. Generally, a raw force data was acquired in LabView at $8000Hz$ sampling rate which provided satisfactory resolution for postprocess analysis and averaging. Simultaneously with the raw data file, an averaged was stored on $2000Hz$ data chunks or at each $0.25s$. (Further details on the design and calibration of the force balance are given in Appendix A.2).

3.4 Experimental test nozzle models

Figure 3.9: Experimental test nozzles

In the current study, five test nozzle models are design, built and experimentally tested and analyzed. Three conical profiled axisymmetric test nozzles were used to analyze effect of the position and of the angle of a circular convergent injector. Other two identical truncated-ideal-contour nozzles were tested for a different shape of the injector. The nozzles were designed using the method of characteristics, which is an isentropic and an inviscid calculation method. The

input parameters of pressure ratio and exit Mach number were complemented with by a smooth throat curvature radii and smaller exit angles ranging which were 5.8° for two conical nozzles and 5.38° for TIC nozzles. The profiles are corrected for viscous boundary-layer, as illustrated in Figure 3.10 and then designed in CATIA® V5 for the aluminium five axis CNC machining. Hole housings for Kulite® pressure transducers and Scanivalve ® pressure scanner connections were produced according to the pressure mapping and CATIA® CAD designs in Figure 3.6 and 3.5. Basic values of the designed test nozzles are given in Table 3.3.

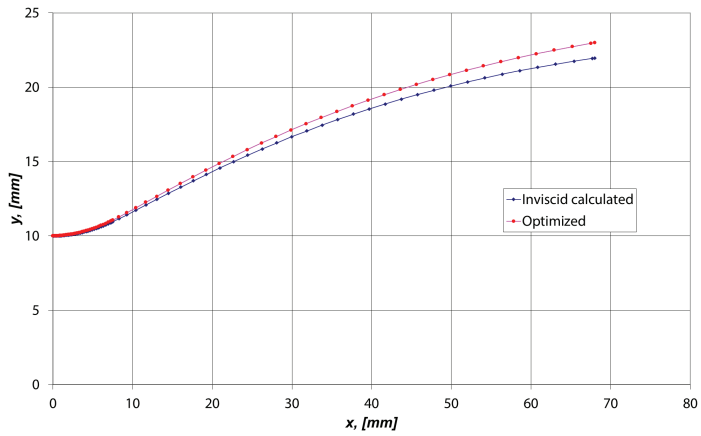

Figure 3.10: TIC profile BL correction

Table 3.3: Experimental test-nozzles isentropic&inviscid parameters

Nozzle	R_{th}	A_e/A_{th}	M_e	NPR_{Di}	l_n, mm	x_j/l_n	A_{tj}
Con. C-i0.7	$9.72mm$	4.234	3.001	37	100	0.7	$32.17mm^2$
Con. C-i0.9	$9.72mm$	4.234	3.001	37	100	0.9	$28.274mm^2$
Con. C-a0.9	$9.87mm$	4.887	3.150	45.8	82	0.9	$28.274mm^2$
TIC-i0.88	$10mm$	4.87	3.03	37.5	68	0.88	$26.42mm^2$
TIC-s0.88	$10mm$	4.87	3.03	37.5	68	0.88	$28.274mm^2$

*TIC profile corrected for viscous effects, Conic inviscid

TIC nozzle contour, designed via 2D axisymmetric inviscid method of characteristics calculation is additionally corrected for the viscous boundary-layer thickness estimated using CFD simulations. MoC yields NPR_{Di} for TIC nozzle in the near wall region at the exit section allowing BL flow to be exhausted tangential to

the exit nozzle wall line. However, the flow at the exit plane of TIC nozzle is highly variable from the center towards the wall, therefore the exhausted plume doesn't appear with a quasi-regular shock reflection. On the other hand, inviscid flow of a conical nozzle is approximated as an uniform at the exit and NPR_{Di} corresponds to the uniform expansion from the center towards the wall.
Analogously to the main nozzles design, the secondary convergent nozzles are designed and manufactured on the 3 and 5 axis CNC machines and shown in Figure 3.11. Their task is to smoothly introduce the flow from the secondary stilling chamber to the injection port at the primary nozzle divergent portion. The same secondary chamber was used both for the circular and for slot rectangular geometries. The circular nozzle was designed with a large and smooth

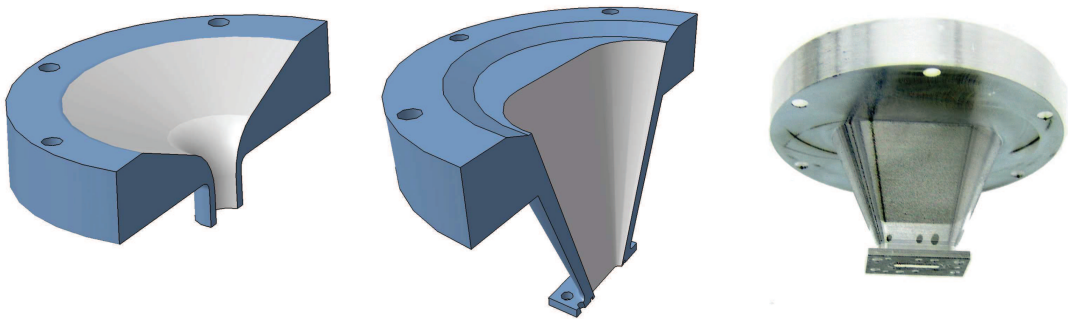

(a) CATIA V5 part design image of circular 2nd nozzle

(b) CATIA V5 part design image of slot shaped nozzle

(c) Photo of a slot shaped 2nd nozzle

Figure 3.11: Secondary injection convergent nozzles

curvature radius forming a convergent section from $d_{cham} = 60mm$ at the chamber to $8mm$ and with a short cone from 8 to $5.8mm$ in the secondary throat. Slot shaped secondary port was profiled as a rounded rectangular and it has a small introduction step from cylindrically shaped chamber to the slot shaped convergent nozzle. Ratio of inlet/throat section of $Aj - in/A_j = 24.7$ and $l_{jn} = 48mm$ length yielded a satisfyingly smooth and uniform flow sonic acceleration at the secondary throat.

Obtained result data from the presented diagnostic tools were collected from the corresponding LabView codes and post-treated via Matlab. The forces data are then presented together with pressure measurements and compared and coupled with the corresponding results from numerical simulations.

Chapter 4

Numerical simulations test environment

4.1 Introduction to CFD approach and numerical environment

Computational fluid dynamics (CFD) approach has been considered as a coupled method to provide reliable comparison and to enhance and give more detailed insight analysis of experimentally observed phenomena. By use of the numerical method combined with experiments it is possible to check and validate adopted CFD approach but also to reduce always existing experimental flaws due both to the inherent nature of experimental work and to the technological limitations. The flow physics is often indirectly inferred from the experimental measurements of mean flow variables or of surface conditions and therefore leaves an uncertainty about the exact nature and the interaction of the phenomena that ultimately produce the measured data. For example an intrusive probe insertion at the wall or taps on the wall will affect the flow which they are supposed to measure and produce discrete data-points which would provide in general a rough map of the rapidly varying pressure field. These problems can be somewhat diminished by using the newer technologies improved in size and acquisition rate but still the data must be taken with precautions of each tool limitations and even more with coupled and inherited flaws of several used techniques. Nevertheless, numerical

simulations may produce a complete cost effective solution through the whole computational domain and by this provide probed data at any location and give deep insight information but they also have drawbacks which makes them far from being an ideal tool that can completely replace the experiments. CFD, based on the fluid mechanics theory which is a mathematical model has its limits of applicability like any other model. More specifically, in a high compressible super/hypersonic turbulent flow these shortcomings come from the absence of full turbulence solution and lesser from the upper flow velocity limitations. The other drawback similarly to the experiments comes from the technological or programming characteristics of implemented mathematical models and it is specific for each numerical code.

Commonly used, "first-order turbulent models" are based on the Bousssinesq assumption which states that principal axes of the Reynolds stress tensor, τ_{ij}, are coincident with those of the mean strain-rate tensor, S_{ij}, at all points in a turbulent flow. The proportionality between τ_{ij} and S_{ij} defined as the eddy viscosity, μ_t, as in Wilcox[72]. These models can be further sorted by number of additional equations added to the basic Navier-Stokes equations to solve the turbulence as: simple or algebraic models, one-equation models and two-equation models. Newer, "second-order turbulent models" as the Reynolds Stress turbulence model do not use Bousssinesq approximation but model each component of the Reynolds stress tensor individually. This results in a model with six additional equations. Lately there are numerous efforts to implement large-eddy-simulation for the high speed compressible flows and cross-flow jets as in Schetz *et al.*[30]. LES, as a low-pass filtering to eliminate small scales in Navier-Stokes solutions, resolves from the domain scales L to the filtered Δ. It should enable better fidelity than RANS with acceptable computation cost. However, using the subgrid-scale for unresolved scales in high interaction compressible flow, increases the numerical grid and computation cost to the large values which makes it very costly for wall bounded compressible flows. Particularly, problem may occur from the filtering and numerical discretization. Some alternatives are developed with the hybrid RANS/LES models as the detached-eddy-simulations (DES) at which large scale domain is resolved with LES and close to the wall or small turbulence scale with RANS. This significantly decreases the computation cost with still some problems

to be resolved as the complex meshing due to the RANS-LES switch.

4.1.1 Numerical environment

Favre (mass weighted) averaged Navier-Stokes solver of the CNES & Bertin developed finite volumes CFD code *CPS_C* was used to process the input data. CPS_C (Code pour la Propulsion Spatiale_Cryogenique) is a three-dimensional CFD code designed for the space propulsive flows, as described in Durand *et al.*[73]. Double-precision FANS solver is designated to solve compressible multispecies reacting flows with a fully accounted viscous effects on the unstructured 3D computational grid. For the multispecies transport models, a multi-chemical species mixing law of convection/diffusion fluxes type was based on the Fick's diffusion law. CPS_C is designed to operate with the real and with perfect gaseous species. In the current study, thermodynamic properties are defined via analytical physical models using the polynomial functions and equation of state which describes a thermally perfect compressible gas.
Time splitting is used for the explicit and eventually implicit temporal scheme. Only the explicit schemes are used in this study and they are of a modified 2nd order of Runge-Kutta which can be up to order 4 in time and 3 in space. Resolution of the linear system is based on the Jacobi and Gauss Seidel algorithm. The fluxes in this numerical work were computed on the cell interfaces with HLLC scheme by Toro[74] for multispecies and high temperature gradient monospecie cases and with the Roe's upwind difference splitting scheme for simple monospecie perfect gas cases. The flux vectors are evaluated at each time step using the second order scheme. For the second-order-in-space discretization a MUSCL (Monotone Upstream-centered Schemes for Conservation Laws) approach was used in which the physical variables were extrapolated with limited slopes for an each cell.

4.2 Governing equations and turbulence modeling

The present study is concentrated on the RANS two-equation turbulence models. In the past years there were numerous works conducted on the numerical modeling and simulation of the secondary sonic injection into a supersonic flow, mainly

for the fundamental 2D and 3D cases of injections at the flat plate. Chenault and Beran[24] considered and compared $k-\varepsilon$ model with a second order Reynolds stress turbulence model (RSTM) for 2D secondary injection cases. In the reported study, they have observed a very good agreement between RSTM and the experimental and analytical results in terms of shear stress and the separation predictions. However, a smaller overestimation is reported in the inflow size of separated vortical regions and in the wall pressures with high increase of the static pressures in a separation region. Unlike the RSTM, the $k-\varepsilon$ model was found as an inconsistent with the experimental results in terms of wall shear stress distribution which was assigned to the Bousssinesq approximation. Nevertheless, it has demonstrated a satisfying estimation of the size which is also reported in Chenault *et al.*[37]. Similarly, Maciel[75] compared the Jones-Launder $k-\varepsilon$ model with the Wilcox-Rubesin $k-\omega^2$ model for the ramped supersonic flow and he has reported a consistent wall-pressure distribution of the $k-\varepsilon$ model with a better plateau pressure width estimation than the $k-\omega^2$, which yielded more pronounced critical pressure zones. However, $k-\omega^2$ predicted more realistic turbulence levels and shock waves ahead of a blunt body and a very good flow axis sizes of the separation zones. Still, the lateral sizes were reported as overestimated. Furthermore, Erdem and Kontis[27] as well in Viti, Neel, and Schetz[34] used $k-\omega$ model, respectively in 2D and 3D numerical investigations of the transverse jet injections into a supersonic flow based on the experiments performed by Spaid and Zukoski[8] and Schetz and Billig[11]. Both demonstrated very good agreement of the numerical and experimental results in terms of a shear stress and shock predictions.

In the current study, available 2-equations turbulent models are considered, Jones and Launder[76] and RNG[77] $k-\varepsilon$ and Wilcox and Rubesin[78] $k-\omega^2$. In the numerical domains with a coarser grid, of $y+$ values above 11, provisions are made for modeling a boundary-layer using an adiabatic wall-function coupled to the turbulence model via modified logarithmic law of Van Driest. In the current study $y+$ values inside the nozzle and secondary injection were considerably below 11, while the $y+$ was above 11 only at the walls of an external domain which served as an intermediate section to introduce the flow to the outlet and slip boundaries.

4.2.1 Governing equations

In the differential form an instantaneous continuity equation Eq. 4.1, momentum equation Eq. 4.2 and energy equation Eq. 4.3 for a compressible fluid can be written as:

$$\frac{\partial \rho}{\partial t} + \frac{\partial}{\partial x_j}\left[\rho u_j\right] = 0 \tag{4.1}$$

$$\frac{\partial}{\partial t}\left(\rho u_0\right) + \frac{\partial}{\partial x_j}\left[\rho u_i u_j + p\delta_{ij} - \tau_{ji}\right] = 0 \tag{4.2}$$

$$\frac{\partial}{\partial\, t}\left(\rho e_0\right) + \frac{\partial}{\partial\, x_j}\left[\rho u_j e_0 + u_j p + q_j - u_i \tau_{ij}\right] = 0 \tag{4.3}$$

Furthermore for a Newtonian fluid assuming Stokes hypothesis, the viscous stress and the viscous strain rate may be written as:

$$\tau_{ij} = 2\mu S^*_{ij} \tag{4.4}$$

$$S^*_{ij} = \frac{1}{2}\left(\frac{\partial\, u_i}{\partial\, x_j} + \frac{\partial\, u_j}{\partial\, x_i}\right) - \frac{1}{3}\frac{\partial\, u_k}{\partial\, x_k}\delta_{ij} \tag{4.5}$$

The heat-flux, given by Fourier's law, and the corresponding Prandtl number finalize the set:

$$q_j = -\lambda\frac{\partial\, T}{\partial\, x_j} = -C_p\frac{\mu}{Pr}\frac{\partial\, T}{\partial\, x_j} \tag{4.6}$$

$$Pr = \frac{C_p \mu}{\lambda} \tag{4.7}$$

To close this set of equations, perfect compressible gas equation of state was assumed, with:

$$p = \rho R T, \;\; C_p - C_V = R_g, \;\; \gamma = \frac{C_p}{C_V}, \;\; e = C_V T \tag{4.8}$$

$$\text{total energy: } \; e_0 = e + \frac{u_k u_k}{2} \tag{4.9}$$

Specific heat at the constant pressure C_p was modeled as a function of the temperature, $C_p(T)$, represented up to a Chemkin standard 7th degree polynomial. C_V was then deduced from the $C_p(T)$ and R_g relation using a thermally perfect gases hypothesis.

Standard Reynolds time averaging considers mean and fluctuating components as velocities represented in Eq. 4.10. Similarly, other scalar quantities like energy, pressure etc. can be defined by global equations as in Eq. 4.11 :

$$u_i = \bar{u}_i + u_i' \tag{4.10}$$

$$\phi = \bar{\phi} + \phi', \quad \text{where:} \tag{4.11}$$

$$\bar{\phi} = \frac{1}{T}\int_T \phi(t)dt \tag{4.12}$$

For the compressible flows, it is convenient to introduce a mathematical transformation on the averaging sequence by representing mass(density)-averaged values. These so-called density weighted Favre-averaged Navier-Stokes equations may be globally represented as:

$$\phi = \tilde{\phi} + \phi'', \quad \text{where:} \tag{4.13}$$

$$\tilde{\phi} = \frac{\overline{\rho\phi}}{\bar{\rho}} \tag{4.14}$$

with $\overline{\phi'} = 0$, and $\overline{\phi''} \neq 0$.

Such a defined averaging techniques can be then applied to the exact form of continuity Eq. 4.1, momentum Eq. 4.2 and energy Eq. 4.3 equations. By introducing a mass averaged decomposition, Eq. 4.13, for u_i and e_0 and a standard time averaged decomposition, Eq. 4.10, of ρ and p yields the following FANS equations set:

$$\frac{\partial \bar{\rho}}{\partial t} + \frac{\partial}{\partial x_j}\left[\bar{\rho}\tilde{u_i}\right] = 0 \tag{4.15}$$

$$\frac{\partial}{\partial t}\left(\bar{\rho}\tilde{u_i}\right) + \frac{\partial}{\partial x_j}\left[\bar{\rho}\tilde{u_i}\tilde{u_j} + \bar{p}\delta_{ij} + \overline{\rho\ u_i''\ u_j''} - \overline{\tau_{ji}}\right] = 0 \tag{4.16}$$

$$\frac{\partial}{\partial\ t}\left(\bar{\rho}\tilde{e_0}\right) + \frac{\partial}{\partial\ x_j}\left[\bar{\rho}\tilde{u_j}\tilde{e_0} + \tilde{u_j}\bar{p} + \overline{u_j''p} + \overline{\rho\ u_j''e_0''}\bar{q_j} - \overline{u_i\tau_{ij}}\right] = 0 \tag{4.17}$$

Denoted density-weighted (mass) averaged total energy is given by:

$$\tilde{e_0} = \tilde{e} + \frac{\tilde{u_k}\tilde{u_k}}{2} + k \tag{4.18}$$

where k represents turbulent energy, defined as:

$$k = \frac{\widetilde{u_k''u_k''}}{2} \tag{4.19}$$

4.2.2 Turbulence modeling

Jones and Launder[76] $k-\varepsilon$ model

Primary turbulence model used in this study was a standard Jones and Launder[76] $k-\varepsilon$ model. This model yields two additional equations to describe the turbulence and to close the equations set with a solution for the Reynolds stress term $\bar{\tau}_{ij} = -\overline{\rho\ u_i''\ u_j''}$. The standard model is based on the coupled transport equations for the turbulent energy density k and turbulent dissipation rate ε. In general form, transport equations for $k-\varepsilon$ can be written as:

$$\rho\frac{\partial k}{\partial t} + \frac{\partial}{\partial x_j}\left[\rho k u_j - \left(\mu + \frac{\mu_t}{\sigma_k}\right)\frac{\partial k}{\partial x_j}\right] = P_k - \rho\varepsilon - \rho\ D_k \tag{4.20}$$

$$\rho\frac{\partial \varepsilon}{\partial t} + \frac{\partial}{\partial x_j}\left[\rho\varepsilon u_j - \left(\mu + \frac{\mu_t}{\sigma_\varepsilon}\right)\frac{\partial \varepsilon}{\partial x_j}\right] = \left(C_{\varepsilon 1}f_1P_k - C_{\varepsilon 2}f_2\rho\varepsilon\right)\frac{\varepsilon}{k} + \rho E_\varepsilon \tag{4.21}$$

Source terms are on the lefthand side while the terms on the righthand side in Eq.4.20 denote respectively the production term, the dissipation term and sum of the molecular diffusion and turbulent transport. Production term is further

equal to:

$$P_k = \bar{\tau}_{ij}^{turb} \frac{\partial u_i}{\partial x_j} = -\overline{\rho \; u_i'' \; u_j''} \frac{\partial u_i}{\partial x_j} = \mu_t S^2 \tag{4.22}$$

Where μ_t represents the turbulent or eddy viscosity modeled as

$$\mu_t = \rho \; C_\mu \frac{k^2}{\varepsilon} \cdot \; f_\mu \tag{4.23}$$

and S the strain tensor mean rate, defined as:

$$S = \sqrt{2 S_{ij} S_{ij}} \tag{4.24}$$

The model closure constants were given after modification by Launder and Sharma [79]

$$C_{1\varepsilon} = 1.44, \;\; C_{2\varepsilon} = 1.92, \;\; C_\mu = 0.09, \;\; \sigma_k = 1.0, \;\; \sigma_\varepsilon = 1.3$$

The transport equations defined above are enhanced with the low Reynolds $k-\varepsilon$ wall treatment consideration. This involves the damping functions f_μ, f_1, f_2 (4.26) and the extra source terms D_k and E_ε (4.25) which are active only near the solid boundaries in order to solve the turbulent kinetic energy and turbulent dissipation down to the viscous sublayer. This additional terms may be written considering the original Jones and Launder[76] and Launder and Sharma[79] coefficients as:

$$D_k = 2\frac{\mu}{\rho}\left(\frac{\partial \sqrt{k}}{\partial x_j}\right)^2 \;\; and \;\; E_\varepsilon = 2\frac{\mu \mu_t}{\rho^2}\left(\frac{\partial^2 u_i}{\partial x_j^2}\right)^2 \tag{4.25}$$

$$f_\mu = \exp \frac{-3.4}{(1 + Re_t/50)^2}, \;\; f_1 = 1, \;\; f_2 = 1 - 0.3 \exp -Re_t^2 \tag{4.26}$$

where, $x_j = y$ is the normal direction from the wall and $Re_t = \frac{\rho}{\mu}\frac{k^2}{\varepsilon}$ is interpreted as the Reynolds number of turbulence. In CPS_C code, damping functions can be regarded in a whole or without viscosity damping term or disregarded for only high Re turbulence calculations. In the current study flow was solved all to the linear viscous sublayer. In addition to the above defined closure coefficients and functions, the axillary relations consider the specific turbulent dissipation ω and

turbulence length scale which can be defined as:

$$\omega = \frac{\varepsilon}{(C_\mu k)} \tag{4.27}$$

$$l_t = C_\mu \frac{k^{3/2}}{\varepsilon} \tag{4.28}$$

RNG[77] $k - \varepsilon$ model

In addition to the standard model, a Yakhot *et al.*[77] or Re-Normalization Group $k - \varepsilon$ was also available. This model contains additional terms for the heavy strained flows with a reportedly good approximation for the separated flows and low Reynolds computations without a wall function. The RNG mathematical technique derives $k - \varepsilon$ alternative turbulence model in order to account for the smaller scales of motion in contribution to the turbulent diffusion. This results in a modified form of turbulence dissipation equation to include different scales through the changes applied to the production term. These new coefficients are derived explicitly comparing to the empirical coefficients in Jones and Launder[76].

$$C^*_{2\varepsilon} = C_{2\varepsilon} + \frac{C_\mu \eta^3 (1 - \eta/\eta_0)}{1 + \beta \eta^3} \tag{4.29}$$

where, $\eta = Sk/\varepsilon$ and new closure coefficients values:

$$C_\mu = 0.0845,\ \sigma_k = \sigma_\varepsilon = 0.7194,\ C_{\varepsilon 1} = 1.42,\ C_{\varepsilon 2} = 1.68,\ \eta_0 = 4.38,\ \beta = 0.012$$

Wilcox and Rubesin[78] $k - \omega^2$ model

In difference to the $k - \varepsilon$ models, in $k - \omega^2$ model the second equation defines the specific dissipation rather than the dissipation rate to determine the scale of turbulence. As denoted in Wilcox and Rubesin[78], ω may be regarded as a frequency characteristic of the turbulence decay under its self-interaction. This can be further developed in ω as a mean square vorticity of the energy containing eddies or, as denoted, ω is the RMS fluctuating vorticity or "enstrophy" defined by Wilcox[72] as a rate of dissipation per unit of turbulence kinetic energy, Eq.4.27.

This formulation of two-equation turbulence model was intended as a more compliant towards the adverse pressure gradient induced separation flows. Transport equations are then:

$$\rho\frac{\partial k}{\partial t} + \frac{\partial}{\partial x_j}\left[\rho k u_j - (\mu + \sigma^* \mu_t)\frac{\partial k}{\partial x_j}\right] = P_k - \beta^* \rho k \omega - \rho\ D_k \tag{4.30}$$

$$\rho\frac{\partial \omega^2}{\partial t} + \frac{\partial}{\partial x_j}\left[\rho \omega^2 u_j - (\mu + \sigma \mu_t)\frac{\partial \omega^2}{\partial x_j}\right] = \alpha\frac{\omega^2}{k}P_k - \left[\beta + 2\sigma\frac{\partial l}{\partial x_j}\frac{\partial l}{\partial x_j}\right]\rho\omega^3 + \rho E$$

$$\mu_t = \rho\frac{k}{\omega} \tag{4.31}$$

with closure parameters as:

$$\alpha = 10/9,\ \ \beta = 3/20,\ \ \beta^* = 9/100,\ \ \sigma = \sigma^* 1/2\ \ and\ \ l = \sqrt{k}/\omega$$

Initial turbulence conditions given at the inlet and outlet boundaries were in the form of minimal turbulent rate (estimated from $\mu_t = 0.1\mu$) and turbulent length in relation to referent hydraulic diameter ($l_t \leq 0.7 \cdot D_H$). The turbulent energy is evaluated from the primary results and input for inlet/outlet boundaries of referent calculations.

4.2.3 Fluid models

Mono-specie calculations were conducted in order to simulate the cold-flow experiments performed with a dry-air. Additionally to these tests, experiments including different species as a secondary gas injectant were experimentally tested and then numerically simulated using the available multispecies transport equations. After coupled experimental-numerical analysis, a numerical multispecies gas flow simulations were conducted on the hot gas combustion products.
The gaseous species physical properties are modeled respecting a thermally perfect gas assumption. Calorically perfect gas assumption with the constant γ, μ and Pr values was used for the initialization cases. Considered 3D problems are modeled then with a fully developed polynomial temperature function dependencies according to the Chemkin-II 7th order polynomial standard. For

some species, polynomial order is further reduced by using a curve fitted functions for a specifically tested temperature range. These thermodynamic data can be found in Lemmon *et al.*[80], Burcat and Ruscic[81], McBride *et al.*[82] and M. W. Chase[83]. Reduced formulations for monospecie dry-air calculations in $(60 - 500K)$temperature range are given as:

$$
\begin{aligned}
&\text{Analytically formulated laminar viscosity } [kg/(m \cdot s)] : \\
&\mu = \mu(T) = C_0 + C_1 T + C_2 T^2 + C_3 T^3 \\
&\text{Analytical conductivity } [W/(m \cdot K)] : \\
&\lambda = \lambda(T) = C_0 + C_1 T + C_2 T^2 + C_3 T^3 \\
&\text{Specific heat capacity under constant pressure } [J/(kg \cdot K)] : \\
&C_p = C_p(T) = C_0 + C_1 T + C_2 T^2 + C_3 T^3 + C_4 T^4 + C_5 T^5 \\
&C_V(T) = R_g - C_p(T), \quad \gamma = \frac{C_p(T)}{C_V(T)}
\end{aligned} \tag{4.32}
$$

To reduce the computational costs of the initialization multispecies cases, mixture was regarded as a mono-specie with parameters derived according to the molar fractions of each specie in the mixture. Detailed elaboration of physical models and species effects is given in Chapter 7.

4.3 Numerical grid and boundary conditions

Primary meshing tool used in the reported study was ANSYS® GAMBIT 2.4.6 while Bertin® *Mesh3* was used for an axisymmetric two-dimensional approximation. The CPS_C code is based on the three-dimensional formulations of Navier-Stokes equations and thus there is no 2D planar possibility, but it can be achieved by minimal angular value slice of an axisymmetric computation domain. In this study the revolving angle for the 2D-axi numerical approximation was 2°. The 2D-axi calculations served as initialization cases for the full 3D simulations. 3D numerical grids were built in three level of quality, for $180^c irc$ or half-3D domain: coarse (1million referent elements), fine (2million referent elements) and very fine (3.9million referent elements). After achieving a convergence of the monitored values, numerical results were symmetrized and inherited to the full,

360° computational domain and iterated till the satisfactory convergence.

Even though the CPS_C is a fully unstructured finite volume code, the numerical grids were designed with the mapped hexagonal elements as it was better to control the mesh cells and to postprocess the data. The O-grid blocking structure was used on the circular cross-sections while the sweeping was used to construct each domain volume section. Controlled meshing of the edge and surface topology preceded the volume meshing. The grid nodes were clustered towards the primary and secondary sonic throats and towards the estimated separation zones. The O-grids, Figure 4.1 were designed to keep the hexagonal mapping with asymmetric secondary injection port and in the same time to smooth as possible transition to the rectangular block.

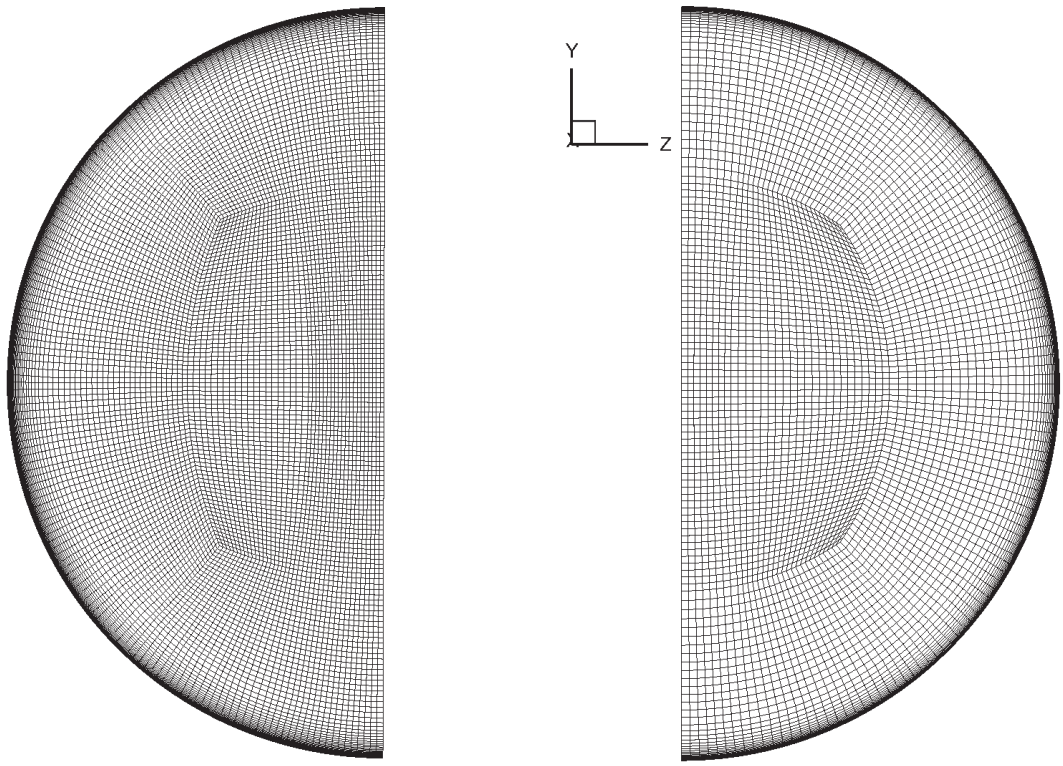

(a) TIC nozzle with slot injection at 88% (b) TIC nozzle with circular injection at 88%

Figure 4.1: Normal circular cross section of the divergent TIC nozzle domain

The O-grid for circular and slot injection cases are given in Figure 4.1 (a)

and (b), respectively. Subsonic inlet boundary is profiled according to the experimental test model stilling chamber exit. The exterior domain served as an intermediate domain between the nozzle exit and the outer boundaries and to smoothly introduce expanding nozzle flow into the outlet simulating intake of the wind-tunnel diffuser. Dimensions of the exterior domain were: 14 nozzle exit diameters ($14 \times D_e$) in downstream direction and ($2 \times D_e$) in upstream direction, while the outer or farfield diameter of the exterior domain was $12 \times D_e$.

Table 4.1: Boundary conditions

Parameters	Inlet	Secondary Inlet	Outlet
Input:	p_s, P_0, T_0	p_{sj}, P_{0j}, T_{0j}	$p_a s, P_a, T_a$
Velocity profile:	$\vec{v}_{tan} = 0$	$\vec{v}_{tan} = 0$	$\vec{v}_{tan} = 0$
Turbulence length:	$l_t \leq 0.7D_i$	$l_t \leq 0.7D_j$	$l_t \leq 0.7D_o$
Turbulence rate	evaluated min	evaluated min	evaluated min

Thse boundaries are also denoted in the symmetry cross-section mesh of the whole computational domain in Figure 4.2.

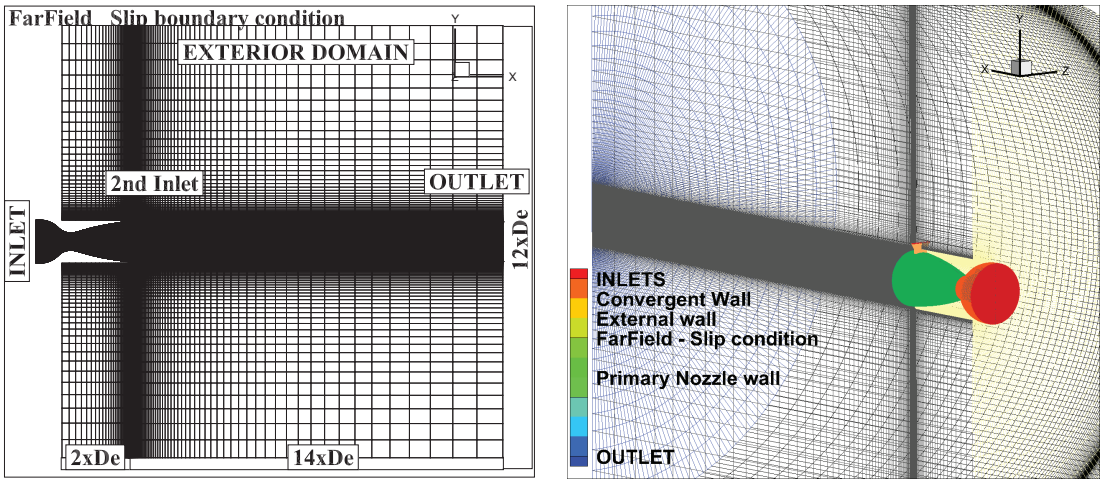

(a) Symmetry cross-section (b) 3D iso view

Figure 4.2: Computational domain with listed boundary conditions

The secondary inlet was designed according to the experimental secondary stilling chamber exit. Referent configuration had a secondary sonic injection normal to the primary nozzle axis. Therefore, the secondary nozzle throat cylinder was

extruded through the nozzle wall forming a deformed ellipsoidal shape of the injection port. Two experimental secondary injectors were modeled with a mapped block around the injection port: a circular and slot shaped as shown in Figure 4.3.

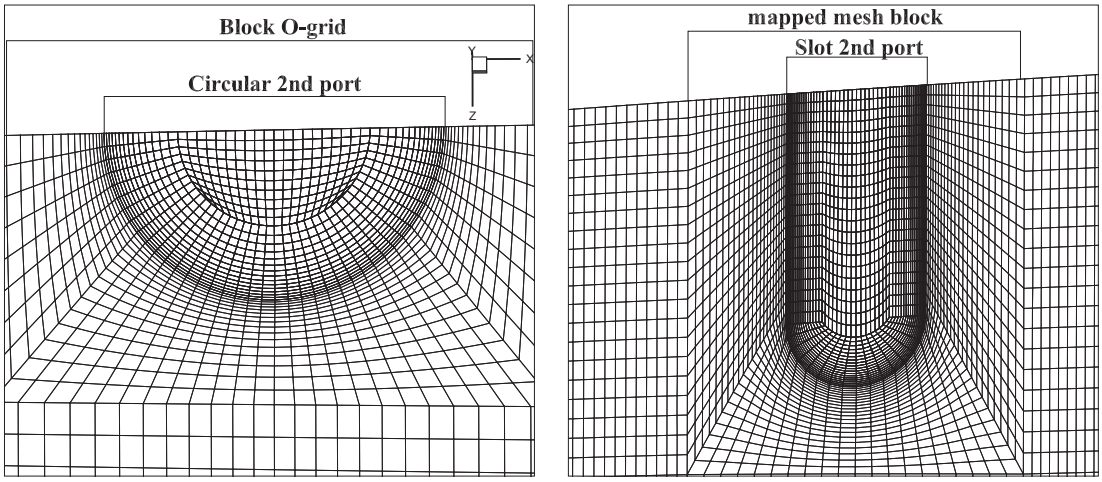

(a) Circular injection port (b) Slot injection port

Figure 4.3: Injection port profiles at the nozzle wall

4.3.1 Near wall meshing

Special attention in meshing needs to be paid to the boundary-layer grid since it represents the most critical zone in the presence of an adverse pressure gradient and shock reflections. Thirty cells normal to the wall is dedicated to the boundary layer where the first cell height and boundary layer growth depend on the model, mesh quality and desired $y+$ value.

For the cells out of BL, grading schemes were applied to smooth up transition between BL and the central hexagonal core. In general, two grading schemes were used, a successive ratio scheme Eq. 4.33 and exponential scheme Eq. 4.34.

$$r_{grad} = \frac{l_{cell(i+1)}}{l_{cell(i)}} \tag{4.33}$$

$$r_{grad} = \exp\left(L_{edge}/n(h_x - 1/2)\right) \tag{4.34}$$

where h_x and n are the grading parameter and the number of cells at the edge.

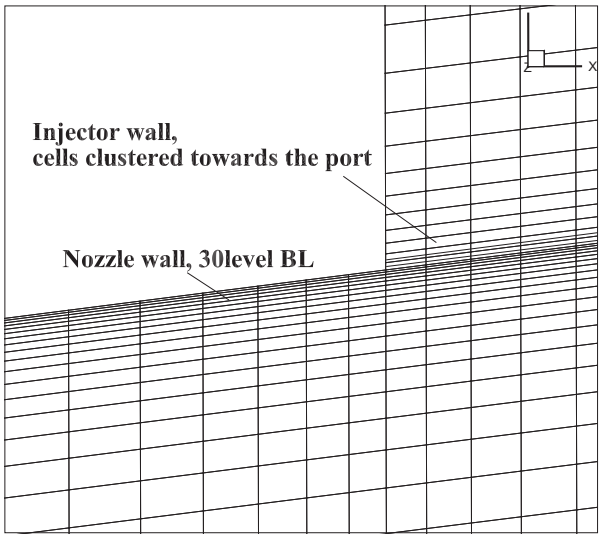

Figure 4.4: BL at injection port zone of the divergent section TIC nozzle symmetry

Numerical grid and boundary details for three quality levels of full 3D meshed referenced models are given in Table 4.2. Corresponding $y+$ profiles along the nozzle wall of each grid case are plotted in Figure 4.5. The fine grid A yielded $y+$ values below 1. Both coarser grids still have the acceptable $y+$ range with $y+ = 1.5$ and 2.1 at the injection section.

Table 4.2: Numerical grids of TIC nozzle with injection at $x_j/l_n = 0.88$

Parameters	Grid A	Grid B	Grid C
No. of cells	7.72E+06	3.96E+06	2.00E+06
Nozzle domain:			
$Ln \times D_n \times Circum$	$330 \times 180 \times 270$	$240 \times 130 \times 200$	$210 \times 90 \times 140$
$y+$ range	0.24-0.92	1.24-4.97	1.92-7.05
BL first-cell-height	$0.8\mu m$	$5.0\mu m$	$8.7\mu m$
BL depth level	30 *cells*	30 *cells*	22 *cells*
BL growth rate	1.20	1.17	1.13
Injector domain:			
$Ln \times D_n \times Circum$	$52 \times 50 \times 80$	$35 \times 42 \times 72$	$30 \times 34 \times 68$

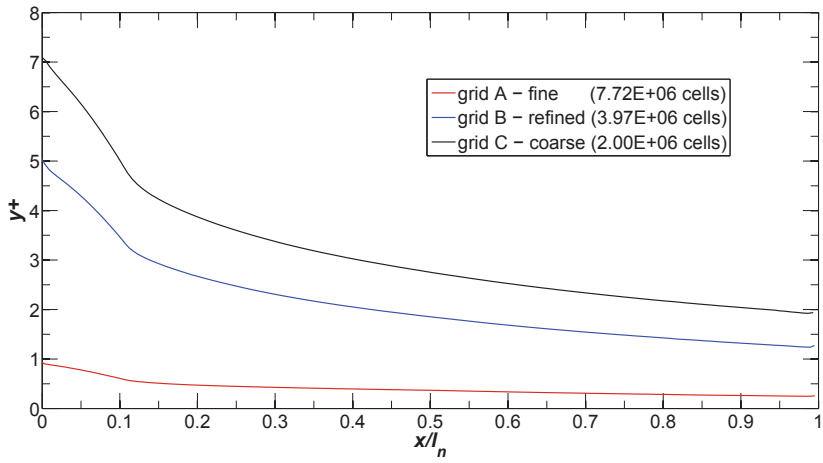

Figure 4.5: $y+$ at 360° TIC nozzle section 3D grid for 3 levels of mesh quality

4.4 Numerical testing approach

In general, the numerical procedure consisted of initial 2°-slice axisymmetric computation of inviscid and viscid non-vectored nozzle, then the axi-2D results are projected to 3D case. 180° 3D model results were inherited from the coarser to the finer meshed models and to the full 360° model.

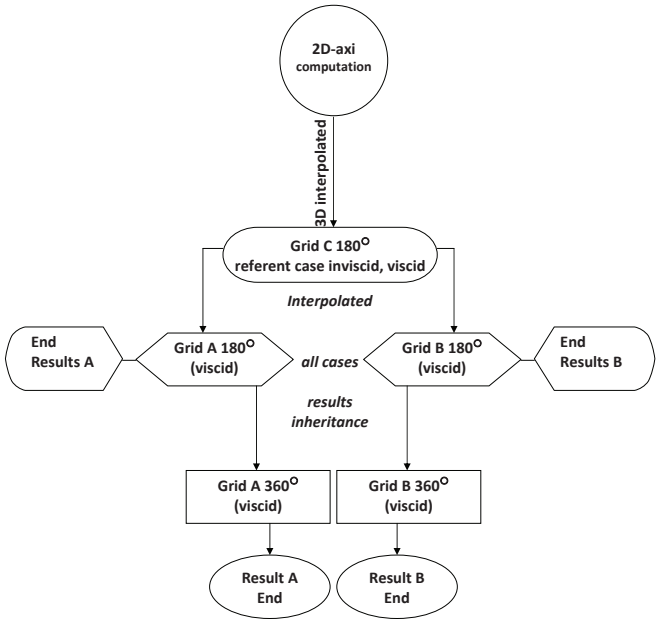

Figure 4.6: Numerical computations process algorithm

There is no specifically defined absolute convergence criterion in CPS_C. However, the probes were built to monitor the iteration convergence of the mass-flow-rate, pressures and temperatures at the inlets and the exit and to monitor each force component at the nozzle wall, injection port and at the nozzle exit. Computations were initialized as an unsteady RANS and then changed to a steady RANS for the faster iteration process. Depending on the test case, uRANS was accordingly run afterwards, initializing from a steady solution. The explicit scheme, that was used, requires a low value of CFL number. Therefore, $CFL \sim 0.1$ was used at the very beginning of computations and then consecutively changed to $CFL = 0.25$ throughout the main iterative process.
Besides the results convergence, a basic grid-convergence checking was also conducted on the beginning. Attention was paid to the wall-pressure distributions in the symmetry plane depicted in Figure 4.7 and to the produced forces. Normalized pressure force coefficient exerted on the axisymmetric nozzle wall was used and the data is tabulated in Table 4.3.

Table 4.3: Pressure force coefficient for axisymmetric non-vectored nozzle

Grid sequence	No. of cells	C_{Fpx}	Difference to $f_{Rich.}$
Coarse	$2.00E+06$	0.22465	-2.482%
Refined	$3.96E+06$	0.22804	-1.011%
Fine	$7.72E+06$	0.22798	-1.037%
	$f_{Richardson}$	0.23037	

The Richardson[84] extrapolation modified by Roache[85] was used on a divergent portion of the axisymmetric conical nozzle wall. In this simple case, wall in axisymmetry is straight under constant angle and pressure is integrated along the wall with orth-vector $\overrightarrow{x}$. In this case F_{px} is defined as:

$$F_{px} = \oint p \cdot \overrightarrow{x} dA \tag{4.35}$$

and corresponding force coefficient as the ratio of this force and the primary jet momentum. In the non-vectored nozzle axisymmetric case, values obtained numerically and via Richardson quasi-exact extrapolation were in a very good agreement. Richardson extrapolation is based on a series of discretization error,

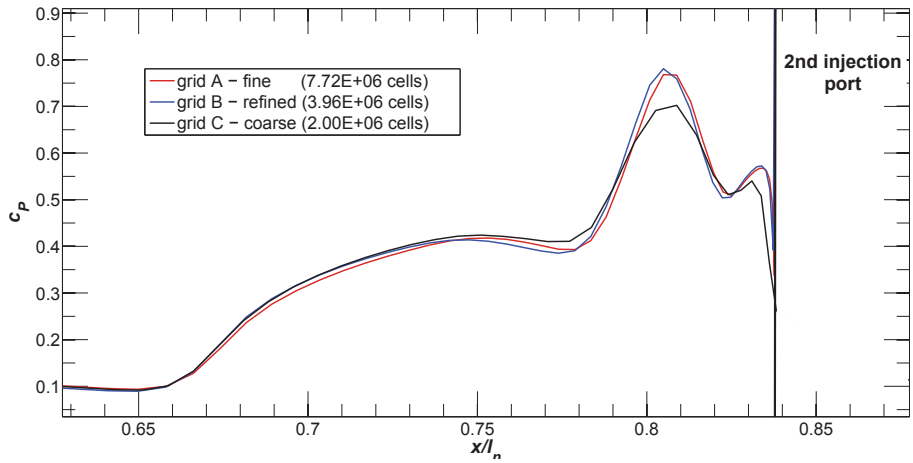

Figure 4.7: Pressure coefficient at the wall of symmetry plane for the given grid sequences

($DE_k = f_k - f_{exact}$) and it yielded as expected a very small difference. The small differences between the grid sequences also come from the fact that all three grid quality levels were of the same order and therefore a clear distinction between them is not emphasized. Richardson extrapolation on a full 3D case with transverse injection and strong shock interactions is a more difficult to be achieved but it can be realistically conducted on a flat plate case. In this simple case, C_{Fpx} deviation for extrapolated value was insignificant for grid-A and grid-B, while a slightly larger deviation is denoted for the grid-C case. All the numerical force measurement differences were below the error margin of the experimental force-balance. The c_P grid-convergence plots, given in Figure 4.7, depict very small variations between the grid sequences. There is no difference in estimation of the separation point. However, it can be noticed that the pressure value in the pressure rise, plateau and pressure peak zones show some slight differences. In the result discussion parts of this study it is found that the plateau pressure is a slightly overestimated while the peak pressure appears to be underestimated comparing to the experimental results. This gird-convergence pressure plot is in the agreement with those results showing that overestimation and underestimation slightly increase with the grid quality decrease.

Similarly, a basic check of the different turbulent models was conducted using the grid-A case. Although, the selected 2-equation models have the positive and

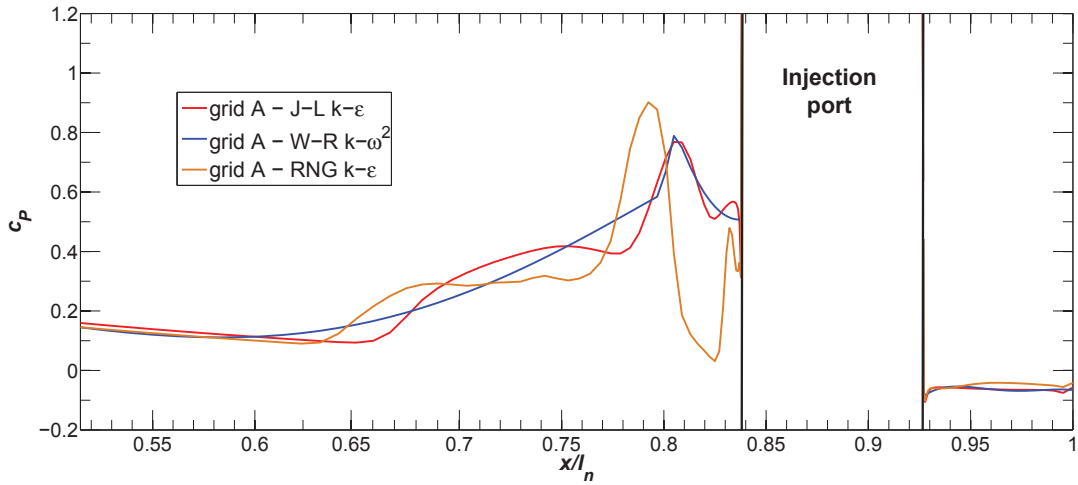

Figure 4.8: Pressure coefficient the wall of symmetry plane for the 3 turbulence models

negative effects which are elaborated previously and which can be found in a large number of publications, the actual performance of these turbulence models largely depends on the technological implementation inside the given CFD code. In the case of CPS_C CFD code, integration of the standard Jones and Launder[76] $k-\varepsilon$ model is fully accomplished and the code performs unexpectedly well using this model which apears to exceed the limitations standardly quoted in available literature. On the other hand, implementation of Wilcox and Rubesin[78] $k-\omega^2$ appears not to be well integrated inside CPS_C code for the intended supersonic nozzle cases and especially for the wall-bounded supersonic cross-flows. In the tested 3D numerical cases, a large overestimation of BL size inside the nozzle is present. Additionally, in SITVC nozzle case the recognizable vorticity zones appears to be omitted with the consequential lack of the pressure regions inside the separation zone and an inaccurate estimation of the separation point. This appears to be invariant of the model coefficients or numerical scheme change.
Otherwise, the RNG[77] $k-\varepsilon$ model, which CPS_C integration is in the ongoing development, appears to perform considerably better. Estimated BL thickness and supersonic flow effects are well achieved. The pressure profile of SITVC nozzle case appears less smoothed than the one of the standard $k-\varepsilon$ and with some overestimation of the detachment point. However, the plateau pressure value and the pressure peak seam to be in a better agrement with the experimental data

than the standard $k - \varepsilon$. The pressure drop zone before the secondary injection appears to be overemphasized in the RNG[77] $k - \varepsilon$ case.

In further result discussion chapters, presented numerical work was based on the standard Jones and Launder[76] $k - \varepsilon$ turbulence model, while RNG $k - \varepsilon$ model was used only in some cases for the comparison and verification purposes of the standard model results.

Chapter 5

Analysis of primary characteristics of SITVC axisymmetric nozzle

5.1 Introduction

Identification of distinctive features should precede an analysis of effects and performances of an applied SITVC to an axisymmetric supersonic nozzle. There are number of different parameters and specificities which can directly or indirectly affect the vectored or undisturbed nozzle flow and thus its performances. By the nature of each characteristic, it is possible to group them as: 1. physical, affecting the flow by change of geometrical characteristics, 2. the governing primary and secondary flow conditions and fluid properties and 3. heated or combusted thermochemical reactive specie or mixture properties. Related to the temporal mode of change and perturbation they can be of permanent, instantaneous or oscillatory character. In the current study, permanent and instantaneous changes to the above mentioned characteristics groups are investigated while due to the complexity of the test rocket engine models and investigation techniques, the instability analysis was omitted. In addition, major instability behavior initiated by the transverse supersonic cross-flow jets occurs downstream of the interaction which for the most test cases was of the secondary or insignificant importance. Some of the first starting points of investigation may be interpreted as to which kind of the nozzle pneumatic actuator is installed, where it should be injected

and what and how much should be injected. To answer these questions each of them is considered as an isolated feature to distinguish action character, but also as a combined effect which is essential for any SITVC system.

The size of the injector was predefined respecting the industrial demands for the moderate secondary to primary mass-flow-rate (3 to 8.5%) and by intended use of the already stored pressurized propellants or reactants from the combustion chamber without the additional pressurization.

5.2 Secondary injection port position [1]

To investigate the effect of a 2nd injection port positioning, two experimental conical $Mach$ 3 nozzles have been designed and produced with the different transverse injector positions. The secondary convergent nozzles were with the throat diameters corresponding to the $SPR = 1$ or $f_m = 0.08$ condition. To support experiments, numerical models are built on the same geometry and preprocessed for the CPS_C numerical simulations. After coupling, comparing and analyzing the results, a verified numerical approach was conducted with the additional secondary injection positions.

5.2.1 Qualitative flow analysis

At first, images obtained in Z-schlieren visualization are considered to qualitatively analyze the flow and to quasi-quantitatively examine observed flow structures via Matlab® image processing. The Toepler's Z-schlieren photos are taken experimentally and also extracted from the corresponding numerical results for two test models with transverse circular injections at $x_j/l_n = 0.7$ and $x_j/l_n = 0.9$, for $NPR = 37, SPR = 1$. In Figure 5.1 and 5.2, experimental and numerical schlieren are depicted and denoted (a) and (b) respectively. The numerical schlieren is defined as a density gradient magnitude at the nozzle symmetry plane while experimental schlieren is taken in the exterior domain at the nozzle exit section. On the experimental schlieren density gradients are superposed laterally

[1] Some of the presented work is also adapted in:
Zmijanovic, Lago, Sellam, and Chpoun[86], *Shock Waves J.* **23** (2013)

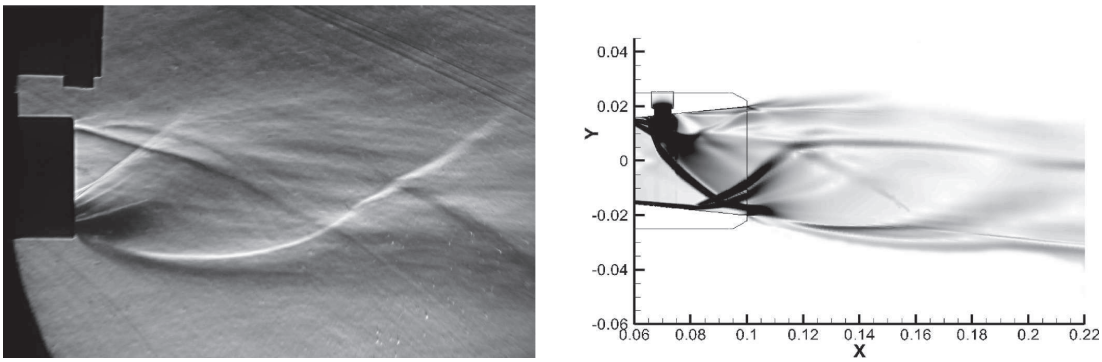

(a) Z-schlieren photograph (b) numerical results schlieren

Figure 5.1: Schlieren images of conical test nozzle with injection at $x_j/l_n = 0.7$

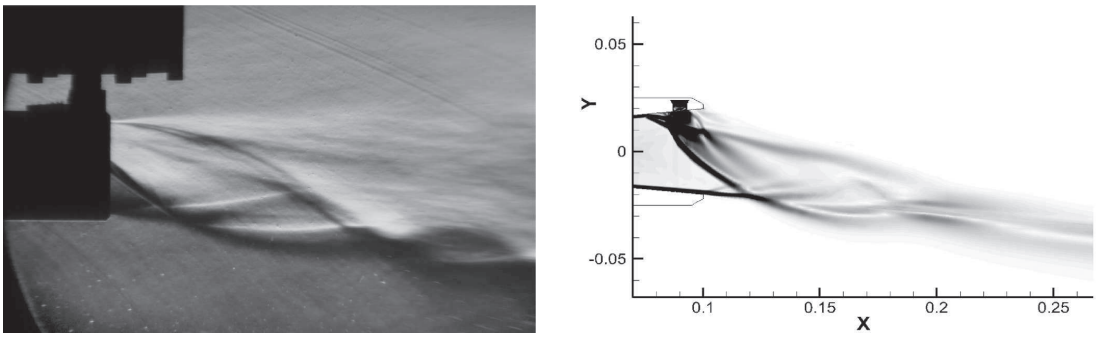

(a) Z-schlieren photograph (b) numerical results schlieren

Figure 5.2: Schlieren images of conical test nozzle with 2nd injection at $x_j/l_n = 0.9$

and projected onto the camera sensor. In the presented images, the density gradients are clearly observable delineating the separation zone, secondary injection plume, boundary-layer separation and the generated shock waves. Bow shock propagation and reflection from the wall side opposite of injection can be observed in Figure 5.1, depicting the case with secondary injection at $x_j/l_n = 0.7$. Density gradient variations depicted in experimental schlieren are traceable back into the nozzle interior domain in numerical schlieren figure. Shock impingement on the opposite wall side, detaches the boundary-layer generating a separation bubble with recirculation and shock reflection. Recirculation zone closes downstream with boundary-layer reattachment close to the exit plane. At the injection side, downstream of injector, the low pressure zone acts over a large area aft of

injection port dominated by the wake vortices and BL reattachment downstream. Contrary to the case in Figure 5.1, in Figure 5.2 it is observable that the main shock reflection doesn't occur inside the nozzle, so that a part of the main undisturbed flow is being exhausted closer to the opposite side. At the injector wall side, the downstream low pressure zone is much shorter which doesn't allow the wake vortex shedding and reattachment. Simple flow deflection through the

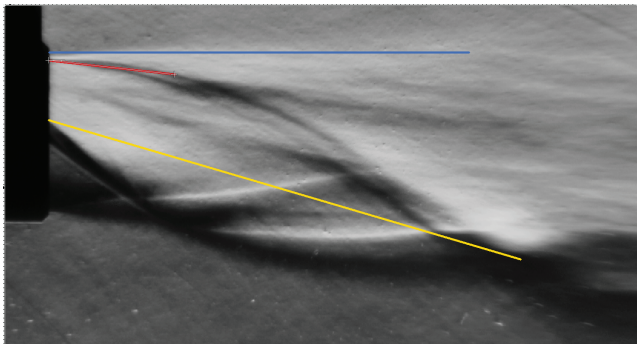

Figure 5.3: Image processing tool deflected flow angle measurement

oblique planar shock can be illustrated via shock polar or heart-diagram in Figure 5.4. The shock polar is approximated for a 2D oblique shock waves for a known Mach number and specific heats ratio. It shows all possible states that the flow can reach passing a single shock. Pressure ratio, $p/p_{(1)}$ is found via Rankine-Hugoniot relations and plotted as a function of the flow deflection angle, φ_D. This shock polar diagram also indicates an existence of the maximum flow deflection φ_{Dmax} beyond which the equations of planar oblique shocks have no admissible solutions. For the oncoming upstream flow of $M = 2.8$, $\varphi_{Dmax} = 32°$ would represent a planar-approximated theoretical maximum value if the flow deflects under the optimal conditions.

Comparing the two injection cases, it is also apparent that the flow deflects under a noticeably higher angle for the case $x_j/l_n = 0.9$ than for $x_j/l_n = 0.7$. However, quasi-quantitative measurements of the deflection angle from the schlieren photographs may mislead to the overestimated pitch vector angle values, since the affected supersonic cross-flow is not homogenous and uniform anymore. As shown in Figure 5.3, measurement of the deflected flow from the center to the Mach disk will yield higher angle values, in this particular case 15.02°. It is found that if in-

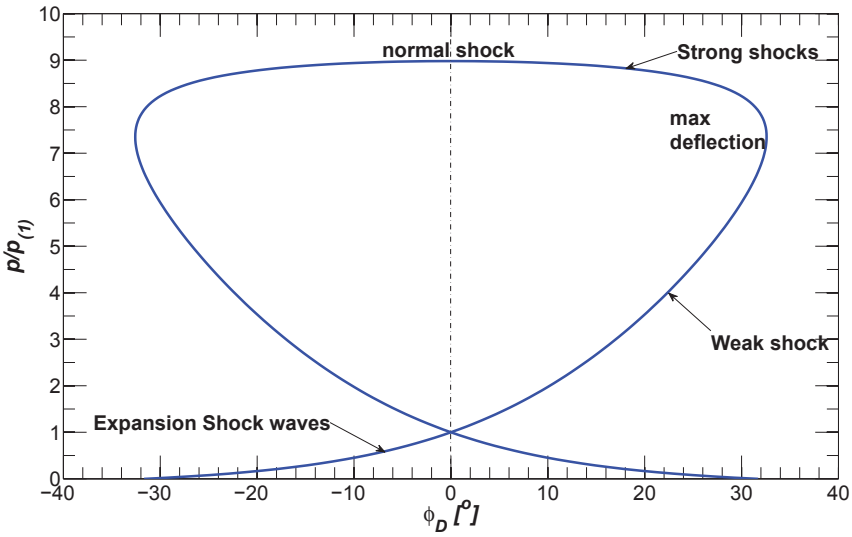

Figure 5.4: Shock polar for 2.8 *Mach* in the hodograph plane

stead of centerline the tangent of the shock line corresponding to downstream BL and injectant plume (red line) is measured, the angle $\sim 8.7°$ is obtained which is much closer to the quantified vector pitch angle values. Additionally, produced 3D flowfield is characterized via Mach 0.5 to 3.7 iso-surfaces in Figure 5.5. Generated primary and secondary upstream vortices and weak but large low-pressure downstream zone are depicted. 3D structures as the separation, bow-shock, horseshoe vortex and downstream wake are traceable in the complex interaction flowfield. After moderate separation shock wave, pressure maximum produced by injection itself transfers the energy via SUV, imposing a steep gradient to the developing bow shock. Its propagation ends on the opposite wall side, separating the flow upstream of the impingement point and creating a recirculation zone, while the bow shock reflects. In between the windward and the leeward bow shock boundaries, the shock surface discontinuity is formed effectively increasing the nozzle pressure. The leeward boundary is coupled with the barrel shock surface surrounding the secondary plume expansion and recompression. After the first sequence ends with the Mach disk, the trailing vortices dominate the flow initiating the mixing with the primary flow, detectable at the exit section in Figure 5.5. In the aforementioned case where injector is placed deeper inside the nozzle, effects governed by the downstream wake zone which is concurrent to the

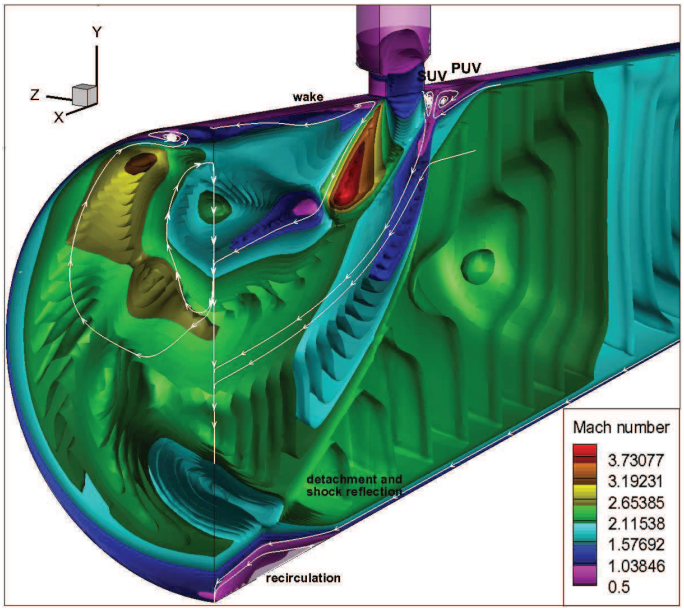

Figure 5.5: $x_j/l_n = 0.7$ case 3D flowfield with iso-Mach contours

upstream separation significantly affect the nozzle performance. Even though, the intensity downstream is weak, the large wake acts over a large area aft of the injector generating a forceful suction as also illustrated in Figure 5.6. The suction pulls back the flow and injectant plume towards the nozzle wall. As can be seen in Figure 5.5, the plume is turned completely to the wall and in this case it even exits the nozzle with a small negative angle in respect to the nozzle axis. The high pressure region ahead of the secondary plume pushes windward side of injectant barrel shock. The contribution of the low pressure region to the nose-down moment about injection point is relative to the downstream size and it is particularly high in this case where the downstream region extends far aft of the injection port.

The experimental test model with the injector closer to the exit, $x_j/l_n = 0.9$, with Mach iso-surfaces depicted in Figure 5.7, exhibits different characteristics which in SITVC case generally improve the performances. Namely, the injection position in this case is close enough to the exit plane so that 3D bow-shock propagation ends and reflects far in exterior domain, while the downstream extension of the wall is short causing a substantially lower suction force than for

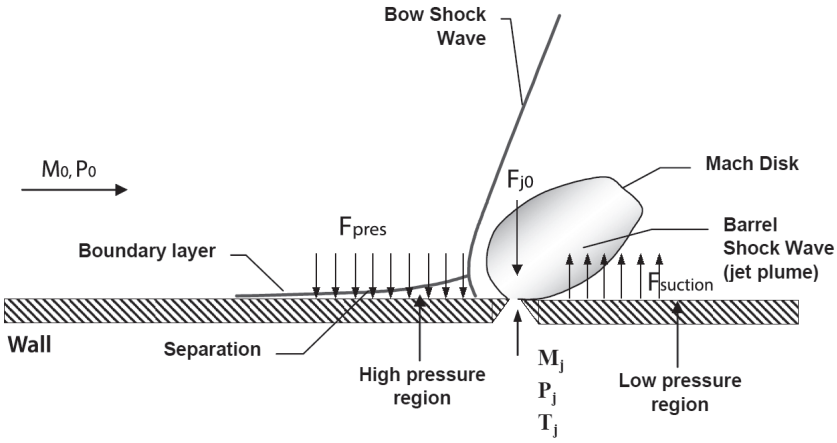

Figure 5.6: 2D scheme of the 2nd injection nozzle wall zone portion

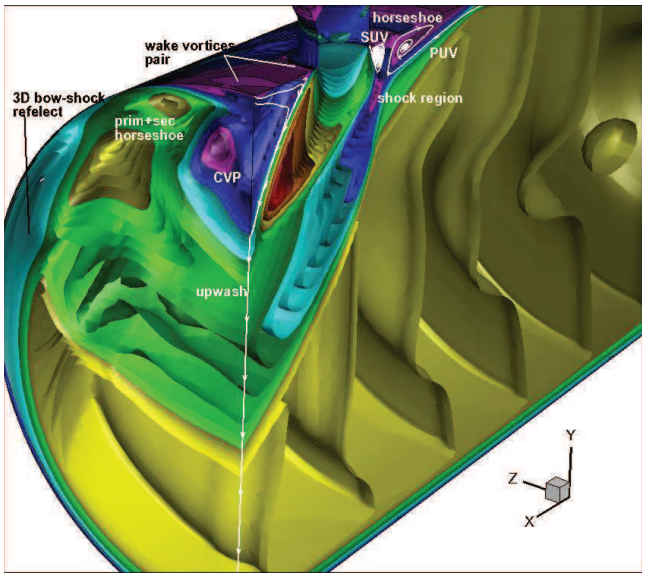

Figure 5.7: $x_j/l_n = 0.9$ case 3D flowfield with iso-Mach contours

the $x_j/l_n = 0.7$ injection case. It is also detectable that the lateral deformation of the complex flowfield structures is milder as the smaller amount of the flow in the nozzle cross section is disturbed by initiated separation and bow shock propagation.

Described effects and characteristics naturally indicate a better SITVC performance rate with the injector position closer to the nozzle exit at the designed operation conditions. However, a different flow conditions as overexpansion, in-

jectant properties and geometry can further affect optimal performances at the selected position.

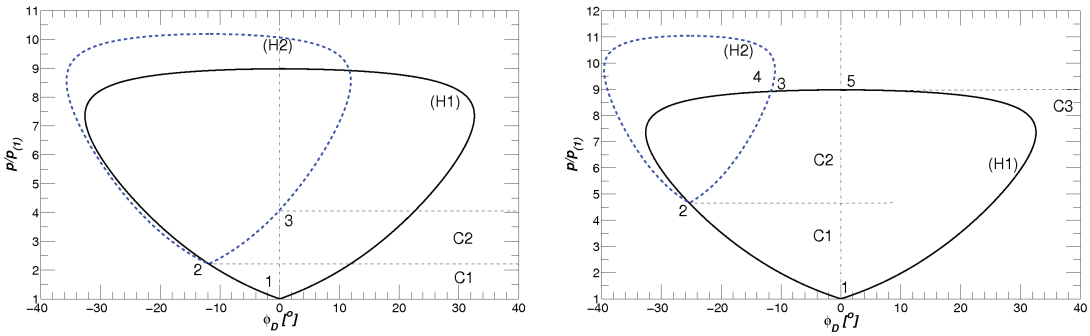

(a) Regular reflection, $\varphi_D = 11.5°$ (b) Mach phenomenon, $\varphi_D = 25°$

Figure 5.8: Combined shock polar diagrams of the regular and Mach wall-reflection for an incident oblique shock wave at $M1 = 2.6$ in polar plane

Characteristic zones of the SITVC nozzle with transverse injection at $x_j/l_n = 0.7$ are depicted via Mach contour plot and the velocity vector streamtraces in Figure 5.10(b). By analyzing streamtraces it can be observed that the stream particles inside BL are being pulled inside PUV and the ones at the most outer BL zone into SUV. The deflection of the streamtraces outside of BL occurs in accordance to the oncoming flow Mach number and the shock wave position. Hence, it can be observed that the streamline closer to the BL, where initiated shock appears stronger, deflects under higher angle than the one away from BL. Additionally, the streamline at the opposite side goes through the incident and reflected shock and changes respectively its attitude twice. For the approximated 1D flow, incident and regular reflection angle may be denoted as $\Delta\varphi_D$ and $-\Delta\varphi_D$. In Figure5.8(a), shock polar (black heart curve)(H1) represents the incident planar shock wave (C1) in an approximated uniform 1D flowfield with an oncoming $M = 2.6$ flow. For the initially evaluated negative deflection $-\Delta\varphi_D = 11.5°$ it is possible to represent the state (2) with reflected (C2) shock and corresponding blue heart curve (H2). In this idealized case (H2) intersects the $\varphi_D = 0$ axis at point (3) illustrating a non-realistic regular reflection case that never happens for an axisymmetric nozzle. With an increase of deflection angle, (C1) corresponds to the stronger shock solutions and thus, (H2) doesn't intersects 0-axis. Hence, the reflection point cannot exist on the wall any longer. In order to satisfy the

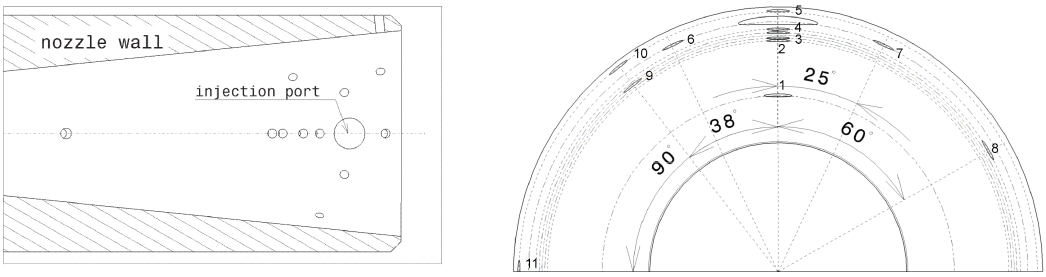

(a) side view (b) upper part front view

Figure 5.9: CAD draft with the Kulite® probes housings distribution for Nozzle C-i $x_j/l_n = 0.9$

slip boundary condition we can define a triple point (T) which exist between (3) and (4) in Figure 5.8(b), along with the Mach disk (C3).

5.2.2 Quantitative measurements

The experimental models were mounted on the force balance, measuring the force components in all three spatial directions and additionally the nozzle C-i0.9 was equipped with eleven Kulite® fast pressure probes. The XCQ-062 Kulite® probes were flush mounted with the head diameter of $1.72mm$ and distributed along the symmetry wall line and along selected meridians in order to characterize iso-pressure lines and capture the incipient detachment and separation zone size. The experimental data is analyzed together with the numerical results and presented in wall-pressure graphs and tables. The pressure data is nondimensionalized by the chamber total pressure as this value was constant during the tests. Numerically obtained wall pressure data for upper and lower symmetry wall boundary is given in Figure 5.10 together with the characteristic zones. After the incipient separation point, there is a steep pressure growth in the *Region* (1) which ends with the pressure flattening or plateau pressure governed by the primary upstream vortex in *Region* (2). After the plateau zone, and a smaller descent between PUV and SUV, the pressure rapidly increases to the pressure peak value in *Region* (3), dominated by the secondary upstream vortex. After reaching the maximum peak, it steeply decays with a staircase-shaped secondary peak caused by the interferences at the edge of the secondary injection port. Downstream of

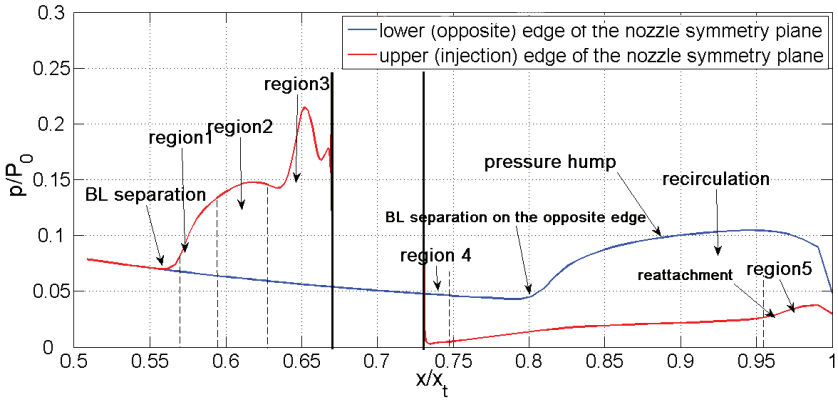

(a) Wall-pressure profiles

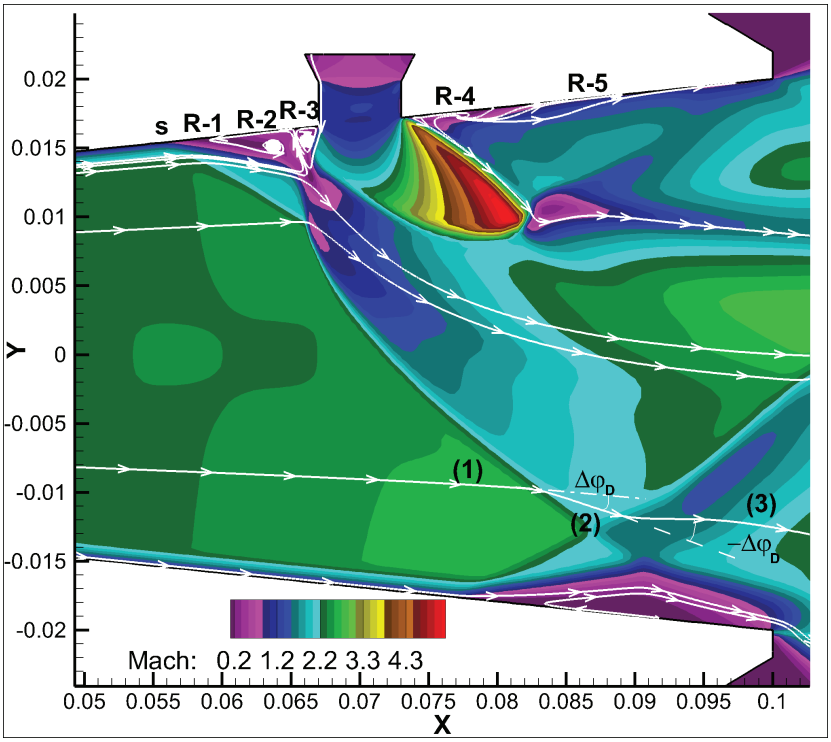

(b) Mach plot with streamlines

Figure 5.10: $x_j/l_n = 0.7$ case symmetry plane

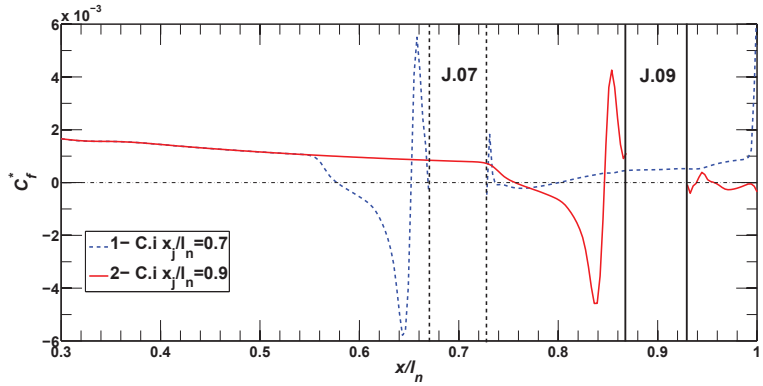

Figure 5.11: Skin friction distribution for 2 experimental/numerical test cases $x_j/l_n = 0.7$ and $x_j/l_n = 0.9$

the injection port, after slight pressure rise due to an injection port trailing edge, there is a widely distributed low pressure zone in *Region* (4) . Weak but large pressure hump is closing the zone of *Region* 5 ending with the trailing edge of SDV, boundary-layer reattachment and the recompression shock. On the opposite side pressure profile, there is a rapid pressure rise due to a boundary-layer detachment caused by the bow shock impingement. The profile is then flatten by the recirculation inside the formed bubble. At the end, there is a pressure drop caused by the recirculation trailing edge and followed by the recompression through the shock. Such a complex interaction flowfield is then analyzed for different injection cases. As it can be preliminary deduced from the qualitative analysis and pressure profiles, the nozzle test case with the injection placed deeper inside the nozzle at $x_j/l_n = 0.7$, greatly disturbs the flow inside the rocket nozzle affecting the complete flow that passes through the nozzle cross-section. This generates the effects as the nozzle pressure loss and additional repercussions in side loads distribution on the nozzle wall, corresponding to the plots depicted in Figure 5.10. These effects reduce the nozzle and vectoring performances which are shown through the forces plots and tables, and may generate dangerous flow unsteadiness.

By finding a normal distance to the wall d_n as denoted in Chapter 2 it was possible to evaluate wall shear stress, τ_w which is then rationalized by the total chamber pressure value and given as an alternative skin friction coefficient

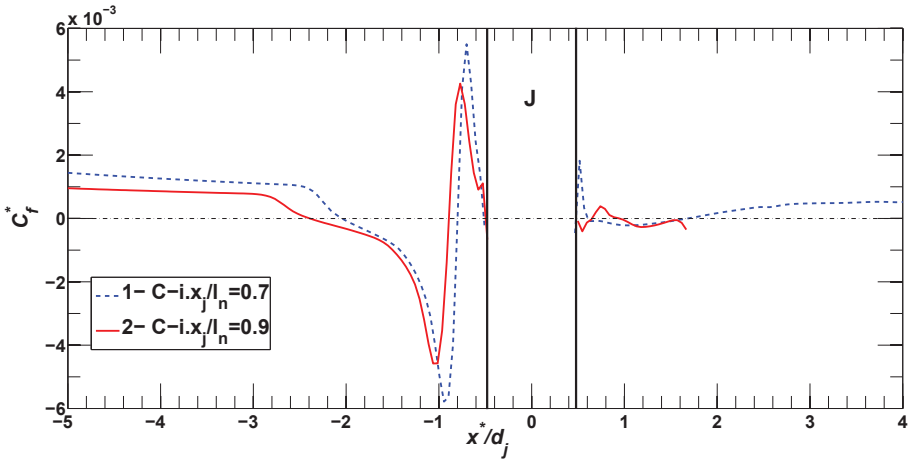

Figure 5.12: C_f^* recentralized to the auxiliary coordinate system at injection point and non-dimensionalized by d_j

C_f^*. In Figures 5.11 normalized friction coefficient is shown for $x_j/l_n = 0.7$ and $x_j/l_n = 0.9$ test cases. For the sake of better clarity of upstream separation, an auxiliary coordinate system is defined at the injection point with the x^* coordinate non-dimensionalized by the injector diameter. In Figure 5.12, an increase in upstream separation of $\sim 16\%$ is detectable for the case with injection closer to the nozzle exit. At the laminar boundary-layer injection case, mentioned in Chapter 2 by Spaid *et al.*[10] the separation is noticeably larger and it is shortly preceded by transition to turbulence. In a difference to that, a turbulent boundary-layer has a considerably shorter separation zone and a thinner BL. Wall shear stress, given in Figure 5.13 for multiple injection cases into Mach 3 conical nozzle, clearly points to the size of the separation zone. It can be observed that this increase is steady with the injector displacement towards the nozzle exit and very slightly decays with the last injection placement at $x_j/l_n = 0.95$ which may be viewed as a consequence of the higher back pressure influence. After the upstream boundary-layer thickening, flow detaches at $C_f = 0$ value. The other two peaks in the wall-shear stress plots comply to the strong eddy zone dominated by the counter-rotating vortex pair, also depicted in the corresponding wall-pressure distribution. Data is analyzed at each injection station cross-section for the injectant penetration (Mach disk) height and for the boundary layer thickness, which is evaluated from the energy-enthalpy criterion and momentum criterion from the injection sta-

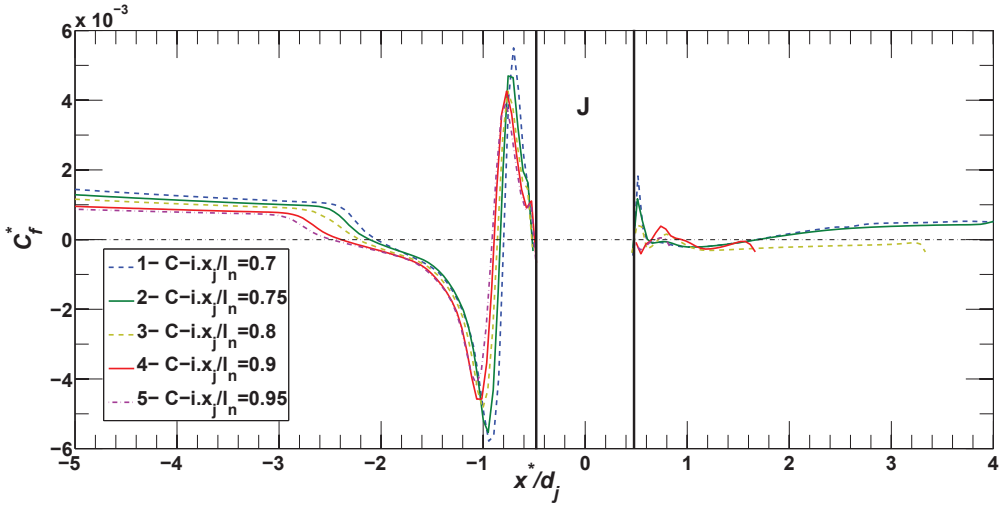

Figure 5.13: Skin friction distributions, recentralized to the auxiliary coordinate system

tion nozzle cross-section profiles. Dimensionless values of the separation incipient point and the plateau in separation are evaluated from the wall shear stress and pressure distribution in Figure 5.17 and presented in Table 5.1. It can be ob-

Table 5.1: Characteristic length and properties of secondary injection nozzle region

Case	D_{jy0}[N]	δ_{BL}[mm]	h_j[mm]	x^*_{sep}/d_j	x^*_p/d_j
$x_j/l_n = 0.70$	10.254	1.88	4.86	-2.51	-1.99
$x_j/l_n = 0.75$	10.28	1.96	4.97	-2.59	-2.08
$x_j/l_n = 0.80$	10.25	2.04	5.19	-2.72	-2.18
$x_j/l_n = 0.90$	10.23	2.116	5.492	-2.895	-2.35
$x_j/l_n = 0.95$	10.25	2.24	5.406	-3.0	-2.44
$^*NPR = 37, SPR = 1, \dot{m}_0 = 223.2g/s, f_m = 0.083$					

served in Figure 5.14 that Mach disk height is minimally changed in regard to the different injection positions along the nozzle. The ratio between *Mach* disk height and separation distance was found to be between 3 and 4 for the given cases of turbulent boundary-layer which well corresponds to the previously discussed analytical model. Very small variation comes from the different nozzle section

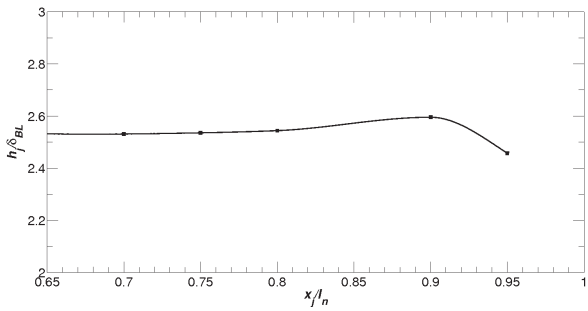

Figure 5.14: Penetration height versus injection position

pressure and a small profile alteration of the injection port at the nozzle wall, as intersection between the secondary throat cylinder and the divergent cone laterally deforms. The only noticeable change, in a rather linear performance profile, can be noticed in the last case, practicably at the nozzle exit, at which exist a slight decrease of the penetration assumingly caused by the exit section effects. Injectant momentum in y-direction is almost a constant with position change along the nozzle wall from $x_j/l_n 0.7$ to $x_j/l_n = 0.95$ and doesn't have the influence on the evolution change of the global side vector force and angle. The second component of the global side force, that is cross-flow interaction force expressed as the wall side force, represents the force-component that is mostly affected by the injection position.

This is then further evaluated using the experimental tools as the wall-pressure and the force-balance measurements. An example of acquisition time history

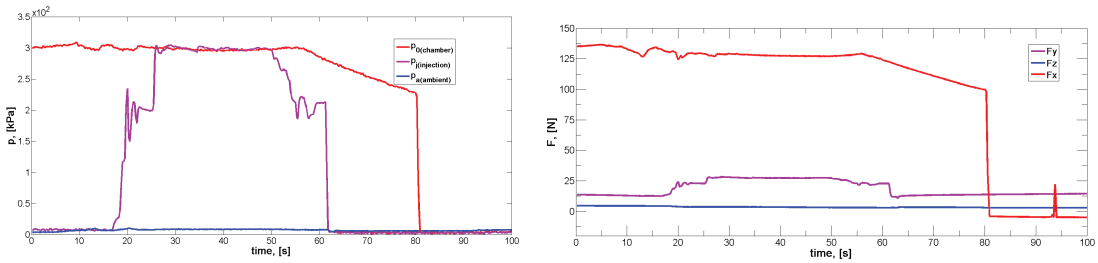

(a) Pressure data (b) Forces data

Figure 5.15: Experimental temporal raw data acquisition history

of the test condition and force balance measurements is depicted via temporal graphs in Figure 5.15. After initial $10s$ of the wind-tunnel operation stabiliz-

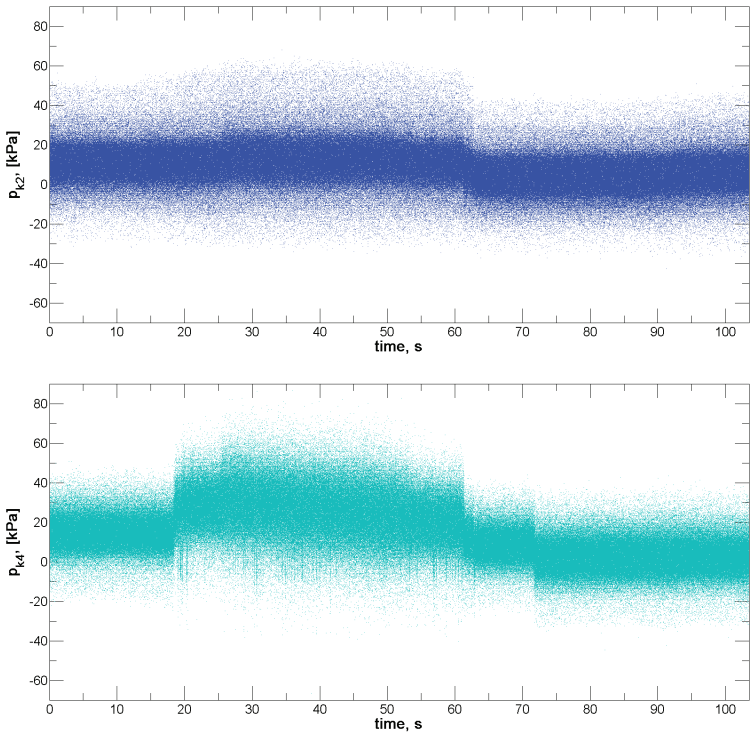

(a) Kulite probe 2 and 4 raw data

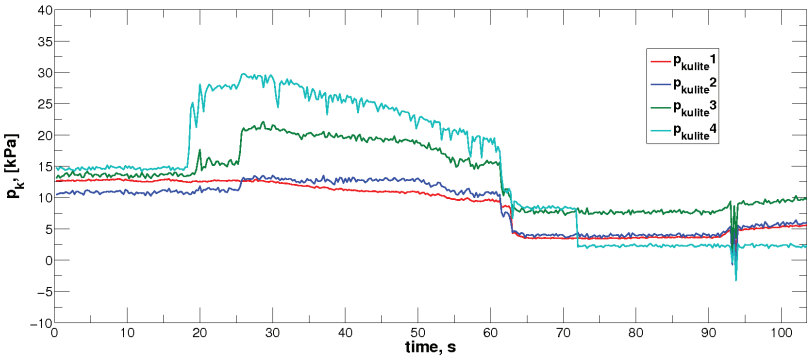

(b) Average wall-pressure data

Figure 5.16: Kulite probes temporal data acquisition history

ing, the valuable test data window was $\sim 50s$. The force balance measurements were acquired synchronously with the pressure data. Raw data from the $Kulite^{®}$ pressure probes were recorded with an acquisition rate of $8000Hz$. Additionally, the data was averaged on 2000 sample chunks and recorded every $0.25s$. Consequentially, standard deviation and absolute, maximum and minimum error are evaluated. The wall-pressure data of the experimental test given in Figure 5.16 depicts the temporal acquisition of the Kulite pressure probes. It can be noted that the measurements were oscillating with an inconsistent occurrence of the peaks, which might be caused by the wall intrusive flush mounting of the probes but also due to oscillations in the flow and measurement signal transferring, as well. However, it was possible to perform standard deviation for each NPR/SPR test case and present along with the averaged data.

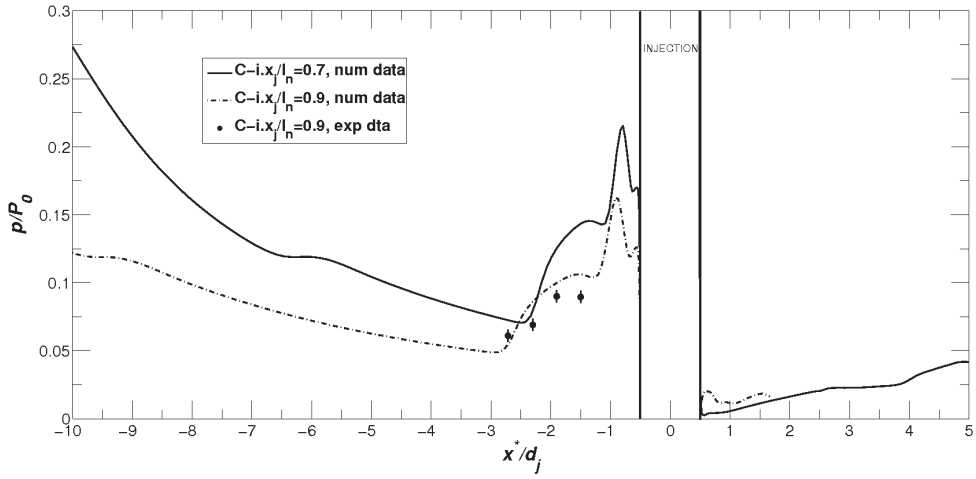

Figure 5.17: Wall-pressure data at the symmetry wall injection side recentralized to the auxiliary coordinate system at injection point and non-dimensionalized by d_j

Numerical and experimental wall pressure data presented in Figure 5.17 shows satisfactory separation distance evaluation. In the graph also appears a slight overestimation of the numerical data inside the separation zone which can be asigned to the aforementioned experimental conditions but also to the limitations of the used numerical model.

The symmetry plane rotated around nozzle axis for series of azimuth angles, $\psi = [0°, 25°, 38°, 60°, 90°]$, defined the probing meridians, used to detect the

three-dimensional lateral separation. Experimental and numerical data were acquired for the selected referent conical nozzle case with injection at $x_j/l_n = 0.9$. Numerical and experimental data were consistent around the nozzle axis and in

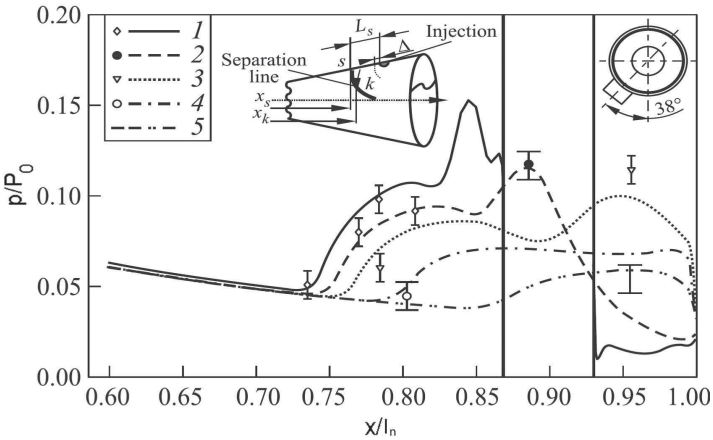

Figure 5.18: Wall-pressure profiles at selected nozzle meridians, detection of the separation line: 1 --→ 0°(*symmetry*), 2 --→ 25°, 3 --→ 38°, 4 --→ 60° and 5 --→ 90°. Curves refer to numerical simulations and signs to experiments

all section planes with some over or under estimation in few points but generally they were inside the measurement uncertainty level. Presented data in Figure 5.18 indicated that maximum separation extends from 0° upstream of secondary port to slightly over the 90° close to the nozzle exit. The wall-pressure inside the separation steady decays from the symmetry, 0° to the lateral side, 90○.

Following the pressure data analysis, the force-balance measurements data are presented in Table 5.2 for the 2 experimental conical test nozzle cases. The note should be made that the experimental nozzle with injection at $x_j/l_n = 0.7$ had 16% larger injection port, ($d_j = 6.4mm$ instead of $d_j = 5.85mm$).

These data are then coupled with the numerically evaluated forces in Table 5.3 and presented along with the performance coefficients. Each component of the net vector force is evaluated separately and then as a resultant. Vectoring angle and amplification factors are calculated according to the formulations presented in Chapter 2. Agreement of force measurements was satisfactory with some smaller underestimation of axial and overestimation of vertical force components. As already mentioned, $x_j/l_n = 0.7$ case was different due to different injector size.

Table 5.2: Experimental force data for conical nozzle SITVC cases

values/case	C-i.$x_j/l_n = 0.7$	C-i.$x_j/l_n = 0.9$
$\dot{m}_j/\dot{m}_0$	0.096	0.082
$F_y, [N]$	2.1	18.4
$F_x, [N]$	131	127.8
δ	0.88°	8.2°
$^*NPR = 37, SPR = 1, \dot{m}_0 = 223.2g/s, F_{x0} = 127N$		

Table 5.3: Numerical force data for conical nozzle SITVC cases

val/case	$x_j/l_n = 0.7$	$x_j/l_n = 0.75$	$x_j/l_n = 0.8$	$x_j/l_n = 0.9$	$x_j/l_n = 0.95$
$\dot{m}_j/\dot{m}_0$	0.083	0.083	0.083	0.083	0.083
$F_{wy}, [N]$	-8.04	0.013	6.308	8.67	8
$F_{jy}, [N]$	9.91	9.914	9.92	9.94	9.94
$\sum F_y, [N]$	1.87	9.927	16.23	18.61	17.94
$\sum F_x, [N]$	131.23	122.44	129.3	127.7	127.6
δ	0.82°	4.6°	7.15°	8.27°	8°
$I_{sp}, [s]$	55.344	51.79	54.96	54.246	54.3
$^*NPR = 37, SPR = 1, \dot{m}_0 = 223.2g/s, F_{x0} = 126.41N, I^0_{sp} = 57.77s$					
Performance coefficients:					
C_{AV}	0.1	0.554	0.861	0.976	0.963
C_{AF}	1.037	0.97	1.03	1.017	1.018
C_{AI}	0.958	0.896	0.951	0.939	0.94

However, in this critical case the main bow shock reflection occurs with a reattachment at downstream side and therefore injectant flux and natural reactive force doesn't have a significant influence on the wall force, which is negative in this case. The y-direction net force exerted on the nozzle wall of this nozzle is canceled by the negative component originating from the secondary flow deflection through the reflected shock. Positive deflection is further deteriorated due to a consequential separation zone on the opposite nozzle wall side and a large suction zone aft of the secondary injection port.

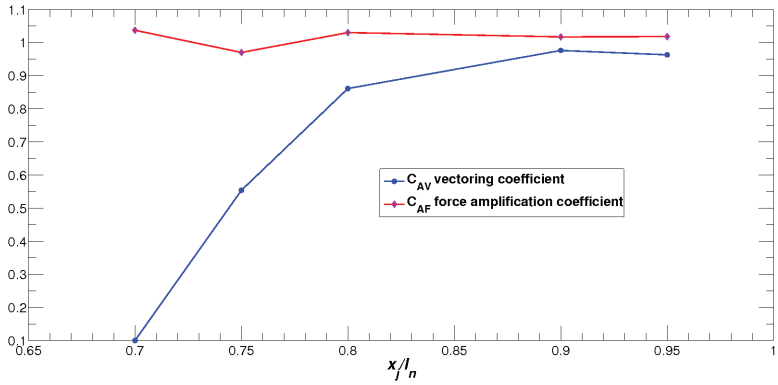

Figure 5.19: Vectoring and force amplification factors vs. non-dimensional injection position

The next injector station at $x_j/l_n = 0.75$ represent the limiting case at which bow shock reflects from the opposite wall side at the nozzle exit. This affects also the axial force as the reflected shock and discontinuity lies at the exit nozzle lip with the wall force reaching 0 in this case. Solely natural reactive force contributing the resultant side force in this case. From this injectant point towards the exit, wall side force steadily increases until the last injection case, $x_j/l_n = 0.95$ where a slight decay is denoted.
In Figure 5.19, vectoring and force amplification factors are given for the tested injector position on the conical test nozzle. As it can be concluded from the graph, an optimal injection position for the given case lies around $x_j/l_n = 0.9$ value.

5.2.3 Injector position observations and remarks

Qualitative analysis at the beginning of this section introduced the fluid dynamics problem of the secondary transverse injection into a supersonic conical nozzle. In the schlieren figures propagation of the bow shock and recompression of the underexpanded secondary jet plume are apparent. In these figures there is a clear distinction between experimental case with injection at $x_j/l_n = 0.7$ and at $x_j/l_n = 0.9$. The first one having additional effects of the shock reflection and reattachment also appears with highly irregular flow exiting the nozzle with the significant part of the flow mixing occurring inside the nozzle which is also

depicted at the numerical iso-Mach contour 3D plots.
Merging the experimental and numerical data, in-depth analysis is performed on the experimental and additional numerical models of transverse injection into the nozzle at different positions. The findings in this analysis point to the several important zones of SITVC operation. The first point is related to the fact that for some injectors positions, the main shock propagates to the opposite wall side affecting the complete cross-section flow. The limiting bow shock reflection case for $Mach3$, 5.8° conical nozzle was found between $x_j/l_n = 0.75$ and $x_j/l_n = 0.765$ at which the wall force is found to be ~ 0. Second test region can be identified between the limiting position and the nozzle exit. Here, the interaction or wall-force and thus the global side force linearly increase with the downstream injector displacement, primarily as a result of the positive disbalance between the upstream high pressure and the downstream low pressure. C_{AV} curve in the last Figure 5.19 supports the standpoint of positive side force increase with the downstream injector positions. On the other hand, force amplification factor appears as an indifferent to the injector position with a very slight performance decay towards the exit with an exception at the shock-reflection limiting case.

5.3 Design characteristics and types of the primary nozzle

In the previous section, an influence of the injector position was analyzed on the $Mach3$ conical nozzle models at which optimal position was found in the nozzle sections close to the nozzle exit. This was justified in the analysis through the physical mechanisms that take place and quantified measurements data. For this nozzle type and given injector design delivering $f_m = 0.08$ under $SPR = 1$ pertinent thrust vectoring angles of $\delta = 8°$ or $C_{AV} \sim 1$ are found. Further, flow deflection and injector positions are analyzed for the higher expansion nozzles. The higher exit $Mach$ number nozzle will normally have a larger cross-section size and a higher momentum flow that needs to be deflected. By examining the isentropic supersonic flow and planar oblique shock, it is convenient to plot the flow deflection curve as a function of the upstream flow Mach number, M1.

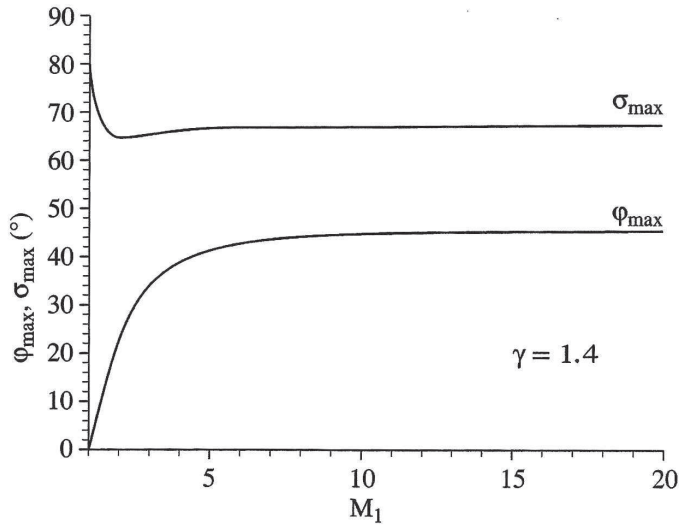

Figure 5.20: Limit deflection angle φ_{Dmax} and corresponding Mach angle for range of upstream incident M1 values

Second to nozzle expansion ratio, we can also denote a peculiar and intrinsic effect of the nozzle wall profile. In the current study several nozzle profiles are considered. Namely, conical and truncated ideal contour (TIC) nozzle models are designed and manufactured for the experiments and also supported in numerical simulations throughout this study. Additionally, the Rao[67] thrust optimized contour (TOC) nozzles and Rao[68] adverse pressure gradient (APG) nozzle model were designed and briefly analyzed in this section. TIC nozzle which is derived from the ideal nozzle by truncation at the particular cross-section, is a shockless type of rocket nozzle. However, it differs from the ideal de-Laval nozzle as the flow at the exit section is not parallel to the axis and uniform. TIC nozzle flow is exhausted under some angle with flow expansion variation from the axis towards the nozzle wall. Previously used conical nozzle includes also weak compression waves inside the nozzle which naturally cross-reflects from the nozzle wall and may cause some effect on SITVC if the compression wave impinges nozzle wall at the separation point. Displacement of the compression wave upstream or downstream eliminates this influence. Furthermore, both Rao optimizations include an internal shock which is substantially stronger than the weak compression waves and may have an important effect depending on the SITVC application.

5.3.1 Primary nozzle sizing and SITVC

Analyzing the maximum possible flow deflection through the planar shock as a function of an upstream Mach number in Figure 5.20, it can be noticed that φ_{Dmax} curve has a maximum climb rate until $M1 \simeq 2.5$. Afterwards, curve gradually and parabolically transforms into an asymptotic climb curve evolving till the limiting value. From the simple analysis it can be deduced that the ratio of the flow deflection and the upstream flow momentum will change along. The flow deflection will quasi-linearly follow the main flow momentum and then this ratio will start to slowly decrease.

To analyze the effect of primary nozzle expansion ratio, previous Mach 3 conical nozzle profile is extended to the area ratio at the exit corresponding to Mach 5 and compared under adapted, NPR_D and $SPR = 1$ conditions. As discussed in the previous chapter, boundary-layer thickness and ratio with the penetration height greatly affect the generated separation and the side force. In the case of a long and small half-conic angle nozzle, boundary-layer will be largely increased, substantially affecting the separation and SITVC nozzle performances. Therefore, a simple inviscid numerical simulation is performed with Mach 3 and Mach 5 conical nozzle models. Analyzing an inviscid SITVC nozzle case, it can

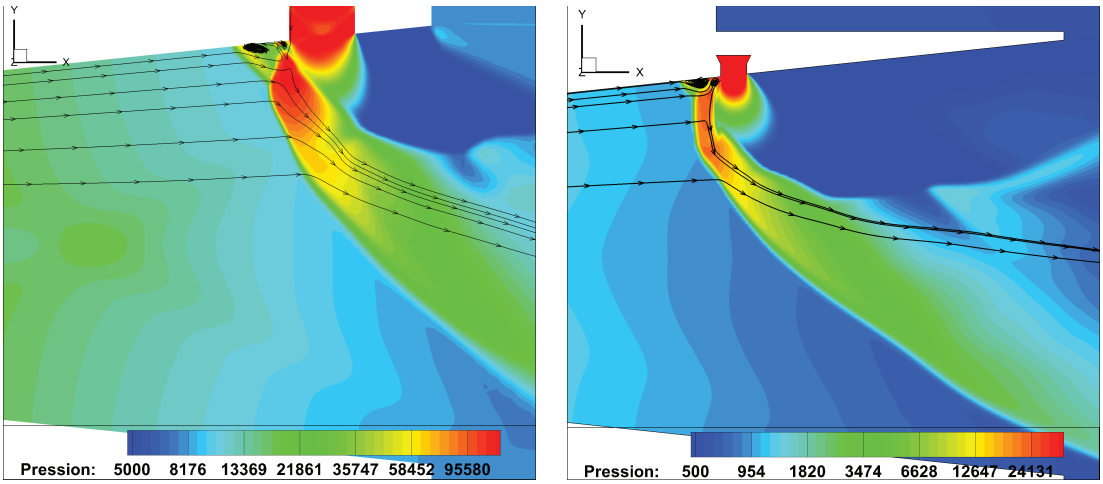

(a) $M_e = 3, C - i.0.9$ (b) $M_e = 5, C - i.0.8$

Figure 5.21: Pressure contour plots for inviscid numerically simulated cases of $\alpha = 5.8°$ SITVC conical nozzles, $[Pa]$

be observed that the separation zone is a noticeably shorter than the one of the viscous boundary-layer case. Moreover, absence of the viscous BL affects the separation shock and the generation of interaction cross-flow interface. Hence, the underexpanded secondary plume propagates in transverse direction normal to the nozzle axis while being recompressed inside the barrel shock wave. The main shock formed in front of the windward side of a barrel shock appears as a strong quasi-normal shock wave that deflects the flow streams in vicinity of the wall under a high angle close to 90°. After compression sequence ends with a Mach disk, the secondary plume downstream deflection starts, which is followed by the bow shock incidence change. At this place, a triple point can be detected originating from the interaction of the main bow shock and the secondary plume barrel shock wave and Mach disk. The force data of analyzed test cases

Table 5.4: Force data of SITVC conical nozzle inviscid numerical calculations

Case	F_{jy}[N]	F_{wy}[mm]	$\sum F_y$[N]	$\sum F_x$[N]	δ,°
$M_e = 3, x_j/l_n = 0.9$	9.935	8.436	18.371	129.213	8.09
$M_e = 5, x_j/l_n = 0.9$	10.24	10.595	20.835	149.869	7.91
$M_e = 5, x_j/l_n = 0.8$	10.165	10.557	20.722	148.736	7.93
$M_e = 5, x_j/l_n = 0.7$	10.111	2.116	12.227	149.323	4.68

in Table 5.4, indicate a rise of the interaction wall-side force component with an increase of the upstream flow momentum. Relation between the two side force components varies with nozzle expansion increase, leading to a higher contribution of the cross-flow interaction force component than the one of the reactive force. However, the augmentation of the deflection rate with an increase of the upstream flow Mach number in this case is a slightly less than the corresponding increase of the primary jet momentum. This smaller change can be observed in the vector pitch angle result data, which represents a ratio of side to axial net forces. For the Mach 5 conical nozzle, upstream displacement from $x_j/l_n = 0.9$ to $x_j/l_n = 0.8$ does not influence the performance in terms of produced forces, with an only insignificantly small increase of δ for $x_j/l_n = 0.8$ case, while $x_j/l_n = 0.7$ case falls below the reflection condition limit.

Furthermore, in the current experimental and numerical study, the conical

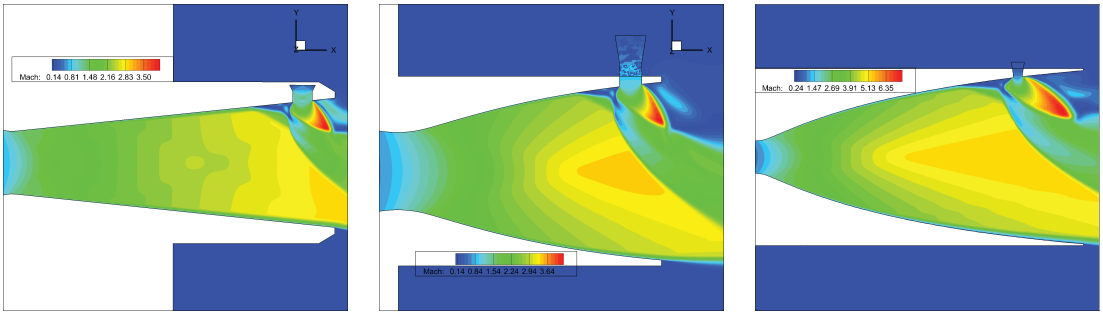

(a) Conical Mach 3 nozzle with injection at $x_j/l_n = 0.9$

(b) TIC Mach 3.23 nozzle with injection at $x_j/l_n = 0.88$

(c) TIC Mach 5.14 nozzle with injection at $x_j/l_n = 0.8$

Figure 5.22: Mach number plots for different SITVC test nozzle models

and TIC supersonic rocket nozzle types are investigated. Comparing to the previously presented conical type, TIC profile derived from MoC calculations will yield a significantly shorter nozzle under the same design criterions, the same flow conditions and throat curvature radii. The method of characteristics is an inviscid method and therefore the calculated profile is corrected for the viscous effects.

Normally, in each nozzle section the boundary-layer varies. For this study, using the energy and momentum condition to determine BL thickness at the throat and the exit, the minimal turbulent boundary layer is evaluated to correct the inviscid profile depicted in Figure 3.9. Produced nozzle profile was slightly larger in cross-sections than the conical one and shorter in the length with $\dot{m}_0 = 236g/s$, $M_e = 3.23$, $A_e/A_{th} = 5.29$ and $l_n = 68mm$. Secondary transverse injection was placed at $x_j/l_n = 0.88$ with circular sonic throat of $A_j = 26.4mm^2$ which under $SPR = 1, T_{0j} = 255K$ conditions delivered $m_j \sim 18.15g/s$ and $F_{j0} \sim 9.6N$. To analyze the effect of the primary nozzle design under same conditions and with the same convergent section and sonic throat, TIC $Mach$ 5 nozzle is designed and numerically tested. $Mach$ number plots in symmetry plane of SITVC nozzles are depicted in Figure 5.22. In these plots, it is observable that the size of primary flow deflection and amount of the secondary jet plume inward folding varies, which is primarily caused by the different upstream flow conditions to which the secondary jet is exposed. The influence on SITVC of the flow conditions at the nozzle injection section can be observed through the components of the global

side vector net force, in the following manner:

1. $F_{jy} = \oint \rho v_{jy}^2 \cdot dA_j + \oint (p_{je} - p_j) dA_j$, second part of the secondary jet thrust equation is affected by the pressure at main nozzle j-section. Moving injection to the lower pressure sections towards the nozzle exit will slightly augment this force component part. However, its effect in compare to the flow momentum is rather minor.

2. F_{wy}, as defined in Chapter 2, represents a wall side force or a force that originates from the cross-flow interactions. In a viscous flow, essential part of this force is a function of the pressure disbalance imposed on an axisymmetric nozzle wall, while a smaller part comes from the viscous effects. According to the afore discussed flow deflection - upstream Mach number relation, it can be assumed that the flow will deflect more at higher Mach number sections.

3. $(F_{jy} + F_{wy}) / \sum Fx$, the ratio of the side to axial global force, given as an *arctan*, is affected by the increase of side force components towards the nozzle exit but also by the increase of the axial thrust.

It has been seen that vectoring angle, δ gradually decays in favor to an axial thrust augmentation with the higher momentum main flow. Assumingly, for the higher expansion or thrust-ratios rocket nozzles, further considerations about the optimal transverse injection position should be made.

Introduction of viscous models to the SITVC analysis imposes substantial effects on the observed fluidic system. Formation of boundary-layer significantly changes the separation mode. Namely, the oncoming flow inside the boundary and parallel to the nozzle wall "foresees" the obstruction produced by a secondary injection and detaches from the wall with initial separation shock. Viscous effects inside the vorticity dominated separation zone favour turbulent energy production and dissipation. These effects are also very pronounced at the turbulent shear flow interaction interface with dissipation and the upcoming diffusion inside the turbulent mixing. Comparing the Figure 5.21 with Figures 5.22 and 5.23, it is possible to detect a difference between the expanding secondary plume normal to the axis with quasi-normal shock generated in front of it for inviscid flow and the $k - \varepsilon$

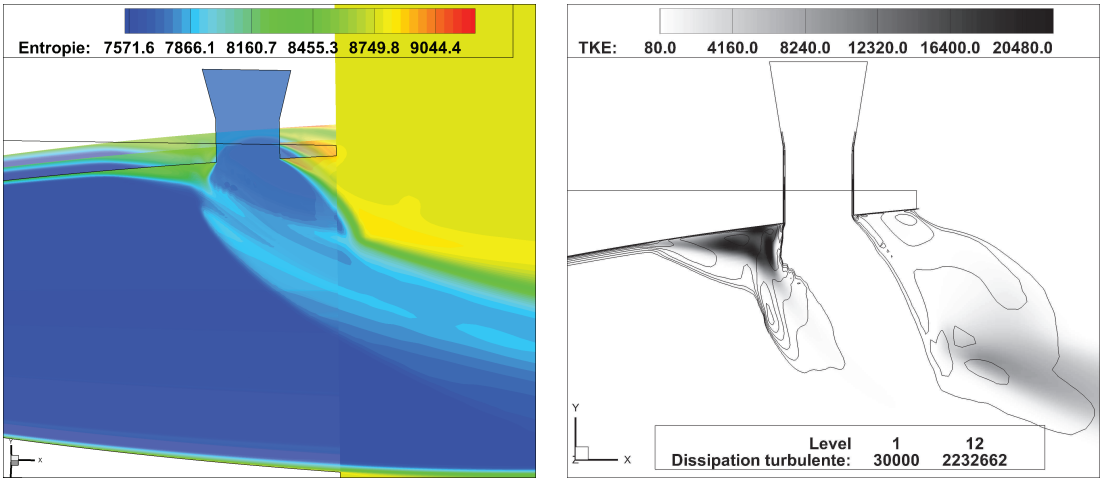

(a) Entropy in radially extracted slices, J/K

(b) Turbulence kinetic energy contour plots with dissipation contour lines, $m^2/s^2, m^2/s^3$

Figure 5.23: Entropy and turbulent production contour plots for Mach 3 TIC $x_j/l_n = 0.88$ nozzle

simulations results. In Figure 5.23, it can be noticed that most of the turbulence production is concentrated inside the separation zone, at cross-flow shear interface and downstream of the secondary plume Mach disk. The longer turbulent

Table 5.5: Secondary injection and separation zone data

Case	D_{jy0}[N]	δ_{BL}[mm]	h_j[mm]	x^*_{sep}/d_j
$TICm3 - i.x_j/l_n = 0.735$	9.654	1.5233	4.988	-2.044
$TICm3 - i.x_j/l_n = 0.882$	9.604	1.707	5.551	-2.261
$TICm3 - i.x_j/l_n = 0.941$	9.597	1.725	5.810	-2.382
$^*NPR(TICm3) = 37.5, SPR = 1, \dot{m}_0 = 236.2g/s, f_m = 0.0762$				
$TICm5 - i.x_j/l_n = 0.60$	9.668	3.441	9.318	- 4.64
$TICm5 - i.x_j/l_n = 0.70$	9.633	4.456	10.537	-5.229
$TICm5 - i.x_j/l_n = 0.80$	9.643	4.687	11.386	-5.916
$^*NPR(TICm5) = 448, SPR = 1, \dot{m}_0 = 236.2g/s, f_m = 0.0762$				

BL separation zone is followed by the separation shock wave and compression fan that introduce a main bow shock and which inducing a high pressure on the windward secondary plume side. This further results in the fast deflecting of the

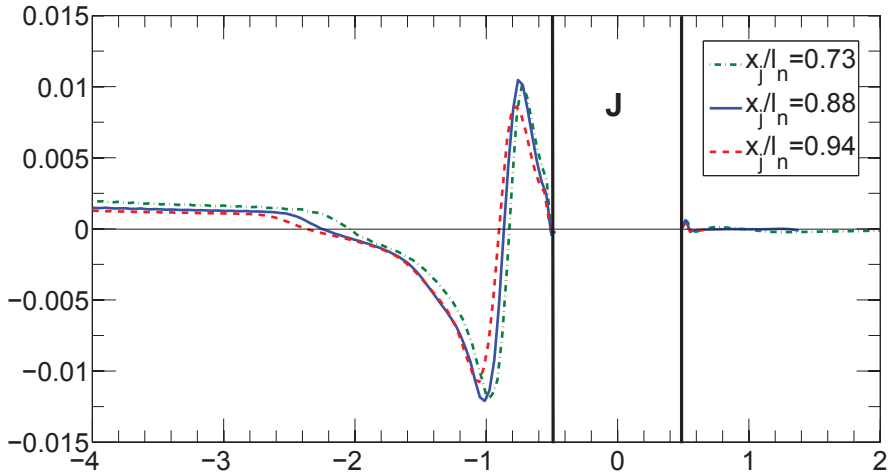

Figure 5.24: Skin friction in symmetry plane of TIC *Mach* 3 nozzle and different 2nd injection positions

secondary plume in downstream direction.

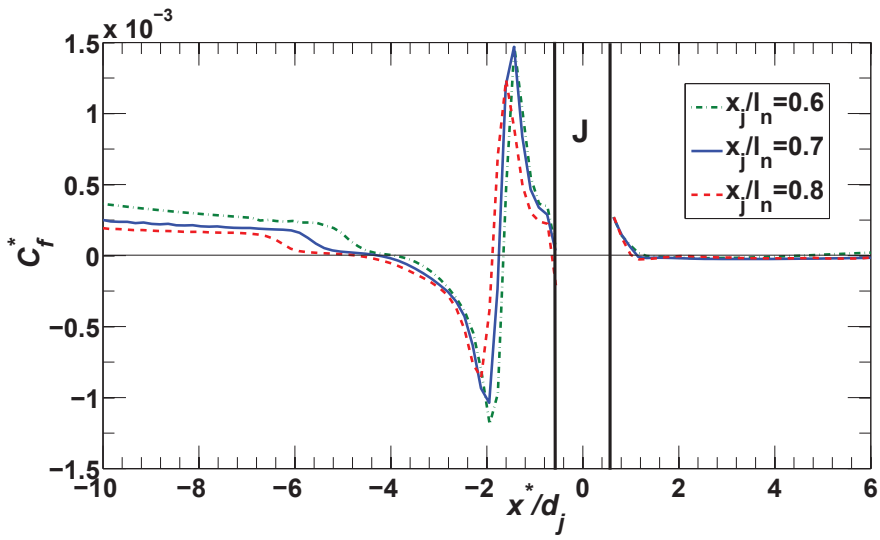

Figure 5.25: Skin friction in symmetry plane of TIC *Mach* 5 nozzle and different 2nd injection positions

Wall shear-stress data plotted in symmetry plane for TIC Mach 3 and Mach 5 nozzles are given as a skin friction coefficients in Figures 5.24 and 5.25. Separation points, identified in presented profiles at zero crossing, are corresponding to the

inference of higher deflection for injection positions at lower pressure sections. Hence, it can be fairly noticed that distances between the profiles of different injection cases slightly decrease as they approach x-axis.
Analogously to the separation length, interaction or wall side force component, F_{wy} depicts the evolution of the main jet deflection with downstream secondary injection displacement. However, as a result of variable slope angle of TIC profile, the secondary injection normal to the nozzle axis will pose a slightly different upstream inclination towards the BL flow. Additionally, injection port is defined as an intersection of the injector cylindrical throat section and the main nozzle wall, resulting in a skewed ellipsoidal shape. These smaller differences of injection angle and shape, between the different injection positions, will result in a slightly changed dynalpy flux in y-direction at injection port, which is defined as a vacuum thrust force and tabulated in Table 5.5. The separation distance and penetration height follow the positive trend with injection positioning towards the nozzle exit.

Table 5.6: Forces and moments probes data

Case	F_{jy}[N]	F_{wy}[N]	$\sum F_y$[N]	$\sum F_x$[N]	$Mz_w[N \cdot m]$	$\sum_{j+w} Mz_{jw}$
TIC $Mach = 3.23$:						
$x_j/l_n = 0.735$	9.337	7.042	16.379	136.77	0.386	0.8102
$x_j/l_n = 0.882$	9.341	7.134	16.475	136.21	0.428	0.997
$x_j/l_n = 0.941$	9.372	6.532	15.904	135.83	0.402	1.008
$^*NPR = 37.5, SPR = 1, \dot{m}_0 = 236.2g/s, F_0 = 134.05N, I^0_{sp} = 57.88s$						
TIC $Mach = 5.14$:						
$x_j/l_n = 0.60$	9.231	7.916	17.147	156.02	1.394	3.001
$x_j/l_n = 0.70$	9.34	9.057	18.397	155.44	1.442	3.078
$x_j/l_n = 0.80$	9.387	9.092	18.479	156.15	1.481	3.124
$^*NPR = 450, SPR = 1, \dot{m}_0 = 236.2g/s, F_0 = 152.7N, I^0_{sp} = 65.96s$						

Furthermore, force and torque data are tabulated in Table 5.6 and corresponding performance criteria in Table 5.7. These data indicate that the injection position displacement for the higher $Mach$ 5 nozzle does not impacting significantly

Table 5.7: Performance coefficients

Case	$\delta[°]$	C_{AV}	C_{AF}	C_{AI}
TIC $Mach = 3.23$:				
$x_j/l_n = 0.735$	6.83	0.896	1.027	0.954
$x_j/l_n = 0.882$	6.89	0.904	1.024	0.952
$x_j/l_n = 0.941$	6.68	0.876	1.021	0.948
TIC $Mach = 5.14$:				
$x_j/l_n = 0.60$	6.27	0.823	1.028	0.955
$x_j/l_n = 0.70$	6.74	0.884	1.026	0.953
$x_j/l_n = 0.80$	6.75	0.886	1.03	0.957

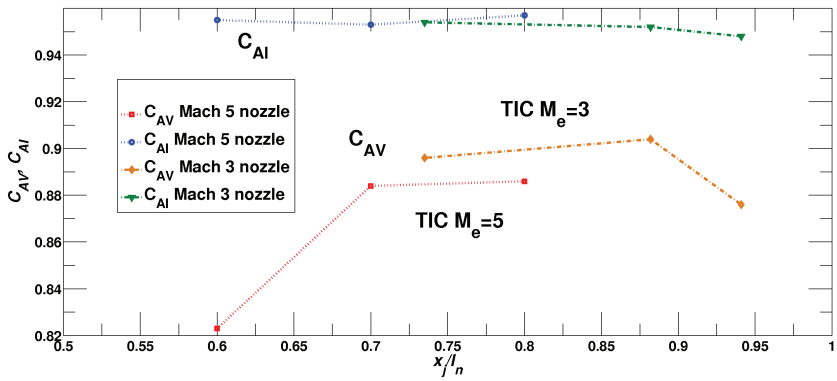

Figure 5.26: Vectoring and specific impulse amplification factor versus different injector positions of TIC test nozzles

the vectoring and nozzle performance in term of produced forces. For both TIC nozzle models tested injection positions follow the trend of side force augmentation with injections closer to the nozzle exit. Some smaller aberrations, detectable in force results, may come from the injection geometry definition, as mentioned above. Vectoring amplification factor of the presented injection position cases at the Mach 5 TIC nozzle is naturally decreased comparing the one of the Mach 3 TIC nozzle. This can be approximated as a function of the shock wave flow deflection with an upstream Mach number, M1, and the produced flow momentum that is axial thrust. In addition to force data, the torques around main z axis are evaluated, as well. Moment around z axis is found as a component of the wall

side force and the reactive force of secondary injection. Naturally, higher torque values are obtained with the forces acting over a longer force-arm.

5.3.2 Supersonic rocket nozzle types

In addition to injector position and primary nozzle expansion ratio, effects of the specific rocket nozzle profiles are analyzed as well. Namely, the de Laval contour provides an ideal flow expansion without shock discontinuities inside the nozzle, which differs to the nozzles with internal shock that may additionally affect SITVC and lead to the multiple shock interactions. In the given conical test nozzles with the small half-conical angle (5.8°), the weak compression waves do not affect strong shock region of the main bow shock. However, they might slightly displace the separation point in the case where the internal wave ends at the induced separation point. Internal shock waves, are intrinsic consequence of the

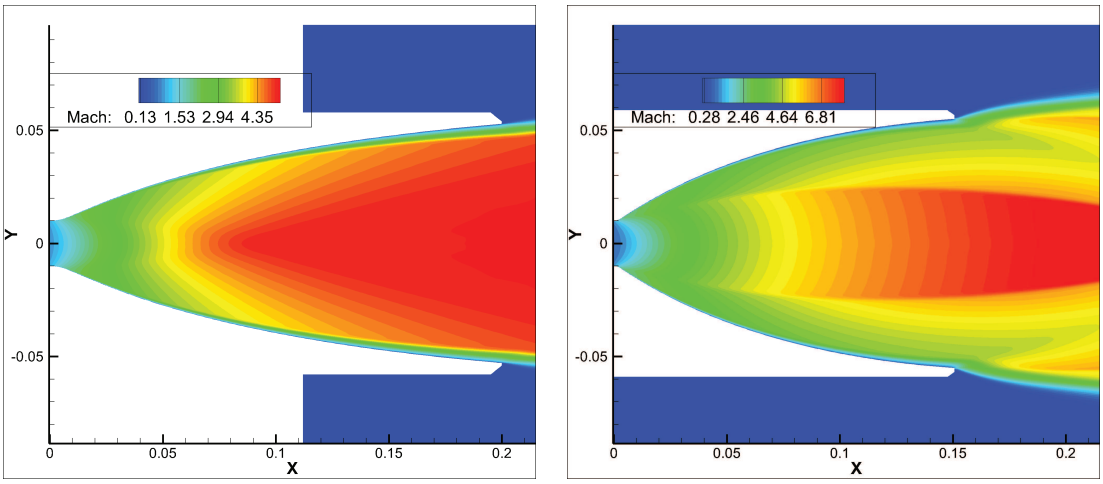

(a) TIC nozzle (b) TOC nozzle

Figure 5.27: *Mach* number plot in nozzle symmetry plane

conical nozzle geometry. Contemporary used, compressed and thrust optimized nozzle contours purposely incorporate an internal shock in order to provide a higher thrust rate on a shorter nozzle. The evolution of a high expansion profile right after the throat section, generates an inflection point on the nozzle profile, initiating an internal shock in the supersonic flow. This nozzle-long internal shock defines two distinctive regions along the nozzle, the high speed core flow and the gradually expanding peripheral flow. This shock structured flow pattern yields an increase in thrust over the wide operation envelope, especially required as a first stage propulsion system end element. In Figure 5.27, test TOC nozzle

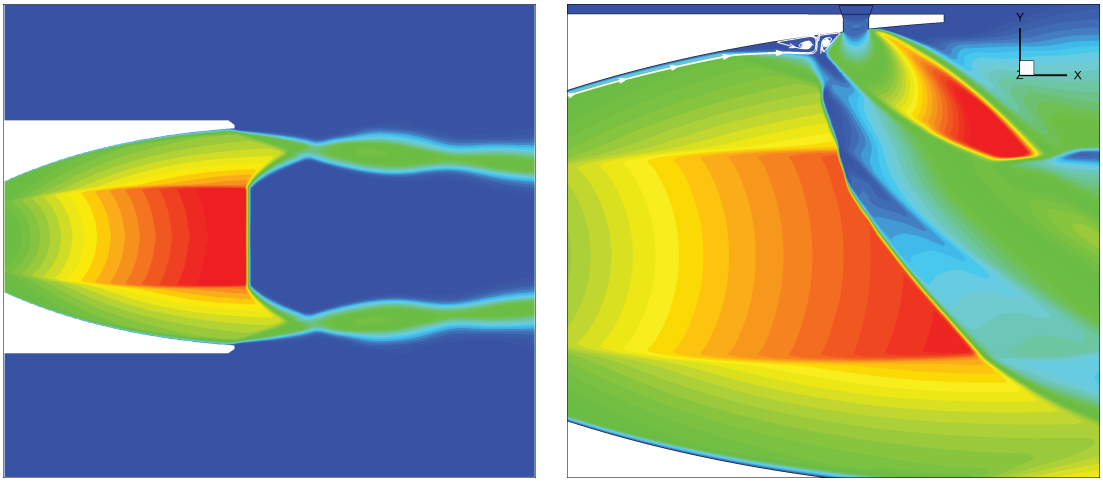

(a) TOC nozzle non-vectored operation at overexpansion regime

(b) TOC nozzle vectored operation at adapted regime

Figure 5.28: *Mach* number plot in TOC nozzle symmetry plane

is depicted. Having the 25% shorter length, it delivers the same thrust force as previously discussed Mach 5 TIC nozzle. However, as a consequence of the more complex plume, unsteady behavior may occur at the critical points during the startup and shutdown transient sequences or at a highly over-expanded regime. Namely, with increased ambient pressure there will be a corresponding increase in the Mach disk size which will grow over the core flow. This action leads to the formation of the so-called cap-shock pattern in Figure 5.28(a). With further increase of ambient pressure, the flow separates with a consequent separation shock, as also described in Zmijanovic *et al.*[87]. The shock interaction of separation, internal and cap-shocks at triple point will eventually lead to the unsteady restricted shock separation and eventually to the dangerous loads at the nozzle wall.

Injection of the secondary flow into the TOC nozzle, leads to the early flow separation and appearance of the bow shock. The investigation emphasis was focused on the adapted flow conditions, where no cap-cap shock pattern and separation inside the nozzle can be expected. The basic characteristics of the TOC nozzle models are given in Chapter 2, Table 2.3.

In Figure 5.28(b) transverse sonic injection into TOC nozzle is presented via Mach contour plot. Due to the different axial flow regions, bow shock profile

will appear as a slightly deviated. Namely, the bow shock propagates across the two main regions, characterized by the large difference in the flow expansion. Increased Mach number of the upstream flow will yield a stronger shock solution in a response to the same blockage.

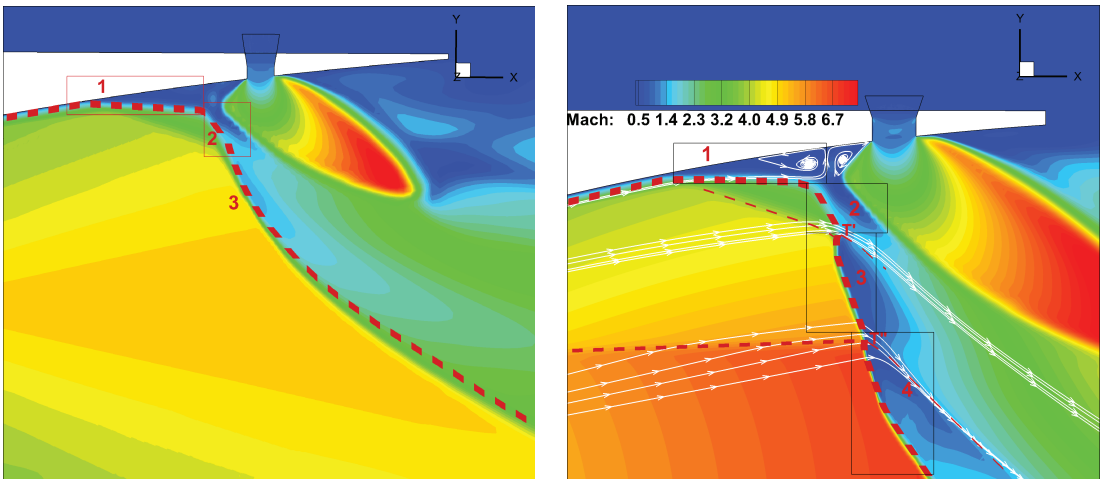

(a) TIC nozzle (b) TOC nozzle

Figure 5.29: *Mach* number plot,streams and characteristic shock zones in nozzle symmetry plane

Observing the planar oblique shock polar in Figure 5.30, given for Mach reflection phenomenon of upstream flow of $M1 = 6.7$ and downstream $M1 = 5.5$ originating at $\varphi_D = 25°$ it can be said that triple point will exist between (3) and (4) for incident, separation and reflected shocks.

In the case of a SITVC TOC nozzle in Figure 5.29(b), we can differentiate four characteristic regions with shock interactions occurring between them. Region (1) is characterized by the separation shock induced by an adverse pressure gradient and it acts as a right-running wave. Between the main bow shock and the separation shock, a turning region (2), governed by the compression waves can be identified. Separation shock and the compression waves merge into a singular strong bow shock, which is accompanied by the weak refracted wave behind point (T'). Strong bow shock propagates through the peripheral flow in region (3). Shock-shock interaction occurs between the downward propagating bow shock and sideward propagating internal shock. This interaction results in merging of internal shock into a stronger bow shock which afterwards propagates

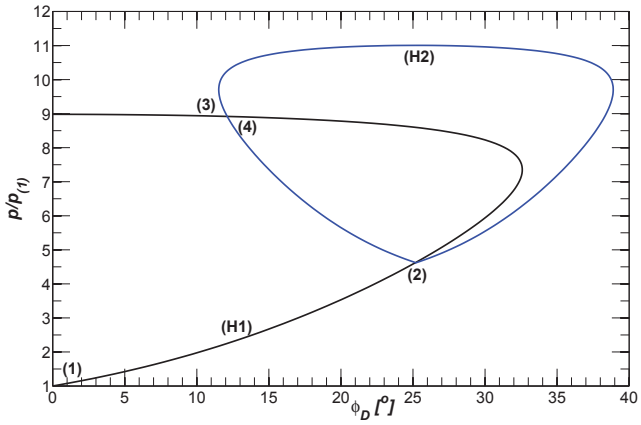

Figure 5.30: Shock polar diagram for triple point at approximated planar shock interaction of core flow M1=6.7 and $\varphi_D = 25°$

through the core flow in region (4). Again, a very weak reflected shock waves occurs shock behind (T") point, serving to adjust velocity directions of the flow behind the bow-internal shock waves. Between the subsonic regions behind the shock interactions, a slip surface(lines) can be fairly identified along which the pressure is constant and velocity directions are parallel.

In the interaction zone behind (2), a pathway interface in shape of a virtual nozzle is formed for aspiration of compressed fluid from the separation zone bounded by the compression waves, the bow shock and the secondary plume barrel shock. The subsonic regions behind the strong bow shock and shock interactions, impose a higher pressure on the windward side of a secondary plume.

The nozzle wall is normally designed in a such manner to allow nozzle expansion and as much as possible effectively accelerate the flow towards the ambient conditions. Therefore the wall-pressure monotonically decreases from the high pressure at the throat towards the low pressure at the nozzle exit which represents a favorable pressure gradient to the oncoming supersonic flow. TOC profiled nozzle results also in an altered wall-pressure profile at the inflection point close to the throat separating the higher pressure values close to the nozzle exit. This makes the mentioned nozzle more prone to the separations imposed by an adverse pressure gradient.

If it is supposed that separation due to a secondary injection or an overexpansion occurs close to the nozzle exit, it can be deduced that an adverse pressure

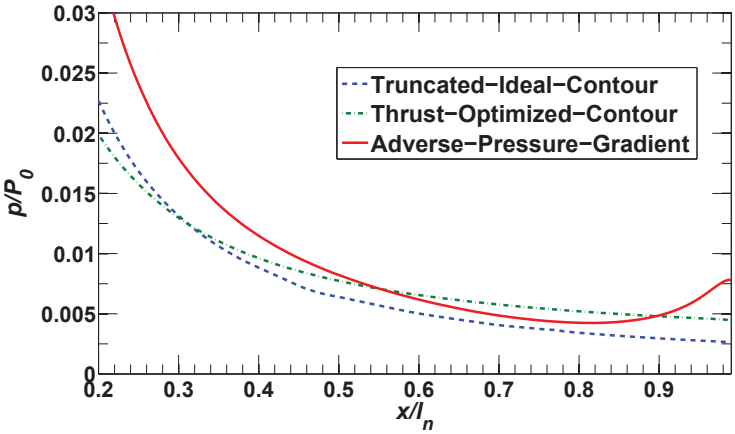

Figure 5.31: Wall-pressure profiles for different Mach 5 rocket nozzle types

gradient will occur in that region. However, even with occurrence of the adverse pressure gradient the main flow will still accelerate and contribute to the nozzle thrust. Therefore, the region of the flow deceleration is enclosed in the small zone near the wall close to the nozzle exit while the large majority of the flow is still expanding. Having this in mind, Rao[68] proposed an alternative in design of the principal nozzle in order to improve the secondary injection thrust vectoring performances without loosing the thrust efficiency. Namely, instead using the favorable wall-pressure gradient which is a characteristic of all rocket nozzles, Rao proposed the modification of the contour to be favorable to an adverse pressure gradient (APG) in the regions close to the nozzle exit. The Rao[68] APG nozzle contour was designed according to Hozaki *et al.*[53], as a conical nozzle with $\alpha = 12°$ half-conic angle which makes transition to the APG calculated contour close to the exit, ending with a 2° profile exit angle. APG $12 - 2°$ nozzle also includes an internal shock which is initiated at the inflection point of conical to APG contour transition close to the nozzle exit, depicted in Figure5.32(a). It can be observed that at APG nozzle, a virtual flow nozzle that is formed in region-2 has a narrow, steep and complex profile due to a short length and vicinity of the wall separation and the internal shock. Pressure profiles in Figure 5.33 depict the transverse injection at $x_j/l_n \sim 0.85$ into examined *Mach* 5 rocket nozzle types. It can be deduced from the presented profiles that the separation occurs at approximately the same distance from the secondary port for all three tested

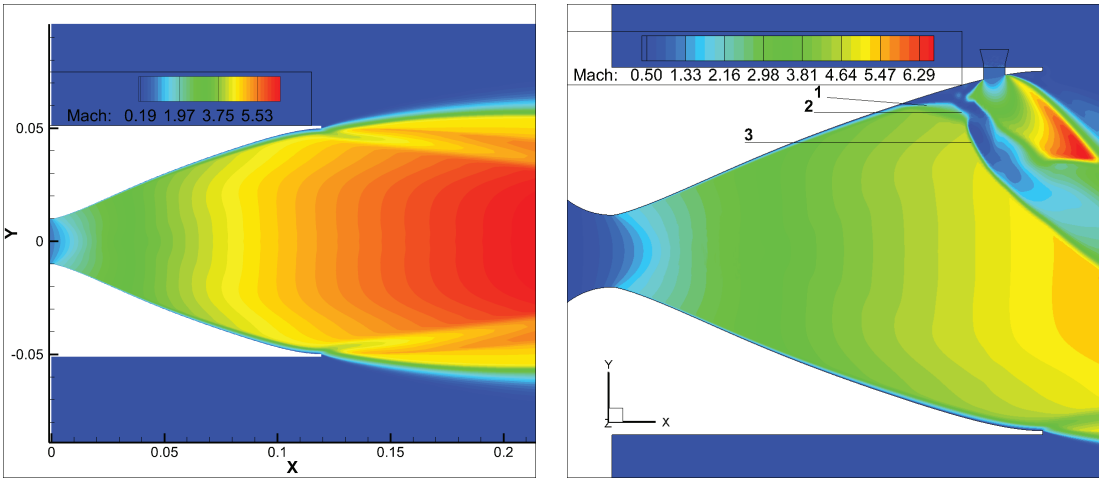

(a) APG nozzle non-vectored (b) APG nozzle vectored

Figure 5.32: Mach number plots of the *Mach* 5 APG nozzle in the symmetry plane

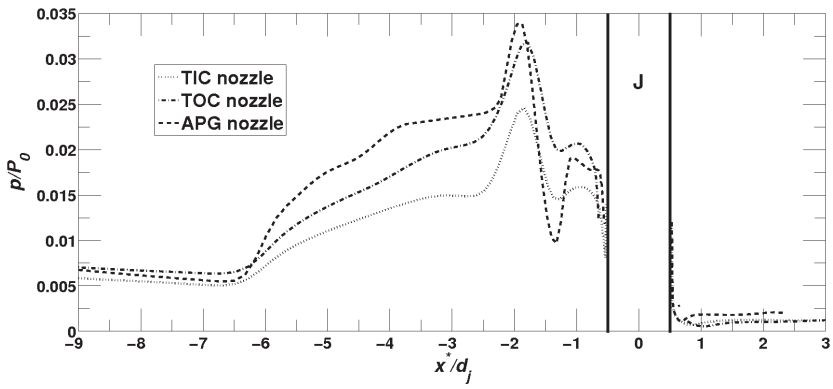

Figure 5.33: Wall-pressure profiles for *Mach* 5 nozzles with transverse secondary sonic injection at injection side of the symmetry plane

nozzle contours. However, there is a noticeable variation in pressure growth inside the separation zone. It is possible to relate the pressure rise to the contour pressure profiles from Figure 5.31. Namely, TOC nozzle profile, which separates at approximately same distance as TIC nozzle, has a larger pressure rise gradient ending on a higher plateau pressure level before the increased pressure peak. The APG nozzle also complies to the presented interaction flowfield. The pressure rise region of APG nozzle appears with the inflection point, separating virtually two plateau pressure levels. After increased plateau pressure level, APG profile

goes into a pressure peak with an accompanying secondary peak which assumingly depicts the secondary plume barrel shock interaction with the wall and an internal shock. In cross-section plots in Figure 5.34 it is possible to trace vortex

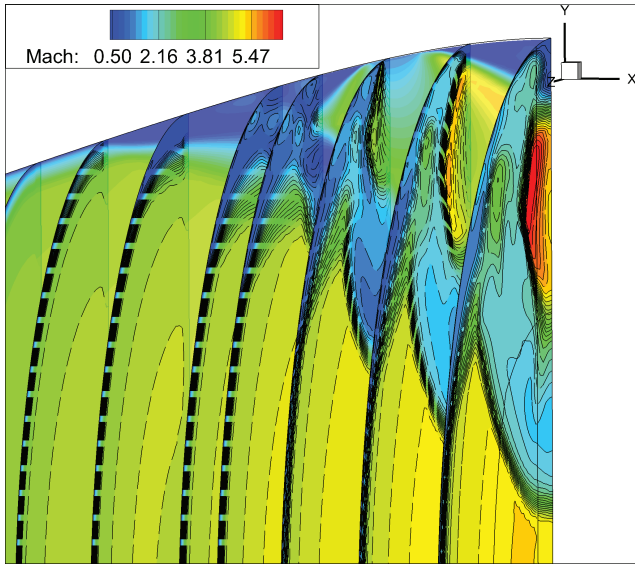

Figure 5.34: Pressure contours and mach number plot for cross-section slices of APG nozzle

generation and its interaction with the secondary plume. Consequentially, this results in generation of secondary lateral pocket of detached boundary layer with re-circulation from the symmetry plane towards the lateral edge. This motion may induce instable lateral forces, however, they were not analyzed in conducted RANS simulations.

Force data tabulated in Table 5.8 demonstrate minor differences between the nozzle types in terms of delivered side force. TIC and TOC nozzles have a very similar ratio between the secondary plume natural reactive force and the interaction wall side force. There is some smaller difference at APG nozzle where slightly less secondary injection momentum yields a slightly larger wall side force component. However, it should be noted that APG corrected contour was originally projected for a smaller secondary port surface area, higher SPR and positioned closer to the nozzle exit.

Table 5.8: Numerical result data for different SITVC nozzle types

val/case	TIC nozzle	TOC nozzle	APG nozzle
x_j/l_n	0.8	0.85	0.88
h_j, [mm]	11.386	11.614	10.684
NPR	450	500	500
F_{x0}, [N]	152.7	151.36	149.7
$F_{wy}, [N]$	9.092	8.98	9.274
$F_{jy}, [N]$	9.387	9.412	9.22
$\sum F_y, [N]$	18.479	18.392	18.494
$\sum F_x, [N]$	155.25	153.64	151.82
δ	6.77°	6.79°	6.95°
$^*P_0 = 300kPa, SPR = 1, \dot{m}_0 = 236.2g/s, f_m = 0.076$			
Performance coefficients:			
C_{AV}	0.881	0.893	0.915
C_{AF}	1.024	1.008	1.008
C_{AI}	0.952	0.937	0.936

5.3.3 Remarks on primary nozzle design effect

In this section, effects of the main nozzle design characteristics on the SITVC system are analyzed. The effect of the expansion ratio or Mach number is given on the example of conical and MoC designed $Mach$ 3 and $Mach$ 5 truncated-ideal-contoured nozzles. It was found that increase of the expansion only slightly changes the vectoring capabilities. The cross-flow interaction or wall side force increases with the increase of the main jet flow velocity, while the reactive force of the secondary jet increases with the main nozzle section pressure decrease. The position of the secondary injection port is, as previously discussed, effective in the regions close to the nozzle exit, with remark that for higher Mach nozzles depending on the operation and configuration is possible to slightly alter this position inwards. However, forces exerted on the nozzle wall close to the nozzle exit will act over the longer moment arm increasing the z torque.

Further to expansion ratio, nozzle contour type was tested also. It was found that internal shock nozzles include additional effect on the separation which can

be observed in the region of the main shock interface and in the BL separation zone. Amount of contribution of these effects depends on the size of the core and peripheral flow and their intensity or the main flow momentum. The Rao[68] modification of the main nozzle contour design was briefly evaluated and tested in the numerical simulations. The gain in wall-side force is registered using the APG nozzle contour, however the instabilities that might occur with this contour and flow overexpansion or RSS were not simulated. Inasmuch the APG modification is implemented on the small end section, it should not affect largely global stability of the system.

5.4 Interaction flowfield & primary and secondary flow conditions

Defining the optimal position of the secondary injection port, the primary and secondary flow conditions effect is investigated on the selected experimental TIC nozzle model. The experimental TIC nozzle model was equipped with the 9 Kulite® fast pressure probes mainly clustered meridionally at the symmetry plane in vicinity of the secondary injection port which were measuring at the $8000Hz$ acquisition rate. To complete the pressure maps, a 32 channel Scanivalve® ZOC22B pressure scanner was used under $500Hz$ scanning rate. Synchronously with the average parietal pressure data, Z-type schlieren photography was taken on every $0.25s$ with $1/6000s$ of exposure time.

The numerical schlieren is evaluated from extracted numerical results as a density gradient:

$$\nabla\rho = \left(\frac{\partial\rho}{\partial x}\right)\vec{i} + \left(\frac{\partial\rho}{\partial y}\right)\vec{j} + \left(\frac{\partial\rho}{\partial z}\right)\vec{k} \tag{5.1}$$

In the given schlieren two features are characteristic comparing to the conical nozzle; First, the upstream flow of the TIC nozzle is not fully expanded to the parallel, thus the flow speed is variable from the center towards the nozzle wall. Secondly, there are no weak compression waves normally observable in the conical nozzle. Other than this, the case of the TIC nozzle with single meridional secondary injection at $x_j/l_n = 0.882$ is quite similar as the secondary injection into conical nozzle at $x_j/l_n = 0.9$. Both, primary and secondary jet plumes and the bow shock exit the nozzle without impinging the internal wall while the major shock interactions and mixing occur in the exterior domain. It is also detectable on both images in Figure 5.35, that downstream of the injection port close to the wall, the flow is decelerated with some recirculation occurring at the nozzle lip and this small portion of the jet continues as a free separated flow. In Figure 5.36 top (xz) view schlieren images are presented. The kidney vortices of the secondary plume and horseshoe vortex are detectable in this figure. Soon after nozzle exit their interaction commences, initiating the shock interaction and afterwards the effective mixing downstream.

Density gradients in the experimental schlieren photographs are superposed lat-

(a) Experimental Z-schlieren photograph

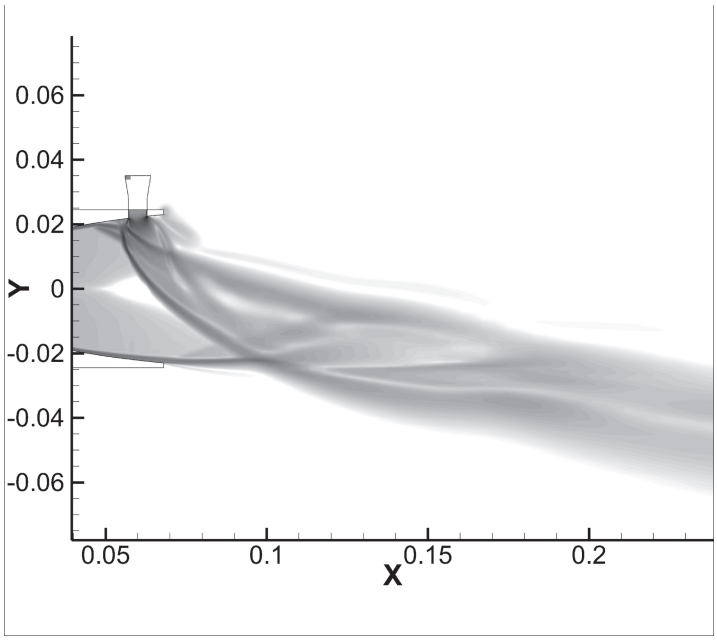

(b) Numerical schlieren

Figure 5.35: xy-plane view of TIC $x_j/l_n = 0.88$ SITVC nozzle schlieren visualization at NPR=37.5, SPR=1

erally and projected on the side, xy or top, xz planes. In Figure 5.37 a three-dimensional numerical schlieren is given ans an iso-surface plot depicting the above projected features in a 3D domain. Previously discussed SITVC cross-flow

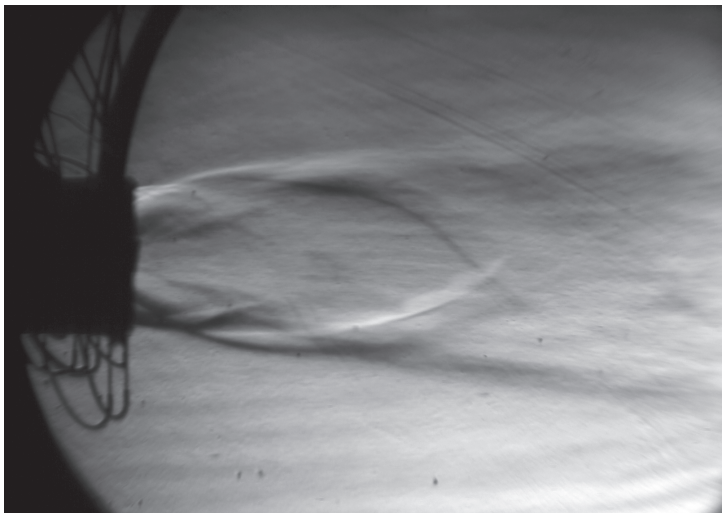

(a) Experimental Z-schlieren photograph

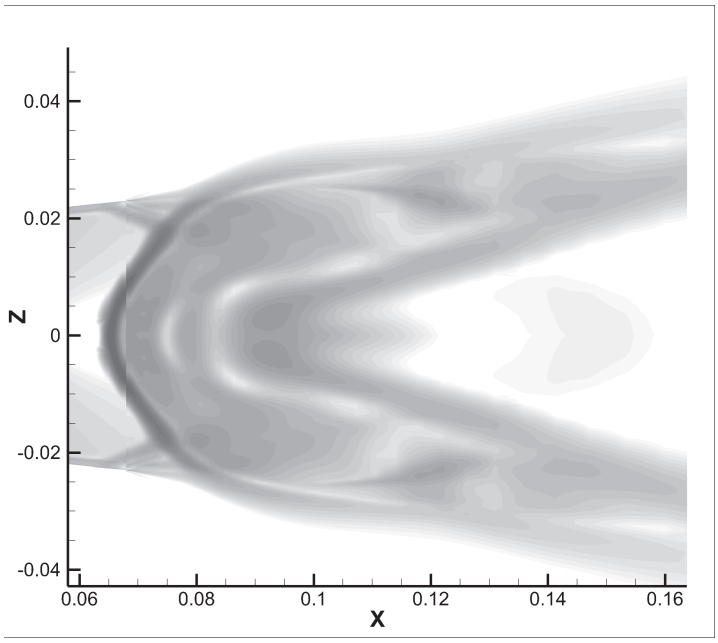

(b) Numerical schlieren

Figure 5.36: xz-plane view of TIC $x_j/l_n = 0.88$ SITVC nozzle schlieren visualization at NPR=37.5, SPR=1

features as the upstream separation, recirculation, deflection through the shock and shock interaction can be also identified on the schlieren - density gradients figures. The secondary plume after first sequence and Mach disk, retains a hemi-

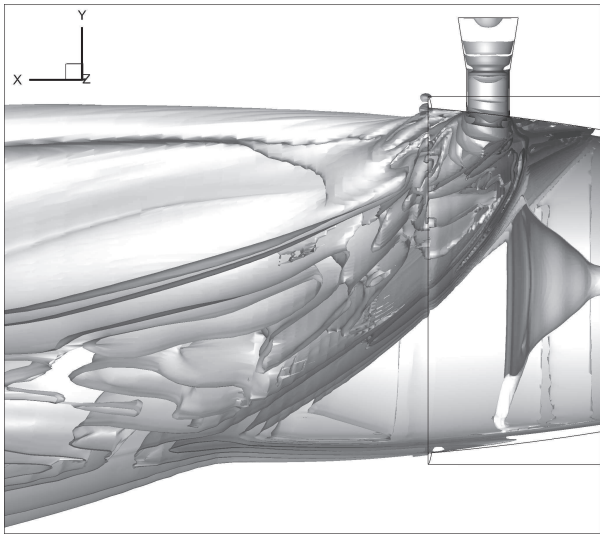

Figure 5.37: 3D numerical schlieren of the TIC test nozzle

cylindrical shape with trailing or kidney vortices that initiating mixing which takes place on the interface.

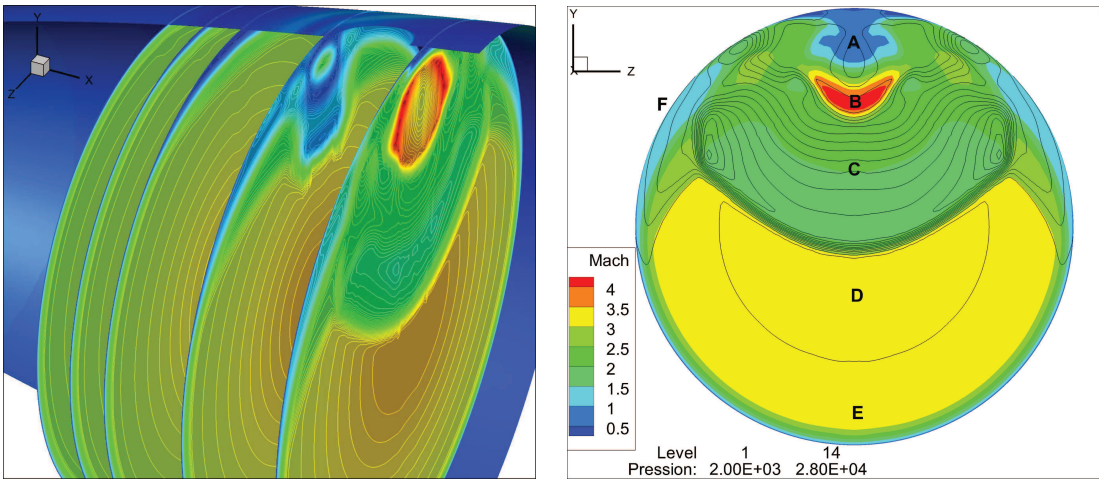

(a) yz slices from the separation towards the exit

(b) Exit plane of the TIC nozzle

Figure 5.38: TIC x_j/l_n nozzle model $Mach$ number plot and pressure level contour lines

In Figure 5.38, cross-section planes are given from unaffected to the exit cross-section with Mach number plots and pressure level contours. In slices of Fig-

ure 5.38(a), it is possible to trace down beginning of separation and its progression towards the secondary plume and formation of the interfaces. In Figure 5.38(b) characteristic regions are depicted denominated as; (A) the low-pressure region between secondary port and the exit with the inflow from the ambient exterior zone and surrounded by the secondary plume expansion; (B) the secondary plume expansion ends with a Mach disk and on the lateral sides horseshoe vortex, observable in pressure contours, delineates the barrel shock interface from the wall; (C) represents the interface between the secondary plume Mach disk and the main bow shock in which mixing occurs, on lateral sides vortex zones are formed between the interface and high pressure induced thickened boundary-layer region (F); (D) region represents a principal, unperturbed jet flow which fits between the bow shock above, enlarged BL on the sides and unaffected BL below; (E) the main flow boundary layer in this case is unaffected or may form a recirculation bubble in case of the bow shock reflection.
Analyzing the complex interaction flowfield and consequential imbalance in force components acting upon the nozzle, we can deduce that jet interaction or wall side force component represents the major factor for optimizing the SITVC system. The natural reactive force of the pneumatic actuator is completely independent of the supersonic cross-flow interactions and only depends on the provided secondary and designed nozzle section pressure conditions, shape of the wall and direction of injection.

5.4.1 Secondary flow conditions

The secondary flow conditions in the current study are nominally set to be identical with the principal nozzle inlet while the secondary injection throat area was designed to provide a 5% to 8% of the main mass flow rate to the secondary port. Having a predefined secondary injection geometry, a secondary flow properties were then altered to analyze the effects on the side force and SITVC performances. The lower or higher secondary inlet pressure will naturally affect the secondary mass-flow-rate and imposed momentum flux which will directly result in reaction force. The change of secondary jet momentum affects the secondary plume penetration height and therefore alters interaction flowfield and resulting

force as well. In the current study secondary pressure ratio, $SPR = P_{0j}/P_0$ was examined for the following steps: $SPR = [0.667, 0.833, 1, 1.167, 1.133, 1.667]$. The numerical and experimental data were analyzed together and they are given in the pressure plots, tables and performance diagrams.

From the data in Figure 5.39, it can be deduced that the separation size quasi-linearly augments with the increase of a secondary injectant mass flow rate. Very slight abberation can be noticed only between the first two and last two injection-rate cases. The effect of secondary injection-rate is further analyzed via parietal pressure distribution data presented together in Figure 5.39, 5.40 and 5.41.

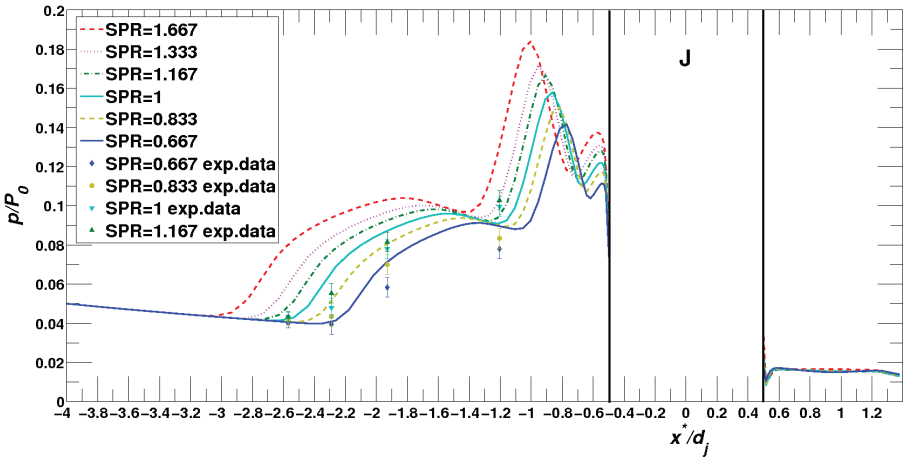

Figure 5.39: Wall pressure distribution at injection side of a symmetry plane for NPR=37.5 and range of SPR, lines representing numerical simulations and symbols experimental data

Analytically determined separation and plateau pressures by the method described in Sellam *et al.*[69] for conical nozzles, are evaluated and connected via Schmucker[88] [89] pressure curve fitting. It can be noticed that analytically determined plateau pressure value complies very well with the experimental and numerical findings. However, there is some slight aberration of the separation pressure values that can be assigned to the boundary-layer character of the conical and TIC nozzle contours.

At the symmetry plane nozzle wall, the experimental data was primarily acquired via flush mounted Kulite® probes which were clustered between the separation and injection point. Outside of the symmetry plane, the differential pressure

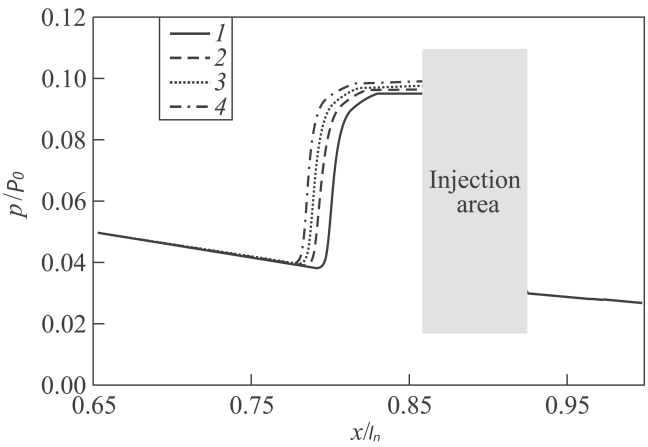

Figure 5.40: Analytical wall-pressure distribution at injection side of a symmetry plane for NPR=37.5 and range of SPR: $1 - 0.667, 2 - 0.833, 3 - 1, 4 - 1.167$

measurement via Scanivalve® ZOC-22B 32 channel was implemented on the 32 $0.6mm$ diameter pressure taps. The pressure taps were distributed along meridional wall lines for the several central angles $[8°, 17°, 30°, 45°, 60°, 75°, 90°]$ and combined with Kulite® probes on critical separation sections. Similarly with the wall shear stress data we can observe, enlargement of all sections in separation zone with the secondary injection-rate increase as PUV governed plateau-pressure section and SUV dominated pressure peak. In addition to the principal pressure peak, the structure and size of the secondary peak are apparent which is caused by the secondary injectant interference with the upstream separation zone. Experiments were conducted for SPR=[0.667, 0.833, 1, 1.167] conditions and plotted together with the profiles evaluated from numerical simulations. It can be observed that experiments and $k-\varepsilon$ numerical turbulence model predicted very-well the separation points. However, there were some overestimation in pressure rise and plateau region and underestimation at low pressure segments before the pressure peak. This indicates that size of the structures in the separation zone may vary between the numerical and experimental data. This discrepancies may be traced back to the experimental and numerical uncertainties. The first one can be identified in the fact that Kulite® probes were flush mounted to the nozzle wall. Therefore, $1.72mm$ diameter flat head may have a disturbance effect on the boundary layer and the separated flow. Secondly, the inner pressure probes were

close to each other and inside intrusively deformed separated region, where the pressure gradient change is high. The difference is detected in standard deviation of these inner probes as a consequence of the pressure probe design, where the gas intake micro holes are distributed on the outer line of the probe head. Therefore, the averaged measurements on the 2000 data chunks taken on every 0.25s were oscillating for the same flow conditions which led to the standard deviation between measurement points of ($\pm 1.49kPa$) which was still acceptable. The experimental Kulite probes data are thus presented with corresponding error bars. Finally some of the discrepancies are also due to the applied numerical model, and known limitations of the used $k-\varepsilon$ model in estimating the credible sizes, inside the supersonic separated boundary-layers.

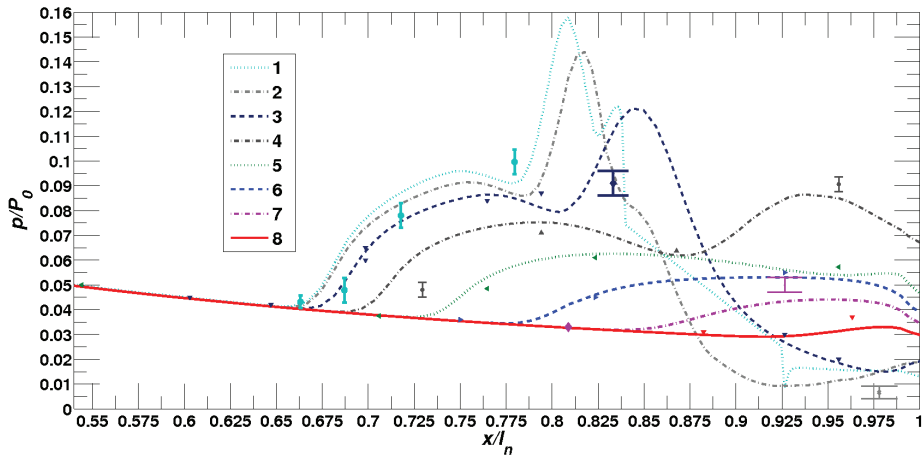

Figure 5.41: Wall pressure distribution at meridional positions around nozzle axis at: $1-0°; 2-8°; 3-17°; 4-30°; 5-45°; 6-60°; 7-75° and\ 8-90°$. for NPR=37.5 and SPR=1; lines representing numerical simulations and signs experimental data *(error bars - Kulites, triangles - Scanivalve pressure taps)*

The small pressure taps distributed along the meridional lines were placed from the both sides of the symmetry plane in order to prevent significant asymmetries. As *Scanivalve* data were synchronously recorded along with the *Kulite* pressure data at $500Hz$ acquisition rate, the 125 data chunks were averaged on every $0.25s$. The differential data was collected along with the referent (ambient) pressure and were very well fitted with some smaller oscillations. Before applying arithmetic mean and mode averaging functions data was filtered for miss-measured points.

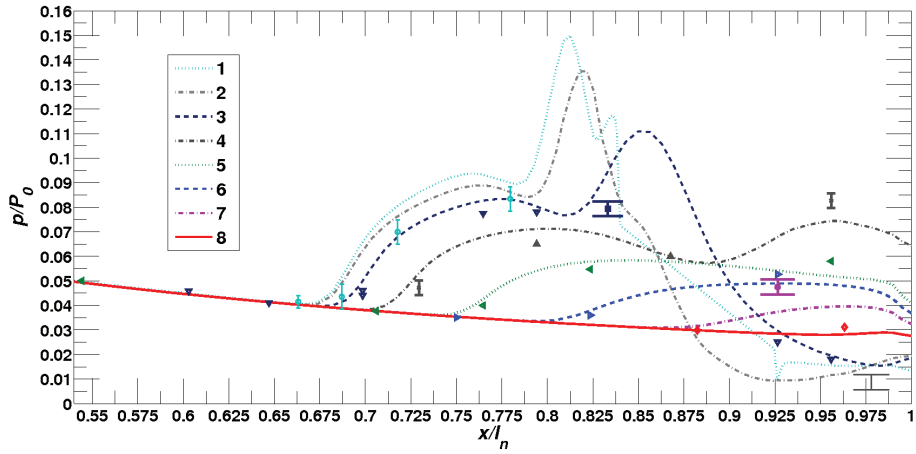

Figure 5.42: Wall pressure distribution at meridional positions around nozzle axis at: $1-0°; 2-8°; 3-17°; 4-30°; 5-45°; 6-60°; 7-75° and\ 8-90°$. for NPR=37.5 and SPR=0.833; lines representing numerical simulations and signs experimental data *(error bars - Kulites, triangles - Scanivalve pressure taps)*

In presented figures, separation zone evolution on nozzle wall sides can be detected. Two primary structures may be traced in the separation zone; the PUV which gradually introduce the separation and delineates the separation region on the wall from the unaffected flow region, and the stronger SUV induced horseshoe vortex which wraps around the secondary injection port, rapidly disturbs the flow and quickly exit the nozzle leaving the low pressure zone which is observable in the profiles laying below the horseshoe vortex affected zones.
The Scanivalve® pressure data complemented very well the Kulite fast pressure probe data with some underestimation comparing to the numerical curves but with the less discrepancy between consecutive measurement points. There is also some smaller overestimation at the experimental profile sections near the nozzle exit. This is identified as a consequence of a slightly increased ambient pressure during side injection operation and loss of the axisymmetry in the wind-tunnel test section diffuser. In the data given for the two secondary-pressure-rations, $(SPR = 0.83, 1)$ difference in the separation distance and size of separation zone can be determined. This can be interpreted as the separation region withdrawal towards the secondary injection point related to the decrease of a secondary injectant rate.

In the result points of the symmetrically placed pressure taps, left and right from the symmetry plane at $x_j/l_n = 0.7$, very slight difference of approximately $\sim 0.9kPa$ is detected in both SPR test cases. This may be explained by a very small misalignment of the injection port hole and the nozzle wall which also can be observed in the schlieren photograph in Figure 5.35(a) and in the lateral force component measurements ($\Delta F_z \simeq 0.85$). The forces acting upon the nozzle are normally measured at static conditions without the flow, then with only principal flow and on the end with secondary injection. The force data was acquired synchronously with the Kulites pressure probe with $8000Hz$ sample rate and then averaged on 2000 samples data chunks. The side and lateral force components, are found as a difference between measurements with injection and measurements without injection, $\Delta F_y = F_{yj} - F_{y0}$ while the axial force is found as a difference between the flow conditions and the static conditions in a pump vacuumed wind-tunnel test section, $\Delta F_x = F_{x0} - F_{st}$. As a cause of not heated primary and secondary flow the temperature was constantly decaying during the tests. It was ranging from $274K$ at beginning to $241K$ at the end of the experiment. The change of temperature directly impacts the analyzed mass-flow-rate, therefore, the average point data are given together with corresponding temperature averaged on the same sample data chunks. In the critical, secondary injection, measuring region temperature was in the range $260K \sim 248K$ thus, $T_0 = 255K$ was selected for the referent one and imposed in numerical simulations. The experimentally and numerically collected force data are tabulated together with the flow conditions in Tables 5.9 and 5.10.

Table 5.9: Experimental flow conditions and forces data

$SPR = P_{j0}/P_0$	$T_0, [K]$	$\sum F_y, [N]$	$\sum F_x, [N]$	$\Delta F_z, [N]$	$\delta, [°]$
$SPR = 0.5$	252	7.49	135	-0.32	3.18
$SPR = 0.667$	249.9	10.8	134.9	-0.29	4.58
$SPR = 0.833$	252.4	12.37	136.06	-0.2	5.20
$SPR = 1.00$	257.6	16.17	136.1	0.08	6.78
$SPR = 1.167$	263.74	18.9	137.7	0.31	7.82

$^*NPR = 37.5, T_{j0} \approx 283 \sim 279K, T_0 = 270K, F_0 = 135.84N$

Table 5.10: Numerical flow conditions and forces data

$SPR = P_{j0}/P_0$	$\dot{m}_j/\dot{m}_0$	F_{jy}, N	F_{wy}, N	$\sum F_y, N$	$\sum F_x, N$	$\delta,^\circ$
$SPR = 0.1$	0.008	0.672	1.202	1.898	134.288	0.81
$SPR = 0.333$	0.025	2.936	3.15	6.086	134.689	2.58
$SPR = 0.5$	0.038	4.57	4	8.57	135.028	3.63
$SPR = 0.667$	0.051	6.158	5.031	11.189	135.61	4.716
$SPR = 0.833$	0.063	7.755	6.033	13.788	135.906	5.8
$SPR = 1.00$	0.076	9.341	7.134	16.475	136.21	6.89
$SPR = 1.167$	0.089	10.976	8.17	19.146	136.47	7.986
$SPR = 1.333$	0.102	12.577	9.173	21.75	136.745	9.037
$SPR = 1.667$	0.127	15.792	11.116	26.908	137.324	11.08

$^*NPR = 37.5, T_0 = 255K, T_{j0} = 280K, \dot{m}_0 = 236.2g/s, F_0 = 134.05N$

The agreement between the experimental and the numerical force measurements is excellent. However, there are some very slight changes on upper and lower ends of tests but they are negligible as well the aberrations in lateral, F_z force. Some smaller measurement differences also exist in the global and axial force measurements which can be assigned to the constantly decaying temperature during the experiments, but overall matching of the data was highly satisfactory.

It can be noticed that vectoring amplification factor C_{AV}, which represents ratio between the vector pitch angle and percent of the secondary to the primary flow rate, is higher for the lower secondary injectant mass-flow-rates and correspondingly decays with the augmentation of SPR. The global force amplification, C_{AF} goes up with the SPR increase, as it is caused by the natural reaction force increase for the higher injection. However, by multiplying the force coefficients with the global mass-flow-ratio and then considering the values sorted as the specific impulse coefficient, C_{AI}, one can deduce a constant decay of the performance in terms of achieved forces versus fuel consumption. The selected analytical models which were designed for conical nozzle were extrapolated to TIC nozzle results and their prediction fits very well with the test results laying between Schilling[71] and Green[70] criterion calculations.

Table 5.11: Performance coefficients

$SPR = P_{j0}/P_0$	C_{AV}	C_{AF}	C_{AI}
$SPR = 0.1$	1.0125	1.002	0.994
$SPR = 0.333$	1.015	1.005	0.981
$SPR = 0.5$	0.955	1.009	0.972
$SPR = 0.667$	0.925	1.014	0.965
$SPR = 0.833$	0.921	1.018	0.958
$SPR = 1.00$	0.904	1.024	0.952
$SPR = 1.167$	0.897	1.027	0.943
$SPR = 1.333$	0.885	1.032	0.936
$SPR = 1.667$	0.872	1.043	0.925

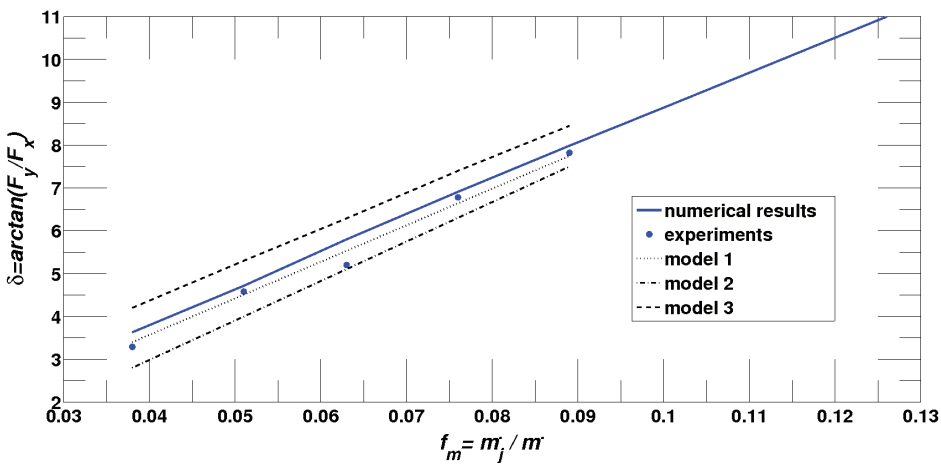

Figure 5.43: Vectoring pitch angle versus mass-flow-rate ratio obtained from numerical and experimental results and from selected analytical models: 1−Green[70], 2−Schmucker[89], 3−Schilling[71]

Further decrease of the secondary injectant mass-flow-rate was simulated numerically as the force components were below the measuring equipment range. The data presented in Table 5.10 and 5.11 and in Figure 5.44, depicts characteristic zones which can be identified in the vectoring performance coefficient, C_{AV}. From right to left, first identified zone is the numerically and experimentally analyzed zone at which C_{AV} smoothly and almost linearly increase with the decrease of the secondary injectant flow rate. In this zone, the natural reactive force of the injectant in $y-$direction is somewhat higher than the interaction or

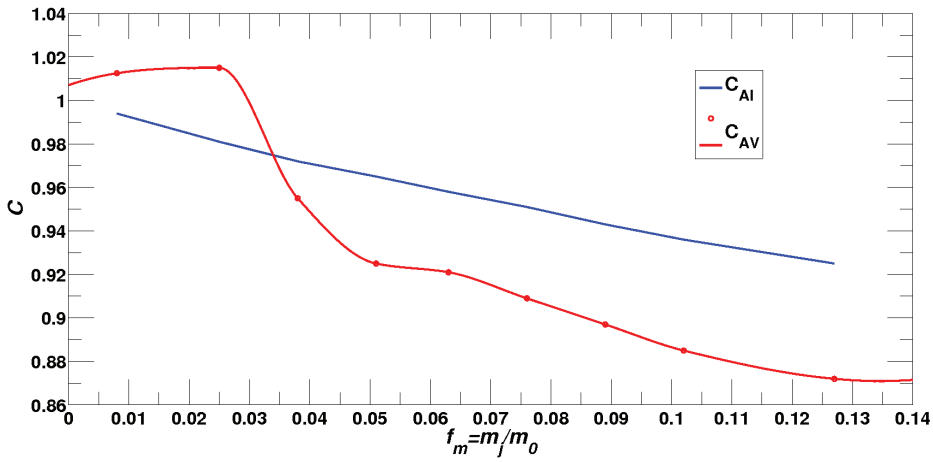

Figure 5.44: Vectoring and specific impulse amplification factor vs mass-flow-rate ratio

$y-$direction wall component of the side force and slowly decays with the injectant rate decrease to the symmetrical values. The balanced force component values are reached for the mass-flow ratios bit under $f_m < 0.05$. After this value zone, interaction force component is dominant and rises with the secondary injectant rate decay. The maximum in C_{AV} is reached around $f_m = 2.8\%$ after which the back pressure acting on a secondary injectant is too strong and the performance decays to zero.

Table 5.12: Characteristic distances

Case	$f_m = \frac{\dot{m}_j}{\dot{m}_0}$	δ_{BL},[mm]	h_j[mm]	x^*_{sep}/d_j	x^*_p/d_j
$SPR = 0.667$	0.051	1.695	4.114	-2.44	-1.94
$SPR = 0.833$	0.063	1.695	5.038	-2.53	-2.09
$SPR = 1.00$	0.076	1.695	5.514	-2.72	-2.26
$SPR = 1.167$	0.089	1.695	5.983	-2.83	-2.35
$SPR = 1.333$	0.102	1.695	6.475	-2.93	-2.44
$SPR = 1.667$	0.127	1.695	7.456	-3.15	-2.63

$^*NPR = 37.5, SPR = 1, f_m = 0.076, \delta_{BL} = 1.695mm$

The penetration height and separation distance values in Table 5.12, as expected, are in direct relation with the flow rates ratio. Again, we can observe

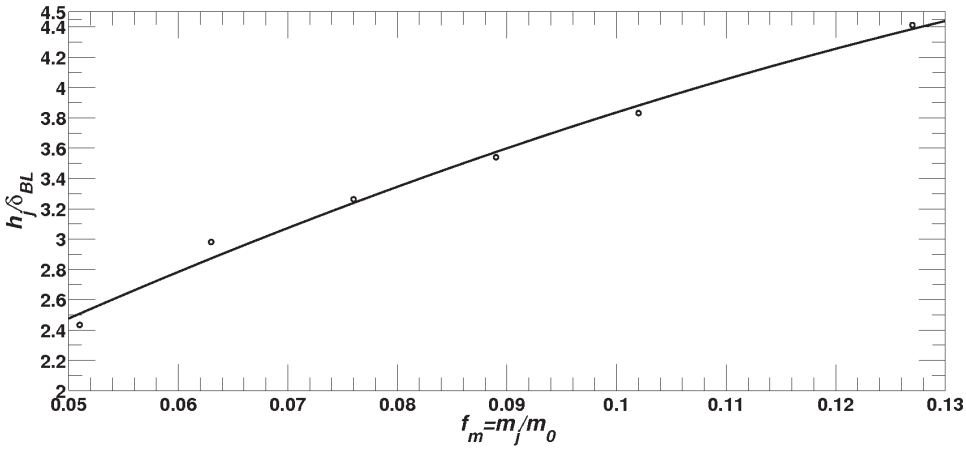

Figure 5.45: Non-dimensionalized injectant mach disk height with related mass-flow-rates

a quasi-linear behavior from the high f_m to the values close to the $f_m \simeq 6.2\%$ after which curve changes its slope towards the force component equalization at $f_m \simeq 4.9\%$.

In the presented subsection, SPR or mass-flow-rate ratio demonstrated, throughout experiments and numerical simulations, substantial effect on the vectoring and nozzle performances for the fixed dry air gas specie and adapted NPR. The secondary injection area was maintained constant, while the f_m variation was achieved by altering the secondary total pressure. However, it is deduced that for smaller injector surface and higher pressure, penetration is deeper which leads to the farther upstream separation point and higher amplification factor.
The presented results have indicated losses in global nozzle specific impulse between 2% and 5% for moderate mass flow ratios $f_m = 4\%$ to 9%. Further increase of the mass flow largely deteriorates the specific impulse to an unacceptable value. The ratio of produced side forces and used mass flows in these cold flow tests was satisfactory ranging from above 1 to 0.91 and then decayed for the higher mass flow rates. However, it should be noted that in the performed cold flow experiments flow was not heated before settling chamber and therefore the temperature was constantly declining during the test, while the secondary flow had a quasi-constant flow conditions. As a consequence, somewhat higher vectoring with the virtually lower f_m are obtained comparing to the flows with identical total

temperatures.

5.4.2 Primary flow conditions

Additionally to analysis of the mass-flow-rates ratio and SPR, the effect of the primary nozzle pressure ratio was investigated, as well. NPR and particularly over-expansion flow regime nozzle operation have an important role for the first and second stage rocket nozzles. Increase of the ambient conditions over the adaptation values will lead to the pressure increase on the exit section which will at first lead to the fast recompression through an increased Mach disk size at each compression sequence. Further increase will thicken a boundary layer and separated it with corresponding compression wave ending on a Mach disk. This leads to the λ shock wall interactions which further affected by the character of the nozzle contour. In this numerical and experimental investigation, truncated-ideal-contour nozzle is considered which is characterized with non-uniform flow at the test section and free-shock-separation FSS mode without unforced flow reattachment. As TIC nozzle is a shockless configuration type, the cap shock and RSS never appear in this nozzle type. Tested experimental TIC nozzle was at adapted flow conditions for $NPR_D = 37.5$. This pressure ratio enables the flow exiting into the exterior domain parallel to the wall-profile.
The overexpansion regime is detrimental for nozzle operation at which delivered thrust ratio decreases from the designed one. Increasing the ambient pressure, that is lowering the NPR, will initially thicken the boundary-layer and then eventually separate it if the imposed adverse pressure gradient satisfies the p_{sep} condition. In the current experimental nozzle, Figure 5.46 and 5.47, some noticeable BL thickening begins at $NPR \approx 30$ while the initial separation occurs at $NPR \approx 20$. This moderate ambient pressure augmentation has a favorable effect on the vectoring performances due to two occurring processes. The first mechanism occurs as a consequence of the supersonic cross-flow physical nature, that is, high pressure upstream and low pressure downstream of the secondary port. The low pressure aft of injector imposes suction to surrounding flow and secondary plume itself, which has detrimental effect of pulling the secondary plume towards the wall. In the case of increased ambient pressure this region fils with the gas

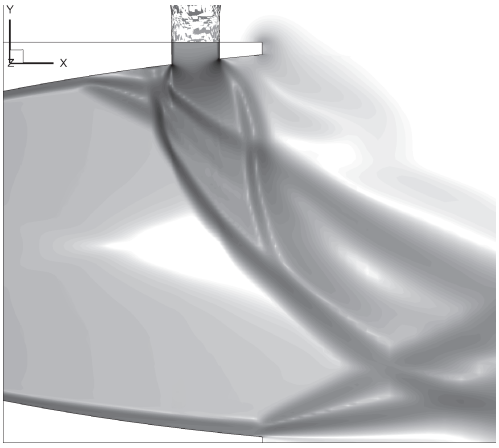

(a) $NPR = 20$ Numerical schlieren

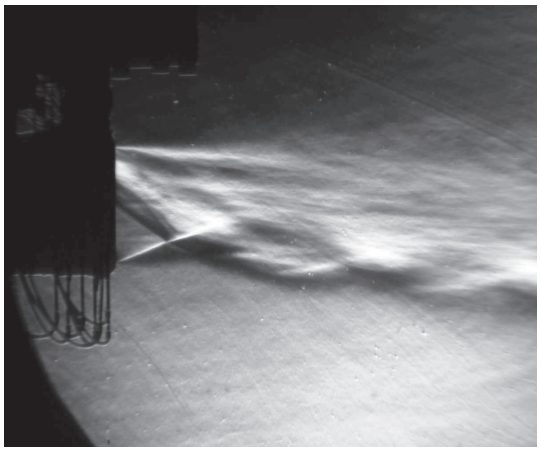

(b) $NPR = 20$ Experimental Z-schlieren

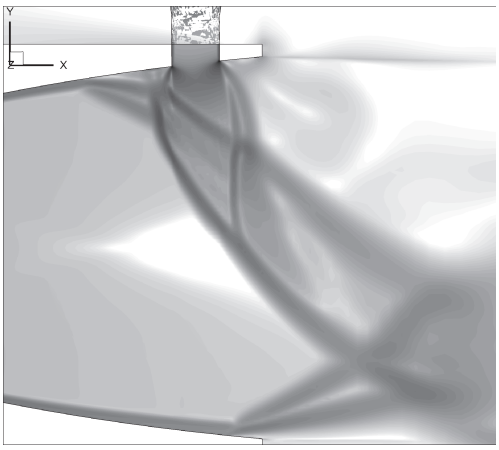

(c) $NPR = 15$ Numerical schlieren

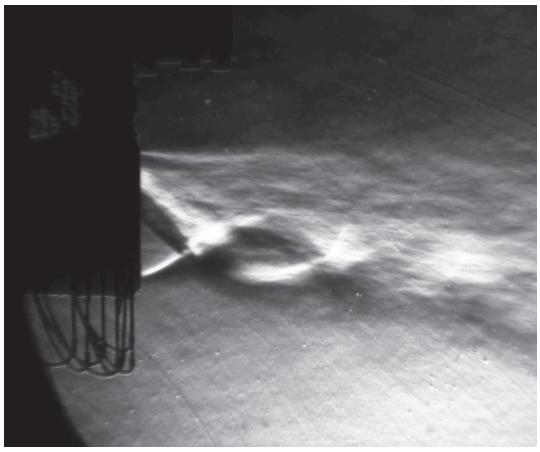

(d) $NPR = 15$ Experimental Z-schlieren

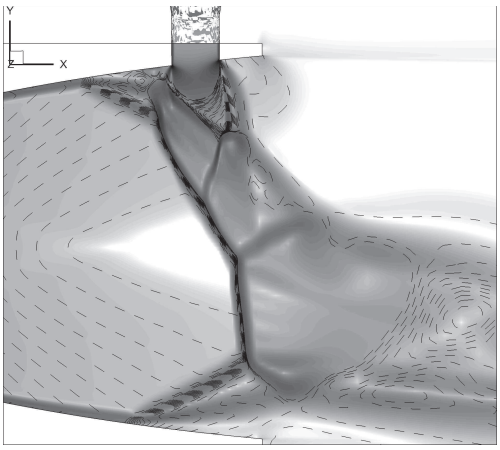

(e) $NPR = 10$ Numerical schlieren with contours

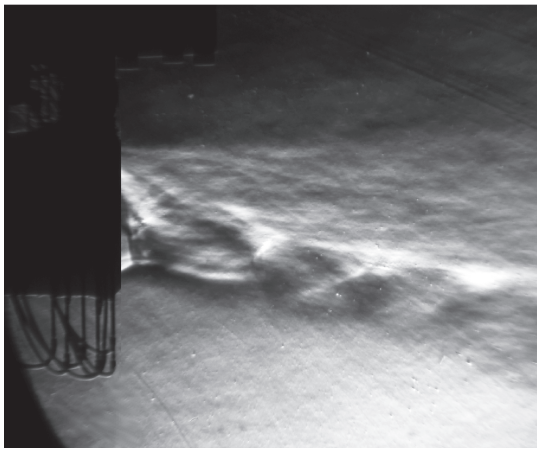

(f) $NPR = 10.4$ Experimental Z-schlieren

Figure 5.46: Numerical and experimental schlieren photos for SPR=1 and series of overexpansion NPRs

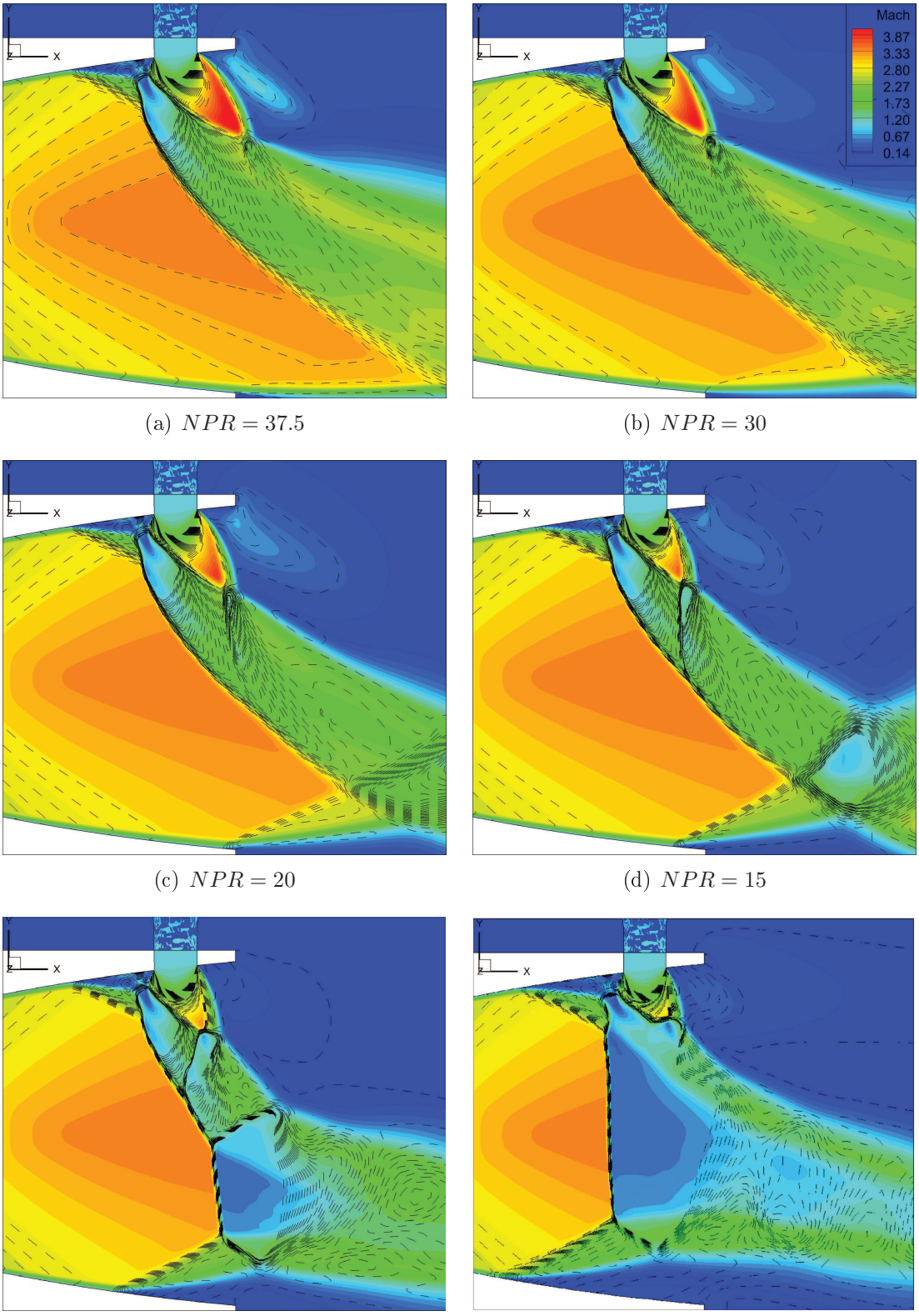

(a) $NPR = 37.5$ (b) $NPR = 30$

(c) $NPR = 20$ (d) $NPR = 15$

(e) $NPR = 10$ (f) $NPR = 7.5$

Figure 5.47: Mach number plot and pressure stream contours for SPR=1 and series of overexpansion NPRs

from the exterior, lowering the suction action on the secondary plume. This relief mechanism prevents strong inward folding of secondary plume, allowing its penetration into main flow under higher angle. On the other hand, the inflow of exterior fluid increases the pressure in the region of a secondary injection, resulting in a lower under-expansion rate. It is possible to notice in Figure 5.47(b) and (c) that changing NPR from 30 to 20, decreases the secondary plume maximum expansion Mach number from 4.02 to 3.76. The increased pressure at the exit also reduces the principle nozzle thrust ratio and thus, implicitly the side/axial force ratio or δ increases.

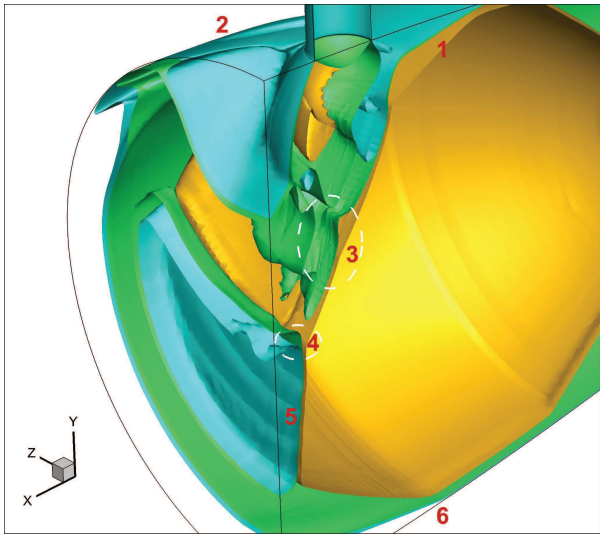

Figure 5.48: 3D iso-surfaces for NPR=10, SPR=1; numbered regions of: 1-separation, 2-horseshoe vortex formation and propagation, 3-secondary plume-bow shock interaction, 4-triple point, 5-Mach disk and 6-opposite wall-side separation

Being aware of this, it can be said that ambient pressure increase naturally reduces expansion of both, the primary and the secondary jet. However, relieving the suction stress on the leeward side of a reduced secondary plume, maintains its original penetration and produced wall side force component.
With further NPR reduction, a shock wave interaction becomes prominent. At $NPR = 20$ in schlieren Figures 5.46(a) and (b) and in contour plot in Figure 5.47(c), it can be observed that windward shock surface of the secondary compression sequence of a secondary plume passes the interface, formed between

the bow shock and the secondary plume, and confluent into bow shock under final small angle. This shock interaction prevents further upstream movement of the secondary plume, small subsonic flow portion is consequentially formed in front of it. Further NPR reduction to 15 moves the established shock interaction interface upwards toward the plume, with an increased flow separation shock incident angle. Together with shock interaction a subsonic region increases in front of it, imposing a higher pressure at the nozzle injection section. Examined overexpansion pressure ratios may be denoted in a following way:

- $NPR = 20$ - quasi-regular (minor Mach disk) shock-shock interaction forms between the right-running bow shock wave and left-running separation wave. Both shock waves are refracted through this intersection and slip line forms between the regions behind a shock.
- $NPR = 15$ - Mach disk slightly grows leading to the prominence of Mach reflection phenomenon
- $NPR < 15$ - Fully developed Mach reflections with characteristic triple points formed between the bow or separation shock, the Mach disk and the corresponding reflected shock waves.

At the opposite wall side of injection port, separation due to overexpansion overgrows the separation due to secondary injection, which generates a negative imbalance of the wall side force component.
It is found that limiting case for any operability of SITVC system is the appearance of the main Mach disk at the injection point cross-section of the nozzle, which for this nozzle occurs for $NPR \approx 9.2$. After this point, the SITVC becomes highly inefficient. For $NPR = 7.5$ in Figure 5.47(f) Mach disk overpass the secondary injection port nozzle section. Furthermore, secondary injection prevents the ambient inflow to the upstream separation zone. This results in predominant separation at the opposite side leading to the Mach disk displacement towards the injection port. Some researches also found that in this negative SITVC case, multiport ring placed injections may be used with small inflows to actually prevent large separations when it is needed or to stabilize the unsteady nozzle flow.

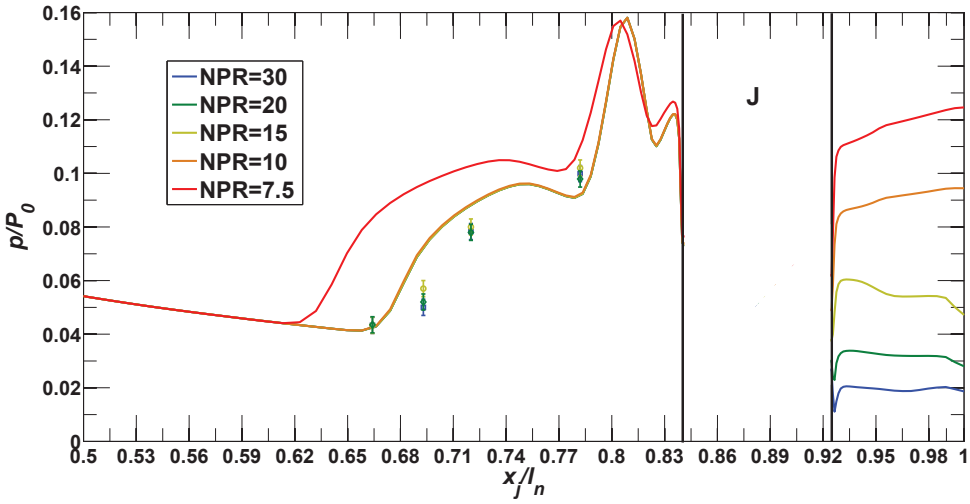

Figure 5.49: Wall-pressure profiles for constant SPR=1 and series of overexpansion NPRs of TIC-i.$x_j/l_n = 0.882$ nozzle, *lines representing numerical simulation results and signs experimental data*

Wall pressure profiles presented in Figure 5.49 display an invariant behaviour of the upstream separation wall-pressures in relation to the ambient pressure rise until the main Mach disk occurs inside the nozzle. For $NPR = 10$ there is a first, hardly noticeable, slight movement backwards which represents NPR value proximate to the limiting case. With $NPR = 7.5$ Mach disk is positioned upstream of the injection port. This results in upstream displacement of detachment point and separation region. Due to equipment limitation, experimental data was collected for $NPR = 30, 20, 15$ cases and Kulite probe diagnosing performed as expected and analogously to the data presented in the previous section. There were again some overestimation in numerically obtained profiles comparing to the experiments. Yet, as mentioned, this is rather assigned to the intrusive measurement placing and some smaller misalignments. Observing the experimental data, it can be noted that it behaved correspondingly to the numerical results.

Tabulated data show the increase of vectoring pitch angle and vectoring amplification with overexpansion growth until the prominent separation occurs due to an overexpansion inside the nozzle. From that point, vectoring decreases until reaching its minimum limit at around $NPR \approx 8$. Observing the force components data, it can be noticed that natural reactive force of the secondary injection

Table 5.13: Numerical flow conditions and forces data

$NPR = P_0/p_a$	F_{jy}, N	F_{wy}, N	$\sum F_y, N$	$\sum F_x, N$	$\delta,^\circ$	F_{x0}, N
$NPR = 37.5$	9.368	7.169	16.537	136.21	6.92	134.05
$NPR = 30$	9.368	7.19	16.558	132.86	7.10	130.73
$NPR = 20$	9.361	7.20	16.561	124.60	7.57	122.41
$NPR = 15$	9.207	7.378	16.585	116.67	8.08	114.11
$NPR = 10$	8.814	1.34	10.154	102.04	5.68	97.5
$NPR = 7.5$	2.67	-3.414	-0.744	91.3	-0.47	81.07

$^*SPR = 1, T_0 = 255K, T_{j0} = 280K, \dot{m}_0 = 236.2g/s, f_m = 0.076$

Table 5.14: Experimental flow conditions and forces data

$NPR = P_0/p_a$	$\sum F_y, N$	$\sum F_x, N$	$\delta,^\circ$
$NPR = 37.5$	16.17	136.1	6.78
$NPR = 30$	15.98	132.	6.9
$NPR = 20$	16.1	123.9	7.4
$NPR = 15$	16.4	110.4	8.45

$^*SPR = 1, \dot{m}_0 = 236g/s, f_m = 0.076$

Table 5.15: Performance coefficients

$NPR = P_0/p_a$	C_{AV}	C_{AF}	C_{AI}	h_j, mm
$NPR = 37.5$	0.909	1.023	0.951	5.514
$NPR = 30$	0.934	1.024	0.952	5.514
$NPR = 20$	0.996	1.025	0.953	5.514
$NPR = 15$	1.063	1.033	0.96	5.514
$NPR = 10$	0.747	1.051	0.977	5.514
$NPR = 7.5$	-0.06	1.121	1.042	5.514

remains the same until the exterior flow imposes higher pressure at the injection port nozzle section. With increased pressure at the injection port natural reactive force starts to decrease gradually until the Mach disk occurrence at the injection

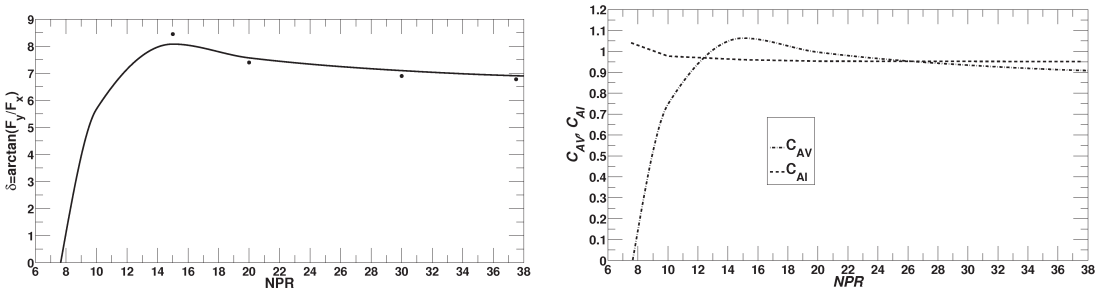

(a) δ, (*lines refer to numerical simulations and signs to experiments*)

(b) Vectoring and specific impulse amplification coefficients

Figure 5.50: Performance data plotted versus NPR for TIC-i.$x_j/l_n = 0.882$ nozzle, $SPR = 1$

position inside the nozzle. After this point reactive force rapidly decays to low values. Wall side force evolution follows the NPR decrease with very slow increase caused by the exterior inflow into the low pressure region aft of injector. After reaching its high between $NPR = 15$ and 20, wall side force rapidly declines with an overexpansion caused separation of the main flow inside the nozzle. The injected secondary flow that doesn't generate strong side force still contributes to the global force amplification factor. In the case of gross overexpansion inside the nozzle, secondary injection opposes to the strong Mach disk and separation blockage still increasing the axial force and thus, the specific impulse amplification factor.
Secondary injection Mach disk height, h_j was evaluated at each selected NPR test case and it was constant during this investigation, appearing always at the same point.

It can be concluded that an overexpansion initially contributes to the smaller increase of vectoring capacity but then rapidly deteriorates performances with strong separation inside the nozzle. Delayed SITVC operation capability for high operating pressure range rocket nozzles, may be achieved by a certain upstream displacement of the pneumatic actuator or by realizing secondary injection through the meridionally distributed multiport injection.

5.5 Conclusion remarks

In this Chapter, major interaction flowfield properties and parameters are investigated to characterize the SITVC cases of a transverse sonic injection into a supersonic rocket nozzle. Experimental and numerical investigation is conducted on number of test cases and different analysis criteria and for some cases compared with the analytically obtained results. Chapter 5 is initially split into three main sections covering the conducted investigations of injection port position; design characteristics and types of the main nozzle; and interaction flow field properties with influence of the primary and the secondary flow conditions.

In Section 5.2, an experimental investigation is conducted on the two same conical type convergent-divergent nozzles with different transverse injection port positions and broadened afterwards with additional numerical cases. The complex flowfield is first qualitatively described via schlieren photographs, Mach number plots and iso-surfaces. Clear distinction between the injection closer to the nozzle exit at $x_j/l_n = 0.9$ and the injection at $x_j/l_n = 0.7$ has been made. The injection case at $x_j/l_n = 0.7$ falls under the limiting case at which the generated bow shock propagates and affects the whole nozzle cross section and finally reflects from the opposite side leaving the nozzle under negative reflection incident angle. This is found as detrimental for the nozzle and SITVC operation, first by reducing the nozzle pressure forcing the whole nozzle flow to go through the strong bow shock, secondly by separating the flow on the opposite side and forming a recirculation bubble. Moving the oppositely separated flow in negative direction, completely cancels the wall side force contribution, leaving only a portion of the secondary injection natural reactive force. Even though the further upstream displacement of injector port would lead to an eventual double shock reflection, the injection beyond reflection limiting point is found as largely detrimental and source of potential unsteadiness. Investigation of the transverse injection port position between the limiting point and exit of the nozzle yielded results which indicated that position close to the nozzle exit was the most optimal. This is found mainly as a consequence of imbalance between the high pressure region in the separation zone upstream of injector and low pressure aft of injector. Performance increase is further achieved by augmenting upstream separation and

shortening the downstream suction zone, by placing the injector closer to the nozzle exit.

In Section 5.3, design parameters of the primary nozzle as the expansion ratio and the nozzle type are investigated with corresponding transverse injection. Shock polar and shock-deflection 1D analysis yielded primary assumptions of the flow deflection progress versus primary momentum increase. Basic inviscid simulations are conducted on the previous conical nozzle model and elongated model corresponding to $M_{exit} = 5$. This primary analysis is further enhanced by viscous numerical investigation of two, $Mach$ 3 and $Mach$ 5 nozzle cases in cold flow tests. It is found that higher expansion has only a secondary effect on the produced side force and vectoring angle and performances. Optimal side force is analogously obtained with the injector positions closer to the exit and it was increasing with Mach and expansion increase of the primary nozzle. However, with side force increase, the primary nozzle momentum and axial thrust augmented with a higher rate, leading to a slightly lower vectoring angles.
Analysis of contour types for Mach 5 nozzles yielded some additional effects for Rao optimized nozzles with an internal shock. However, the global nozzle vectoring performances at adapted conditions was maintained with these contours as well. Additional optimization proposed by Rao to design an adverse-pressure-gradient contour which at the exit portion of contour favors adverse instead of favorable expansion pressure, yielded some minor improvements. However, this contour optimization needs to be further investigated for definite optimization recommendations.

In Section 5.4, complex interaction flowfield of the selected experimental TIC test nozzle is investigated. The qualitative analysis is conducted and flow features are described via side-frontal and top schlieren photographs and nozzle cross-section numerical slicing. The influence of secondary and primary flow conditions is then examined for the selected nozzle. It is found that SPR or mass-flow-rate ratio, f_m has a major effect on the main flow deflection and the global side force. Increase of secondary injectant flow rate linearly augments the vector pitch angle. However, its performances in relation to fuel consumption are constantly decreasing. On the lower end, a breakdown point is found around $SPR \sim 0.3$ after which the back pressure acting on the secondary injection port impacts the

performances.
It is found that NPR and overexpansion have secondary positive effect on the vectoring performances for lower overexpansion NPRs. With further increase of ambient pressure and separation due to an ambient pressure imposed pressure gradient, SITVC performance rapidly deteriorates.

In this chapter, main interaction flow features have been identified and described and data have been presented in terms of SITVC and general nozzle flow effects. It is shown that with a single port circular sonic injection of $f_m = 0.076$ it is possible to achieve pertinent vector side force and vectoring amplifications ranging around $C_{AV} \approx 1$.

Chapter 6

Properties of pneumatic actuator nozzle and secondary injection types

6.1 Introduction

In the previous, Chapter 5, interaction of supersonic cross-flowfield and SITVC effects are characterized on the multiple primary nozzle configurations with a single transverse secondary injection through the circular throat, normal to the principal nozzle axis. Attention was paid to the primary nozzle flowfield and coupled with the position and injection rate of circular secondary sonic injection perpendicular to the axis. It is found that these parameters essentially define the SITVC system operability performance and have the global effect on the primary nozzle operation.

Considering the fixed secondary nozzle throat area and secondary-pressure-ratio, further optimization can be expected by altering the secondary nozzle geometrical parameters. It has already been noted that even a small variation in the secondary port shape and attitude angle, due to a variable primary nozzle contour, affect the interaction flow field and principal supersonic flow response. To analyze these effects, an experimental and a numerical investigations have been conducted on the additionally designed and build test nozzles. In addition to investigated nozzle

cases, a solely numerical investigation is conducted on a supersonic secondary nozzle design and for multiport injection configuration and presented in the brief analysis at the end of this chapter.

6.2 Secondary nozzle geometry [1]

With regard to the structure of separated flow, it can be deduced from the previous analysis that interaction force component is related to the upstream separation distance and amount of separation affected primary flow, while the reactive force in general depends on the secondary throat flow momentum. Having this in mind, one can assume that further augmentation of interaction force may be obtained by increasing the amount of affected flow. This can be achieved by controlling and increasing laterally separated flow size.

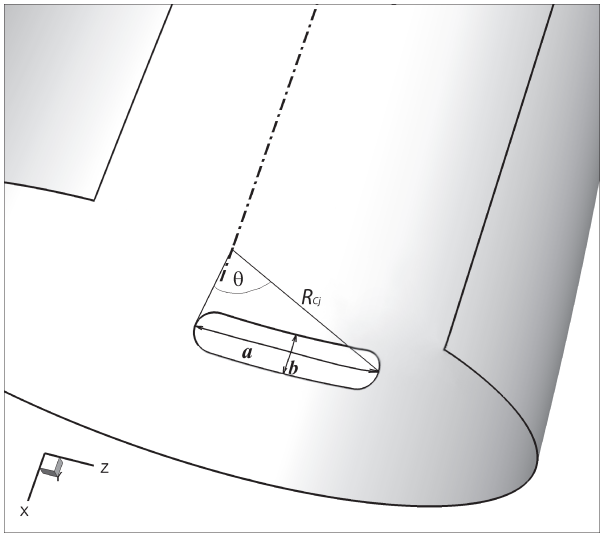

Figure 6.1: Definition of the slot contour on the divergent section of the TIC nozzle

Dimensions of a slot shaped sonic injection port on the divergent nozzle wall section can be defined by tracing the circular arc around scope of a divergent wall from the center placed at the injection point projection on the nozzle axis.

[1]Some of the presented work is adapted in:
Zmijanovic *et al.*[90], *P. Propulsion Phys.* **4** 227-256 (2013)

By this, the longer side of the slot is defined as the arc over central angle θ and radius R_{Cj} of primary nozzle cross-section at the injection point. The rectangular throat with identical area as the circular one can be defined then by the chord of the central arc and the given area.

$$a = 2 * \pi R_{Cj}(\frac{\theta}{360}), \quad a_j = 2R_{Cj}\sin(\frac{\theta}{2}), \; b_j = A_j/a_j \tag{6.1}$$

It can be correctly assumed that with an increase of the θ central angle and

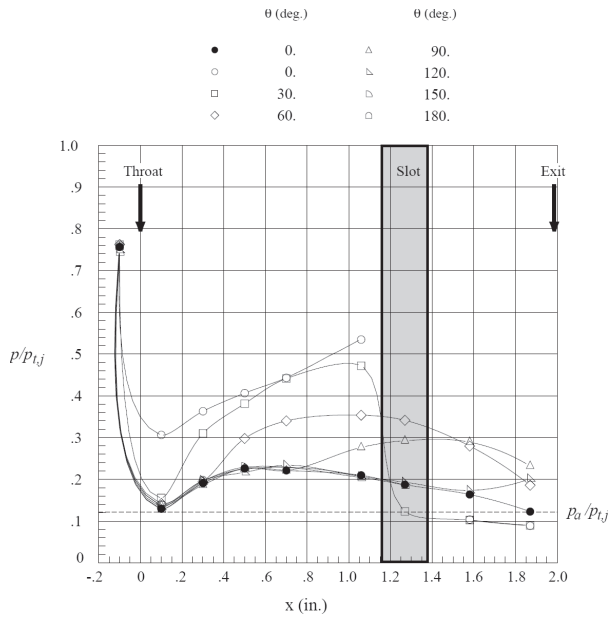

Figure 6.2: Static pressure distributions for SITVC slot configurations at $NPR = 8.26$ and $SPR = 1$ found in Wing and Giuliano[52]

the width of the slot, the lateral separation will increase. Wing and Giuliano[52] conducted experiments with adjustable θ configuration conical nozzle. It was found that highest pressure rise inside the separation region is obtained for slots up to $\theta = 30°$. With slots at larger, $\theta > 90°$, sub-ambient pressure dominated the side separation region in compare with the central upstream separation. This resulted in somewhat recuperated primary nozzle thrust due to pressure relief mechanism and therefore weaker bow shock but the vectoring performances were relatively lower. However, in Wing and Giuliano[52] work tested conical nozzles were reportedly too short and with injection ports too close to the nozzle

throat. Considering the experiments performed by Wing at NASA Langley and the structural limitations of a typical launcher used rocket nozzle at higher NPR and expansion conditions, the slot configuration with central angle $\theta = 30°$ was selected in the reported experiments.

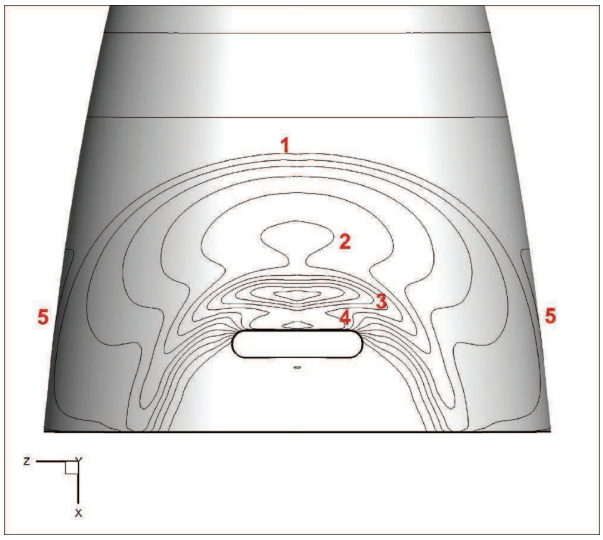

Figure 6.3: Numerical pressure contours of separation and affected zones with slot SITVC nozzle at $NPR = 37.5, SPR = 1$ conditions

Similarly to the nozzle with circular injection, the characteristic zones may be sorted as: 1 - Wide separation extending from the incipient point widely in lateral direction; 2 - Plateau pressure reached after pressure increase from separation point, at about half-slot width; 3 - Pressure peak with laterally extending horseshoe vortex; 4 - Trapped secondary peak region between horseshoe and the slot; 5 - Weaker nozzle free-shock separation on lateral side due to separation lateral extension and sub-ambient adverse pressure gradient imposed to the boundary-layer.

6.2.1 Characterization of $\theta = 30°$ slot shaped secondary injection case

Initially designed sharp rectangular injection port geometry in Figure 6.4(b), manifests some typical effects encountered for the sharp and blunt structures in a

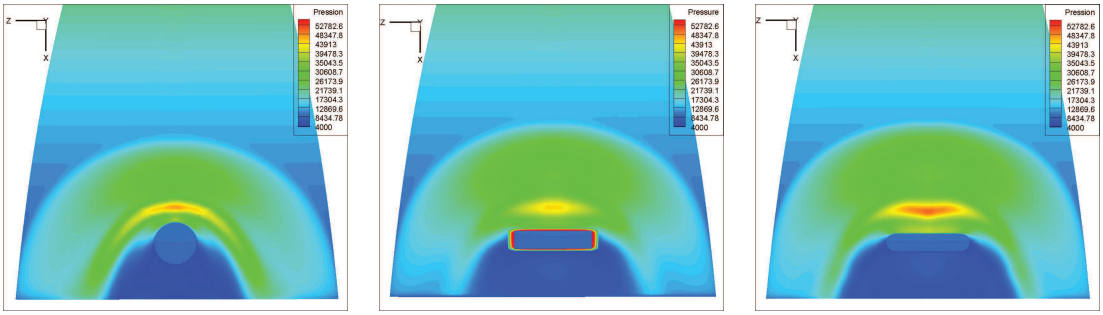

(a) Axisymmteric circular injection

(b) Sharp rectangular slot injection

(c) Rounded rectangular slot injection

Figure 6.4: Wall-pressure plots for different injection port geometries of SITVC TIC nozzle at $f_m = 0.08,\ SPR = 1,\ NPR = 37.5$ conditions

supersonic flow. Namely, the flow pattern significantly deviates from the uniform distribution especially near the sharp angle corners where detachment is present. At the outer shell around the port, stress concentration on the rectangular edges and corners is depicted while the pressure peak and SUV appears weakened.

The rounding of sharp edges smooths the interface between the slot and separation zone and relieves the pressure stress imposed on the slot edges which results in a larger horseshoe region. Figure 6.5 depicts the separation line on the

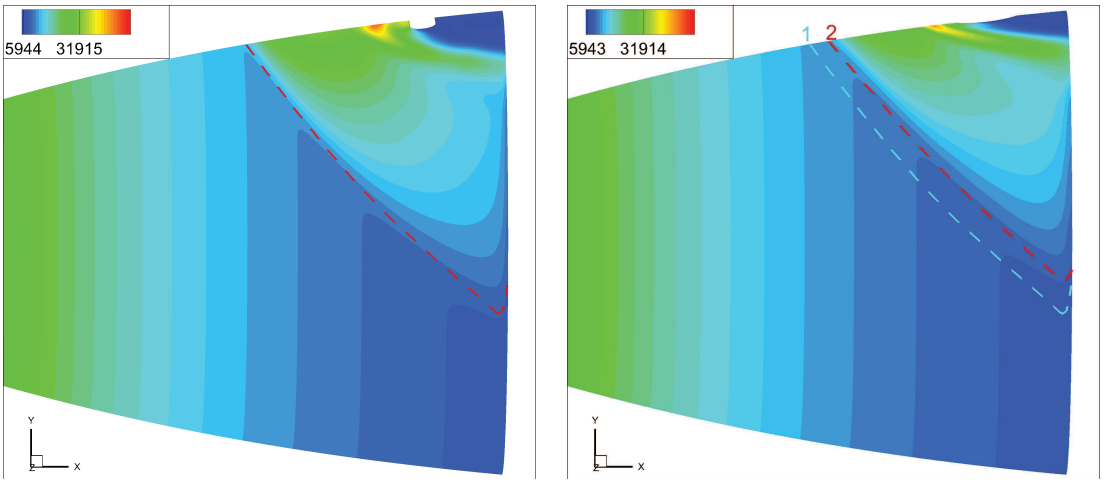

(a) Slot shaped injection port

(b) Axisymmetric circular injection port

Figure 6.5: Wall-pressure plots with separation line of SITVC TIC nozzle at $f_m = 0.08,\ SPR = 1,\ NPR = 37.5$ conditions

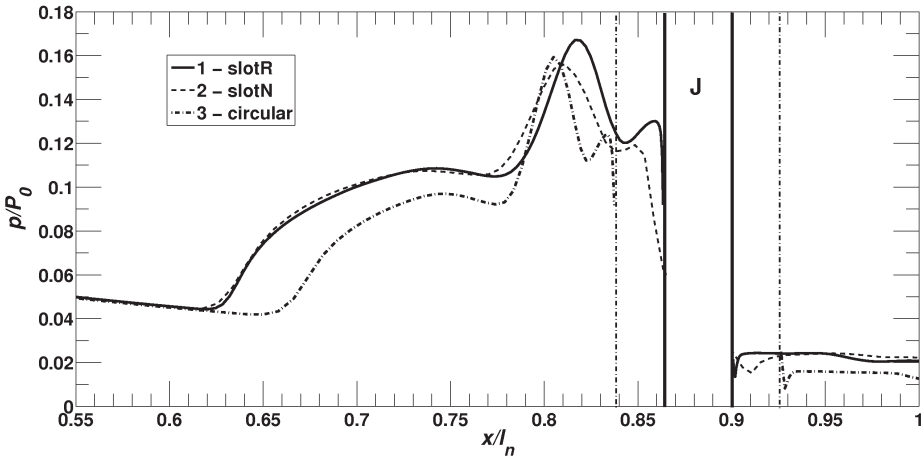

Figure 6.6: Wall-pressure profiles for slot and circular SITVC nozzle at $NPR = 37.5, f_m = 0.08, SPR = 1$ conditions, *1 - rounded rectangular slot, 2 - sharp rectangular slot, 3- axisymmetric circular port*

wall pressure plots figures for TIC nozzle with slot and circular shaped secondary injection port. Perceptible increase in the size of separation wall region can be observed in Figure 6.5(b), at which separation line (2) and projected separation line (1) of the slot injection case are given. This separation increase on the nozzle wall is also observable in the evaluated pressure profiles given in Figure 6.6. For the both $\theta = 30°$ slot cases separation point moves upstream for 15.5% at the x/l_n non-dimensional length scale. Considering the length scale centered at the injection point and non-dimensionalized by the injection width the upstream separation significantly increases. It can be also observed that SITVC TIC nozzle case with sharp rectangular slot appears with the pressure peak smaller than the rounded slot and the circular injection port cases, which corresponds to the pressure plots in Figure 6.4.

Schlieren photographs, given in Figures 6.7 and 6.8, matched very well the experimental and numerically obtained results. They depict mentioned increase of upstream separation but also an emphasized separation shock region interface with the compression waves which precede a strong bow shock. In Figure 6.8 secondary small lateral motion from the nozzle wall can be detected. It is resulting from a response to the blockage in lateral direction starting from the symmetry plane with an imposed pressure gradient, referred as a sub-ambient by Wing and

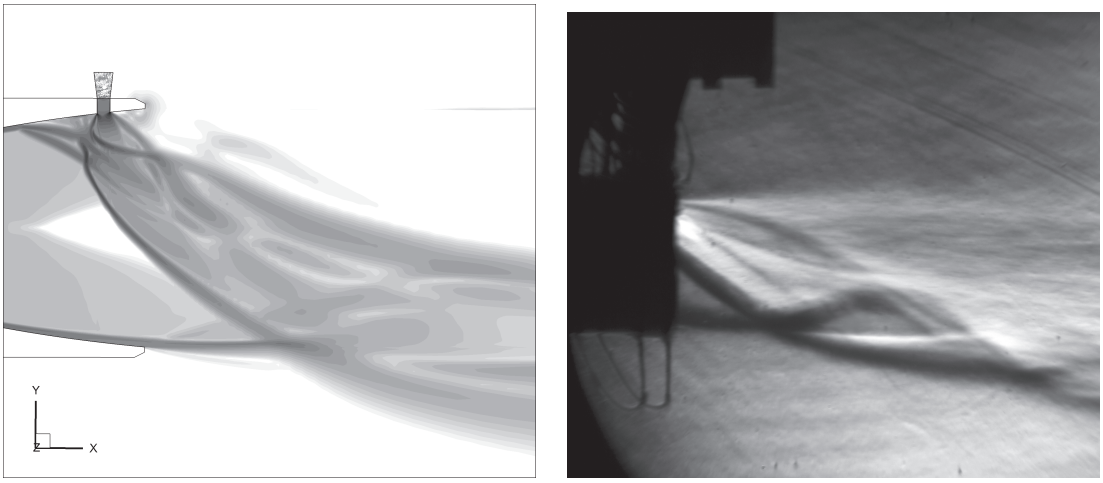

(a) Numerical schlieren in symmetry plane (b) Z-schlieren photograph

Figure 6.7: Schlieren photographs of SITVC TIC nozzle with slot shaped port at $f_m = 0.08,\ SPR = 1,\ NPR = 37.5$ conditions

(a) Numerical schlieren in xz plane (b) Z-schlieren photograph

Figure 6.8: Top view schlieren photographs of SITVC TIC nozzle with slot shaped port at $f_m = 0.08,\ SPR = 1,\ NPR = 37.5$ conditions

Giuliano[52]. The experimental top view schlieren corresponded well downstream in exterior domain, however, the exit of the nozzle was obscured by the secondary settling chamber.

Mach number iso-surfaces given in Figure 6.9 complemented very well the wall-pressure plot and delineated the SUV horseshoe vortex region. In green su-

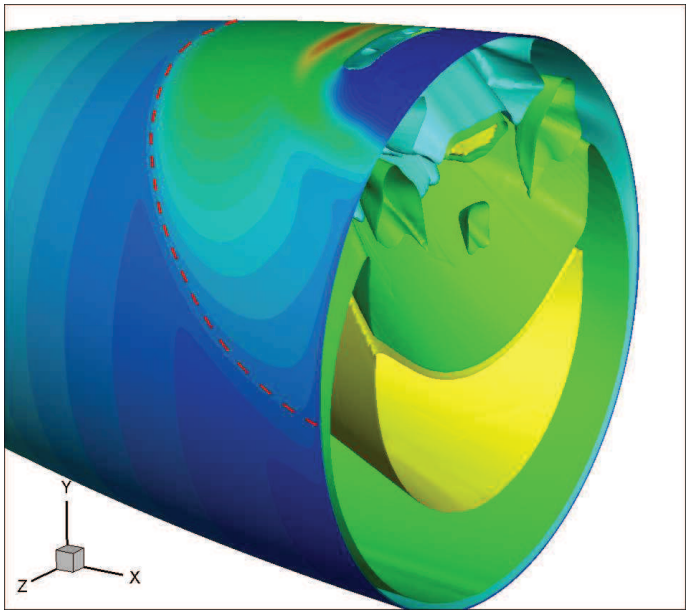

Figure 6.9: Wall-pressure plot with Mach number iso-surfaces for slot SITVC nozzle at $NPR = 37.5, f_m = 0.08, SPR = 1$ conditions

personic shelled region, below secondary plume Mach disk, a Mach=1 iso-surface surrounds the slot injectant plume. It depicts secondary plume distancing from the suction region above and the vortices shedding at the sides. This surface appears deformed on its outer sides by the inflow from the exterior domain and the portion of the horseshoe vortex aspirated flow. Lateral sides of the horseshoe vortex zone also appear deformed inwards at the interaction with the initial separation zone which gradually separates the flow at the nozzle cross-section, thickening and detaching the boundary-layer from the unaffected region towards this interaction.

6.2.2 Quantitative pressure and forces measurements

Analogously to the circular injection case, parietal pressures and forces have been diagnosed via deployed static and fast pressure probe acquisition and designed 3-axis force-balance. It can be observed in Figure 6.8(b), that the flow symmetricity was well conserved with the used secondary injection and only negligible lateral irregularities may appear. This was achieved partly by the pocket installation

of Kulite® probes inside the nozzle wall instead of flush mounting. In the case of pocket mounting, the probes were measuring the static wall conditions but they were less intrusive to the analyzed nozzle flow. The Kulite® pressure probes

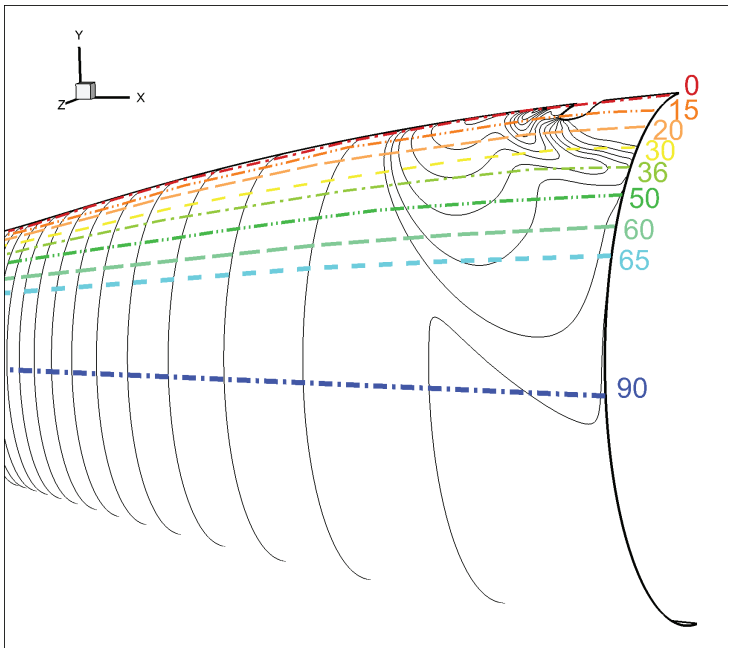

Figure 6.10: Meridians of TIC-slot nozzle at which the experimental and numerical data was probed

and pressure taps connected to Scanivalve® ZOC22B scanner were sorted along the nozzle meridians at $0°, 15°, 20°, 30°, 36°, 50°, 60°, 65°$ and $90°$, illustrated in Figure 6.10. The raw pressure data was examined for the instantaneous values and as averaged at every $0.25s$ or on 2000 data chunks. Analogue to the previous cases, experimental and numerically evaluated pressure data is presented for each meridian. These results are then use to define separation zone and characteristic region inside it and to verify the experimental-numerical approach. Bypassing of the detached boundary-layer flow around the injector port and gradually larger incremental steps of separation point downstream displacement are noted with the meridians larger than 36°. It can be also observed that separation at the symmetry longitude cross section appears considerably further upstream than for the circular shaped secondary injection port. The experimental data collected from the pocket mounted *Kulite* probes were more balanced with a smaller stan-

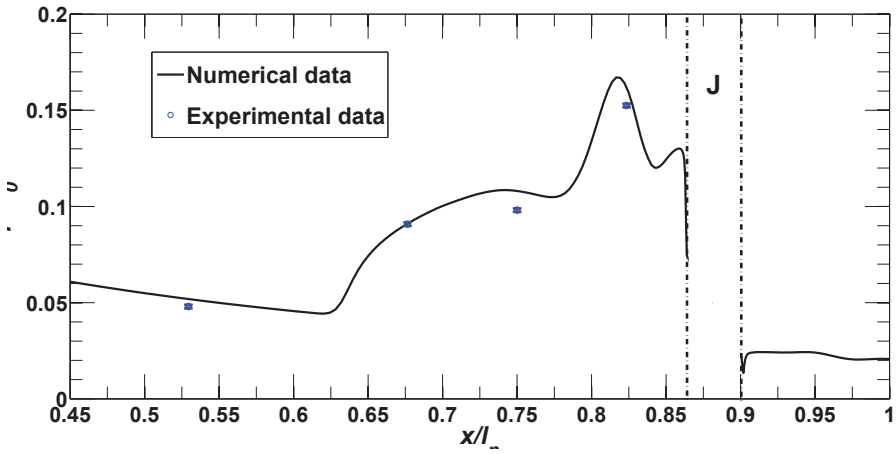

Figure 6.11: Experimental and numerical pressure data at 0° meridian, at $NPR = 37.5, SPR = 1$

dard deviation error at the same pressure conditions than the previously flush mounted probe case.

The pressure data presented in Figure 6.11 manifest excellent matching with the numerically evaluated pressure profile. Pressure tappings were grouped and positioned in that manner that there were no obstacles for the expanding flow. Probe in unaffected zone, pressure rise zone and secondary peak were excellently matched in the numerical evaluated profile. However, some deviation due to $k-\varepsilon$ RANS overestimation of pressure appeared at the plateau zone. Nevertheless, the parietal pressure mounting and measurement technique, alignment and data comparison appeared as a more credible in this case.

Experimental and numerical wall pressures are then presented along the corresponding meridians to delineate the separation zone and to verify the numerical approach. Besides a very satisfying agrement of the *Kulite* probes data and the numerical results, the Scanivalve measurement data were also in a satisfactory range. Apparent numerical underestimation in some points at downstream region is caused by the slight fluctuations of the ambient pressure conditions in experiments and monotone total temperature decay. Along with the total conditions, forces and performance coefficients are presented and tabulated in Tables 6.1, 6.2. The agreement between the experimental and the numerical results was found very satisfactory. Small oscillations in the recorded forces data for the same

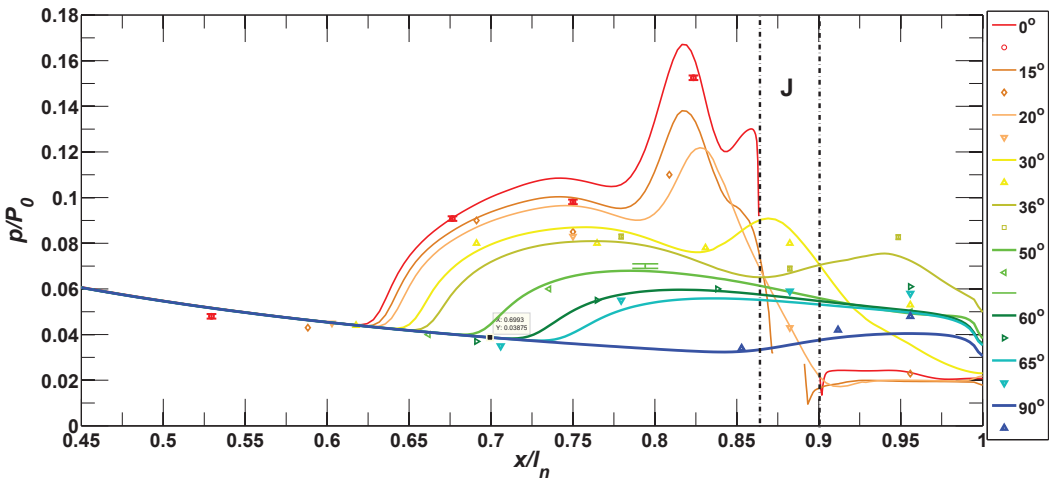

Figure 6.12: Experimental and numerical pressure data for range of meridian positions, at $NPR = 37.5, SPR = 1$, *lines represent numerical results and signs experiments (errorbar -Kulite)*

Table 6.1: Experimental force data for TIC nozzle slot injection case at $x_j/l_n = 0.882$

P_0, kPa	P_{j0}, kPa	T_0, K	T_j, K	$\sum F_y$, [N]	$\sum F_x$, [N]	δ
300.12	300.06	$256K$	$281K$	$19.97N \pm 0.76$	$135.98N \pm 1.1$	8.35°

Table 6.2: Numerically evaluated forces results

Case	$\dot{m}_j$, [g/s]	F_{jy}, [N]	F_{wy}, [N]	$\sum F_y$, [N]	$\sum F_x$, [N]	δ
circular	19.63	10.21	7.71	17.92	136.23	7.493°
slot	19.83	10.23	9.43	19.66	136.64	8.187°

$^*NPR = 37.5, SPR = 1, f_m = 0.082, F_0 = 134.05N, I^0_{sp} = 57.88s$

Performance data:

case	dim., mm	h_j, mm	x_{sepj}, mm	C_{AV}	C_{AF}	C_{AI}
circular	$d_j = 6$	5.512	15.664	0.914	1.025	0.946
slot	$b_j = 2.5$	5.205	17.595	0.986	1.029	0.951

pressure conditions points, that were observed in the previous experimental model were smoothed as the results of no intrusion at the wall and overall better test

model manufacturing. Numerically evaluated forces data were falling completely into the experimental range. About $\sim$ 20% increase in the interaction, wall-side force, component can be noticed in the presented data which is a direct consequence of the farther and wider upstream separation, while the reactive force component is approximately the same. The same trend can be followed then in the performance coefficients data, with 8.3% increase in vectoring amplification and 5% in the global force impulse amplification comparing to the circular injection case. The circular injection case, with identical throat area as the slot, has a throat diameter of $d_j = 6mm$. It is observed that the penetration height is identical or negligibly lower than the previous circular case with $d_j = 5.8mm$. This is inline with the previously referenced works at which amplification factors increase by lowering the injection port area and increasing the injection pressure conserving the same mass-flow-rate. Similar reasoning may be followed with slot injection in the symmetry plane, where characteristic dimension of the slot width $b_j = 2.5mm$ favors increased penetration into the main flow. Additionally, as a cause of a laterally-wide obstacle to the oncoming supersonic flow, separation point is displaced farther upstream with the somewhat smaller penetration height. The separation-penetration ratio varies then from $x_{sep}/h_j = 2.84$ to 3.38.

6.3 Secondary nozzle attitude angle

Alike the port geometry shape optimization, the flow interaction, generated separation and the side force component may be directly affected by changing the attitude of a secondary injection plume. It can be observed in the TIC nozzle results presented in Chapter 5 that even the small changes caused by the variable nozzle contour slope affect the SITVC performances. Nielson *et al.*[54] investigated the secondary injection inclination effect on the SITVC nozzle performances and found that a downstream inclined injection is gradually detrimental for the SITVC performance while upstream inclination considerably augments produced side force. Even though, downstream inclination is detrimental regime, it can be advantageous for the overexpansion generated separation or where a stronger axial force is needed. Therefore, Woodberry and Zeamer[51] reported usage of a gimballed secondary injection for a larger operation envelope. Nielson

et al.[54] found that increase of an upstream inclination, monotonously augments the side force until some breakdown value that was for their nozzle case found at around 47°.

Secondary injection attitude was experimentally investigated on the conical *Mach* 3 nozzle model with an upstream inclination of 20°. Further angle increase is investigated numerically. The diagnostic methods comprised of the schlieren visualization, total condition monitoring and the force balance acquisition. Isentropically evaluated basic conical C-a.0.9 nozzle properties are given in the Table 3.3.

6.3.1 Characterization of 20° upstream inclined SITVC conical nozzle

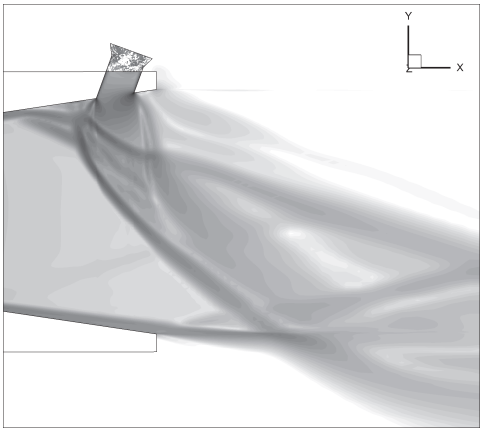

(a) Numerical schlieren in symmetry plane

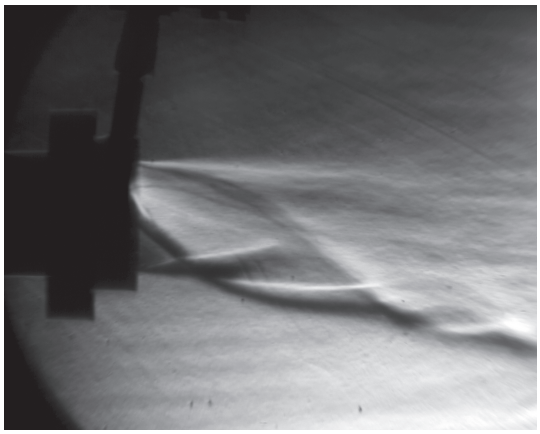

(b) Z-schlieren photograph

Figure 6.13: Schlieren photographs of SITVC C-a.09 nozzle with inclined circular injection at $SPR = 1,\ NPR = 37.5$ conditions

In the given schlieren image, portion of the secondary plume resides upstream of the injection port between the separation shock and the wall. The interface that is formed between the main bow shock and the secondary underexpanded plume aspirates trapped flow inside the separation and it is defined by the secondary plume windward side and the bow shock front. Due to occurrence of secondary plume portion in upstream region, the interface increases in size. This can be

interpreted as an additional blockage and "push" action on the separated flow increasing its size and slope gradient. The main flow responds to the additional blockage by the stronger bow shock and higher adverse pressure gradient imposed to the upstream boundary layer moving its detachment point notably upstream. The presence of a secondary plume in separation region causes that some fluid particles detach from secondary plume and then being caught in SUV and also in PUV as depicted in streamtraces in Figure 6.15(a).

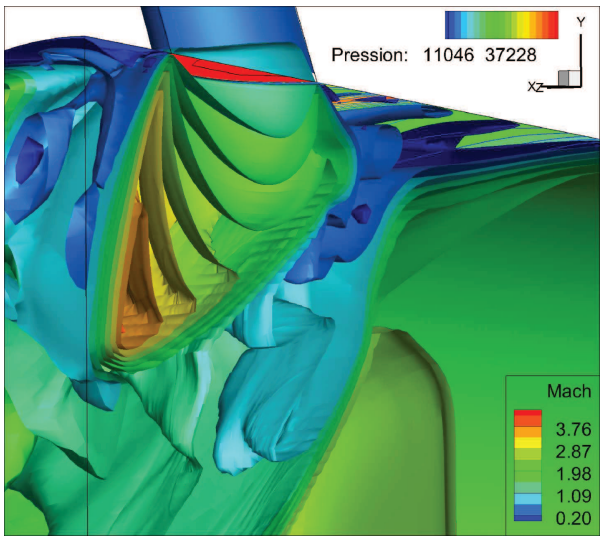

Figure 6.14: Wall-pressure contours and flow iso-mach surfaces for 20° inclined circular injection of C-a.0.9 nozzle at $SPR = 1,\ NPR = 37.5$ conditions

There is also a change in the plume profile due to an injection port geometry, that can be observed in Figures 6.14 and 6.15. Specifically, an inclined throat section cylinder intersects the principal nozzle wall under a high angle at its windward side and a sharp angle at its leeward side. This causes a stretched appearance of the ellipsoidal injection port shape with a non-uniform secondary flow profile. Namely, at the short leeward side flow will be introduce to the nozzle sooner while the flow expansion will be allowed towards the windward side.
It can be reasoned that smaller pre-expansion at one part of the flow will allow a lightly higher natural reactive force of the injectant but also will consequently decrease a pressure in that section of injection port slightly depreciating its opposition to the bow shock. Along with the change of attitude, the y-direction

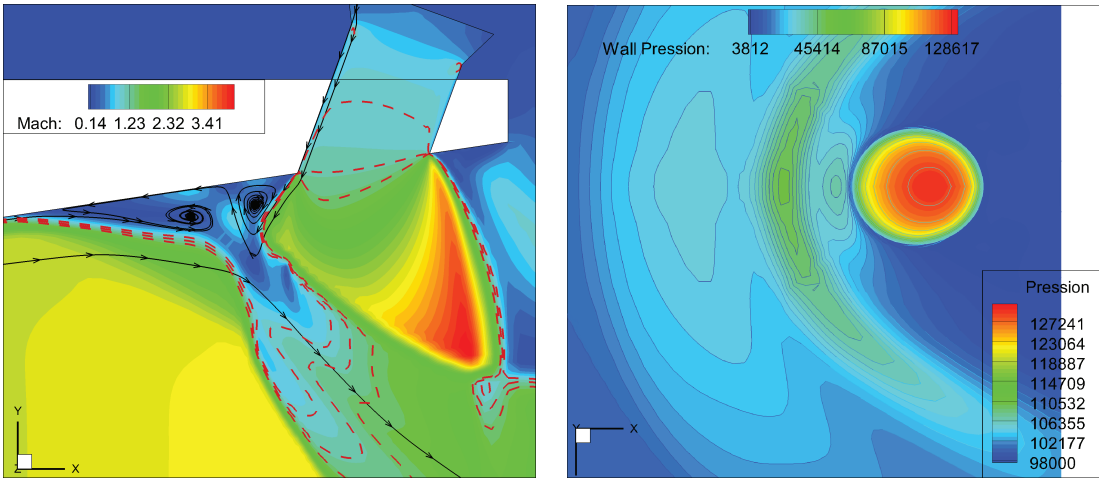

(a) Mach number in symmetry plane (b) Wall and secondary port pressure contours

Figure 6.15: Pressure and Mach number plots of SITVC C-a.09 nozzle with inclined circular injection at $SPR = 1,\ NPR = 37.5$ conditions

force component of the reactive force will decrease, while negatively oriented x-direction component increases. However, the favorable action optimization of the cross-flow interaction force is substantial comparing to the reactive force component.

Table 6.3: Experimental and numerically evaluated force data of C-a.09 nozzle at $NPR = 37.5, SPR = 1$ conditions

Case	$\dot{m}_j$, [g/s]	F_0, [N]	$\sum F_y$, [N]	$\sum F_x$, [N]	δ
experimental	19.3	131.7	19.8	130.6	8.6°
numerical	19.71	130.31	20.04	130.981	8.7°

The measured force data is given in table 6.3. It can be noticed that axial contribution to the global axial force from the secondary injection is rather minimal in this case. The agreement of the experimental and numerically obtained forces was found satisfactory enough and allowed further numerical investigation of an angular attitude effect on the SITVC nozzles.

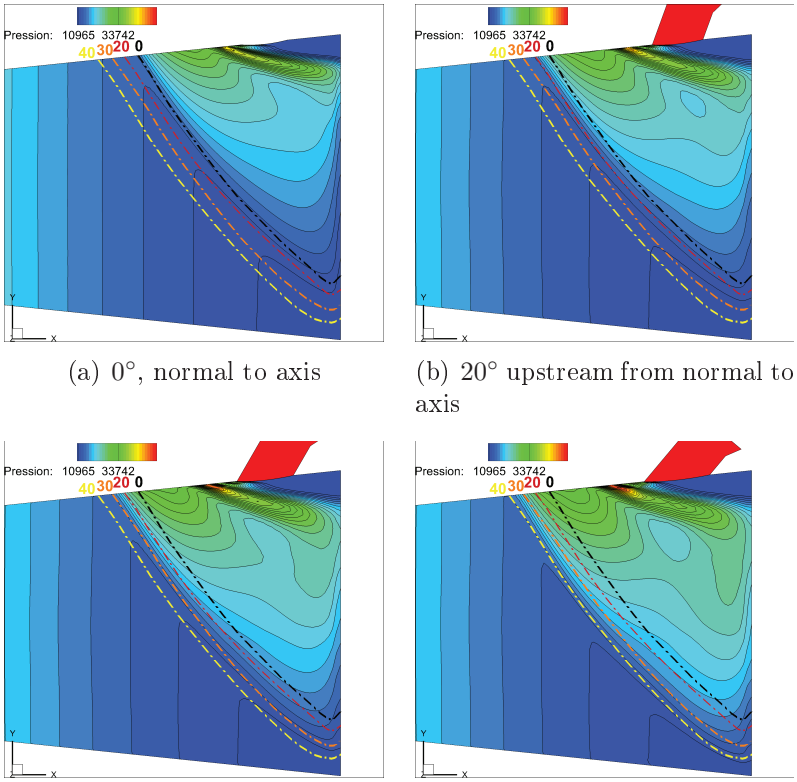

(a) 0°, normal to axis

(b) 20° upstream from normal to axis

(c) 30° upstream from normal to axis

(d) 40° upstream from normal to axis

Figure 6.16: Wall-pressure and separation delineation along wall of conical $Mach3$ nozzle with injection at $x_j/l_n = 0.9$, $SPR = 1$, $NPR = 37$ and various inclination angles of secondary injection

6.3.2 Upstream inclined secondary injection thrust vector control performance analysis

The upstream inclination is further numerically investigated with the previous conical and TIC nozzle models and confronted to the results of a secondary transverse injection normal to the main nozzle axis. The separation delineation along the nozzle wall represented in Figure 6.16 depicts the evolution of separation related to an increase of injector upstream inclination. In presented pressure contours, it can be observed that with each inclination step, the zone originating laterally from the incipient separation, increases the pressure imposed on the wall. The separation increase can be furthered followed in the pressure profiles in

Figure 6.17. The separation and pressure inside the separation zones scaled-up

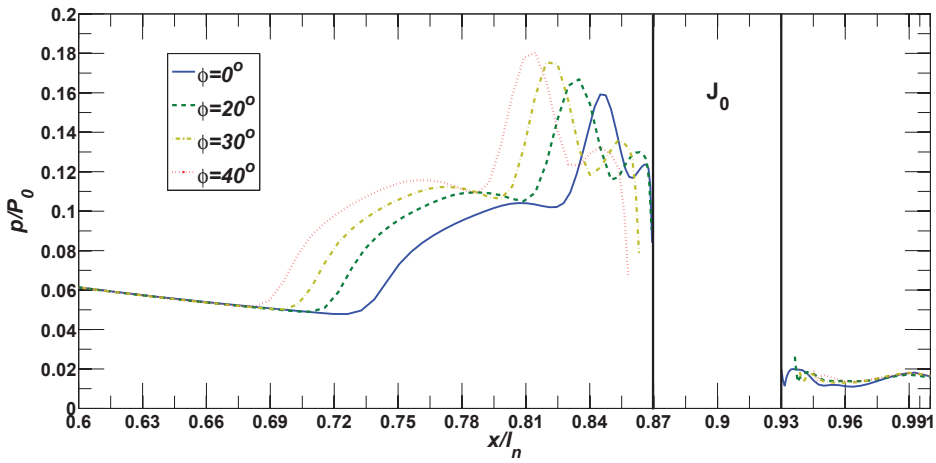

Figure 6.17: Wall-pressure profiles of $x_j/l_n = 0.9$ SITVC conical nozzles and various inclination angles, φ

with the each consecutive inclination step.

Similarly to the conical nozzle tests, TIC nozzle with the selected injection position, $x_j/l_n = 0.882$ was analyzed for several inclination angles relative to the main axis normal, up to $\varphi = 70°$. Analogously, gradual growth of the separation was detected with the upstream inclination increment. However, with inclination steps larger than $\varphi = 40°$ produced flow field becomes largely deviated and more complex. Namely, largely stretched injection port along with the elongation of windward side and shortening of the leeward side generates a highly variable profile at the secondary injection port. The flow in the zone closer to windward side is largely expanded with a substantially lower pressure than the core flow placed closer to the leeward side. The pressure value appears lower than the pressure at the peak zones at the wall separated region. This implies that some of the pressurized gas in this zone escapes through the large aspiration interface but some also towards the low pressure of injection port. Furthermore, the interface between the laterally developed primary, PUV zone, and the secondary zone moves backwards and towards the port. This action leaves an enlarged secondary high pressure zone which evolves laterally while the backwards movent of interface between these two zones generates inflection region on the separation line, as depicted in Figure 6.18(b). These combined effects lead to an unstable

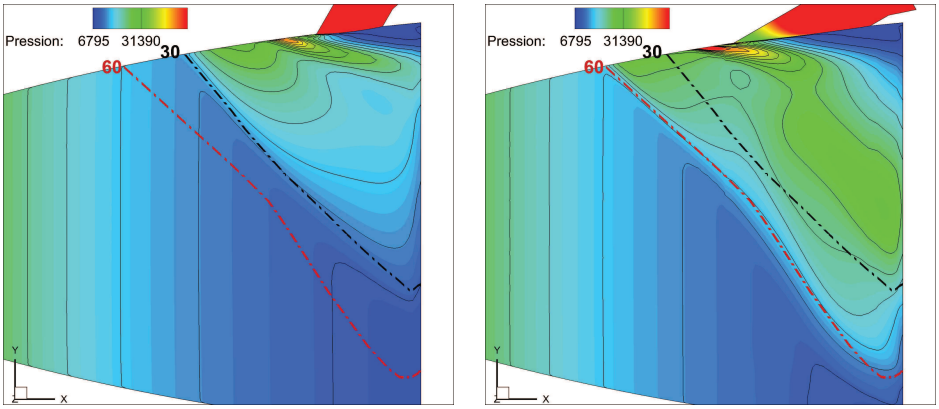

(a) $\varphi = 30°$ (b) $\varphi = 60°$

Figure 6.18: Wall-pressure and separation delineation along wall of TIC nozzle with upstream inclined injection at $x_j/l_n = 0.88$, $SPR = 1$, $NPR = 37$

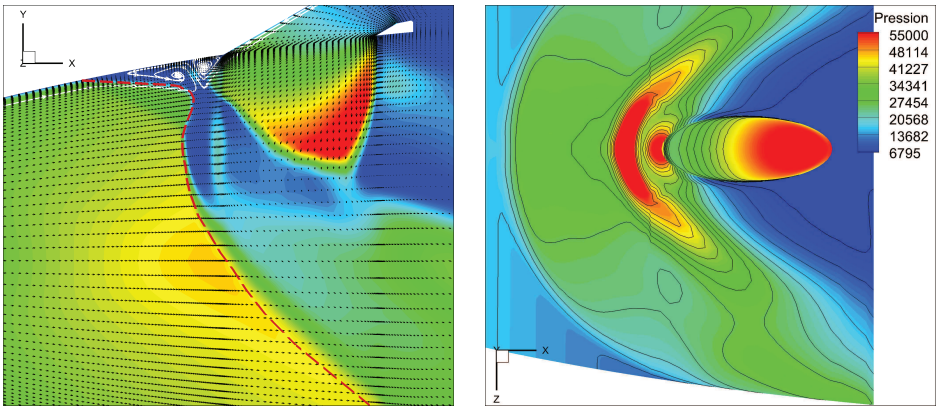

(a) Symmetry plane *Mach* and velocity-vector field

(b) Wall and injection port pressure contours

Figure 6.19: Contour plots of TIC nozzle with $\varphi = 60°$ upstream inclined injection at $x_j/l_n = 0.88$, $SPR = 1$, $NPR = 37.5$

and complex flowfield.

In Figure 6.20 it can be observed that for $\varphi = 60°$ primary and secondary pressure peaks are in the range of maximum pressure at injection port. The secondary peak approaches closely the secondary port windward edge and after it decays rapidly inside the port. The action of the low pressure region inside the injection port with vortices produces an unsteady action of the interaction field appearing in the form of flapping inside the separation zone. This can be observed by

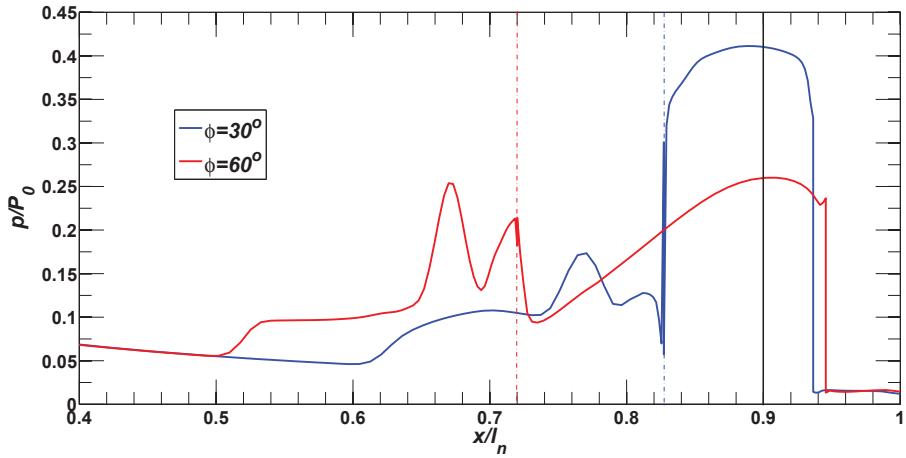

Figure 6.20: Pressure profiles of wall and injection port in symmetry plane for $x_j/l_n = 0.88$ SITVC TIC nozzle

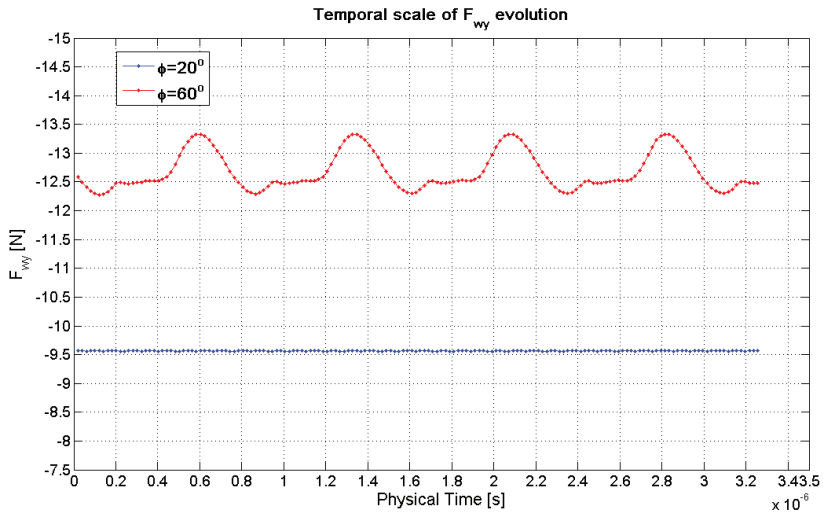

Figure 6.21: Interaction - wall side force temporal evolution for $x_j/l_n = 0.88$ SITVC TIC nozzle and 2 inclination cases

probing the interaction wall side force during the simulation. As depicted in Figure 6.21, there is a substantial and non-negligible increase in oscillatory amplitude behavior of the interaction force component with the higher injection inclination angles. However, using the available RANS approach inclination caused instabilities were not further investigated in this study. $k - \varepsilon$ turbulence production terms of energy and dissipation in Figure 6.22 depict the concentration in the

Table 6.4: Numerically evaluated force components for $x_j/l_n = 0.9$ conical nozzle

Conical $x_j/l_n = 0.9$ nozzle:						
Case	F_{jy}, [N]	F_{wy}, [N]	$\sum F_y$, [N]	F_{xj}, [N]	F_x, [N]	$\sum F_x$, [N]
$\varphi = 0°$	9.94	8.67	18.61	-0.217	127.99	127.77
$\varphi = 20°$	10.03	10.28	20.31	-0.63	126.931	126.301
$\varphi = 30°$	10.02	10.98	21.	-1.84	126.143	124.303
$\varphi = 40°$	10.05	11.42	21.47	-3.41	125.462	122.055
$^*NPR = 37, SPR = 1, f_m = 0.083, F_0 = 126.41N, I^0_{sp} = 57.77s$						
TIC $x_j/l_n = 0.88$ nozzle:						
$\varphi = 0°$	10.20	7.71	17.72	-0.197	136.427	136.23
$\varphi = 20°$	10.22	9.61	19.83	-0.56	135.23	134.67
$\varphi = 30°$	10.03	10.39	20.42	-1.81	134.1	132.24
$\varphi = 40°$	10.05	10.81	20.86	-3.5	133.37	129.87
$\varphi = 50°$	10.14	11.48	21.62	-6.18	132.62	126.44
$\varphi = 60°$	10.19	12.52	22.71	-9.02	132.01	122.98
$^*NPR = 37.5, SPR = 1, f_m = 0.082, F_0 = 134.05N, I^0_{sp} = 57.88s$						
Performance data:						
case	$\delta, [°]$	h_j, mm	C_{AV}	C_{AF}	C_{AI}	
C.$\varphi = 0°$	8.27	5.47	0.995	1.021	0.939	
C.$\varphi = 20°$	9.13	6.43	1.088	1.011	0.933	
C.$\varphi = 30°$	9.59	7.40	1.143	0.997	0.92	
C.$\varphi = 40°$	9.97	7.91	1.188	0.98	0.904	
TIC$\varphi = 0°$	7.5	5.51	0.914	1.025	0.946	
TIC$\varphi = 20°$	8.38	6.78	1.011	1.015	0.938	
TIC$\varphi = 30°$	8.78	7.82	1.064	0.998	0.922	
TIC$\varphi = 40°$	9.13	8.36	1.113	0.981	0.906	
TIC$\varphi = 50°$	9.7	9.37	1.18	0.957	0.884	
TIC$\varphi = 60°$	10.46	10.38	1.272	0.932	0.861	

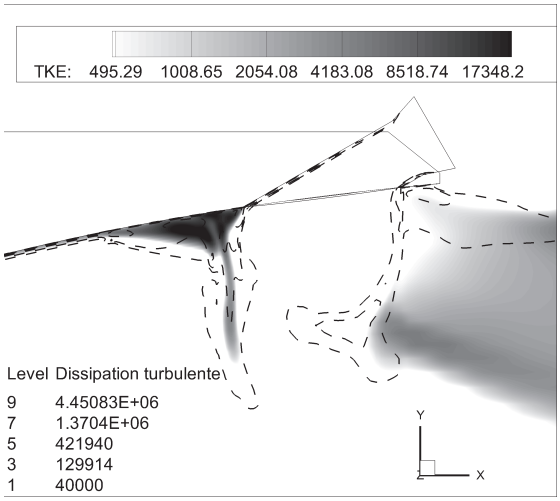

Figure 6.22: $k - \varepsilon$ Turbulence kinetic energy and dissipation in symmetry plane of the TIC nozzle $\varphi = 60°$ inclined injection case

boundary-layers, interaction interfaces and in downstream mixing zone. Turbulence dissipation peaks are naturally concentrated near the walls and especially at the sharp edged intersecting contours. Turbulence kinetic energy grows from BL inside the separation zone with counter-rotating vortex pair and in this case prolongs with a flange inside the shear interface formed between the main flow bow shock, compression waves and the secondary plume. It indicates a high exchange in this zone between the irregularly expanded secondary flow and the main flow trapped by the separation vortices. Naturally at the downstream portion, mixing process occurs followed by trailing kidney shaped vortices.

The forces evaluated from the investigated cases, indicated that the interaction side force component is directly related to the amount of inclination. In that terms, a breakdown point was not reached. However, angles larger than $\varphi > 40°$ gradually produce a very complex and deviated flowfield with detrimental effects on the other force components and nozzle stability. With an inclination, axial component of the reactive force was growing correspondingly in the opposite direction of the main thrust force. Furthermore, vertical reactive force component was decaying with deviation from the normal injection direction but for larger angles it was compensated with a larger separation. This coupled effect led to the fast decay of global force amplification, largely decreasing delivered axial force

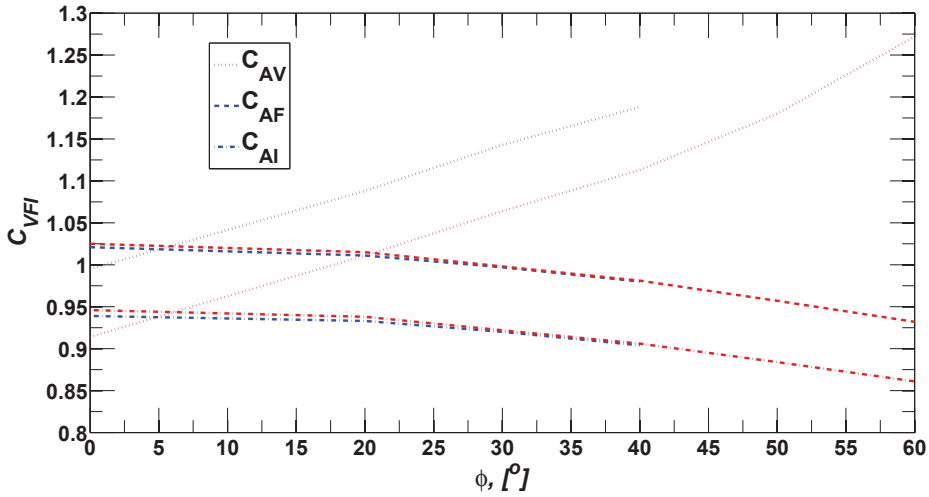

Figure 6.23: Performance coefficients versus inclination angles, *blue - conical nozzle, red - TIC nozzle*

and thus the global net force. Considering all occurring effects, it can be argued that optimal positive effects in terms of vectoring and nozzle performances are reached between $\varphi = 20°$ and $\varphi = 30°$. With regard to vectoring and global force and impulse amplification, the optimal inclination angle value for the selected TIC nozzle case was evaluated around $\varphi \approx 24°$.

The examined test cases showed the substantial effect of the injection angular attitude on the SITVC nozzle performances. Considering the previously investigated moderate effect of the secondary nozzle geometry, one can assume that further optimization may be achieved by combining these two parameters. For the selected position and predefined mass flow rate at SPR=1, optimal performances of the SITVC nozzle with single pneumatic actuator convergent nozzle can be reached with the upstream inclined slot geometry. Appraising the previous circular injector test cases, inclination angles of 20° to 65° were investigated. Using the same slot geometry as in Section 6.2 and changing upstream its attitude provides an increased blockage to the upstream separation. As a result of the smaller longitudinal width, b_j, intersection with the nozzle divergent wall section produces smaller deviation in longitudinal-axial direction. Therefore, it was possible to obtain less detrimental effects with higher inclination angles. In

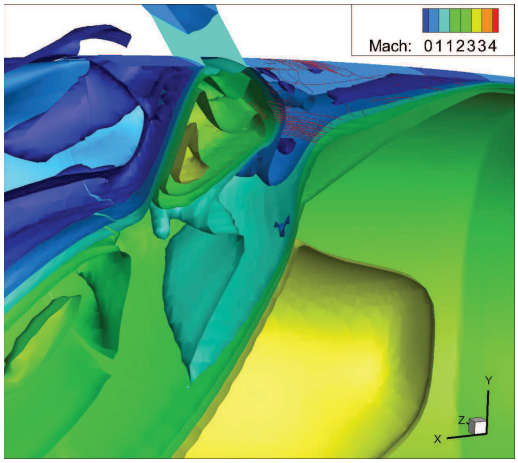

Figure 6.24: Mach iso-surfaces with turbulence-kinetic-energy evolution contours of the TIC nozzle $\varphi = 30°$ inclined slot injection case, $NPR = 37.5, SPR = 1$

the case of slot shaped inclined injection, nonconformity of the flow profile and an expansion are more pronounced at the lateral sides resulting in secondary plume deviation from the side, being pushed towards the center. Evaluated force and

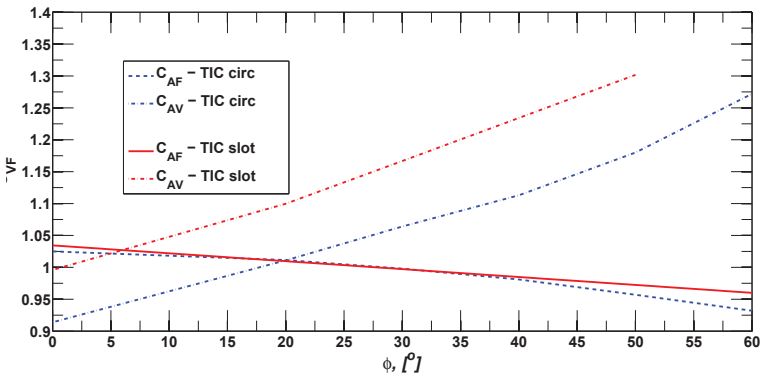

Figure 6.25: Performance coefficients versus inclination angles of circular and lot SITVC TOC nozzle case at, $SPR = 1, NPR = 37.5$

performance data indicate an analog behaviour with the circular injection. There is a slightly increased vectoring amplification evolution and a partially smaller decay of global force coefficient at higher inclination angles.

6.4 Secondary nozzle types and configurations

The experimentally and numerically investigated optimization parameters are complemented with numerically based analysis of secondary nozzle types and configuration which appear in number of previously referenced works.
In light of that, observing that expansion of the secondary jet affects the global parameters, convergent-divergent secondary nozzle type has been examined. In addition a multiport injection with meridional and radial distributions are investigated for potentially beneficial effects.

6.4.1 Convergent-Divergent secondary nozzle type

In the previous analysis it was found that a partially expanded secondary flow has some negative effects in terms of interaction component and global side force but it can increase the reactive force component. Mangin[38] assumed in conclusion that positive effects might be achieved by producing a secondary injection C-D nozzle with the exit conditions matching the ones at the plateau pressure zone. In addition to this assumption, in axisymmetric nozzle case, it was found that secondary pressure peak which is governed by SUV, has an important effect close to the injector port edge. In that light, two secondary conical nozzles with $P_{0j} = 300kPa$ and different expansion rates were tested. The first was with adapted pressure conditions above the pressure peak and the secondary with adapted conditions slightly above the plateau pressure value. The basic properties are given in Table 6.5.

Table 6.5: Basic 1D isentropic properties of secondary CD conical nozzle

NPR_j	$\sigma = A_{ej}/A_{tj}$	d_{jt}, mm	p_{ej}, kPa	T_j, K	l_{nj}, mm	$\alpha,^\circ$
5.1	1.358	6	58.8	280	5.6	5.2
8.64	1.78	6	38.4	280	6.3	8.1

Supersonically accelerated secondary injectant enters the main nozzle with naturally higher velocity and therefore momentum. In Figure 6.26(a) it can be identified that the supersonic secondary flow is still underexpanded going into

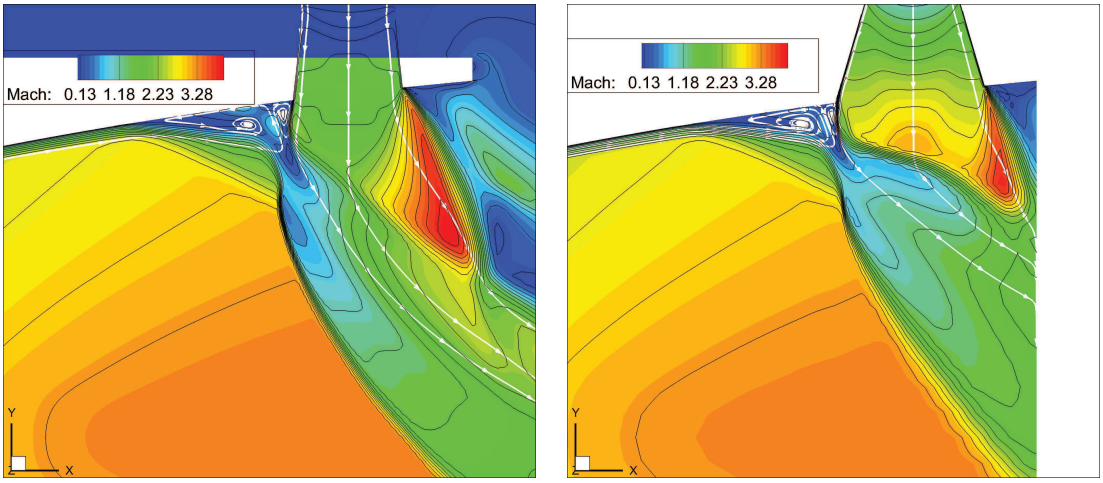

(a) Secondary C-D nozzle1 with smaller expansion

(b) Secondary C-D nozzle2

Figure 6.26: Mach number plot and contours in symmetry plane of TIC nozzle with supersonic secondary transverse injection

the smaller barrel shock expansion. However, underexpanded, accelerated and lower density injectant is susceptible to the pressure conditions in the main nozzle. Specifically, the higher pressure is imposed from the upstream interface region formed behind the bow shock, while at the downstream region low pressure region provides a relaxation to the secondary plume. This leads to the increase of interface between the main bow shock and the windward side of expanding secondary plume rapidly reaching the Mach disk. Additionally, the shape of the plume in interaction field is somewhat deviated from the sonic injection case. These effects are even more pronounced with the further acceleration of the secondary flow as depicted in Figure 6.26b. In this case the secondary nozzle is adapted to the plateau pressure and similarly to the high inclination case there is a sudden pressure drop from the pressure peak caused by the lower pressure of the injectant. As represented in Figure 6.27, the secondary peak moves towards the secondary plume and a pressure drop occurs at their interface allowing an amount of the flow particles to detach from the secondary plume and then to be pressurized inside the separation recirculation zone. In Figure 6.28 and previous contour plots, it can be observed that strong influence of the upstream high pressure coming from the separation and SUV deforms the secondary exhaust plume with an external

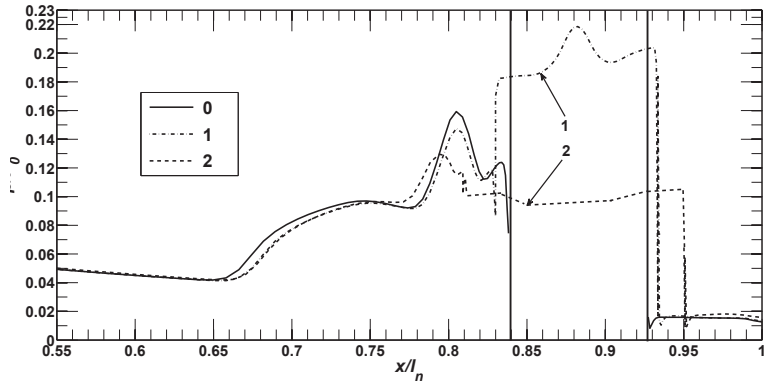

Figure 6.27: Pressure profiles in symmetry plane of TIC nozzle with sonic and supersonic secondary transverse injection cases at $SPR = 1, NPR = 37.5$

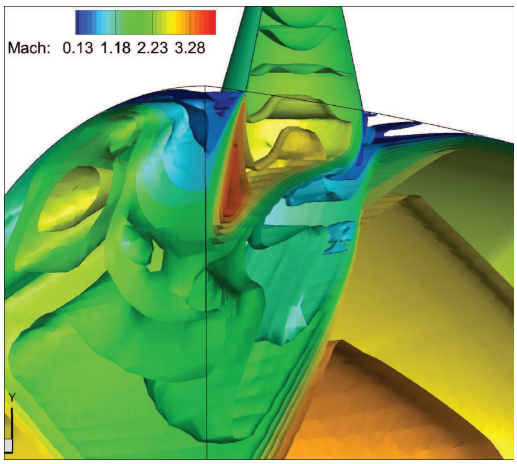

Figure 6.28: Iso-surfaces of secondary plateau pressure adapted supersonic M=2 injection into a TIC nozzle at $x_j/l_n = 0.88, SPR = 1, NPR = 37.5$

inflow to the core of the plume. This significantly affects the penetration or Mach disk height and consequently shortens the separation distance and amount of the interaction wall side force component.

Evaluated force data showed expected increase in the natural reactive force of the injectant and opposite, a decrease of the wall side force component. It can be also observed that reactive force component in x-direction is practically equal to zero. Effect on the penetration height is noticeable, with 10% decrease in the first case and 35% decrease in the second. Due to larger size of the leeward injectant plume side which allows a larger ambient inflow, there is a slight decrease in the

Table 6.6: Force component data and performance criteria

NPR_j	F_{jy}, [N]	F_{wy}, [N]	$\sum F_y$, [N]	F_{xj}, [N]	F_x, [N]	$\sum F_x$, [N]
5.1	11.09	6.871	17.961	−0.011	135.86	135.85
8.64	11.65	5.571	17.22	−0.009	133.03	133.02
$^*NPR = 37.5, SPR = 1, f_m = 0.082, F_0 = 134.05N, I^0_{sp} = 57.88s$						
Performance data:						
case NPR_j	$\delta, [°]$	h_j, mm	C_{AV}	C_{AF}	C_{AI}	
5.1	7.53	4.997	0.912	1.022	0.944	
8.64	7.36	3.548	0.892	0.999	0.923	

axial thrust force component.

Overall effects of the smaller supersonic secondary injection into divergent section of the main nozzle proved as a rather negative. There is a negligible improvement in the first case with a very small secondary expansion in the vectoring but equally negative in the global impulse amplification, while the secondary case and further increase of the injectant momentum yield largely detrimental effects.

6.4.2 Multiport injection pneumatic actuator

In the previous chapters and sections, a single transverse injection into the divergent section of an axisymmetric supersonic nozzle has been discussed over various fluid dynamics effects. Some of referenced investigations have also been concentrated on the multiport secondary injection thrust vectoring and its usefulness. Namely, for certain SITVC application, injection of a secondary fluid through the several holes grouped together at a divergent section region may provide a better control. Nielson *et al.*[50] and Wing and Giuliano[52] investigated several configurations and interrelated ports positions. While Nielson *et al.*[50] found multiport SITVC as a negative and completely disregarded it, Wing and Giuliano[52] reported a limited performance increase which was identified at its highs in the range of single port or slightly below. In that work, it was also reported that performance seams invariant of the experimented interrelated distances between the holes, with the used 3-port test rig. Similarly, earlier works reported by

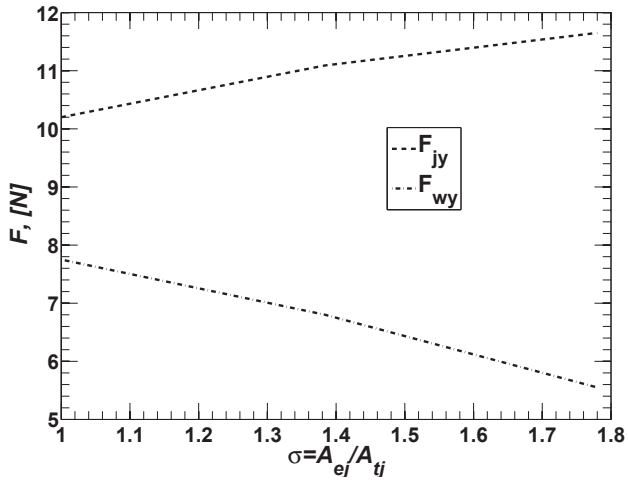

Figure 6.29: Side force components produced by sonic and supersonic secondary transverse injection cases into primary TIC nozzle at $x_j/l_n = 0.88, SPR = 1, NPR = 37.5$

McAuley and Pavli[49] and Hozaki *et al.*[53] reported analogue performances with the remark that multiport was less effective when placed close to the nozzle exit where single port was most effective. Considering associated data it can be said that multiport was not found as an effective solution for the low Mach number and short nozzles but can importantly improve the performance for a longer and large range rocket nozzle and where distant position from the exit is needed.

Having this in mind, standard multiport configurations have been numerically investigated on the longer TIC $Mach5$ nozzle and compared with the same net surface area single port. Reasoning from the physical point of view yields that energy transfer to the system via several small deliveries usually prevails over the instantaneous input. However, in the supersonic flow initial blockage governs the main flow supersonic response and further inputs into the system act over already disturbed flowfield.

Two configurations are taken into further investigation, a meridional, where injection holes are distributed along the same nozzle meridian and a radial one, at which the holes are distributed along the same nozzle parallel. Multiport is configured in that manner that holes lying on the same nozzle section circumference in respect to the central angle of $\theta = 30°$, meaning that each hole was at 15° from the adjacent one. The same distances were kept in the meridional distribution.

Three injectant ports are deigned having one third of the single port area using at the $SPR = 1$ conditions the same global secondary mass-flow-rate as the single injection.

6.4.2.1 Meridionally grouped multiport SITVC

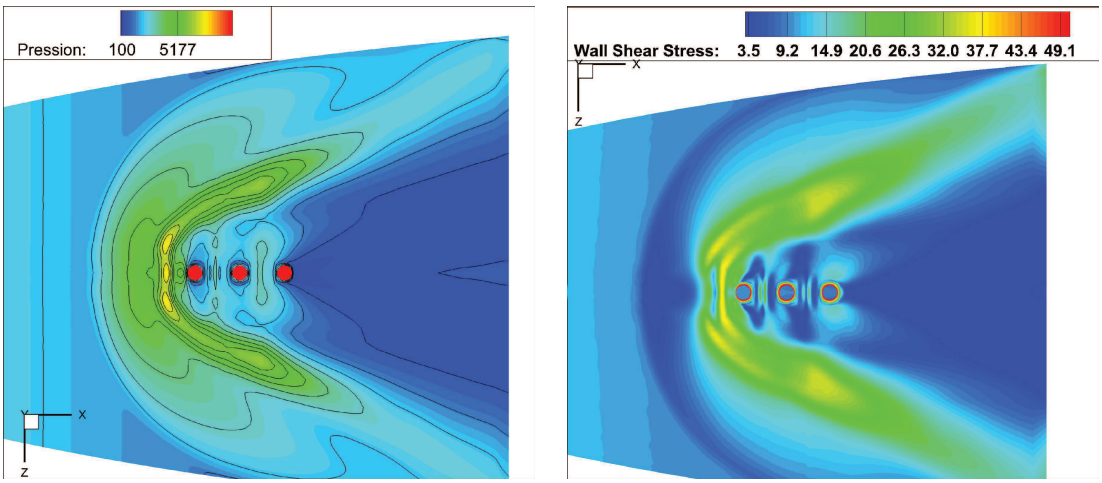

(a) Pressure contour plot (b) Wall shear stress magnitude

Figure 6.30: Meridionally grouped multiport SITVC, wall separation and interface zones

Following previously reported performance findings, multiport SITVC was centered at $x_j/l_n = 0.7$ nozzle section. Interaction and wave interference in axial direction are the main characteristics of the meridionally grouped multiport SITVC. Namely, the first transverse plume in the upstream direction initializes the main flow bow shock and a consequent upstream separation which imposes high pressure on its windward side. On its leeward side, naturally a low pressure imposes a pulling action on the underexpanded plume towards the wall but in this case, a second transverse plume prevents it by acting with a high pressure on the first plume. Analogously, the first acts on the second protecting it from the bow shock and enabling a higher penetration of the plume. Finally the third injection has the largest pressure relief on its windward side penetrating more in y-direction before it is bent towards the downstream wall portion enclosing the combined secondary plume obstruction in the main flow. Entropy produc-

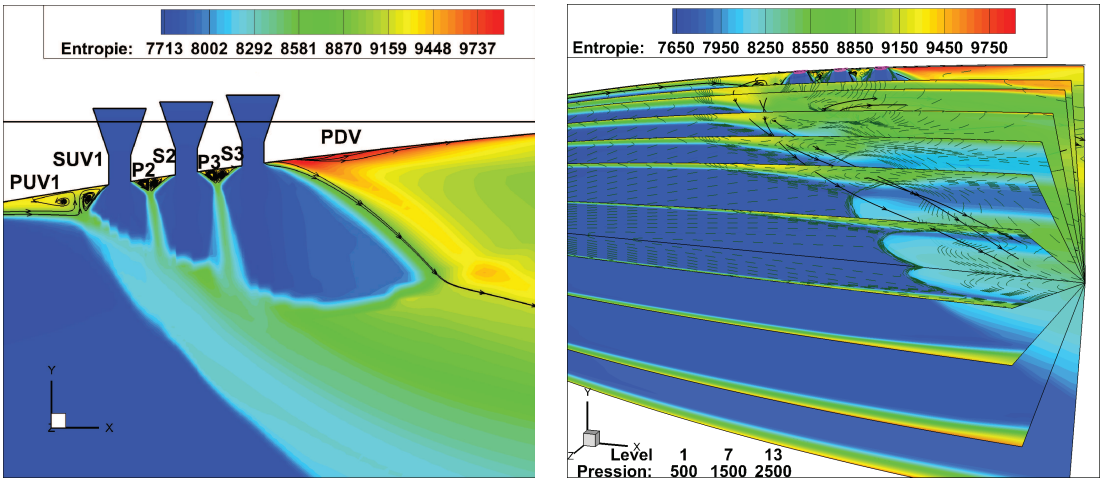

(a) Symmetry plane contour plot with stream-traces

(b) Radially extracted planes

Figure 6.31: Meridionally grouped multiport SITVC, entropy plots depicting separation interaction evolution and dissipation, $[J/K]$

tion shown in Figure 6.31 is pronounced in the near wall separated regions with increased turbulent production and separation which is then dissipated laterally. Downstream of the last injector strong diffusion and mixing of the secondary jets take place accelerating and increasing the exchange with the main flow, depicted as an entropy trail. In the combined transverse plumes zone, between the interfaces and the wall, recirculation regions including the counter-rotating vortex pairs are generated. The portion of the flow from the ports is compressed and aspirated at this zone with flow particles being ejected laterally from the short vorticity zone into the mixed secondary flowfield towards the nozzle exit. Flow inside the primary separation zone is forwarded wider laterally through the horseshoe vortex, defining the main flow separation. Multiport injection produces an additionally very complex flowfield with a multiple shock interaction system. The underexpanded barrel shocks of the multiport plumes interact in axial downstream direction forcing the expansion core of the transverse plumes to move axially and laterally from the symmetry as in Figure 6.32(a). At the bottom side of combined secondary flows, interface is formed between the main flow bow shock surface and the plumes. This interface appears highly perturbed by the secondary flows changes in compression sequences with assumed possible

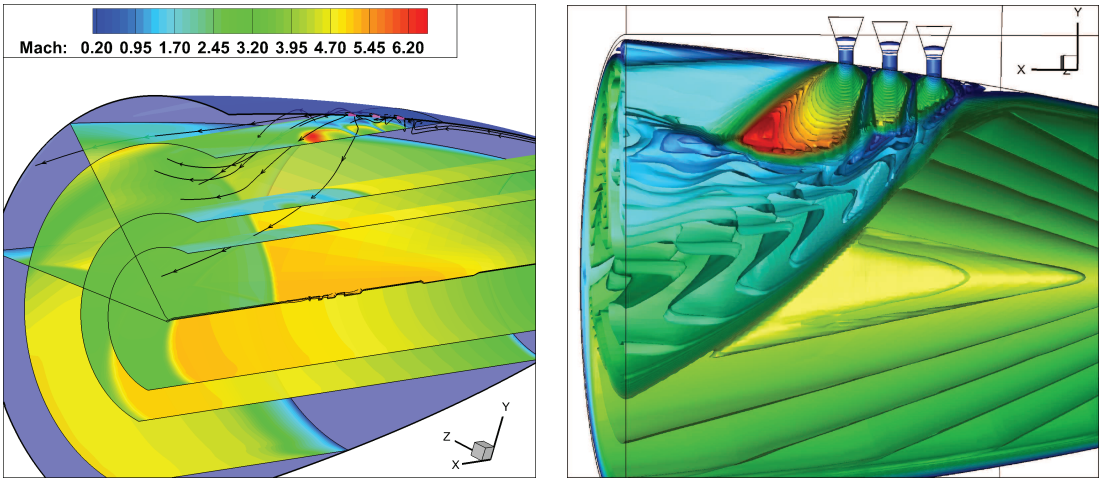

(a) Radially extracted shells and slices (b) 3D iso-surfaces

Figure 6.32: Meridionally grouped multiport SITVC, 3D Mach number plots

instabilities developing downstream. Internal surface of the interface divided into two regions, defined by the primary and secondary upstream vortex propagation, is mainly affected by multiport in the secondary region. SUV approaches closely the transverse plume and develops accordingly, enveloped by the highly perturbed secondary flow.

6.4.2.2 Radially grouped multiport SITVC

Radial distribution of multiport injectors affects the flow similarly to the previously analyzed slot injection case. Therefore, the separation appears over a wide front with pronounced lateral development. Additionally, there are effects produced by internal interaction in the secondary flow zone by multiport injections. Wide front detaches the flow at the far lateral sides and at downstream it develops along the walls in radial direction as depicted in yz planes in Figure 6.33. In the secondary flow zone, central port is sandwiched between the two side ports. Its barrel shock propagation is concentrated towards the main axis and ends with a flat head Mach disk. Plumes of the side ports are oriented towards the axis as well, but there is also a portion at outer side which is free to propagate into a low pressure of laterally detached flow. Compressed separated flow is aspirated through the interface between main shock - secondary plume, and also in this

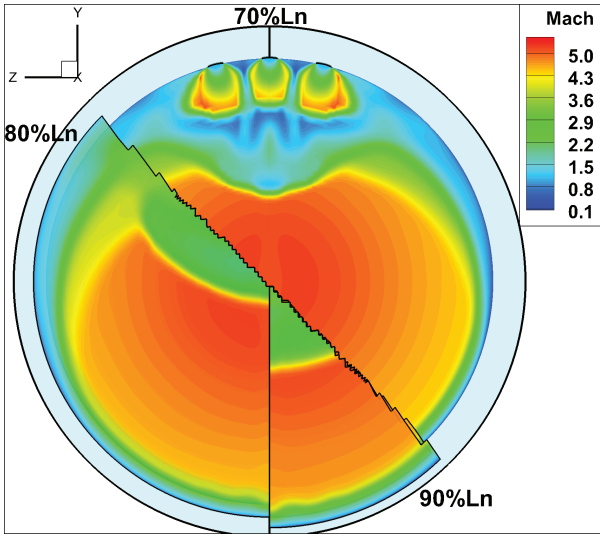

Figure 6.33: Mach number plot at yz planes from the injection section towards the exit

case in-between the ports of the multiport system. This generates multiple vortex zones shedding at the downstream wall section with the consequent increase in turbulent energy production as depicted in the contours of Figure 6.34(b). From the upstream side, oncoming main flow incipient separation occurs facing the central port with an almost flat surface. In-between the injection ports, footprints of developing local vortices can be identified in Figure 6.34. Contrary to the meridional case, there is no multiple separation induced small recirculation zones but rather a main upstream recirculation that propagates widely in lateral direction. 3D horseshoe vortex zone developing laterally from the symmetry section and wrapping around the whole secondary flow affected zone is observable in velocity streamlines and wall shear stress modulus plots. In the downstream region of presented figure, a strong and large wake zone can be identified which is characterized by the strong main vortex at the symmetry plane.

Comparing the pressure profiles given for the symmetry upper wall section, it can be deduced that radially distributed multiport injection yields a notable increase in separation distance, size of the PUV and SUV governed plateau and the pressure peak. Longitudinal multiport group gives an equal or negligibly lower separation distance than the single port case. Obtained plateau and pressure

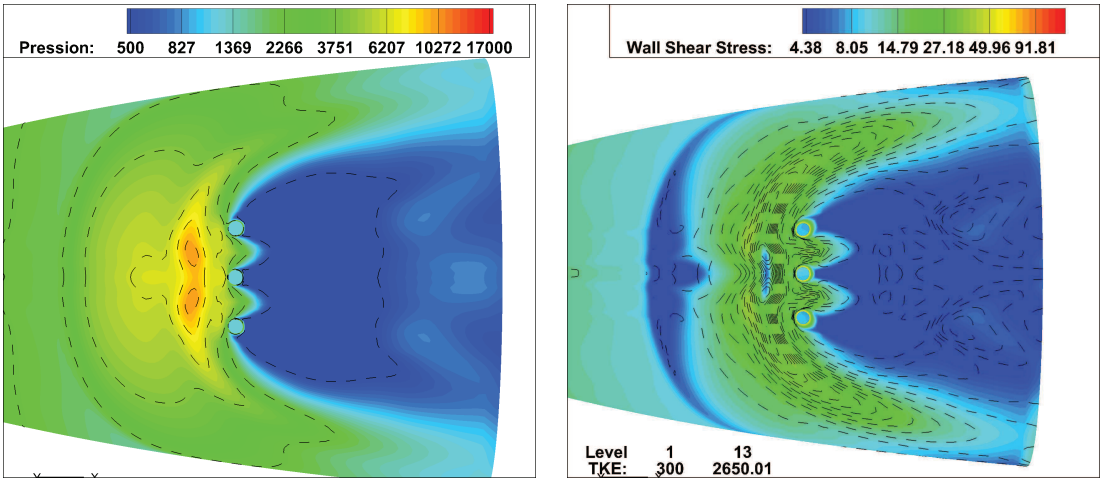

(a) Pressure contour plot (b) Wall shear stress magnitude

Figure 6.34: Radially grouped multiport SITVC, wall separation and interface zones

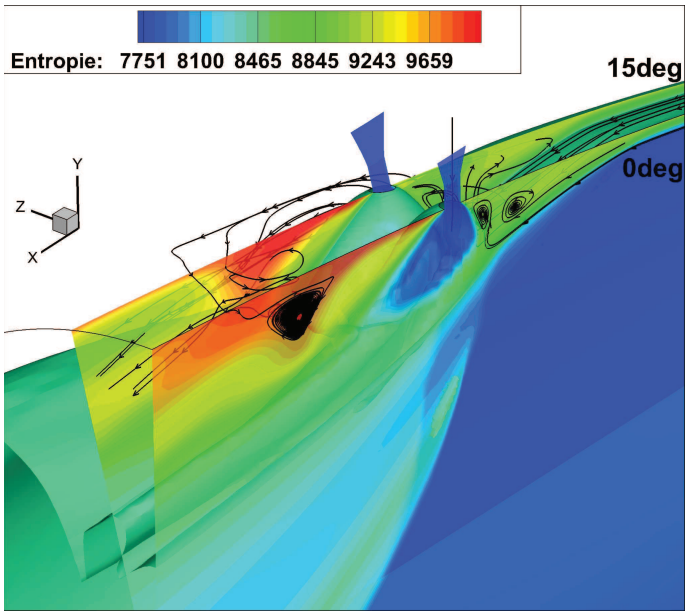

Figure 6.35: Radially extracted entropy plots with leading iso-surface and velocity vector streamlines

peaks, in this case, are lower but they are accompanied by the smaller secondary and third pressure increase zones between the meridionally placed injection ports.

Tabulated force and performance data in Table 6.8 corresponds to the pressure

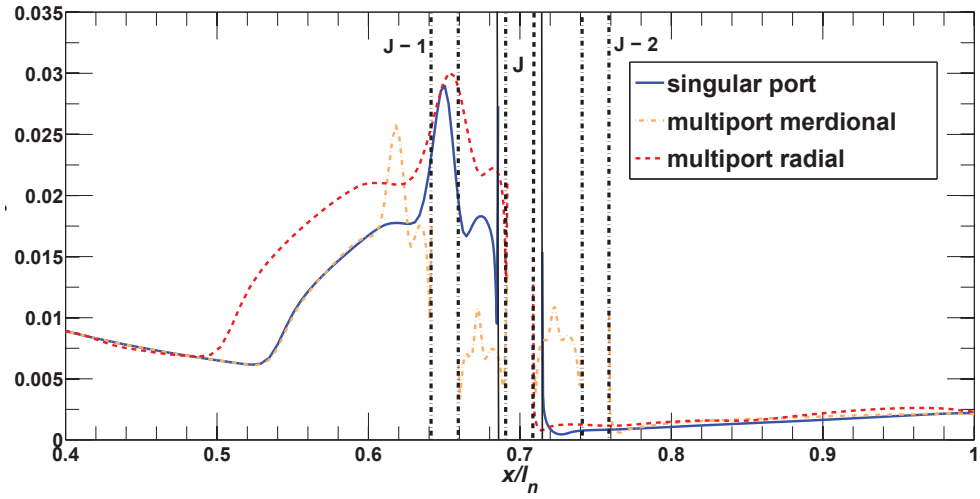

Figure 6.36: Wall pressure profiles for single and multiport radially and meridionally grouped injection into primary TIC nozzle at $x_j/l_n = 0.7, SPR = 1, NPR = 450$

Table 6.7: Design characteristics and flow conditions of multiport nozzles

$nozzle$	m_j	d_{jt}, mm	p_{ej}, kPa	T_j, K	$x/l_n, mm$	$\theta,^\circ$
$J-1L$	5.89	3.35	1.452	280	0.65	0
$J-0L$	5.85	3.35	1.199	280	0.7	0
$J-2L$	5.79	3.35	0.92	280	0.75	0
$J-0R$	5.85	3.35	1.199	280	0.7	0
$J-12R$	5.87	3.35	1.199	280	0.7	± 15

$^*L - longitudional, R - radial$

profiles and indicate a very close side force and amplification factor values. However, there is some negligible gain in the case of radial multiport SITVC while the meridional multiport SITVC appears with a slightly lower performance. Interaction or wall side force component follows the global trend and it is around 7% lower for the meridional multiport SITVC than the radial. Reactive force components are naturally close, with the very small difference due to an angular nozzle wall- injector position. It can be concluded that numerical simulation of the multiport SITVC cases yielded results that very well corresponded to the results obtained in different experimental investigations by referenced researchers.

Table 6.8: Unified force component data and performance criteria

case	F_{jy}, [N]	F_{wy}, [N]	$\sum F_y$, [N]	F_{xj}, [N]	F_x, [N]	$\sum F_x$, [N]
single	9.34	9.074	18.414	−0.847	155.55	154.71
multiportL	9.356	8.421	17.77	−0.82	155.19	154.37
multiportR	9.244	9.23	18.474	−0.941	156.09	155.14

$^*NPR = 450, SPR = 1, f_m = 0.076, F_0 = 152.7N, I^0_{sp} = 65.96s$

Performance data:					
case NPR_j	$\delta, [^\circ]$	x_{sep}/d_{j0}	C_{AV}	C_{AF}	C_{AI}
single	6.787	5.987	0.887	1.02	0.938
multiportL	6.566	5.97	0.865	1.018	0.936
multiportR	6.8	7.266	0.896	1.023	0.941

There is no real gain in terms of obtained force or vector angle by use of this kind of multiport SITVC system. However, the multiport system may be desirable from the structure and operation point of view and for the finer attitude corrections. In that light, similarly to mentioned previous works, radially grouped multiport SITVC proves as a best selection. It should be mentioned that the same $\theta = 30^\circ$ 3-holes multiport SITVC was implemented in ICBM *Minuteman* 2 rocket nozzle illustrated in Figure 1.5.

6.5 Concluding remarks

Cold flow investigation of secondary pneumatic nozzle, under static conditions, presented fluidical effects of various secondary nozzle types and configurations. It indicated possible optimizations in terms of the geometry and the resulting supersonic cross-flow effects.

Most influential in terms of performance gain and flow perturbation was the investigated angular attitude of the secondary injector. Even small changes in the injection angle are notable in terms of obtained side forces yielding positive effects with an upstream inclination. However, large upstream angles produce growing detrimental effects as the axial and injectant reactive force decay with further flow perturbation and assumably possible occurrence of the unsteady hysteresis

regimes. Optimal operation angles were evaluated around 25° upstream inclined from the normal to the primary nozzle axis.

Second to upstream inclined injection, increase in lateral separation by slot injection proved as a fairly well enhancement. The experimental investigation in this case led to an excellent agrement of the experiments and performed numerical simulations. Widening of the separation front yielded farther detachment point, along with the moderate and favorable increase in the interaction wall side force. Comparing the fluid effects, there was a slight improvement for the rounded rectangular slot, by eliminating the negative effects of concentration and shedding on sharp corners. Further optimization of the slot geometry supposedly would lead to the complex ellipsoidal shape.

Change of the sonic secondary injection to the supersonic one, proved as detrimental in the investigated cases and to further it is discarded. Smaller improvement in reactive force with the low supersonic nozzle lead to the growingly detrimental effects of interaction force decay and rise of the pressure imposed on the exhausting secondary supersonic jet. Further increase in secondary flow expansion lead to the complete deterioration of the secondary exhaust.

Multiport SITVC numerical investigation fall into previously referenced works on this point. Radially distributed, similarly to the slot injection proved to be a slightly better selection enabling the finer steering and eventually possible roll control.

Overall effects were very close to the single port case, without any major shifts in the performances.

Chapter 7

Gas properties effect, multispecies and hot-gas analysis

7.1 Basic introduction to gas properties analysis

In the reported cold flow dry-air investigations, nature of the interaction flowfield and its impact on the force generation and SITVC nozzle performances have been analyzed. These analysis were concentrated on the fluid dynamics mechanisms involved in the specifical supersonic nozzle cross-flows generated under various geometrical and flow conditions. In addition to the set flow type and conditions, the intrinsic properties of the specie are crucial to the supersonic cross-flow characteristics, as well.

Primary properties of the specie featured by the molecular weight and specific heats ratio represent essential thermodynamic aspects in the formation of the cross-flow fluid dynamics system. Next to this, quantities as the molecular viscosity and diffusivity influence the effects related to the viscous boundary layer, separation zones, shock interfaces and supersonic mixing processes.

In the current study, dry-air cold flow experiments were complemented with the different gasses secondary injectants as helium, argon and carbon-dioxide. These non-reacting and inert gaseous species were used as a secondary injectants to describe the effects of specie properties on SITVC system. Previously described and used measurement techniques as the parietal pressure mapping and force balance

acquisition are supported by the bi-color schlieren visualization. Bi-color schlieren is realized via dual slit red-green color filter and the two cutting edges in the focal plane, and is used to more easily identify the secondary flow plume. These experiments are supported and enhanced by the numerical simulations performed via multispecies compressible numerical solver of the CPS_C CFD code. Experimental and numerical tests are performed on the reported TIC $Mach$ 3 nozzle with the secondary transverse sonic injection through the circular $d_j = 5.8mm$ throat.

7.2 Model of species physical properties

Air was the principal gas in the previous mono-specie and the current bi-specie investigation. The injectant gases in the experiments are provided by $AirLiquide$® with certified properties. Species properties under test total conditions are given in Table 7.1. In the numerical and analytical investigation air is modeled as a

Table 7.1: Specie properties at $T_{0j} = 280K, P_{0j} = 300kPa$ conditions

specie	M_g [g/mol]	C_p [J/kgK]	R_g [J/kgK]	γ C_p/C_V	μ_M [kg/m·s]	λ [W/m·K]
Air	28.96015	1003.8844	287.102	1.4	1.779E-5	2.484E-2
He	4.0026	5192.86912	2077.265	1.66673	1.9021E-5	1.48869E-1
Ar	39.948	521.740582	208.132	1.66367	2.14E-5	1.672E-2
CO_2	44.0098	833.298	188.923	1.297	1.405E-5	1.53E-2

$^*Air = 78.084\%N_2 + 20.9476\%O_2 + 0.9365\%Ar + 0.0319\%CO_2$

four component gas mixture with its composition defined in standard atmosphere as:

$$78.084\%N_2 \;\; ; \;\; 20.9476\%O_2 \;\; ; \;\; 0.9365\%Ar \;\; ; \;\; 0.0319\%CO_2 \tag{7.1}$$

$$\overline{M_{air}} = \sum_{i=1} \chi_i \cdot M_i \tag{7.2}$$

where, χ_i represents the mole fractions of the components and M_i their molar masses. Furthermore, air composition properties are derived from the species molar properties respecting the above mentioned mole fractions in air mixture. Species data are collected from the Burcat and Ruscic[81] and McBride *et al.*[82] which also can be found in the American National Institute for Standards and Technology (NIST) reference data JANAF[83]. Very precise fitting for air mixture is provided by Lemmon *et al.*[80] with 2 degree temperature increments starting from $T_{i0} = 59.77K$.

All the gas species are considered as a thermally perfect gas which implies a non-reacting thermochemical equilibrium with internal energy, enthalpy and specific heats as the functions of temperature only. Only for the first initialization cases the gas was considered as a calorically perfect with constant specific heats ratio. Therefore, the physical properties of specific heat under constant pressure, vis-

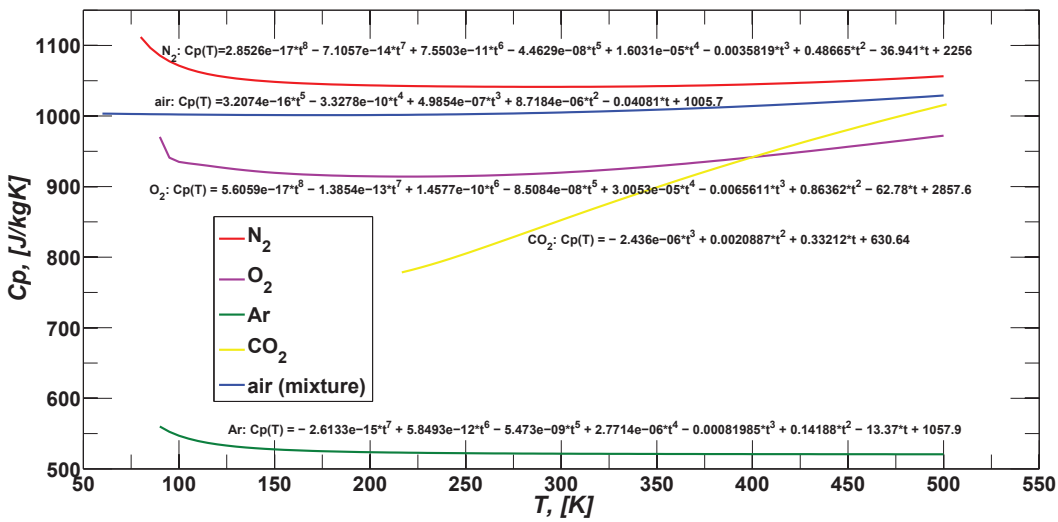

Figure 7.1: $C_p(T)$ for $60-500K$ temperature range of components and air mixture

cosity and thermal conductivity may be reasonably defined as the temperature dependent polynomial functions. As the gases are considered thermally perfect,

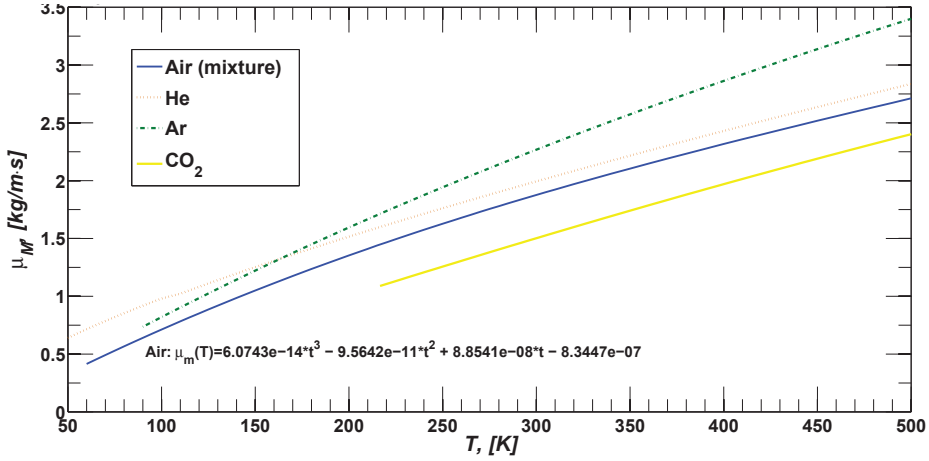

Figure 7.2: $\mu_M(T)$ for $60 - 500K$ temperature range of injectant species and air mixture

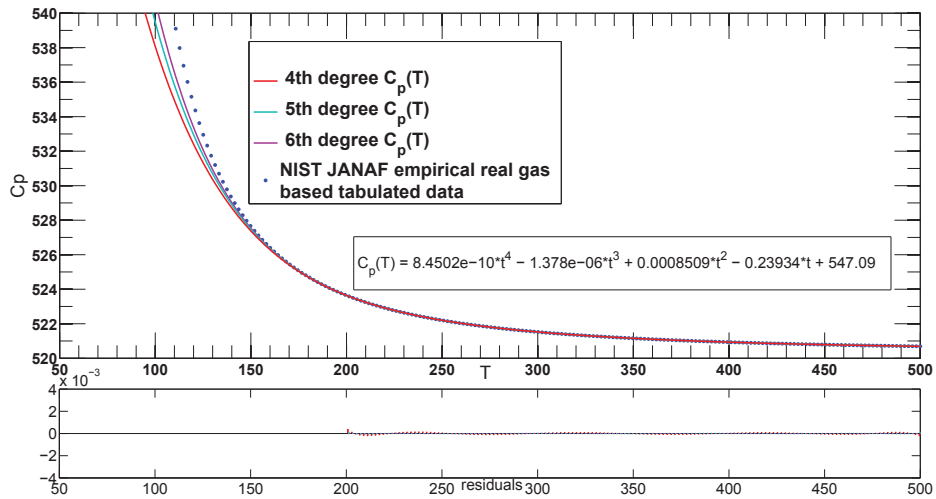

Figure 7.3: $C_p(T)$ for Argon with curve fitting polynomial functions

the Mayer's relation is valid, leading to:

$$C_p - C_V = R_g = \Re/M_g \tag{7.3}$$

$$\gamma = \frac{C_p}{C_V} = \frac{C_p}{C_p - R_g} \tag{7.4}$$

All physical properties were corresponding to Sandia Chemkin-II standard 7th degree polynomials and 80K to 1000K temperature range. Additionally, temperature range corresponding to the experimental criteria is established between 60K and 500K. Polynomial order is then reduced using a curve fitting for a given temperature range. The $\mu(T)$ and $\lambda(T)$, viscosity and thermal conductivity are derived as 2nd or 3rd degree polynomial temperature functions for all the species which reproduces a satisfactory definition. Specific heat, $C_p(T)$, was ranging between 4th and 7th degree polynomial depending on the specie tabulated data for a given temperature range, which in this cold flow study was $60 - 500K$. In a cold-flow based investigation, the temperature was constantly decreasing in experiments with referent total temperature evaluated as $T_0 = 255k$. Evaluated mean total temperature will produce a very low temperature value at the nozzle exit and in a plume expansion in exterior domain, ranging low as $70K$. This temperature values are very close to the certain species boiling point values which normally affects the polynomial curvature slope. However, polynomial curve fitting extrapolation provided fitted model for a whole temperature range.
In the previous cold-flow experiments conductivity was modeled via Prandtl number, $(Pr = C_p\mu/\lambda)$, representing constant ratio between the viscosity and the conductivity for the given conditions. To include species diffusion model, Schmidt number is varied for the same flow conditions. Diffusion coefficient is manually evaluated according to Chapman–Enskog theory and with tabulated Lennard-Jones potential collision integral and diameters, σ_{ij}^2, Ω_f.

$$Sc = \frac{\mu}{\rho\mathcal{D}} \tag{7.5}$$

$$\mathcal{D} = \frac{1.858 \cdot 10^{-3} T^{3/2}\sqrt{1/M_i + 1/M_j}}{p\sigma_{ij}^2\Omega_f} \tag{7.6}$$

Default value of $Sc = 0.75$ for oxygen in air diffusion represented a quite well approximation for cold-flow air calculations. Aforementioned, Sc derivation was applied with bi and multi-specie calculation. For a cold-flow condition, the change was very slight, $\sim 8\%$ as diffusivity coefficient changes with the pressure-temperature approximately as $\mathcal{D} \propto T^{3/2}/p$.

Mass-flow-rate and SPR

Change of the secondary injectant specie and thus the molar mass and specific heats ratio directly alters the injectant flow rate under the predefined geometry and total flow conditions. As analyzed in the previous chapters, these values indirectly affect the natural reactive force and the penetration height and therefore the separation distance and interaction wall side force. The mass-flow-rate, evaluated as the critical one in a sonic throat may be represented as:

$$\dot{m} = \rho_c a_c A_c \tag{7.7}$$

$$\dot{m} = \frac{\rho_c}{\rho_0}\frac{a_c}{a_0}\rho_0 a_0 A_c \tag{7.8}$$

Using the isentropic expansion relations above equation may be expressed as:

$$\overline{\dot{m}} = \left(\frac{\gamma+1}{2}\right)^{-\frac{\gamma+1}{2(\gamma-1)}} \cdot \frac{P_0}{R_g T_0} A_c \sqrt{\gamma R_g T_0} \tag{7.9}$$

$$\overline{\dot{m}} = \frac{\gamma}{\sqrt{\gamma-1}}\left(\frac{\gamma+1}{2}\right)^{-\frac{\gamma+1}{2(\gamma-1)}} \cdot \frac{P_0 A_c}{\sqrt{C_p T_0}} \tag{7.10}$$

Finally, by grouping the gamma expressions and using the thermally perfect gas relations ideal mass flow rate may be denoted in following way:

$$\psi(\gamma) = \gamma\left(\frac{\gamma+1}{2}\right)^{-\frac{\gamma+1}{2(\gamma-1)}} \tag{7.11}$$

$$\overline{\dot{m}} = \psi(\gamma) \cdot \frac{P_0 A_c}{\sqrt{\gamma R_g T_0}} \tag{7.12}$$

Ideal mass-flow-rate evaluated in aforementioned manner is used to obtain primary and secondary mass flow rates. Mass-flow-rate of the secondary injection, diagnosed via *Bronkhorst*® mass flow meter and via numerical simulations, is then divided with an ideal one to obtain secondary injection coefficient of discharge, C_{dj}. Mass-flow meter measures a calorically perfect gas with a constant C_p at given conditions. Further details are given in the experimental setup descrip-

Table 7.2: Isentropically evaluated mass-flow-rates and SPR for $d_j = 5.8mm$ circular sonic transverse port at $x_j/l_n = 0.88, T_{0j} = 283K$ of TIC nozzle

specie	M_g [g/mol]	γ C_p/C_V	$m_j(SPR = 1)$ [g/s]	$SPR(f_m = 0.076)$ P_{0j}/P_0
Air	28.96015	1.4	18.147	1.
He	4.0026	1.66673	7.1694	2.534
Ar	39.948	1.66367	22.635	0.803
CO_2	44.0098	1.297	21.826	0.833

$^*C_{dj} = 0.955$

tion and Appendix A.2. In general, coefficient of discharge depends on the specific values as the Reynolds number, flow velocity, friction level and geometry of the throat. The curvature of the throat was rather small but the convergent ratio between the secondary inlet and the throat section was small, as well. The numerical model had an identical geometry. Hence, due to a complex and threaded connection surfaces a slightly lower experimental discharge was registered. Total pressure and temperatures are measured at the mass-flow-meter section. These values are then used to determine the C_p value. The conversion factor, defined by Bronkhorst as $C_B = (C_{pn}\rho_n)/(C_{pb}\rho_b)$, is used then to evaluate normalized values to the real ones.

Mass flow rate of the secondary air injection was found $m_{jexp} = 18g/s \pm 1$ comparing to the numerical value, $m_j = 18.167$ and ideal of $\overline{m_j} = 18.987g/s$. Using these values it can be deduced that discharge coefficient ranges in a very narrow region between 0.951 and 0.96. Even though C_d depends on the flow specie, the $C_{dj} = 0.957$ obtained in the numerical air injection is the used as the referent one and inserted in Equation 7.12 to obtain mass flow rate ratios of other injectant species. Furthermore, for the same throat area and total temperature a pressure ratio between the air and the other species injection is evaluated in order to obtain the injection pressure rates at which the mass-flow rates are identical. These data is tabulated and presented in table 7.2.

$$\dot{m}_j = C_{dj} \cdot \psi(\gamma_j) \cdot \frac{P_{0j}A_{cj}}{\sqrt{\gamma R_{gj}T_{0j}}} \tag{7.13}$$

$$P_{0j} = P_{0a}\frac{\psi(\gamma_a)\sqrt{\gamma_j R_{gj}}}{\psi(\gamma_j)\sqrt{\gamma_a R_{ga}}} \tag{7.14}$$

7.3 Bi-species SITVC results discussion

Conducted experimental and numerical investigations on the bi-specie secondary injection TVC were performed on the nominal flow conditions, $NPR = 37.5, T_0 \sim 255K$, of the $x_j/l_n = 0.882$ and using the SITVC $Mach$ 3 TIC nozzle with SPR values fixed to unit or varied in order to impose the same mass-flow-rate condition. Similar to the previous analysis, the cross-flowfield is qualitatively examined using the schlieren visualization and color plots. The effects are then quantified via parietal pressure measurements and obtained force balance data.

7.3.1 Qualitative flow analysis of bi-specie injection case

The flow is visualized via bi-color Z-schlieren photography. In this case the exposure time of $CanonEOS$® 60D camera was increased, due to light filtering, from $1/4500s$ to $1/250s$, which may slightly reduce the sharpness. As the test-system was mounted on the oscillating force balance, only averaged states are considered and not unsteady ones.

The schlieren photos presented in Figure 7.4 depict the secondary injections of helium, argon and carbon-dioxide into main supersonic air stream at $SPR = 1$ condition. Naturally, mass flow rates are variable for different species under the same test conditions and these values are given in Table 7.2. The schlieren images of CO_2 and Ar are very similar, there is only a fairly noticeable visual change in the deflection and in the secondary plume penetration.

Observing the helium-air injection case, it can be noticed that the boundary line delineating the interfaces of a secondary plume and a primary bow shock is faded and color-mixed, both in numerical and experimental case. It also can be detected that the region of these interfaces is notably thicker suggesting that some mixing occur at formed layer in-between.

This is additionally supported in massic fractions surface plots in Figure 7.5. Principal mixing and mass transfer occurs in the vorticity zones and therefore presence of helium can be noted in region of these vortices; upstream recircu-

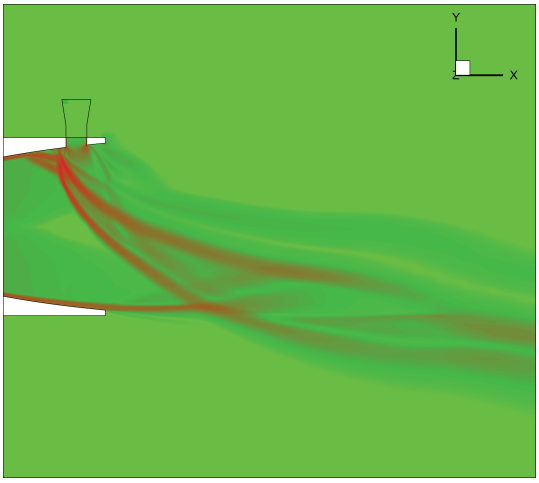

(a) $He - Air$ Numerical bi-color schlieren

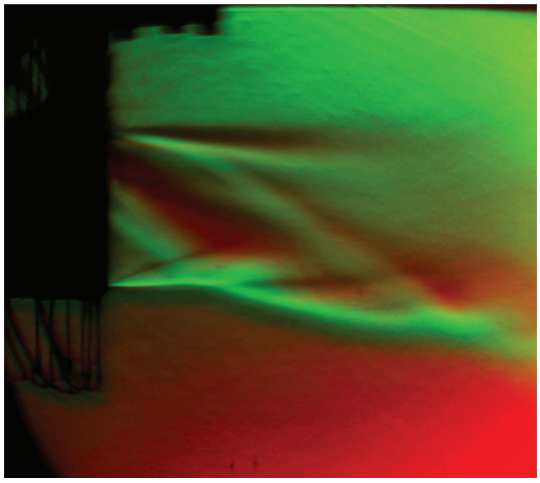

(b) $He - Air$ Experimental color Z-schlieren

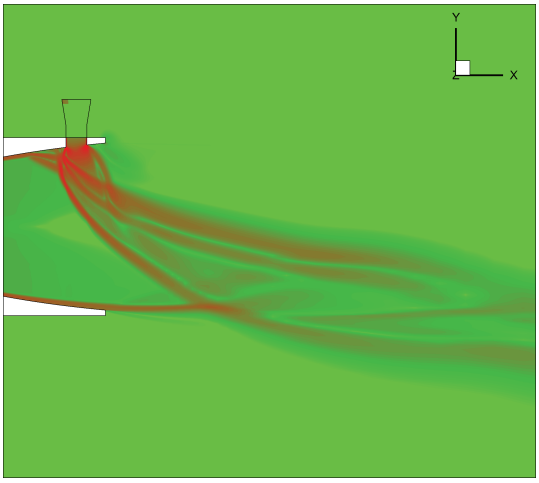

(c) $Ar - Air$ Numerical bi-color schlieren

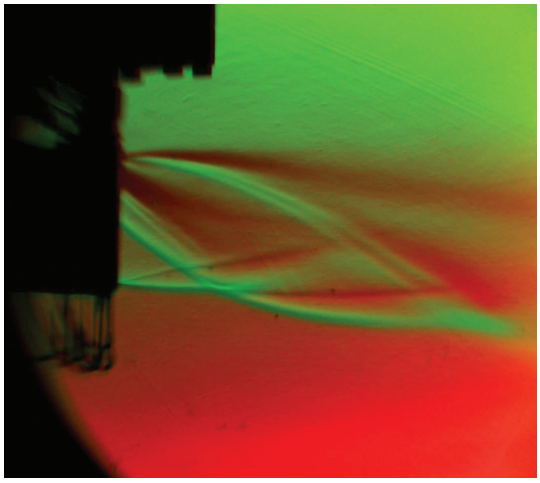

(d) $Ar - Air$ Experimental color Z-schlieren

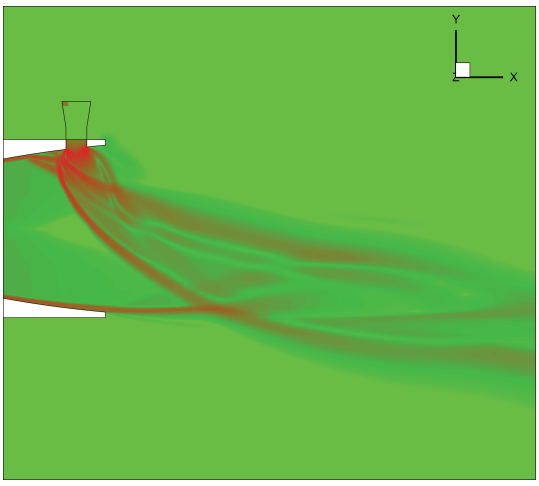

(e) $CO_2 - Air$ Numerical bi-color schlieren

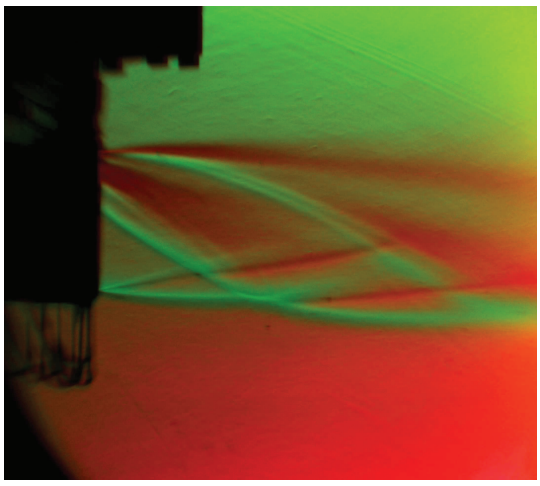

(f) $CO_2 - Air$ Experimental color Z-schlieren

Figure 7.4: Bi-color schlieren images of secondary gas transverse injection into primary nozzle supersonic air flow at $NPR = 37.5, SPR = 1$

lation, horseshoe vortex and main kidney-shaped trailing vortex. One can also

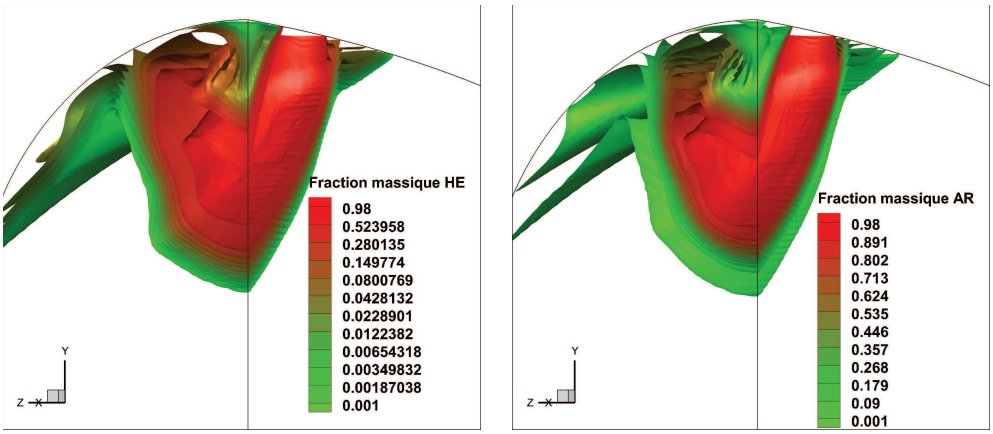

(a) He into air secondary injection (b) Ar into air secondary injection

Figure 7.5: Massic fractions surfaces of SITVC TIC nozzle at $x_j/l_n = 0.88$, $SPR = 1$, $NPR = 37.5$

detect a stronger influence of vorticity zones in He case, enabling He mixing in air in lateral direction. In this case, a strong, green colored, low injectant concentration interface appears diluted and gradually widens into the red colored higher concentration, which corresponds well to the obtained schlieren figures. This can be related to the fact that He injectant at this pressure conditions has a less mass flow rate and thus a less concentration with additionally altered Schmidt number. Additionally to the mass-flow-rate, correlation considering concentration and molar mass of species can be made. It is noticed that the injectant plume velocity affects the produced interaction force and thus the main flow deflection. Namely, as the tested species were inert non-reacting cold gases, their action principally depends on the injection velocity and the molar mass. In the case of helium, its $\sqrt{\gamma R_g T}$ sonic speed value is nearly one order greater than one of the argon or carbon-dioxide. This enables a high momentum and inertia even with the small mass rates and concentration which is of second importance in a shock dominated supersonic cross-flow. In Figure 7.6 this significant difference in the sidewise velocity can be detected. A strong shear layer interface is formed between the oppositely directed flows which increases vertical component of the main flow. It can be seen that this vertical velocity component increases also a spanwise lateral separation as a response to this action. The streamtraces illus-

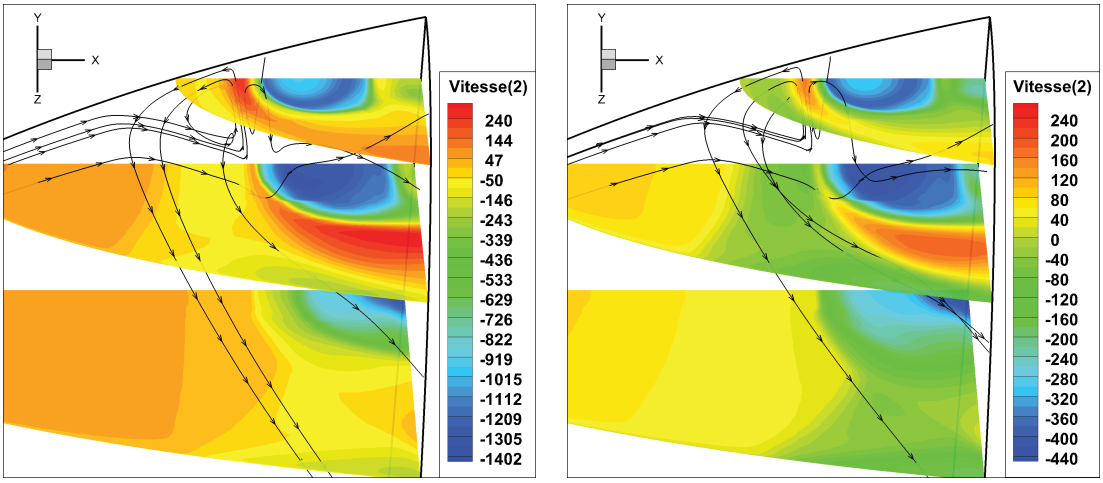

(a) He into air secondary injection (b) Ar into air secondary injection

Figure 7.6: Sidewise $y - direction$ velocity contour plots, $[m/s]$ at $y/y_e = 0.565, 0.913, 0.783$ extracted slices of SITVC TIC nozzle at $x_j/l_n = 0.88$, $SPR = 1$, $NPR = 37.5$. Streamtraces illustrate formed vortices

trate a backward movement of the recirculation zone in case of He injection. For

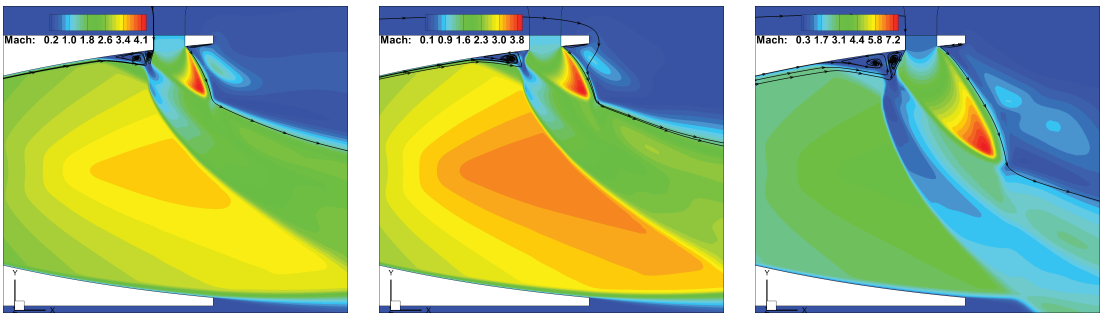

(a) Ar into air secondary injection (b) CO_2 into air secondary injection (c) He into air secondary injection

Figure 7.7: Mach contour plots in symmetry plane of SITVC TIC nozzle at $x_j/l_n = 0.88$, $f_m = 0.076$, $NPR = 37.5$

the case when the mass-flow rates are fixed to the referent one of $f_m = 0.076$ difference between the injection cases becomes larger. In Figure 7.7 Mach contours are shown for the symmetry plane of Ar, Co_2 and He secondary injection with SPR matching a fixed f_m, as given in Table 7.2. Helium injection under $761kPa$ increases injectant expansion velocity and penetrates deeply inside the main flow,

increasing the upstream and spanwise lateral separation. Accordingly, cases of CO_2 and Ar injection with corresponding secondary total pressures of $250kPa$ and $241kPa$, appear with the decreased penetration and shortened separation distances.

7.3.2 Quantified diagnostics via pressures, forces and performance data

Wall-pressure profiles in Figure 7.8 and 7.9 correspond completely to the presented flow visualization plots. Separation distance of He injection case for fixed

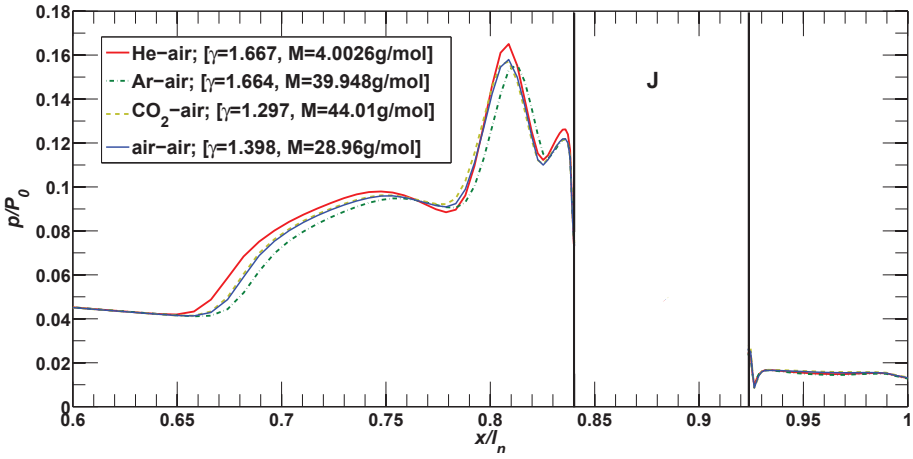

Figure 7.8: Wall-pressure profiles at injection side of symmetry of different secondary injectants into main air flow at fixed $SPR = 1$ and $NPR = 37.5$

$SPR = 1$, is larger for about $\sim 2\%$. This trend can also be noticed in the length of a pressure rise region, the plateau pressure zone and in the height of a pressure peak. On the lower end is the $Ar - air$ injection case which appears with separation length decreased for an approximately same amount as He increase, while the $CO_2 - air$ and $air - air$ injection were on closely the same cote. Observing the pressure profiles, a distinction between the cases according to the species molar mass and γ can be made, indicating that penetration and deflection increase with decreased values of these two physical properties. This observation is further confirmed in the wall-pressure plots for the fixed mass-flow rate, $f_m = 0.076$ in Figure 7.9. It is found that the ratio of injectant $\gamma_j M_{gj}$ product in the primary

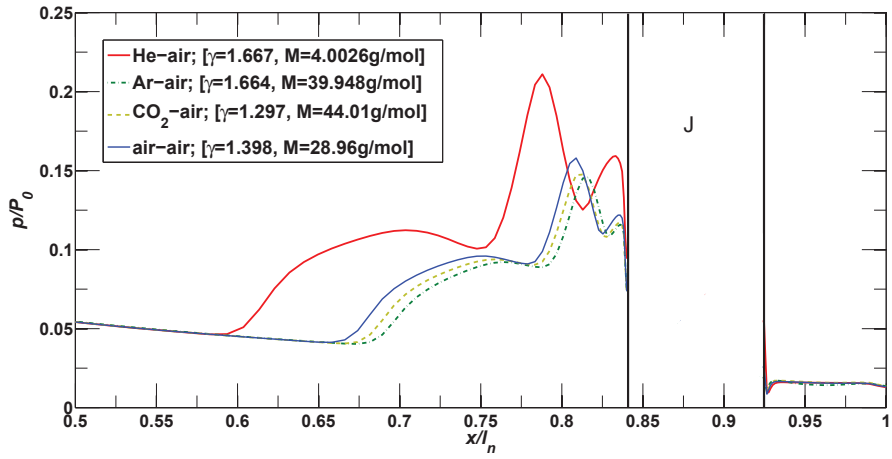

Figure 7.9: Wall-pressure profiles at injection side of symmetry of different secondary injectants into main air flow at fixed $f_m = 0.076$ and $NPR = 37.5$

one $\gamma_i M_{gi}$ is inversely proportional to the separation zone growth.

Forces and derived coefficient data are tabulated and given in Table 7.3. It can be denoted that both, reactive force injection component and the interaction-wall side force component augment with the decrease of γM_g ratio. Further to that, in the case of fixed $SPR = 1$ difference of produced thrust and side loads were in a very small range. However, by including the mass-flow-rate ratio criteria, vectoring and specific impulse amplification factors reveal the manifold difference between the low and high γM_g species. The smaller differences in obtained forces between the tested injectants species, are significantly magnified in the fixed mass-flow ratio $f_m = 0.076$ test case. In this case, obtained values of global specific amplification factor are very close for the 3 species. The cases with He injection, which has the γM_g factor at the lower limit, yields the oversized values comparing to the other analyzed species. In this case, pitch vector angle of 16.2° was achieved with the global side force of $\sim 40N$, or a bit lower than the one third of the axial thrust force. Both, reactive force of 2nd injection and the interaction wall side force increase. Higher weighted, CO_2 and Ar injectant species, with correspondingly lower injection pressures, yield the lower performance rates in terms of produced side forces and contribution in global thrust. The global vectoring and impulse amplification factor evolutions are in the same range. However, as remarked in the previous chapters, deflection rate favors higher pressure injection

Table 7.3: Evaluated force components for the $x_j/l_n = 0.88, NPR = 37.5$ TIC nozzle bi-specie SITVC

$SPR = 1$: Case	f_m	F_{jy}, [N]	F_{wy}, [N]	$\sum F_y$, [N]	$\sum F_x$, [N]	$\delta, [°]$
$air - air$	0.076	9.473	7.134	16.473	136.21	6.89
$He - air$	0.0303	9.551	7.407	16.958	136.13	7.10
$CO_2 - air$	0.092	9.302	7.313	16.615	136.22	6.95
$Ar - air$	0.096	9.576	6.559	16.135	135.97	6.76
$f_m = 0.076$ Case	SPR	F_{jy}, [N]	F_{wy}, [N]	$\sum F_y$, [N]	$\sum F_x$, [N]	$\delta, [°]$
$air - air$	1	9.473	7.134	16.473	136.21	6.89
$He - air$	2.534	24.279	14.972	39.251	135.11	16.20
$CO_2 - air$	0.833	7.713	6.254	13.967	135.946	5.87
$Ar - air$	0.803	7.636	5.426	13.062	135.682	5.49
Performance data: case	h_j, mm	l_{sep}/l_n	C_{AV}	C_{AF}	C_{AI}	
$SPR = 1$:						
$air - air$	5.514	15.708	0.904	1.024	0.952	
$He - air$	5.046	15.98	2.343	1.023	0.993	
$CO_2 - air$	5.482	15.71	0.753	1.023	0.937	
$Ar - air$	5.046	14.688	0.702	1.022	0.932	
$f_m = 0.076$:						
$air - air$	5.514	15.708	0.904	1.024	0.952	
$He - air$	8.964	19.653	2.124	1.049	0.975	
$CO_2 - air$	5.046	14.212	0.769	1.019	0.947	
$Ar - air$	4.582	13.804	0.719	1.017	0.945	

over the lower one. Global vectoring and specific impulse amplification versus γM_g ratio are plotted in Figures 7.10 and 7.11. It can be seen that values below the referent critical point of $\gamma_j M_{gj}/\gamma_i M_{gi}$ at unit value, significantly increase the performance rate. For the inert and heavier than main flow injectant species, performances curves decay.

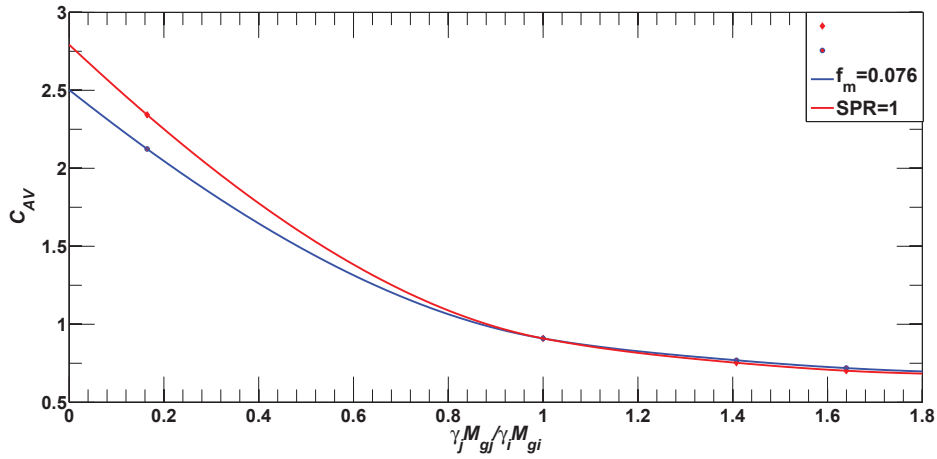

Figure 7.10: Vectoring amplification versus γM_g product ratio of injectant in the main flow

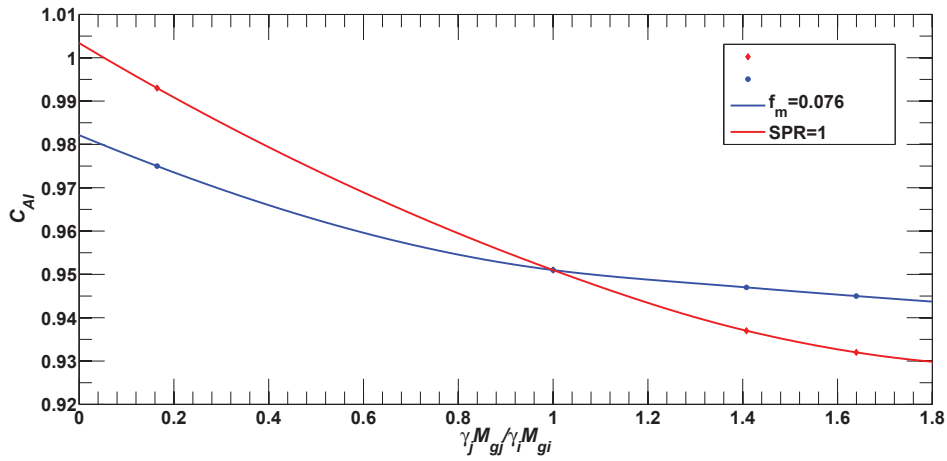

Figure 7.11: Specific impulse amplification versus γM_g product ratio of injectant in the main flow

7.4 Introduction to hot-gases analysis

Following the extensive research based on the monospecie air and after on bi-species cold-flow experiments, a numerical investigation on the combustion products under elevated temperature is conducted in order to simulate an intended use on the CNES *Perseus* aimed launcher with secondary injection thrust vector control. Two oxidizer-fuel pairs are considered, a liquid hydrogen fuel, $lH_2 - lO_X$ and liquid ethanol fuel, $C_2H_5OH - lO_X$. The first bi-propellant configuration was examined for elaboration and comparison with the contemporary launcher technologies while the second one was the option for the actual use in *Perseus* program. Thermochemical reaction processes inside the combustion chamber were calculated using NASA CEA2 code based on the NASA Glen[82] and NIST JANAF[83] thermodynamic polynomial coefficient tables. The computation code was able to solve infinite thermochemical equilibrium problem and the finite volume thermochemical kinetics for predefined geometry and combustion chamber inlet conditions. Total and static conditions at the combustion chamber exit were obtained for the inlet and the throat regions. These data were then used as the inlet conditions for 3D numerical CPS_C simulations on the combustion products considered as a frozen, non-reacting mixture under elevated temperature. Finally, the obtained data were compared to the cold-flow investigation and to the 1D numerical calculations based on the GRI-Mech 2.11 subsets and optimized non-equilibrium thermochemical kinetics reactions mechanism of ?].

7.5 Thermochemical equilibrium calculations of reactions in combustion chamber

In the current study, thermochemical equilibrium computations are performed on the reactions occurring inside the rocket combustion chamber. Combustion chamber can be modeled as an infinite area combustor or a finite area combustor with a constant cross-section. The infinite area combustor (IAC) assumes one combustion point cross-section of an infinite area to which the thermochemical equations are applied to and the corresponding nozzle sonic throat area. In the fi-

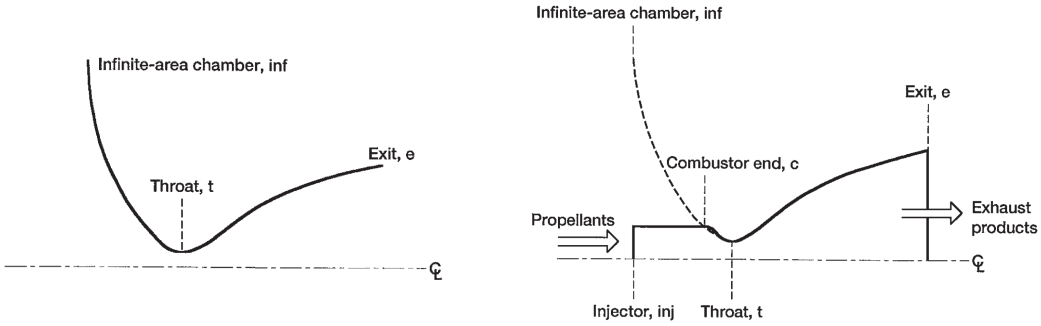

(a) Infinite combustor area (b) Finite combustor area

Figure 7.12: Scheme of rocket combustion chamber cross sections by Gordon and McBride[91]

nite combustor calculations, equations are set for the rocket combustion chamber inlet, combustion chamber end and an adequate nozzle throat sonic area. In the current cold-flow study, experimental nozzle was mounted on the settling chamber that was designed with a large cross section area and therefore an assumption of the infinite combustor equilibrium process is selected as an appropriate for further hot-gas simulations. This is also compared to the finite area rocket combustion chamber (FAC) calculation.

Chemical equilibrium can be defined either by equilibrium constants or by minimization of free enthalpy (Gibbs energy) which was used in Gordon and McBride[91] model. The IAC model procedure for obtaining equilibrium performance consists of determining first the combustion properties, then the exhaust properties at the throat and then all other assigned nozzle sections. The injector input conditions consist of specie reactants designation, weight percentage in the mixture, enthalpy (temperature) of reactants, chamber pressure, estimated temperature which is then recalculated and desired oxidant-fuel ratios. The stations at throat and the nozzle exit are defined with the area ratios A_c/A_t *and* A_t/A_e and/or with the pressure ratios for each section. IAC model assumes constant combustion entropy s_{inf} during isentropic expansion in the nozzle. However, for the FAC model, entropy is not constant during the combustion process but changes from s_{inj} to s_c with pressure change from P_{inj} to P_c. After combustion process equilibrium composition other stations are calculated for the nozzle isentropic expansion.

For the $C_2H_5OH - lO_X$ propellants, combustion chamber thermochemical re-

action calculations are iterated for the three elements $C\ H\ O$ and 58 obtained species. Combustion was simulated on the three oxidant to fuel mixture ratios $o/f = 1.2,\ 1.4,\ 1.5$, with mention that $o/f = 1.4$ is selected for the referent one. For the $lH_2 - lO_X$ the $o/f\ range : 4.,\ 5.,\ 6.$ where $o/f = 6.$ was selected for the referent oxidant to fuel ratio, even thought o/f 8 would be closer to the stoichiometric value. Nevertheless, oxidant/fuel ratios for both propellant configuration was close to stoichiometry and suited for equilibrium calculations. Reduced reaction mechanisms are simulated and final massic fractions of the species above $2E-06$ value in total share are considered. The combustion chamber results are given in Table 7.4 for $C_2H_5OH - lO_X$ and in Table 7.5 for $lH_2 - lO_X$.

Table 7.4: $C_2H_5OH - lO_X$, IAC chamber equilibrium thermochemical calculation

$o/f = 1.4$	injector(inf.)	combustion chamber	throat
$T\ (K)$	$o90.17/f293$	3106.10	2915.61
$\rho\ (kg/m^3)$	$o1145.4/f789$	1.6707	1.0300
$P\ (kPa)$	$2.E+03$	$2.E+03$	$1.1476E+03$
P_{inf}/P	1	1	1.7427
$u(m/s)$	0	1171.1	1133.0
$I^r_{sp}(m/s)$	0	1132.9	2176.2
$H(kJ/kg)$	/	-2751.73	-3393.51
$C_p(kJ/(kg \cdot K)$	/	4.4755	3.8492
γ	/	1.1457	1.1521
$Mass\ fractions :$			
	CO	0.34762	0.34053
	CO_2	0.24990	0.26104
	H	0.00080	0.00059
	HCO	0.00001	0.00000
	H_2	0.01178	0.01180
	H_2O	0.36665	0.37176
	O	0.00131	0.00063
	OH	0.01834	0.00178
	O_2	0.00359	0.00178

Table 7.5: $lH_2 - lO_X$, IAC Combustion chamber equilibrium thermochemical calculation

$o/f = 6.$	injector(inf.)	combustion chamber	throat
$T\ (K)$	$o90.17/f20.17$	3341.84	3174.83
$\rho\ (kg/m^3)$	$o1145.4/f73.364$	0.95518	0.58860
$P\ (kPa)$	$2.E+03$	$2.E+03$	$1.1563E+03$
P_{inf}/P	1	1	1.7296
$u(m/s)$	0	1539.6	1490.9
$I^r_{sp}(m/s)$	0	1490.9	2907.3
$H(kJ/kg)$	/	-986.31	-2097.71
$C_p(kJ/(kg \cdot K)$	/	10.8090	9.9370
γ	/	1.1321	1.1315
$Mass\ fractions:$			
	H	0.00344	0.00287
	H_2	0.03782	0.03686
	H_2O	0.87204	0.89323
	O	0.00635	0.00435
	OH	0.06766	0.05346
	O_2	0.01269	0.00922

7.6 1D & axisymmetric nozzle calculations

The combustion chamber thermochemical process results are used as an input for the nozzle flow simulations. Calculations are performed using a 1D code based on the subsets of the $GRI-Mech$ 2.11[92] reaction mechanisms for $O\ H\ C\ N\ Ar$ formation elements species. These 1D calculations considered 3 modeled approaches:

1. thermochemical equilibrium reactions
2. frozen species composition calculation
3. thermochemical reacting kinetics mechanism

Obtained, Chemkin-II formatted results, are analyzed and confronted to the 2D-axisymmetric simulation performed as a frozen composition using the CPS_C code. Both 1D codes, CEA2 code and $GRI - Mech$ 2.11 based calculation used CEA2 combustion chamber calculated conditions as a starting point. The static

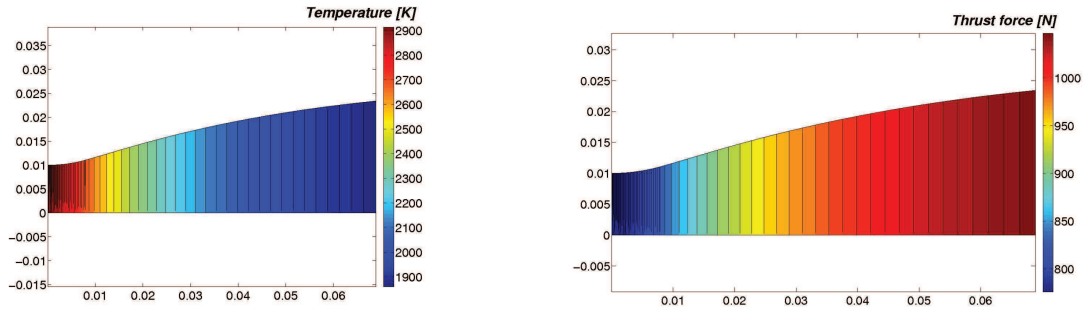

(a) Temperature evolution

(b) Thrust force at selected cross sections

Figure 7.13: 1D thermochem. equilibrium computations temperature and thrust force

conditions were the same in the throat, while a slight difference between the codes is observed due to the different thermodynamic data obtained from JANAF[83] NASA Glenn[82] or Sandia Chemkin Burcat and Ruscic[81]. For $C_2H_5OH - lO_X$ kinetics considered 5 formation elements, 32 species and 177 reactions and for $lH_2 - lO_X$ 10 species and 28 reactions. The properties of considered gas species and referent performance data as the thrust force and specific impulse are obtained and tabulated in Table 7.6 and Table 7.7. Force and specific impulse are given as the dynalpy flux and specific impulse in weightless ($g = 0$) state.

$$F_{th} = \dot{m} \cdot u + p \cdot A \tag{7.15}$$

$$I^r_{sp} = \frac{F_{th}}{\dot{m}} = u + \frac{pA}{\dot{m}} \tag{7.16}$$

The sonic velocity is calculated as $a = \sqrt{(\frac{dp}{d\rho})_S}$ under constant entropy and constant specie composition. What can be seen in result data is that section at point approximately $x = 0.5mm$ from the throat had the same mass-flow-rate and the same specific impulse in all calculation approaches. This section was considered as an initial point for frozen composition and reaction kinetics mechanism calculations. The equilibrium calculations implies infinitely slow reactions-rate but allowing composition change during the nozzle expansion, eg. when pressure is perturbed the gas properties are changed as well. The frozen calculation does not allow any composition change but keeping it freezed from the inlet to the exit. The corresponding curves from 1D calculations are plotted in Figures 7.14,

Table 7.6: $C_2H_5OH - lO_X$ 1D thermochem. calculation

$o/f = 1.4$	$p, [Pa]$	$T, [K]$	M	$F_{th}, [N]$	$I^r_{sp}, [m/s]$
Equilibrium :					
Throat	1.1460E+6	2.9141E+3	1.001	7.7594E+2	2.1153E+3
Exit	5.7574E+4	1.8596E+3	2.8074	1.0466E+3	2.8533E+3
Frozen :					
Throat	1.1460E+6	2.9141E+3	1.001	7.7594E+2	2.1153E+3
Exit	5.3600E+4	1.6927E+3	2.8738	1.0327E+3	2.8154E+3
Kinetics :					
Throat	1.1460E+6	2.9141E+3	1.001	7.7594E+2	2.1153E+3
Exit	5.5807E+4	1.7796E+3	2.8237	1.039E+3	2.8327E+3

Table 7.7: $lH_2 - lO_X$ 1D thermochem. calculation

$o/f = 1.4$	$p, [Pa]$	$T, [K]$	M	$F_{th}, [N]$	$I^r_{sp}, [m/s]$
Equilibrium :					
Throat	1.1550E+6	3.1741E+3	1.001	7.7430E+2	2.8067E+3
Exit	6.3153E+4	2.2959E+3	2.7246	1.0581E+3	3.8357E+3
Frozen :					
Throat	1.1550E+6	3.1741E+3	1.001	7.7430E+2	2.8067E+3
Exit	5.4037E+4	1.8627E+3	2.8629	1.0324E+3	3.7423E+3
Kinetics :					
Throat	1.1550E+6	3.1741E+3	1.001	7.7430E+2	2.8067E+3
Exit	5.9297E+4	2.0968E+3	2.7631	1.0477E+3	3.7979E+3

7.15, 7.16.

As detectable in result data and obtained profiles, inclusion of chemical reaction kinetics in calculation yields properties and performance data that lie approximately between the frozen and equilibrium calculation. In the current case this is approximately at the middle or somewhat closer to the frozen composition. This can be argumented hereafter. In chemical kinetics calculation, reaction speeds are high compared to the velocity of expanding flow. However, some species reactions are slower than the others. Therefore, these slower reac-

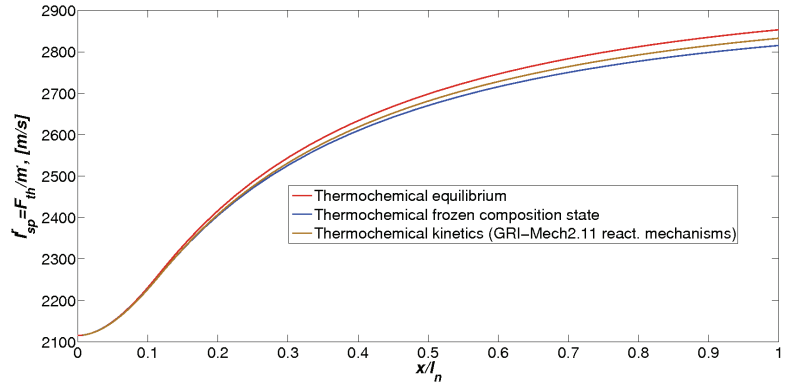

Figure 7.14: $C_2H_5OH - lO_X$ 1D Specific impulse profile

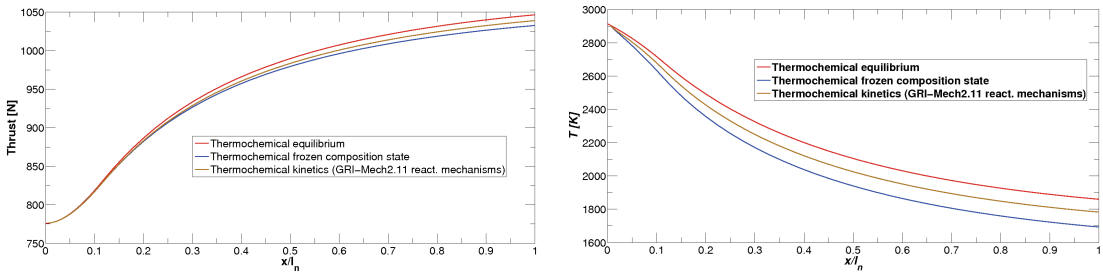

(a) Thrust force (b) Temperature evolution

Figure 7.15: $C_2H_5OH - lO_X$ Thrust force and temperature profiles

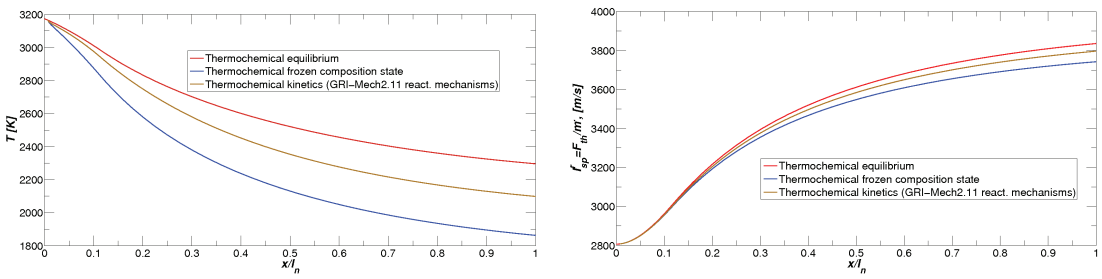

(a) Temperature evolution (b) Specific impulse

Figure 7.16: $H_2 - lO_X$ Specific impulse and temperature profiles

tions are trailing behind the faster ones, which lead to a conclusion that some species reactions are closer to the frozen case model and some to the thermochemical equilibrium model. This relation is also scalable in compare to the nozzle geometry, U/l_n and total conditions at the inlet as the enthalpy and entropy. If the total pressure is decreased from $P_0 = 2000kPa$ to $P_0 = 300kPa$ result

data of the thermochemical kinetic model will be noticeably closer to the frozen mixture case. Therefore it can be concluded that the shorter nozzles with short residence time for species will result in kinetics closer to the frozen case while the longer, for example full launcher nozzles, with large residence time result in kinetics quite close to the thermochemical equilibrium. As it is detectable for $lH_2 - lO_X$ case some reactions are faster and therefore the presented profiles are in-between thermochemical equilibrium and frozen mixture or a bit above.

The used experimental nozzle was approximated as a shorter in relation to the

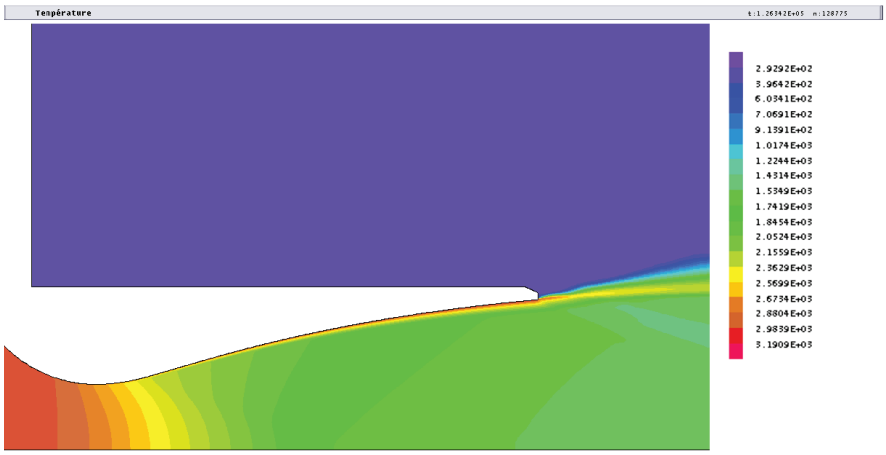

Figure 7.17: $C_2H_5OH - lO_X$ 2D-axi viscous CPS_C temperature plot

length and momentum produced at $P_0 = 2000kPa$ and therefore shorter residence time. Hence, the following numerical 2D and full 3D investigation can be adequately approximated with the frozen composition assumption input and indefinite reaction rate.

However, as afore mentioned, assumption of the infinite area inlet conditions influence on the flow chocking and mass flow rate. In order to slightly improve estimation of the mass flow rate, the massic fractions can be extracted from the combustion chamber result data of CEA2 code at the throat area. In Figure 7.17 2D-axi nozzle expansion with accounted viscous effects is depicted. The detectable viscous boundary-layer inflicts an increasing temperature/enthalpy profile along the wall opposite to the decreasing one in the core flow, Figure 7.18a. However, due to frozen composition assumption, no species recombination in the nozzle cross-sections is possible. Two possible mechanisms can affect the compo-

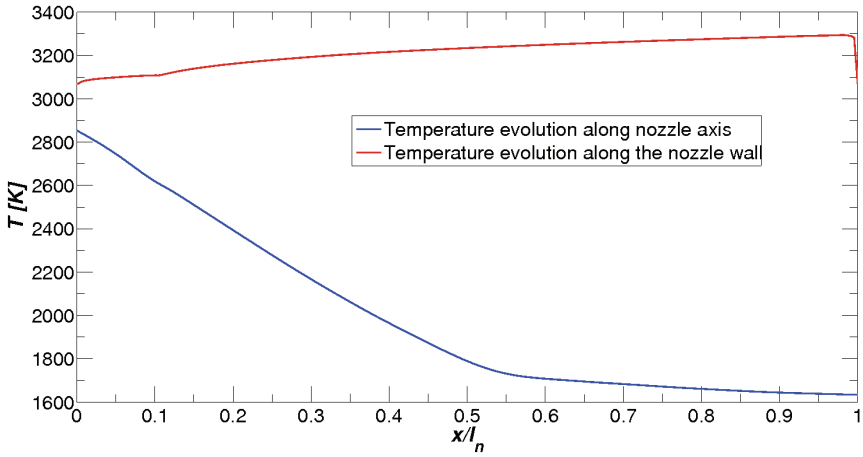

Figure 7.18: $C_2H_5OH - lO_X$ 2D-axi viscous CPS_C temperature evolution at the axis and wall

sition at the wall, as thermodiffusion and species diffusion, from inside to outside. Thermodiffusion effect is rather small and it was not included in the numerical approach, while the species diffusion may affect composition only in first 2-3 cells at the exit section.

7.7 SITVC nozzle 3D hot-gases simulations

The obtained 2D-axi results were interpolated to the 3D case as initialization values, while the same chamber exit conditions (p, T, M and mass fractions) were imposed to the secondary injection inlet. High enthalpy largely increase the jet momentum and favors diffusion and dissipation processes inside the turbulent boundary-layer. Analogously, major temperature (enthalpy) and entropy increase is concentrated in BL, separation and shear interface zones, as depicted in Figure 7.19. At the shear interface of cross-flow interaction zone, temperature changes from $\sim 1500K$ in front of the bow shock to $\sim 2900K$ behind the shock. This highly elevated temperature further favors exchange in the cross-flows interaction zone. Oppositely, a largely decreased temperature of around T $300K$ is detectable aft of injector in a low pressure zone.

One of the analysis goals was to compare the effects of cold flow and elevated temperature cases. Cold flow analysis of $C_2H_5OH - lO_X$ combustion product

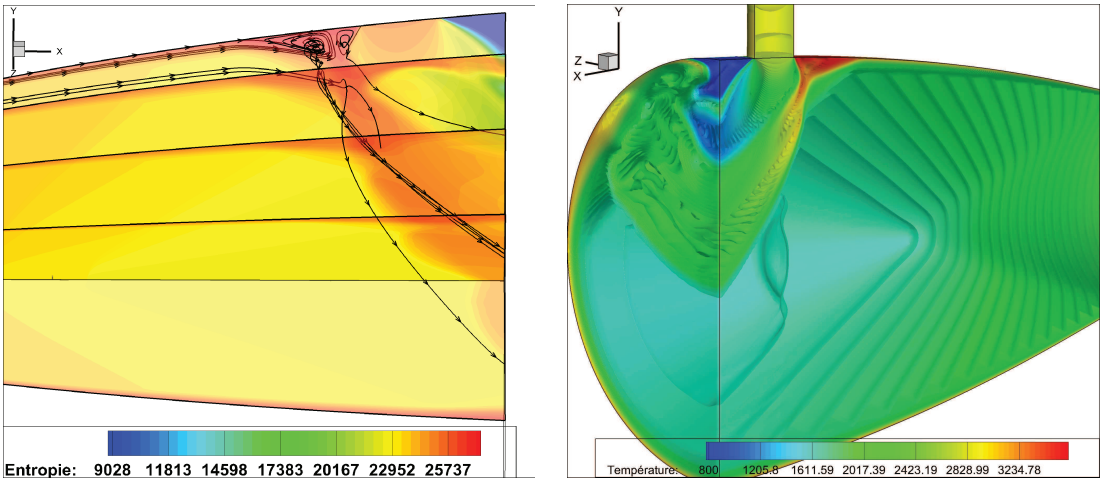

(a) Entropy, J/K in radial extracted slices with streamtraces

(b) Iso-temperature surfaces, K

Figure 7.19: $C_2H_5-OH-lO_X$, 3D entropy and temperature evolutions in SITVC TIC nozzle at $NPR = 37.5$, $SPR = 1$, $x_j/l_n = 0.88$,$P_{0c} = 2000kPa$, $T_{0c} = 3106K$

cases is conducted analogously to bi-species simulations. $C_2H_5OH - lO_X$ combustion products are modeled as a single, monospecie compound at which physical properties are modeled according to molar-fractions of each species inside the mixture. In Figure 7.20 wall-pressure profiles are depicted for hot and cold ethanol numerical case together with profile extracted from cold air investigations.

It can be identified that cold $C_2H_5OH - lO_X$ case produced almost identical wall-pressure profile as the one extracted from the cold air simulations. Which can be traced back to the fact that $C_2H_5OH - lO_X$ mixture physical properties were relatively close to the ones of dry air, especially cold mixture molar mass and specific heats ratio ($\overline{\gamma_{mix}} \sim 1.3323$, $\overline{M_{mix}} = 28.498g/mol$). Therefore, cold air analysis may provide a solid cold flow reference point for further hot gas and combustion simulations with ethanol fuel. At elevated temperature case, flow momentum and thus the axial velocity is substantially increased. Therefore, a higher Mach number upstream flow will possibly have higher deflection through the main shock wave. On the other hand, wall pressure of high temperature/momentum flow appears as a slightly increased in Figure 7.20, with higher plateau pressure value which indicates a stronger vorticity motion in PUV.

Shorter separation distance comparing to the cold flow case is also apparent in

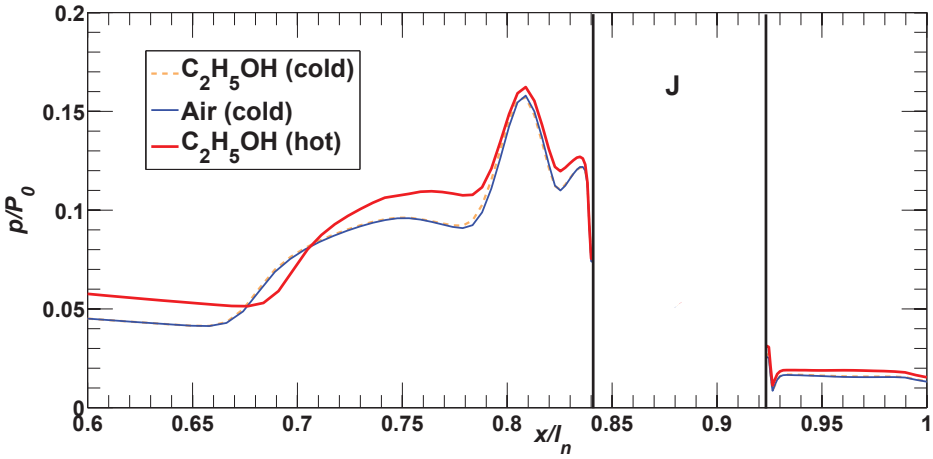

Figure 7.20: Wall-pressure profiles in symmetry plane for hot and cold $C_2H_5OH-lO_X$ case and monospecie cold air case in SITVC TIC nozzle at $NPR = 37.5$, $SPR = 1$, $x_j/l_n = 0.88, P_0 = 300kPa$

skin friction profile given in Figure 7.21. Numerical force data tabulated in Ta-

Table 7.8: Numerical force data for hot and cold gases at $NPR = 37.5, SPR = 1, P_0 = 300kPa$

Test case	Air	$C_2H_5OH - lO_X$	$C_2H_5OH - lO_X$
T_{0c}, K	255	255	2950
T_{0j}, K	283	283	2950
f_m	0.0762	0.0771	0.0803
$F_{wy}[N]$	7.134	6.851	7.075
F_{jy}[N]	9.341	9.146	9.286
$\sum F_y$[N]	16.475	15.997	16.36
$\sum F_x$ [N]	136.21	134.06	141.67
$\delta[°]$	6.89	6.80	6.59/

ble 7.8 presented a very similar SITVC performance data of all three cases. However, it can be detected that interaction wall side force, F_{wy} increases with the temperature elevation but insufficiently to match the axial thrust force increase.

Finally, two fuel-oxidant cases of $C_2H_5OH - lO_X$ and $lH_2 - lO_X$ are numerically investigated simulating an inflight intended chamber pressure of $P_{0c} = 2000kPa$. Force and performance data of frozen mixtures SITVC numerical simu-

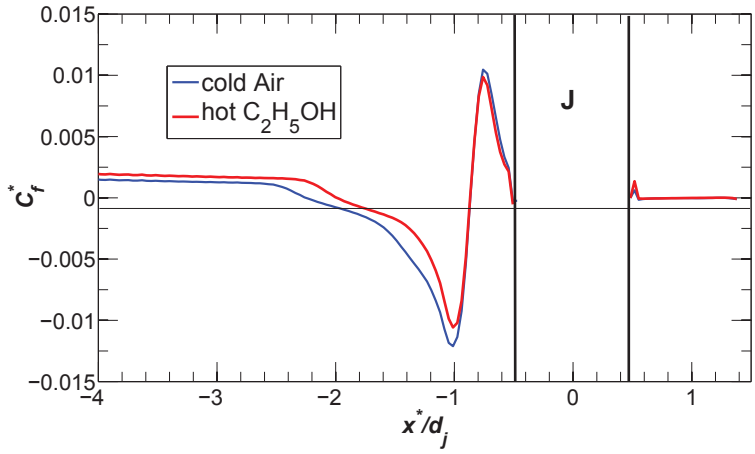

Figure 7.21: Skin friction in symmetry plane for hot $C_2H_5OH - lO_X$ case and cold air case in SITVC TIC nozzle at $NPR = 37.5$, $SPR = 1$, $x_j/l_n = 0.88$, $P_0 = 300kPa$

lations are given in Table 7.9. Wall-pressure profiles in Figure 7.22 depict different

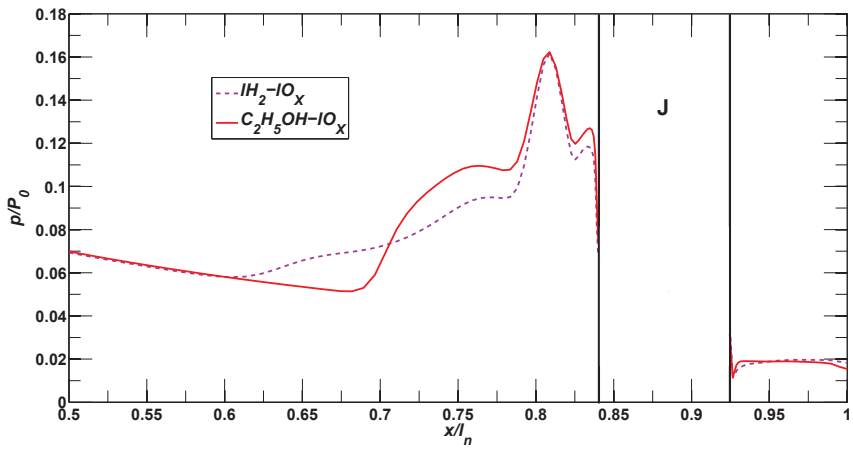

Figure 7.22: Numerical wall-pressure data of 2 fuel-oxidant cases in symmetry plane in SITVC TIC nozzle at $x_j/l_n = 0.88, NPR = 37.5, SPR = 1$

separation modes of two fuel-oxidant cases. Namely, $lH_2 - lO_X$ case appears with a significantly longer separation distance and smaller plateau pressure level, while the $C_2H_5OH - lO_X$ case was completely analogue to the previous cold and hot $P_{0c} = 300kPa$ cases. Assumingly, this can be assigned to the lighter and faster $lH_2 - lO_X$ mixture components with an essentially lower density at nozzle exit

sections. The tabulated data show a similar SITVC behavior as the one of cold

Table 7.9: Numerical force data and performance coefficients for hot gas non-reacting frozen mixture at $NPR = 37.5, SPR = 1$

Test case	$C_2H_5OH - lO_X$	$lH_2 - lO_X$
T_{0c}, [K]	3106	3340
f_m	0.0805	0.078
F_{wy}, [N]	41.838	42.48
F_{jy}, [N]	60.878	62.36
$\sum F_y$, [N]	102.716	104.84
$\sum F_x$, [N]	935.47	956.3
$\delta[°]$	6.27	6.26
F_{0x}, [N]	920.4	946.73
C_{AV}	0.777	0.805
C_{AI}	0.946	0.943

flow analysis. Global amplification factor C_{AI} is in the range or somewhat higher for elevated pressure temperature cases. On the other hand, the vectoring coefficient, C_{AV} decreases and its range drops from values close to 0.9 in cold flow results to around 0.8 representing a 9% decrease in global vectoring. However, significant effects of reacting gases and possible reignition in the separation and shear interface zones are not investigated. The SITVC was simulated with primary and secondary flows using the combustion products from the chamber exit. Using a different fluidic source of secondary injection as fuel or oxidant tanks or different storage fluid, performance will correspondingly be changed according to the fluid physical properties and flow conditions.

7.8 Conclusion remarks

Species physical properties which are considered in this chapter, indicated basic effects on the wall bounded supersonic cross-flow and SITVC system. Modelling of the fluid properties via polynomial functions derived from NIST and Sandia standard data for low temperature gaseous species appeared as valid for performed numerical simulations. Three inert, non-reacting gaseous species other than air are used in the investigation; helium, argon and carbon-dioxide. Interaction cross-flowfield generated by the secondary gaseous injection in divergent nozzle section is visualized via bi-color schlieren photographs and examined together with the numerical bi-color schlieren images and flow properties iso-surfaces and contour plots.
Distinction was made between the $He - air$ injection case and other 2 species, mainly in mixing and shear layer interfaces. Furthermore, these qualitative descriptions are supported in pressure and force quantities analysis. Separation distance, diagnosed via the wall-pressure plots, and size of the pressure regions inside the separation zone clearly indicated a substantial influence of the selected secondary injection species physical properties. Proportionality coefficient derived from the extracted numerical data defined injectant specie relation to the produced side loads in air supersonic flow. This derived coefficient corresponded very well to the evaluated interaction wall side force and secondary injection reactive force components.
It is found that same imposed stagnation flow conditions of the lighter and faster fluid favors the production of the side force components over the heaver species. Considering these remarks with the analysis presented in Chapter 5, it can be said that for the same specie, pressure increase effect considerably exceeds the effect of the increased mass-flow-rate. Generally, cold flow analysis indicated that γM_g ratios below unit value will cause a notably higher SITVC performance.

Thermochemical processes in the combustion chamber were simulated in Gordon and McBride[91] NASA-CEA2 code using the infinite combustor area and thermochemical equilibrium assumptions. Basic hot gas analysis was performed using 1D thermochemical reaction kinetics model. The analysis indicated that thermodynamic and performance data of a short nozzle with the small residence

time and length are somewhat closer to the frozen non-reacting mixture approximation then to the thermochemical equilibrium. Correspondingly, multispecies numerical simulations are performed on the combustion products considered a non-reacting frozen mixture with no recombination of mixture components. At first, data were compared with the cold flow cases and show that loads and pressures corresponding to cold flow numerical models. Some effects as the separation distance shortening and plateau pressure elevation are observed, as well. Finally, two fuel-oxidant cases under flight operating pressure conditions were briefly analyzed. Investigation indicated positive effects without significant increase or decrease of SITVC performances. However, full analysis with the combustion models and/or experimental verification is needed to completely define an in-flight operation.

Summary, study conclusions and perspectives

The wall bounded supersonic cross-flows are investigated for the purpose of a secondary injection thrust vector control. Generated highly complex interaction flowfield by the secondary transverse injection into a supersonic nozzle section contains a number of compressible aerodynamics effects as the adverse pressure gradients, flow separation, shock-shock and shock wave-boundary layer interactions, vorticity and coupled recirculations, shear layers, vorticity induced mass transfer and mixing zones. Multiple scientific and engineering approaches to the problem investigation are needed. The present study was conducted in the framework of the CNES *Perseus* project. Hence, the numerous aspects and features of this study were focused towards the possible engineering application of a secondary injection thrust vector control system.

Some of the study theoretical basis are drawn from the referenced investigations of fundamental, two and three dimensional cases of a transverse sonic injection at the flat plate into a supersonic cross-flow. Additionally, early empirical and experimental analysis were considered in building and adapting an analytical model. Constructed analytical model has yielded some starting inputs as the separation distances, separation plateau pressure range and the side to axial force ratios as a function of the mass-flow rates. This was used to position the experimental and the numerical investigation which are conducted over a broad range of fluid mechanics and aerothermodynamics aspects.

Experimental installation was built during this study on the basis of EDITH blowdown type super/hypersonic wind-tunnel, which was specially rearranged to support the supersonic rocket nozzle cold-flow tests. Monochromatic and bi-

color Toepler's Z-schlieren configurations enabled the visual access to the flow and qualitative analysis of the exhausting plume at the nozzle exit and in the exterior domain. Diagnostic tools included the total pressure and temperature measurements at the primary and secondary stilling chambers and in the exterior domain, the mass-flow-rate metering of the secondary flow, nozzle wall parietal pressure measurements and the 3-axis force balance. This set of experimental tools was very well suited for diagnosing changes of the wall pressure, to capture global force components exerted on the nozzle and to visualize the effects present at the nozzle exit.
To support and complement experiments, RANS numerical simulations were conducted using the finite-volume compressible solver of the Bertin-CNES CPS_C CFD code. $k-\varepsilon$ 2-equation turbulence model was used in viscous 3D numerical simulations performed on a large number of produced numerical grids. Results obtained in the numerical simulations, were generally in a very good agreement with the experiments at all analyzed points. However, there were minor issues, as some slight over or underestimations at critical points inside the recirculation zones, but the overall estimation of the flow effects and force component integration were excellently matched. More problems were identified in the experimental tests related to pressure probe mounting, balance calibration and small misalignments which were in majority eliminated during this study.

Results Synthesis

Chapter 5 results discussion reflect the effects of the secondary injection positioning and primary nozzle design along with the primary and secondary total flow conditions. It is shown that position of transverse injection on the nozzle wall have an important role in deflecting the main flow. Injection positions were grouped in to 2 major categories, when the main shock reflection occurs inside the nozzle and the SITVC nozzle without shock reflection. Shock reflection inside the nozzle was found highly detrimental and the limiting value was identified for the case when the bow shock impinges the nozzle lip. Between the limiting position and the nozzle exit, it was found that positions closer to the nozzle exit

yield higher side loads mainly due to upstream-downstream positive pressure imbalance. Secondly, global moment around z-axis, M_z will have higher values due to a longer lever-arm.
Shock polar analysis accompanied with the numerical simulations on different main nozzle expansion ratios showed a flow deflection increase with the increase of main flow expansion rate. However, at high Mach number nozzles, the axial thrust rise is predominant leading to a slightly decreased vectoring rates. The nozzle profiles that have been tested, include conical, truncated ideal contour and the two Rao optimized contours, thrust optimized and adverse pressure gradient nozzles. Additional effects due to internal, separation and bow shock interactions are observed for the optimized contours and analysis indicated a possible implementation of SITVC at these nozzles. Adverse pressure gradient nozzle simulations pointed to the potentials of further contour optimization.
Flow conditions analysis of the secondary nozzle, evidenced a direct relation of the secondary injectant pressure to the penetration height and upstream separation that defines amount of interaction or wall side force component. It is also shown that global impulse amplification factor, representing the ratio of specific impulses for vectoring and non-vectoring mode, decreases with the increased secondary mass flow rate. As further presented, initial overexpansion positively affects the global SITVC performances by relieving the pull force but it starts to be largely detrimental with further ambient pressure increase. Limiting case was found when the Mach disk occurs at the secondary injection cross-section.

Chapter 6 results discussion was focused on the secondary injection parameters that affect the SITVC system. The angular attitude of the secondary injection was identified as an essential to the SITVC performance. Relatively to the oncoming flow profile, the upstream inclination of the secondary injection will significantly affect the early separation and the slope gradient of the main flow deflection. However, negative effects of the x-negative secondary reactive force component, deformed secondary plume profile and unsteadiness identified at high inclination angles discredit highly upstream inclined injections. Optimal inclination angles from the axis normal ranging around $\varphi = 25°$ have been reported.
Additionally, secondary nozzle geometry was investigated for further optimization possibilities. Radially positioned rectangular shaped injection slot proved as

a fairly positive optimization increasing the upstream separation span-wise laterally. Convergent-divergent secondary nozzle model was found as a negative optimization mainly due to prexpanded secondary flow in front of the high-pressure behind the bow shock.
Investigation of the multiport secondary injection did not provide any significant increase in the side force and deflection. Meridionally grouped multiport SITVC was found as a rather negative in terms of produces side loads and pitch angle, while the radial one was in the same range as the single port SITVC. However, from the engineering and implementation point of view this may be considered for better and more precise steering. In this case additional effects of the secondary flow inner interaction between the ports and coupled interaction with the main flow were detected.

Chapter 7 discussion was based on the multispecies and hot-gas investigation results. Cold flow air investigation was complemented with different gaseous specie injections, to identify the effects of the secondary fluid physical properties on the main flow interaction. In the analysis of the cold flow multi-specie investigation it is found that the pressure of the secondary flow has a substantial effect regardless of the secondary mass-flow-rate. Ratio of the secondary to primary products of specific heats ratio and molar mass, γM_g is identified as an inversely proportional to the generated side force components and the obtained vector pitch angle.
Hot-gas numerical investigation was performed using the 1D reduced thermochemical reactions mechanisms and after as a full 3D CFD simulation with non-reacting frozen mixture approximation. Effects of the elevated temperature and basic specificities of approximated in-flight test conditions were analyzed with no significant implications on produced side force and performance coefficients.

From the author's point of view, presented study makes a valuable contribution to the investigation of the wall bounded supersonic cross-flows for secondary injection thrust vector control use. Study has considered number of aspects contained in SITVC flow control problematic and presented possible explanations. Generally, pertinent side force values and vector pitched angles have been achieved. Vectoring amplification, is found in unit range for the fixed $SPR = 1$,

under adapted nozzle operation, moderate secondary mass-flow-rates and injector positions close to the nozzle exit.
Conducted investigations gave a satisfactory representation of the analyzed aspects and their implication on the SITVC nozzle case. However, aspects as the separation induced flow instabilities, and effects of the reactive injectant species were not addressed in this study.

Perspectives

Following the last remark, further investigation should consider additional effects and research approaches. Even though the low-frequency instabilities in case of the SITVC nozzle with injection close to the nozzle exit are expected to occur downstream of the injector, which is of less significance to this particular case, they can generate unsteady loads under the certain flow regimes and injection angles. In light of that, a developed experimental installation can be further improved by actively regulating the flow temperature conditions and turbulence levels and implementing the tools as the PIV, color oils and supersonic-adapted hot-wire anemometry.
LES or *DES* numerical approach might be considered in order to perform an instability analysis and include the reactive mechanisms for the real operating case simulations. In terms of SITVC parameters, control by activating the full or partial injection from the multiple opposing ports should be considered with afore mentioned analysis of expected unsteady flow zones. This can be also complemented with the study on dynamic response of the SITVC system and eventual multiport SITVC actuated roll control.

References

[1] J. Riebe. Investigation of gaseous secondary injection thrust vector control considering primary nozzle overexpansion, frequency response and injection angle. Technical Report NASA CR-66533, Langley NASA, 1968. 4, 20, 32

[2] J. D. Flamm. Experimental study of an axisymmetric dual throat fluidic thrust vectoring nozzle for supersonic aircraft application. Number AIAA-2007-5084, *AIAA paper* - 43rd Joint Propulsion Conference & Exhibit, July 2007. 4, 20

[3] K. A. Deere. Summary of fluidic thrust vectoring research conducted at NASA Langley research center. Number AIAA-2003-3800, *AIAA paper* - 21st Applied Aerodynamicsn Conference, June 2003. 5, 16

[4] L. Simurda, K. Hornstein, A. Boiron, and K. Stober. Design and development of a thrust vector controlled paraffin/nytrox hybrid rocket. Number AIAA-2012-4310, *AIAA paper* - 48th Joint Propulsion Conference & Exhibit, July 2012. 6

[5] A. Karabeyoglu, J. Stevens, D. Geyzel, B. Cantwell, and D. Micheletti. High performance hybrid upper stage motor. Number AIAA-2011-6025, *AIAA paper* - 47th Joint Propulsion Conference & Exhibit, July 2011. 6

[6] H. Hingre, R. Bec, J. Oswald, and S. Pernon. European university and scientific space research program PERSEUS. 4th European Conference for Aerospace Sciences. 6

[7] R. Bec, K. de Groote, and F. Amouroux. PERSEUS - a nanosat launch system project focusing on innovation and education. Proc. UN/IAF 58th International Astronautical Congress. 6

[8] F. W. Spaid and E. E. Zukoski. A study of the interaction of gaseous jets from transverse slots with supersonic external flows. *AIAA J.*, 06(2):205–212, 1968. 10, 12, 54

[9] F. W. Spaid. Two-dimensional jet interaction studies at large values of Reynolds and Mach numbers. *AIAA J.*, 13(11):1430–1434, 1975. 11, 12

[10] F. W. Spaid, E. E. Zukoski, and R. Rosen. A Study of Secondary Injection of Gases into a Supersonic Flow. Technical Report 32-834, NASA, 1966. 11, 12, 82

[11] J. A. Schetz and F. S. Billig. Penetration of gaseous jets injected into a supersonic stream. *AIAA J. Spacecr. Rockets*, 03(11):1658–1665, 1967. 11, 12, 15, 33, 54

[12] F. S. Billig. Shock-wave shapes around spherical and cylindrical-nosed bodies. *AIAA J. Spacecr. Rockets*, 04(6):822–823, 1967. 11, 37

[13] F. S. Billig, R. C. Orth, and M. Lasky. A unified analysis of gaseous jet penetration. *AIAA J.*, 09(6):1048–1057, 1971. 11, 15, 33

[14] H. D. Thompson, J. D. Hoffman, and S. Murthy. Note on a parametric analysis of thrust vector control by secondary gas injection. Technical Report TM-63-5, Purdue Univ. Jet Propulsion Center, 1963. 11, 19

[15] R. D. Guhse. An experimental investigation of thrust vector control by secondary injection. Technical Report NASA CR-297, Purdue Univ. Jet Propulsion Center, 1965. 11, 20, 32

[16] Jean Allegre. *Deviation aerodynamique d'un jet supersonique par injection parietale.* PhD thesis manuscript, Mention Sciences, Universite de Paris, June 1963. 11

[17] Jean-Francois Devillers. *Etude et optimisation d'une injection secondaire bidimensionnelle en ecoulement supersonique.* PhD thesis manuscript, Mathematiques, Universite de Paris 6 - Pierre et Marie Curie, Mai 1979. 11, 12

[18] Gerard Dupuichs. *Action d'un jet transversal a un ecoulement supersonique.* PhD thesis manuscript, Mention Sciences, Universite de Paris, Mai 1963. 11

[19] V. S. Avduevskii, K. I. Medvedev, and M. N. Polyanskii. Interaction of a supersonic flow with a transverse jet injected through a circular aperture in a plate. *Fluid Dynamics J.*, 5(5):888–891, 1970. 11, 15

[20] E. E. Zukoski and F. W. Spaid. Secondary injection of gases into a supersonic flow. *AIAA J.*, 02(10):1689–1696, 1964. 11

[21] E. E. Zukoski. Turbulent boundary-layer separation in front of a forward-facing step. *AIAA J.*, 05(10):1746–1753, 1967. 11, 37

[22] J. E. Broadwell. Analysis of fluid mechanics of secondary injection for thrust vector control. *AIAA J.*, 01(10):580–585, 1963. 12, 19

[23] R. E. Walker and M. Shandor. Influence of injectant properties for fluid-injection thrust vector control. *AIAA J. Spacecr. Rockets*, 01(4):409–413, 1964. 12, 19

[24] C. F. Chenault and P. S. Beran. $k-\varepsilon$ and Reynolds stress turbulence model comparisons for two-dimensional injection flows. *AIAA J.*, 36(8):1401–1412, 1998. 12, 54

[25] D. Papamoschou and D.G. Hubbard. Visual observations of supersonic transverse jets. *Experiments in Fluids J.*, 14(6):468–476, 1993. 12

[26] D. Papamoschou, A. Zill, and A. Johnson. Supersonic flow separation in planar nozzles. *Shock Waves J.*, 19(3):171–183, 2009. 12

[27] E. Erdem and K. Kontis. Numerical and experimental investigation of transverse injection flows. *Shock Waves J.*, 20(2):103–118, 2010. 12, 54

[28] J. Delery and J.-P. Dussauge. Some physical aspects of shock wave/boundary layer interactions. *Shock Waves J.*, 19(6):453–468, 2009. 13

[29] J.-P. Dussauge, P. Dupont, and J.-F. Debieve. Unsteadiness in shock wave boundary layer interactions with separation. *Aerospace Sci. Tech. J.*, 10(2): 85–91, 2006. 13

[30] J. A. Schetz, S. Cox-Stouffer, and R. Fuller. Integrated cfd and experimental studies of complex injectors in supersonic flows. Number AIAA-1998-2780, *AIAA paper* - 20th Advanced Measurement and Ground Testing Technology Conference, June 1998. 13, 52

[31] J. G. Santiago and J. C. Dutton. Crossftow vortices of a jet injected into a supersonic crossftow. *AIAA J.*, 35(5):915–917, 1997. 14, 15

[32] J. E. Broadwell and R. E. Breidenthal. Structure and mixing of a transverse jet in incompressible flow. *J. Fluid Mech.*, 148:405–412, 1984. 14

[33] B. A. Haven and M. Kurosaka. Kidney and anti-kidney vortices in crossflow jets. *J. Fluid Mech.*, 352:27–64, 1997. 14

[34] V. Viti, R. Neel, and J. A. Schetz. Detail flow physics of the supersonic jet interaction flow field. *Physics of Fluids J.*, 21(4):046101–1–16, 2009. 14, 15, 54

[35] J. N. Hefner and J. R. Sterrett. Secondary jet interaction with emphasis on outflow and jet location. *AIAA J. Spacecr. Rockets*, 09(11):845–847, 1972. 15

[36] V. V. Vlagov, N. E. Masyakin, and M. N. Polyanskii. Penetration depth of a jet injected into an oncoming supersonic flow. *Fluid Dynamics J.*, 15(4): 599–602, 1980. 15

[37] C. F. Chenault, P. S. Beran, and D. W. Bowersox. Numerical investigation of supersonic injection using a Reynolds-stress turbulence model. *AIAA J.*, 37(10):1257–1269, 1999. 15, 54

[38] Bruno Mangin. *Vectorisation fluidique de la poussee d'une tuyere plane supersonique.* PhD thesis manuscript, Physics, speciality: Fluid mechanics, Universite d'Orleans, December 2006. 16, 17, 18, 158

[39] Vincent Jaunet. *Etude d'un jet rectangulaire supersonique a nombre de Mach 1.45 vectorise par actionneur fluidique.* PhD thesis manuscript, speciality: Fluid mechanics and acoustics, Universite de Poitiers, December 2010. 16, 18

[40] K. A. Waithe and K. A. Deere. Experimental and computational investigation of multiple injection ports in a convergent-divergent nozzle for fluidic thrust vectoring. Number AIAA-2003-3802, *AIAA paper* - 21st Applied Aerodynamicsn Conference, June 2003. 16, 17

[41] D. J. Wing. Static investigation of two fluidic thrust-vectoring concepts on a two-dimensional convergent-divergent nozzle. Technical Report NASA TM-4574, Langley NASA, 1994. 16, 17

[42] K. A. Deere. Computational investigation of the aerodynamic effects on fluidic thrust vectoring. Number AIAA-2000-3598, *AIAA paper* - 36th Joint Propulsion Conference & Exhibit, July 2000. 16

[43] B. Mangin, A. Chpoun, and L. Jacquin. Experimental and numerical study of the fluidic thrust vectoring of a two-dimensional supersonic nozzle. Number AIAA-2006-3666, *AIAA paper* -24th Applied Aerodynamics Conference, June 2006. 17

[44] J. D. Flamm. Experimental study of a nozzle using fluidic counterflow for thrust vectoring. Number AIAA-98-3255, *AIAA paper* - 34th Joint Propulsion Conference & Exhibit, July 1998. 17

[45] D. J. Wing. Static performance investigation of a skewed-throat multiaxis thrust-vectoring nozzle concept. Technical Report NASA TP-3411, Langley NASA, 1994. 17

[46] K. A. Deere, B. L. Berrier, J. D. Flamm, and S. K. Johnson. Computational study of fluidic thrust vectoring using separation control in a nozzle. Number

AIAA-2003-3803, *AIAA paper* - 21st Applied Aerodynamicsn Conference, June 2003. 17

[47] R. E. Walker, A. R. Stone, and M. Shandor. Secondary gas injection in a conical rocket nozzle. Technical Report CM-1010, John Hopkins Univ. Aplied Physics Lab. & Naval Weapons, 1962. 19, 22

[48] G. Masuya, N. Chinzei, and S. Ishii. Secondary gas injection into a supersonic conical nozzle. *AIAA J.*, 15(3):301–302, 1977. 20

[49] J. E. McAuley and A. J. Pavli. A cold-flow investigation of jet-induced thrust-vector control. Technical Report NASA X-416, Lewis Research Center, 1960. 20, 32, 162

[50] J. H. Nielson, A. Gilchrist, and C. K. Lee. Control forces in rocket nozzles produced by multiport gaseous injection. *J. Mech. Eng. Sci.*, 11(6):609–610, 1969. 20, 161

[51] R. F.H. Woodberry and R. J. Zeamer. Solid rocket thrust vector control. Technical Report NASA SP-8114, Lewis Research Center & Hercules inc., 1974. 20, 21, 22, 146

[52] D. J. Wing and V. J. Giuliano. Fluidic thrust vectoring of an axisymmetric exhaust nozzle at static conditions. Number FEDSM97-3228 in Proc. ASME Fluids engineering division summer meeting, June 1997. 20, 22, 137, 140, 141, 161

[53] S. Hozaki, R. L. Chapkins, J. Tromblay, and G. V. R. Rao. Thrust vector control system utilizing an adverse pressure gradient in the nozzle. Technical Report NASw 249, National Engineering Science Co., 1962. 20, 21, 22, 29, 105, 162

[54] J. H. Nielson, A. Gilchrist, and C. K. Lee. Control forces in rocket nozzles produced by a secondary gas stream inclined at various angles to the nozzle axis. *J. Mech. Eng. Sci.*, 11(2):175–180, 1969. 20, 146, 147

[55] J. F. Newton and F. W. Spaid. Experiments on the interaction of secondary injectants and rocket exhaust for thrust vector control. Technical Report NASA 32-203, NASA JPL, Caltech, 1962. 21, 22

[56] R. D. Guhse. On secondary gas injection in supersonic nozzles. *AIAA J. Spacecr. Rockets*, 03(1):147–149, 1966. 21

[57] R. D. Guhse and H. D. Thompson. Some aspects of gaseous secondary injection with application to thrust vector control. *AIAA J. Spacecr. Rockets*, 09(5):291–292, 1972. 21

[58] J. H. Nielson, A. Gilchrist, and C. K. Lee. Side thrust control by secondary gas injection into rocket nozzles. *J. Mech. Eng. Sci.*, 10(3):239–251, 1968. 22

[59] V. Viti, J. A. Schetz, and R. Neel. Numerical studies of the jet interaction flowfield with a main jet and an array of smaller jets. Number ICAS-2002-4.7.1 in Proc. 23rd Congress of International Council of the Aeronautical Sciences, September 2002. 22

[60] H. Ko and W.-S. Yoon. Performance analysis of secondary gas injection into a conical rocket nozzle. *AIAA J. Propul. Power*, 18(3):585–591, 2002. 22

[61] T. H. New and W. L. Tay. Cross-stream radial fluid injection into a round jet. Number AIAA-2004-2403, *AIAA paper* - 2nd Flow Control Conference, July 2004. 22

[62] Nabegh Maarouf. *Modelisation des phenomenes dissymetriques dans le divergent des tuyeres supersoniques propulsives: application a la vectorisation de la poussee*. PhD thesis manuscript, speciality: Fluid mechanics, Universite d'Evry-Val d'Essonne, December 2008. 22, 33

[63] H. W. Liepmann and A. Roshko. *Elements of Gasdynamics*. John Wiley & Sons, New York, 1957. 23

[64] Jean Delery. *Compressibile Aerodynamics*. John Wiley & Sons, New York, 2010. 23, 30

[65] Maurice J. Zucrow and Joe D. Hoffman. *Gas Dynamics*. John Wiley & Sons, New York, 1976. 27, 28, 217, 218, 221

[66] S. Deck. Delayed detached eddy simulation of the end-effect regime and side-loads in an overexpanded nozzle flow. *Shock Waves J.*, 19(3):239–249, 2009. 29

[67] G.V.R. Rao. Exhaust nozzle contour for optimum thrust. *Jet Propul. J.*, 28 (6):377–382, 1958. 29, 91

[68] G. V. R. Rao. Thrust vector control system utilizing an adverse pressure gradient in the nozzle. Technical Report NASw 249, SN/60, National Engineering Science Co., 1961. 29, 91, 105, 109

[69] M. Sellam, A. Chpoun, V. Zmijanovic, and V. Lago. Fluidic thrust vectoring of an axisymmetric nozzle: An analytical model. *Int. J. Aerodynamics*, 2(2, 3, 4):193–209, 2012. 33, 115

[70] L. Green. Flow separation in rocket nozzles. *ARS J.*, 23:34–35, 1953. 33, 36, 120, 121

[71] T. W. Schilling. Flow separation in rocket nozzles. MSci, University of Buffalo, 1962. 36, 37, 120, 121

[72] David. C. Wilcox. *Turbulence modeling for CFD*. DCW Inc., La Cañada, California, 2nd print edition, 1994. 52, 59

[73] P. Durand, B. Vieille, H. Lamban, P. Vuillermoz, G. Boure, P. Steinfeld, F. Godfroy, and J.-F. Guery. CPS : A three-dimensionnal CFD numerical code dedicated to space propulsive flows. Number AIAA-2000-36976, *AIAA paper* - 36th Joint Propulsion Conference & Exhibit, July 2000. 53

[74] E. F. Toro. *Riemann Solvers and Numerical Methods for Fluid Dynamics*. Springer-Verlag, New York, 3rd edition, 2009. 53

[75] E. S. G. Maciel. Comparison between the two-equation turbulence models of jones and launder and of wilcox and rubesin applied to aerospace problems. *J. Mech. Eng. Research*, 3(7):248–263, 2011. 54

[76] W. P. Jones and B. E. Launder. The prediction of laminarization with a two-equation model of turbulence. *Int. J. Heat and Mass Transfer*, 15(2): 301–314, 1972. 54, 57, 58, 59, 69, 70

[77] V. Yakhot, S. A. Orszag, S. thangam, T. Gatski, and C. G. Speziale. Development of turbulence models for shear flows by a double expansion technique. *Phys. Fluids A*, 4(7):1510–1520, 1992. 54, 59, 69, 70

[78] D. C. Wilcox and M. W. Rubesin. Progress in turbulence modeling for complex flow fields including effects of compressibility. Technical Paper NASA TP-1517, DCW Inc. & NASA Ames research center, 1980. 54, 59, 69

[79] B. E. Launder and B. I. Sharma. Application of the energy-dissipation model of turbulence to the calculation of flow near spinning disc. *Letters Heat and Mass Transfer*, 1(2):131–138, 1974. 58

[80] E. W. Lemmon, R. T. Jacobsen, S. G. Penoncello, and D .G. Friend. Thermodynamic properties of air and mixtures of nitrogen, argon, and oxygen from 60 to 2000K at pressures to 2000MPa. *J. Phys. Ref. Data*, 29(3):331–385, 2000. 61, 173

[81] A. Burcat and B. Ruscic. Third millennium ideal gas and condensed phase thermochemical database for combustion with updates from active thermochemical tables. Technical Report ANL-05/20, Argonne National Laboratory Chicago for the U.S. department of energy, 2005. 61, 173, 190

[82] B. J. McBride, M. J. Zehe, and S. F. Gordon. NASA Glenn coefficients for calculating thermodynamic properties of individual species. Technical Publication NASA/TP-2002-211556, NASA Glenn, 2002. 61, 173, 186, 190

[83] Jr. M. W. Chase. NIST-JANAF thermochamical tables - fourth edition. *J. Phys. Ref. Data*, Monograph 9:1961, 1998. 61, 173, 186, 190

[84] L. F. Richardson. The approximate arithmetical solution by finite differences of physical problems including differential equations, with an application to the stresses in a masonry dam. *Philosoph. Trans. Royal Society of London.* 67

[85] P. J. Roache. Quantification of uncertainty in computational fluid dynamics. *Annu. Rev. Fluid. Mech.*, 29:123–160, 1997. 67

[86] V. Zmijanovic, V. Lago, M. Sellam, and A. Chpoun. Shock vector control of an axisymmetric conical C-D nozzle via secondary transverse gas injection. *Shock Waves J.*, 23, 2013. 72

[87] V. Zmijanovic, B. Rasuo, and A. Chpoun. Flow separation modes and side phenomena in an overexpanded nozzle. *FME Transactions*, 40(3):193–209, 2012. 102

[88] R. H. Schmucker. Stroemungsvorgaenge beim betrieb ueberexpandierter duesen chemischer raketentriebwerke, teil 1: Stroemungsabloesung. Contractor Report NASA-CR-143044, TU Munich, 1973. 115

[89] R. H. Schmucker. Status of flow separation prediction in liquid propellant rocket nozzles. Technical Memorandum NASA-TM-X-64890, Marshall Space Flight Center, 1974. 115, 121

[90] V. Zmijanovic, V. Lago, L. Leger, E. Depussay, M. Sellam, and A. Chpoun. *Progress in Propulsion Physics*, volume 4., chapter Thrust vectoring effects of a transverse gas injection into a supersonic cross flow of an axisymmetric convergent divergent nozzle, pages 227–256. EDP Sciences, 2013. 136

[91] S. F. Gordon and B. J. McBride. Computer program for calsulation of complex Chemical Equilibrium compositions and Applications. Reference Publication NASA/RP-1311, NASA Lewis (Glen) Research Center, 1996. 187, 199

[92] C.T. Bowman, R.K. Hanson, D.F. Davidson, W.C. Gardiner Jr., V. Lissianski, G.P. Smith, D.M. Golden, M. Frenklach, and M. Goldenberg. GRI-MECH 2.11 reaction mechanisms, September 1995. URL `http://www.me.berkeley.edu/gri_mech/`. 189

Appdx A - Design of an axisymmetric CD nozzle contour

To design *de Laval* and thrust optimized nozzle contours, Method of Characteristics (MoC) was employed using the model equations for a three-dimensional axisymmetric nozzle. The procedure used throughout this study corresponds to the one given in Zucrow and Hoffman[65].
After obtaining series of profiles for each nozzle type under test conditions, solutions have been iterated for maximum thrust. Finally, selected nozzle models are tested for viscous effects and small correction according to turbulent boundary has been imposed.

A.1 Method of characteristics

Initially throat geometry and corresponding sonic line is calculated using the Sauer's analysis. This model is a straightforward method that gives closed solutions and thus making it very suitable for smooth curvature changes. Even not the most accurate method, it yields very good results especially for the large curvature radius where $R_c > R_{th}$ which is the usual case for regular and experimental setups. Sonic line by Sauer is attached a bit upstream to the wall corresponding to the throat area and intersects with axis downstream which represents 0-coordinate for beginning of the Sauer's analysis.

As well as other methods, Sauer's model also incorporates method of small perturbations to describe the flow field at critical cross-section. Universal set of

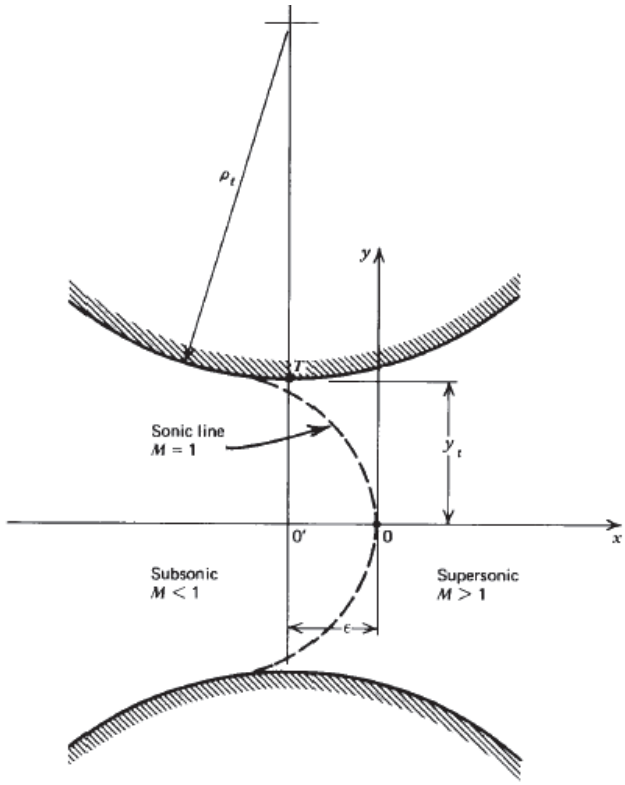

Figure A.1: Sauer sonic line approximation after Zucrow and Hoffman[65]

perturbation equations that can be employed for planar and axisymmetric may be written as:

$$(1 - M_\infty^2)u_x + v_y + \delta\frac{v}{y} = 0 \tag{17}$$

$$(1 - M_\infty^2)u_x + v_y + \delta\frac{v}{y} = M_\infty^2(\gamma + 1)\left(\frac{u}{U_\infty}\right)u_x \tag{18}$$

where δ is defined as switch between planar ($\delta = 0$) and axisymmetric nozzle case ($\delta = 1$). Further by substituting $U_\infty = a^*$ and $M_\infty = 1$ with corresponding

perturbation set, $u' = u/a^*$ and $v' = v/a^*$, yields the following equation set:

$$(\gamma + 1)u_x - v_y - \delta\frac{v}{y} = 0 \tag{19}$$

$$(\gamma + 1)u'u'_x - v'_y - \delta\frac{v'}{y} = 0 \tag{20}$$

Assuming throat flow as irrotational it is possible to define potential function for velocity

$$\Phi = U_\infty x + \phi = a^8(x + \phi') \tag{21}$$

$$\widetilde{u} = a^* + u = a^*(1 + u') = \Phi_x = a^*(1 + \phi'_x) \tag{22}$$

$$\widetilde{v} = v = a^* v' = \Phi_y = a^*\phi'_y \tag{23}$$

with substitution into above defined perturbation set, governing equation for non-dimensional perturbation velocity potential for a transonic flow is defined as:

$$(\gamma + 1)\phi'_x\phi'_{xx} - \phi'_{yy} - \delta\frac{\phi'_y}{y} \tag{24}$$

This equation is further developed into series and since it still has non-linear terms, the techniques for solving non-linear differential equations needs to be employed on higher order terms. Sauer in his method is neglecting all terms higher than order 4, substituting into the developed governing equation yields:

$$\phi'(x, y) = f_0(x) + \frac{(\gamma + 1)\alpha^2 xy^2}{2(1 + \delta)} + \frac{(\gamma + 1)^2\alpha^3 y^4}{8(1 + \delta)(3 + \delta)} \tag{25}$$

$$u'(x, y) = \alpha x + \frac{(\gamma + 1)\alpha^2 y^2}{2(1 + \delta)} \tag{26}$$

$$v'(x, y) = \frac{(\gamma + 1)\alpha^2 xy^2}{(1 + \delta)} + \frac{(\gamma + 1)^2\alpha^3 y^3}{2(1 + \delta)(3 + \delta)} \tag{27}$$

Finally, critical curve where M=1 is established by setting u'=0 and neglecting powers of the perturbation terms.

$$x = -\frac{(\gamma+1)\alpha y^2}{2(1+\delta)} \tag{28}$$

To proceed with marching potential value of MoC it is necessary to locate the origin of the coordinate system by Sauer, which is defined where $v = v' = v\ = 0$ and where $x = \epsilon$.

$$\epsilon = -\frac{(\gamma+1)\alpha y_t^2}{2(3+\delta)} \tag{29}$$

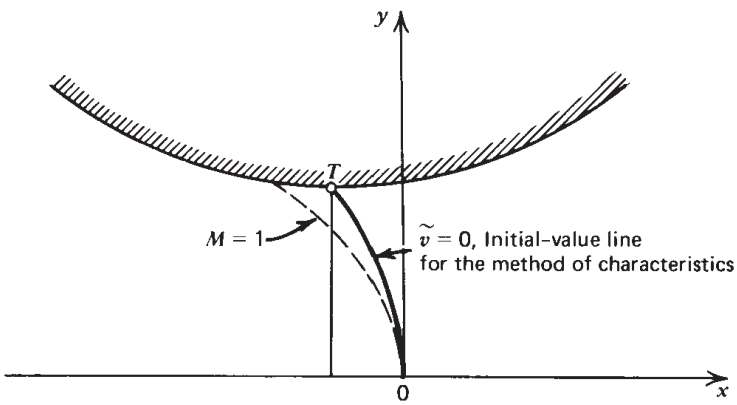

Figure A.2: Illustration of initial-value line

Following determination of the initial-value line, the radius of the throat curvature ρ_t and its throat and attachment point are defined using the model related to Sauer analysis. In reality curvature κ at the throat region is divided into two parts, subsonic and supersonic enabling shortening of the overall length. In the experimental nozzle models used in this study some minimal length was needed in order to employ diagnostic tools properly. Therefore subsonic and supersonic part of the throat curvature are identical matching the $\rho_t = 2.5 \times\ R_{th}$. This

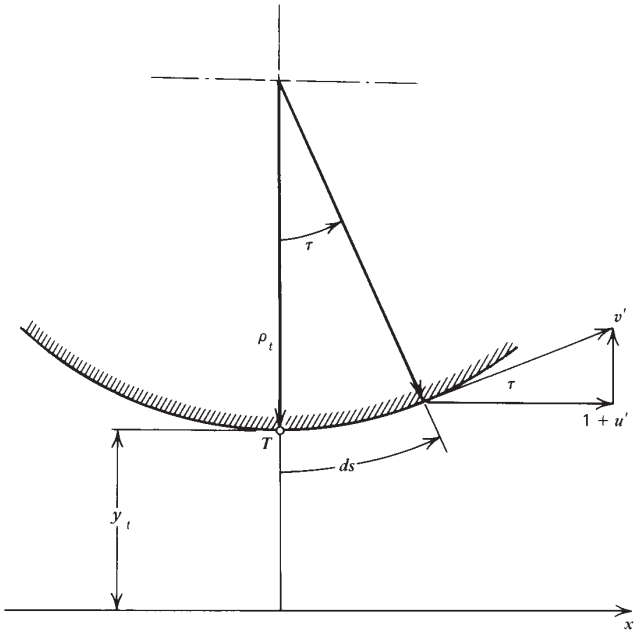

Figure A.3: Model for determining the curvature κ at the narrowest cross-section by Zucrow and Hoffman[65]

model is illustrated in Figure A.3, and it yields:

$$\tan\tau = \frac{v'}{(1+u')} \cong \; v' \tag{30}$$

At the T-point and for derivative dv'/ds this can be given as:

$$\kappa = \frac{1}{\rho_t} = \left[\frac{d(\tan\tau)}{ds}\right]_\tau = \left(\frac{dv'}{ds}\right)_\tau \tag{31}$$

$$\frac{dv'}{ds} = vx'\left(\frac{dx}{ds}\right) + vy'\left(\frac{dy}{ds}\right) \tag{32}$$

Further downstream the potential velocity is used as a marching characteristic to close the iteration process until the full parallelism of the flow to the main axis at the nozzle exit; which is also illustrated and briefly described in Section 2.3.2.

A.2 Selection of TIC nozzle and boundary-layer correction

Used method of characteristics is an inviscid model for calculating nozzle profiles. Axisymmetric approximated 3D CPS simulations are performed using the several viscous models to test obtained profiles for viscous effects. Boundary-layer border

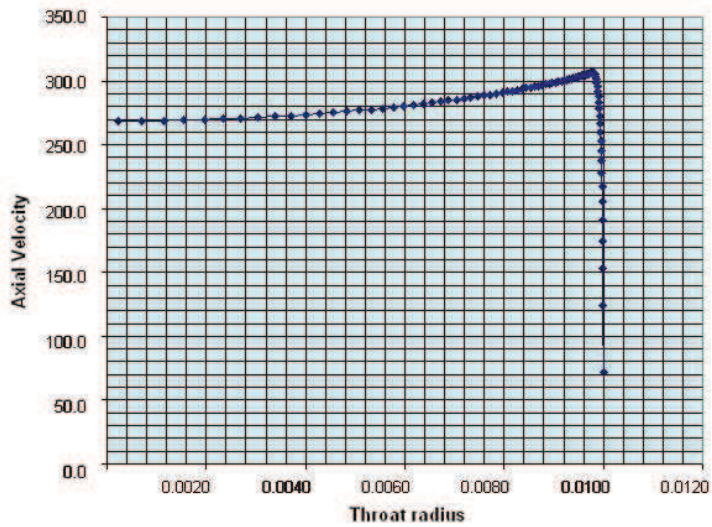

(a) Velocity profile

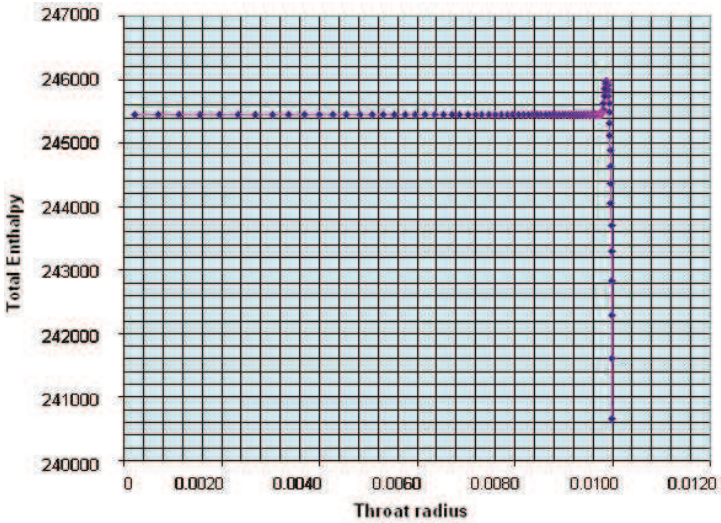

(b) Energy (enthalpy) profile

Figure A.4: Profiles at the nozzle throat section

may be found using the momentum or more precisely enthalpy condition and integrating it for maximum value along the nozzle. Boundary-layer border profile obtained using these methods may appear in a rather wavy form. Therefore, minimal boundary layer thickness to correct inviscid contour for viscous effects is

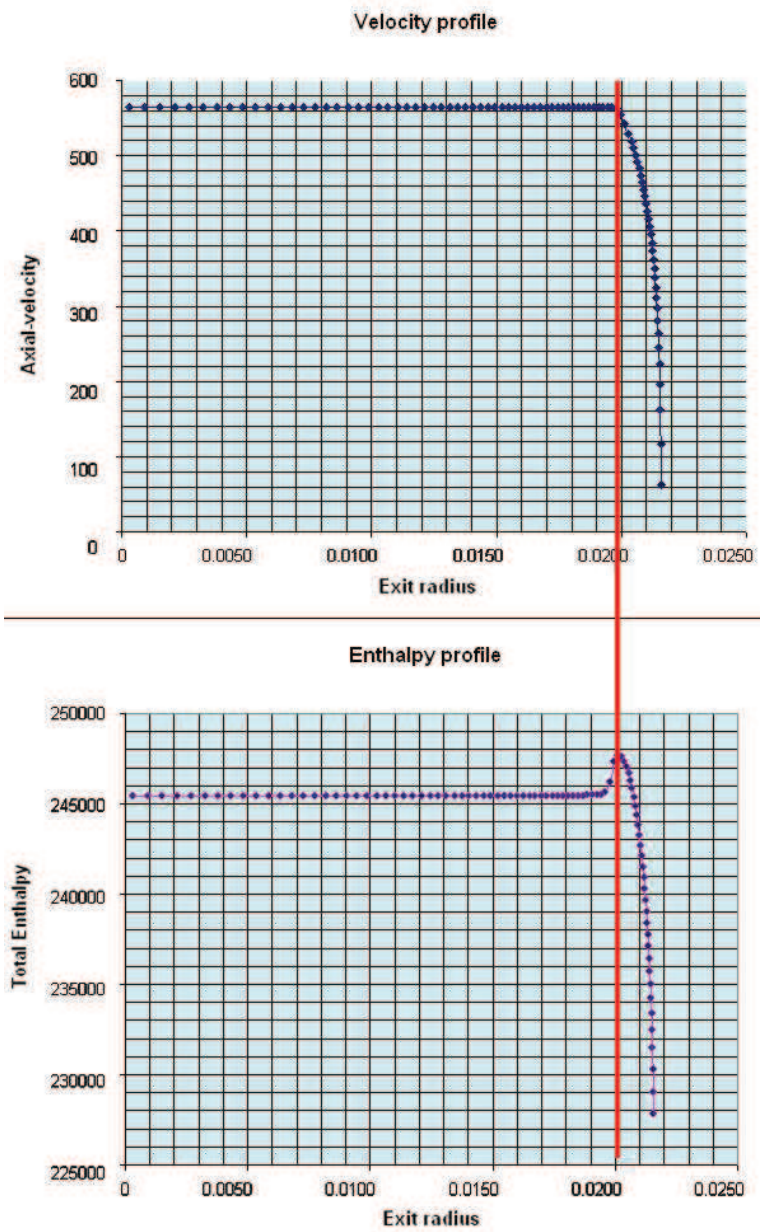

Figure A.5: Velocity and energy profiles at the nozzle exit

defined by finding and connecting energy/velocity profiles at characteristic cross-sections as throat, exit and high angle change. As depicted in Figures A.4 and A.5 energy and momentum conditions are found from profiles at throat and exit nozzle sections. In the throat cross-section it is also possible to use weather energy method for more precise profile or momentum one since difference between them and error is negligible. Finally, corrected profile for viscous-turbulent supersonic flow is found and after truncation imposed on the final TIC nozzle, as well, as depicted in Figure 3.10.

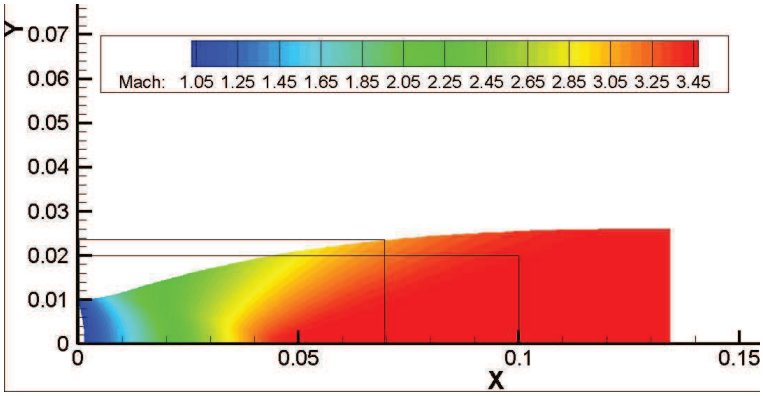

Figure A.6: MoC calculated ideal nozzle Mach plot and truncation sequences

After obtaining ideal nozzle profiles using MoC calculation, truncation was performed to attain TIC contours. Truncation is performed according to the

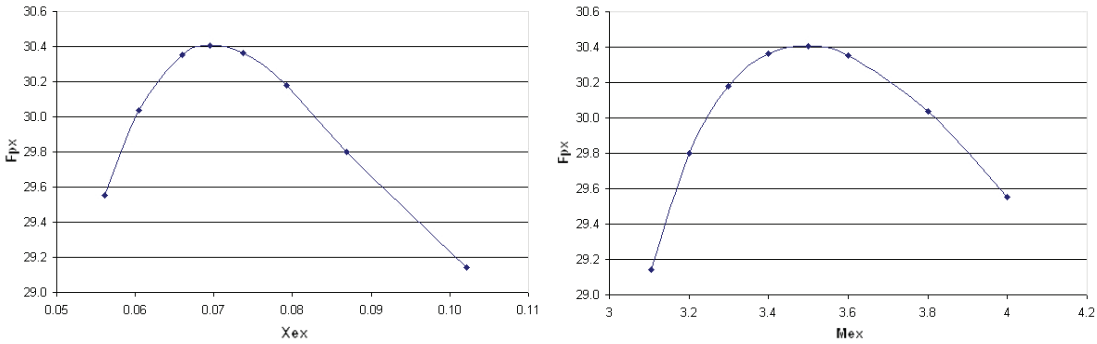

(a) Axial length (b) Mach number selection

Figure A.7: Integration scheme for max pressure force of calculated profiles

experimental test conditions. Namely, the pressure conditions at the test section

are matched to the one on the nozzle wall at the nozzle exit. Therefore the flow exiting the nozzle would have tangential profile to the exit wall section, approximating the adapted flow regime. Series of profiles that correspond to aforementioned conditions were build. Obtained TIC nozzle contour profiles are then further treated in order to find best selection according to the maximum achieved pressure force integrated over the nozzle wall. Best performed TIC nozzle with $x_t = 68mm$ and inviscid $M_e = 3.33$ is selected for this study.

Appdx B - Force data acquisition

The force balance is designed and constructed to diagnose aerodynamic forces acting on the experimental nozzle models in this study. It consisted of a moving frame connected to other two frames via Boch-Rexroth® slide bearings which were further fixed to the test-section support. The primary and attached secondary nozzle with the stilling chambers were attached to the frame placed at the nozzle-chamber center of gravity. The system was then attached to the frame via Boch-Rexroth slide bearings allowing a translation in vertical y-direction. The y direction moving frame, colored rose in Figure B.1, is then attached to the HBM transducers, on both sides in red color, which were fixed on the other end to the other two moving frames, colored green in Figure B.1, measuring the strain dilatations in axial x-direction and lateral z-direction via HBM transducer which were fixed to the test-section support with the other end.

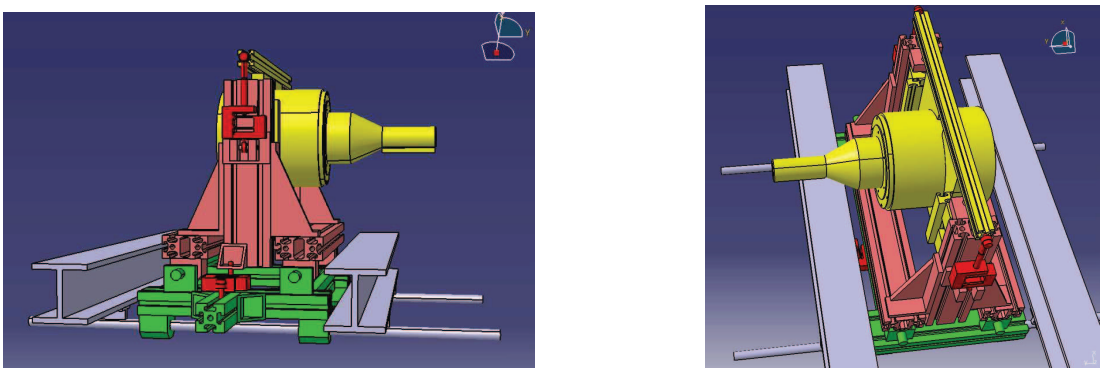

(a) side view (b) isometric top view

Figure B.1: CATIA V5 CAD view of the balance system assembly

B.1 Static calibration and sensor data treatment

Each transducer and the mounted balance system were calibrated under the static conditions and then verified in the test flow environment. HBM® S2M S-type strain-gauge force transducers of 200N max force range in tensile and compressible directions, were used to measure global vertical y-force and global axial x-force, while the small 20N range S2M transducer was used on lateral z side to detect eventual asymmetries.

HBM® S2M is a S-type strain-gauge cell that measures loads via small dilatations of its measuring sides. It operates with electric signal output of $2mV/V$ and with high accuracy class of 0.02. Linearity for this transducers type is very well maintained throughout the whole measurement range. Nominal linearity error

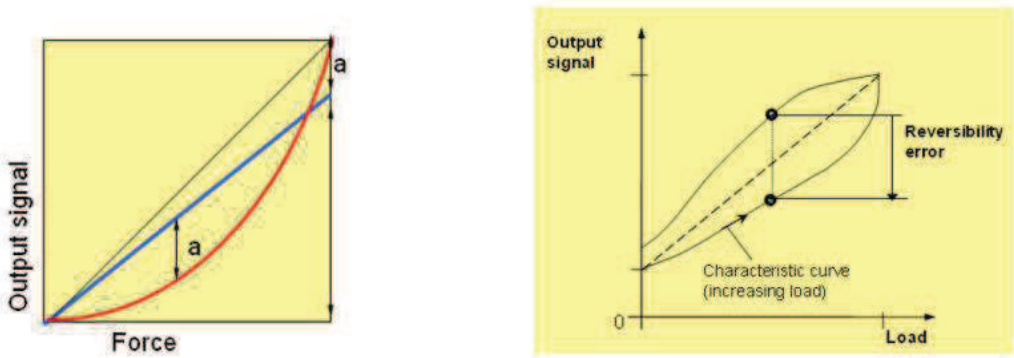

(a) Linearity: blue-ideal line ; red-actual line a-deviation

(b) Reversibility error

Figure B.2: HBM S2M linearity and reversibility

or deviation for S2M is defined at $a = 0.1\%$ which for 100N loads yields 0.1N deviation from the nominal data sheet value. Along with the linearity, a small reversibility error may occur which can be largely reduced and eliminated by calibrating the real measurement range. Reversibility error for S2M between the positive and negative loads is projected between 40% and 60% of the linearity error. Also small error due to creep upon loading is pronounced at the preloaded measuring directions as vertical y-direction, at which the high load is applied during considerable amount of time. For HBM S2M transducers relative creep upon loading/unloading is considered with the constant loading over time period

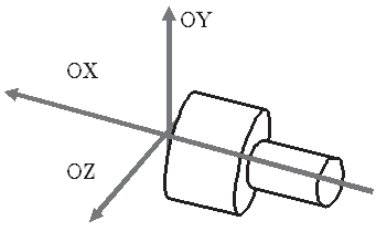

(a) measurement directions

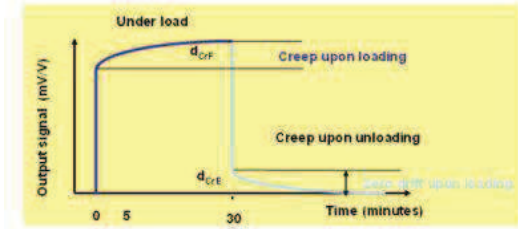

(b) S2M creep upon loading scheme

Figure B.3: HBM S2M directions and creep

larger than 30min. This function is exponential and should not be considered at linear calibration. For static measurements it can be significantly reduced by increasing number of measuring samples. For dynamic environment, like during the testing window, creeping is relatively eliminated.

After verifying and calibrating each transducer for a defined range, whole system is calibrated using a series of small weights. Additional deviations due to static frication and system creeping are included in this static calibration process. y-axis calibration was conducted putting a series of laboratory-weights from 50g

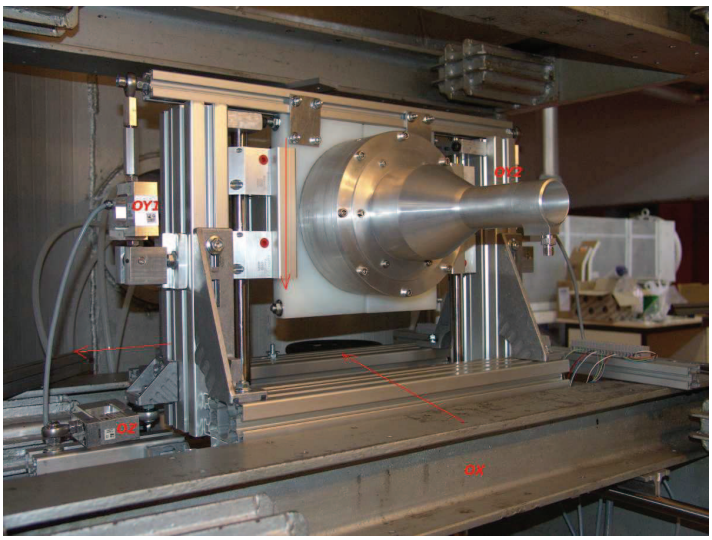

Figure B.4: Mounted nozzle chamber system on the force balance system and measuring axes

to 15kg on top of a stilling chamber as depicted in Figure B.4. The balance was preloaded with weight of a nozzle-chamber system in $y-$direction of 13kg.

The use of two 200N transducers in this direction, provided a measuring range between 1/3 and 1/2 of the nominal range where linearity is at optimal condition. Transducers in axial x and lateral z directions were calibrated using the pulleys

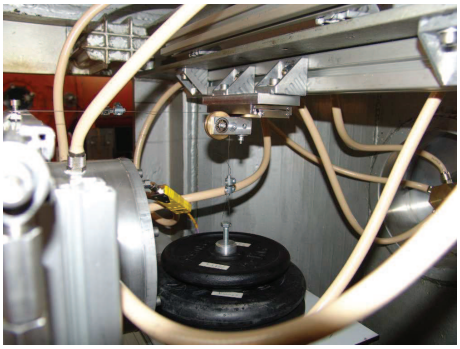

(a) Axial x-direction

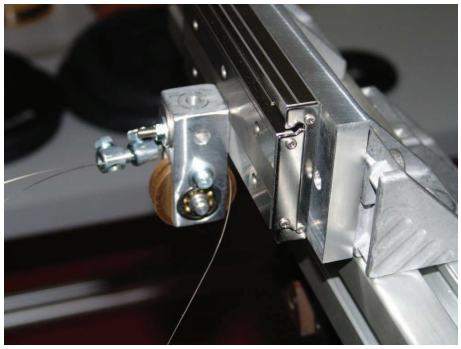

(b) Lateral z-direction

Figure B.5: Calibration using pulley supports

which were mounted on the frictionless slide bearings and aligned via laser level pointers, Figure B.5.

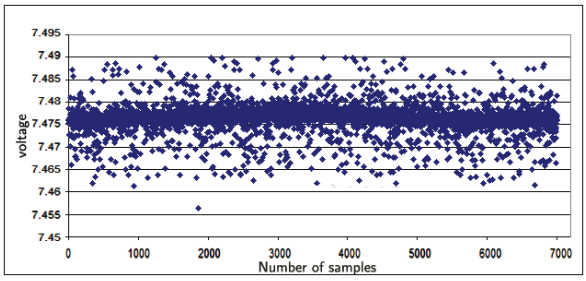

(a) x-axis under $139.4N$ static load

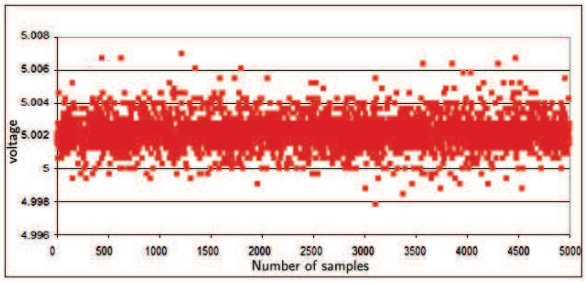

(b) y-axis under $5.14N$ static load

Figure B.6: Examples of static load signal test raw data

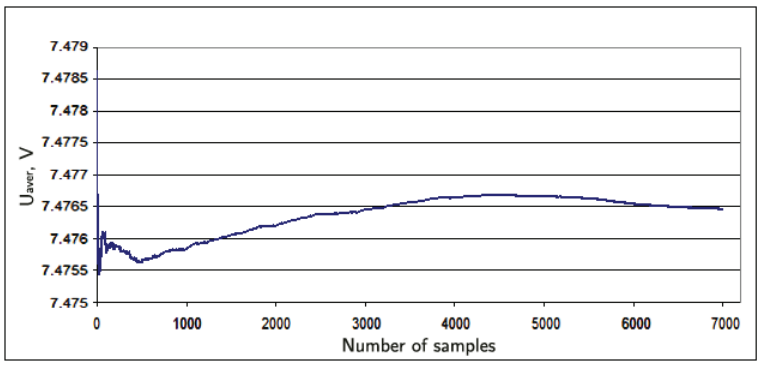

(a) x-direction, 7000 samples chunk under 7kHz sample rate

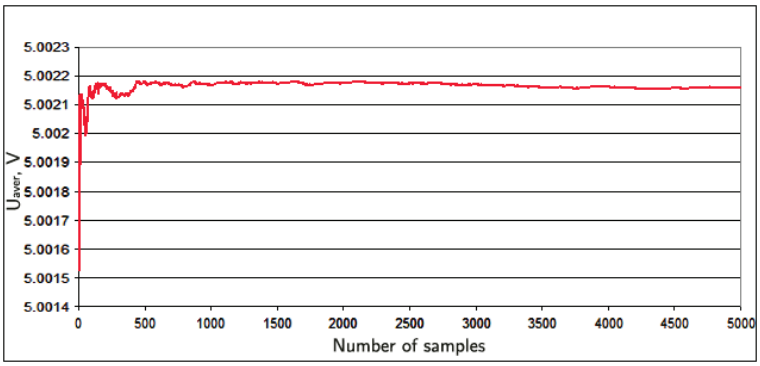

(b) y-direction, 5000 samples chunk under 5kHz sample rate

Figure B.7: Examples of convergence of averaged values curve

Following previously mentioned force transducer characteristics along with the mounted system calibration, the standard deviation, zero return, repeatability and reversibility are tested, as well. Examples of raw signal treatment and averaging are given in Figures B.6 and B.7 for x and y axes. In Figure B.7(a) dependance of convergence to given static load can be observed in relation to the chunk size. There is a difference with the case depicted in Figure B.7(b) as the y-axis force transducers were preloaded with $\sim 127N$ and satisfying convergence may be reached somewhat sooner. Examples of the calibration curves, which are obtained by using progressing series of small loads to the mounted balance, are given in the Figure B.8. In these figures well maintained linearity may be observed with some minor deviations originating from the balance installation. Calibration curves corresponded well with the 3rd degree polynomial translation equations, while the complete matching of all static loads points was reached with

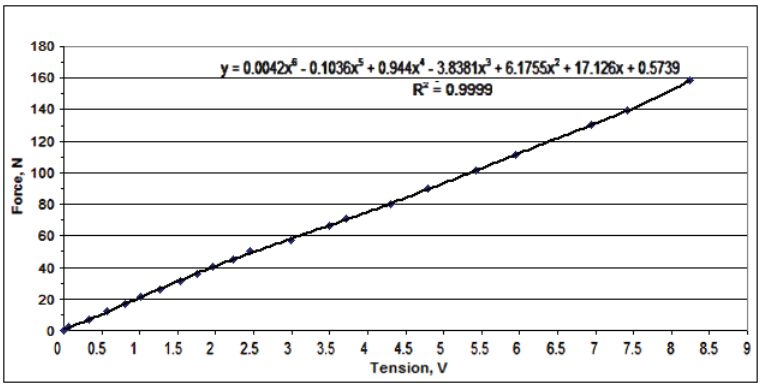

(a) x-axis, calibration curve

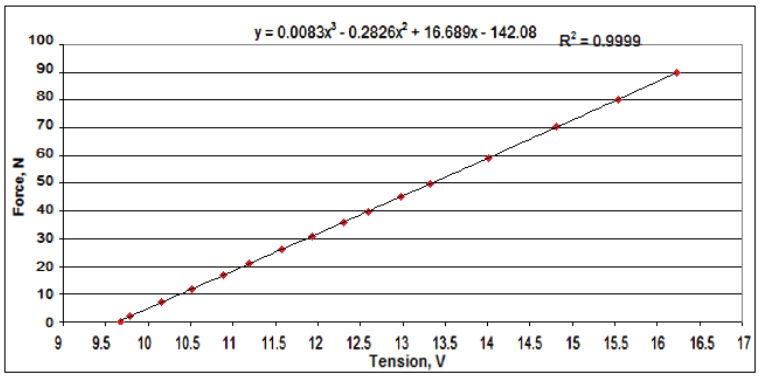

(b) y-axis, calibration curve

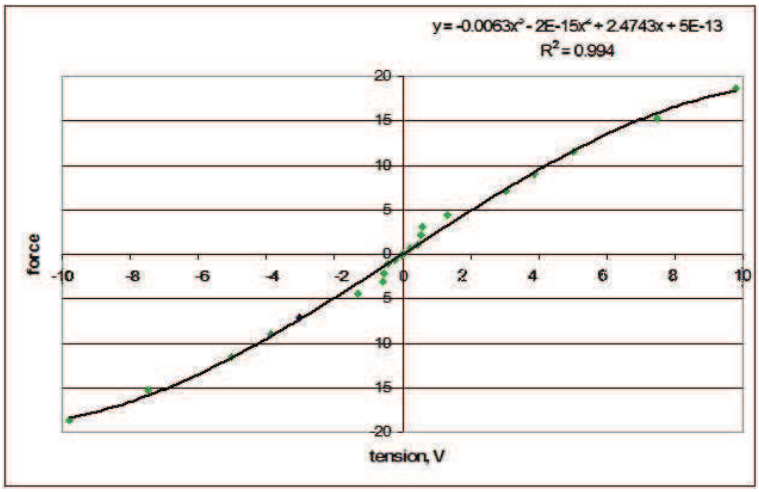

(c) z-axis, calibration curve

Figure B.8: Examples of calibration using series of small weights

6th degree curves. Reversibility, standard deviation and repeatability were measured on several sampling series and sample rates. In Figure B.9 an example of

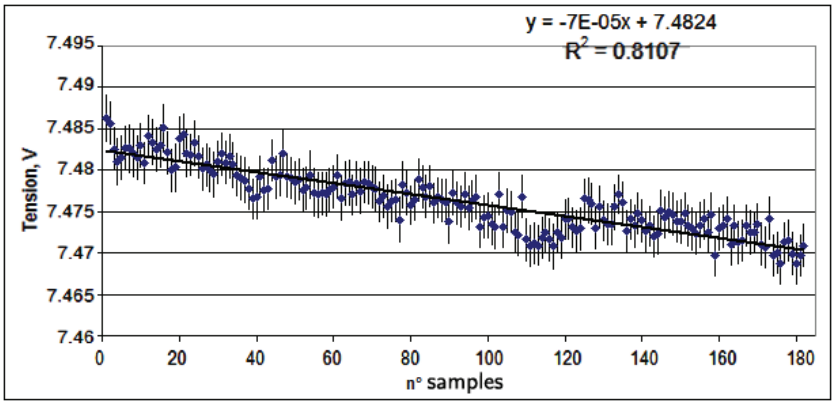

Figure B.9: Temporal evolution of x-transducers measurement at $0.25Hz$ and 182 samples for 139.4N of static load, with drift and deviation

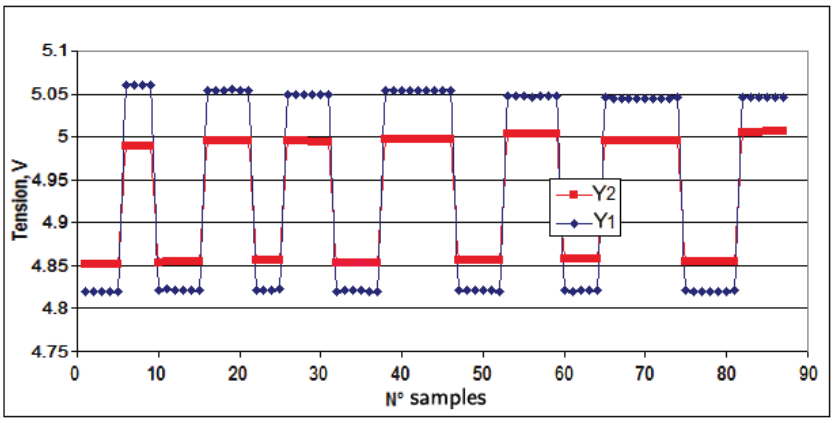

Figure B.10: Examples of repeatability test for y-axis force transducers under $5.14N$ of static load

x-axis transducer using 182 sample chunk at $0.25Hz$ sampling rate is given under load of $139.4N$. Raw signal data points are plotted together with their evaluated standard deviation values and drift from the median line, which evaluated equation is plotted on the graph. Repeatability of the y-axis which force component is measured with two HBM strain transducers were evaluated for each of them as depicted in Figure B.10. It can be observed that there were some slight difference in alternating values during signal sampling of two transducers. This factor, as

well as calibration and standard deviation are obtained as global values defined as arithmetic averaged values between 2 force transducers data. The final static evaluated data of mounted force balance are given in Table B.1.

Table B.1: Characteristic static calibration values of the three-axes force-balance

Axis:	X	Y	Z
standard deviation (mean)	0.05/(139.4N)	0.02/(5.14N)	0.002/(11.63N)
standard deviation (max), N	0.24	0.06	0.17
mean sensibility, V/N	0.053	0.073	0.783
repeatability, N	0.84	0.18	0.52
neutral return, N	1.7	0.1	0.41
creep, N/min	0.025		0.002
global precision, N	1.7	0.18	0.52

Given values are inline or slightly over the datasheet values of HBM transducers. It can be observed that better precision is obtained with y and z directions which measuring range is projected to be smaller, while the x axis has the largest range and therefore somewhat coarser characteristic values.

B.2 Flow meter and force measuring

Force balance under flow conditions is under constant unsteady loading which comes from air feeding system and from wind tunnel pumping group. In these conditions static kinematic friction of bearings is overcame and zero value slightly oscillates around the neutral value. The valuable force data is found as difference between the values after full flowing and before the full flowing. In Figure B.11 evolution of the chamber pressure is depicted with the axial force balance transducer. It can be noted that increase in sample chunk will lead to the better convergence and reaction of force transducer to the changes in chamber pressure.

Along with the y-force measurement, the mass-flow of the secondary injection was measured also using the Bronkhorst® EL-FLOW mass-flow meter (MFM). Laboratory profiled EL-FLOW F-111B gas mass-flow meter was selected with its range covering mass-flows from $0.04 l_n/min$ to $7.5 l_n/min$, where l_n/min represents

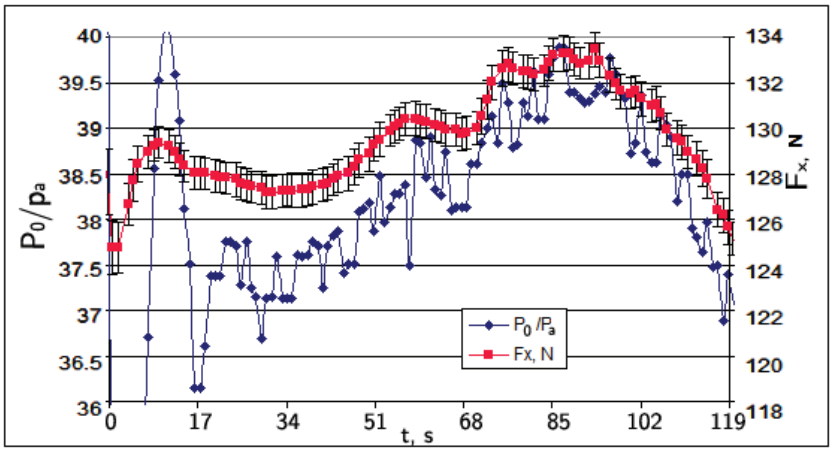

Figure B.11: Temporal evolution of chamber pressure along with the axial force

normalized air liters per minute. MFM consists of a thermal sensor microproces-

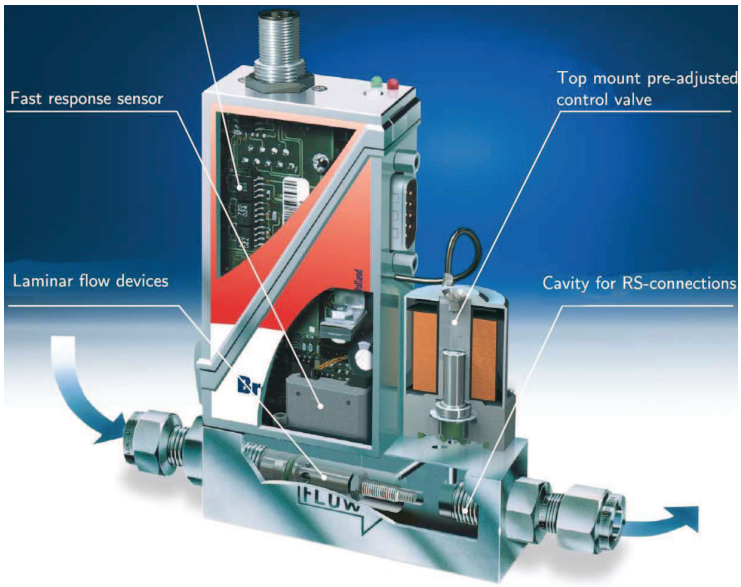

Figure B.12: EL-FLOW mass-flow meter

sor based PC-board with signal and fieldbus conversion. The mass flow, expressed in normal litres per minute, is provided as analog signal or digitally via RS232 or fieldbus. The heart of the thermal MFM is the sensor, that consists of a stainless steel capillary tube with resistance thermometer elements. A part of the gas flows through this bypass sensor, and is warmed up heating elements. Consequently

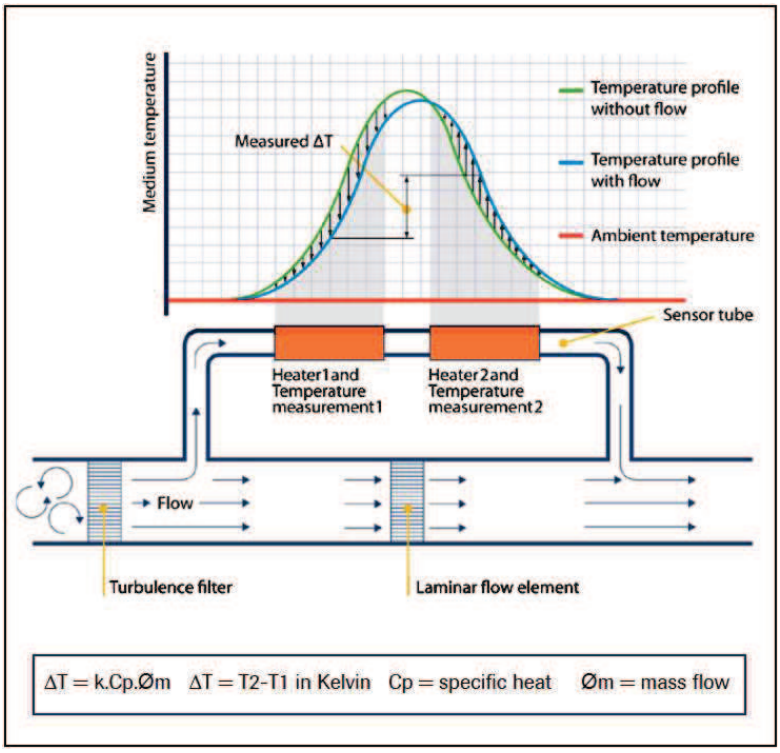

Figure B.13: Functional scheme of the thermal mass flow sensor by Bronkhorst®

the measured temperatures T1 and T2 drift apart. The temperature difference is directly proportional to mass flow through the sensor. In the main channel patented laminar flow element is applied consisting of a stack of stainless steel discs with precision-etched flow channels, as illustrated in Figure B.13. Thanks to the perfect flow-split the sensor output is proportional to the total mass flow rate.

Mass-flow rates of other gas species than air are evaluated in the same manner, imposing a translation coefficient to the thermally perfect gas equation. To verify MFM calibration and to obtain pressure loss values, pressure was measured before and after MFM flow section. Evaluated pressure loss using a cold air flow was in the range of $\sim 8.7\%$. Final pressure sensor on the secondary branch was mounted close to the end of secondary stilling chamber to verify the total chamber pressure before injection into the supersonic stream.

Appdx C - Version Française

C.1 Introduction générale

Le contrôle de la poussée (TVC) (Thrust vector control) d'un véhicule spatial dans les couches peu denses de l'atmosphère où l'usage de la réponse aérodynamique du système pour le pilotage de l'engin s'avère inopérante, est une nécessité. Dans ces conditions plusieurs systèmes peuvent être envisagés pour le contrôle de la poussée. Les méthodes conventionnelles sont généralement basées sur l'utilisation d'actionneurs mécanique ou électromécanique pour l'orientation de la poussée. Les systèmes mécaniques utilisent des vérins hydrauliques pour orienter la tuyère, ou des volets rétractables dans le cas des avions de chasse ou le pivotement de la nacelle du moteur.

L'origine et le concept du contrôle de la poussée datent d'avant l'invention du premier vol motorisé en 1903. Cependant, depuis, son évolution va de pair avec le développement prodigieux de l'industrie aéronautique et spatiale.
Les premiers aéronefs à orientation de la poussée datent d'avant la première guerre mondiale. On peut citer notamment l'aéronef *Delta* de la Figure 1.1(a) qui a été conçu avec un système propulsif comprenant des hélices orientables. Depuis, de nouveaux concepts de vectoriastion de la poussée ont été introduits comme la modification de l'angle des pales des hélices propulsives, l'invention de l'hélicoptère et des concepts hybrides d'hélicoptère/avions à surfaces portantes et enfin les technologies du type *Tiltrotor* comme l'exemple de la Figure 1.1(b).

Ces concepts ont largement prouvé leur robustesse et efficacité et sont à l'usage dans un grand nombre de cas de systèmes aéronautique et spatiale. Les systèmes

propulsifs comme turbopropulseur, turboréacteur, ramjet et moteur-fusée incorporent une tuyère pour accélérer le fluide et délivrer la poussée. La tuyère comme élément terminal du système est un candidat idéal pour l'implantation du dispositif du contrôle de la poussée. Les systèmes mécaniques de contrôle de la poussée comprenant des vérins hydraulique sont utilisés dans le cas des avions militaires pour accroitre leur manœuvrabilité, assurer le décollage et atterrissage courts (STOL) ou encore le décollage et l'atterrissage verticaux (VTOL).
On peut citer comme les premiers aéronefs intégrant la vectorisation de la poussée, l'avion Mirage IIIV de Dassault ou le fameux Haker-Siddeley Harrier utilisant pour ce dernier le moteur Rolls-Royce Pegasus vectorisé en poussée et hautement manœuvrable capable de VTOL. Les avions de dernière génération comme le MIG29 OVT, utilisent des moteurs avec une tuyère d'éjection faite de plusieurs segments (pétales) ou chaque segment est contrôlé séparément de manière à modifier la section de passage et aussi assurer un contrôle multiaxial de la poussée. La déviation de la poussée obtenue peut atteindre 90° dans toutes les directions.La technologie TVC (contrôle de vecteur-poussée) et les commandes électriques (Fly by Wire) semblent être les aspects dominants des avions de dernière et de futures générations.

Dans le cas d'un grand nombre de lanceurs tels les lanceurs de la famille Ariane, Figure 1.3, le lanceur JAXA H-IIB et dans le cas des moteurs principaux de la navette spatiale (SSMEs), on utilise habituellement des vérins hydrauliques couplés à un système de balancier pour déplacer la tuyère et la chambre de combustion dans son ensemble. L'écoulement à l'intérieur de la tuyère demeure axisymétrique alors que l'on cherche à faire diverger l'axe de la tuyère par rapport à l'axe de la fusée pour modifier ou corriger ainsi sa trajectoire.
Une variante de ce système de TVC est l'utilisation d'un ensemble de plus petites tuyères monté par exemple sur les lanceurs de la famille Soyouz-TMA ou sur le module de descente martien NASA-MLS *Curiosity*. L'orientation d'une plus petite tuyère requiert moins de puissance et offre une réponse dynamique plus rapide. Pour améliorer le système de contrôle de la poussée et accroitre la réponse dynamique, dans le cadre du projet du nouveau lanceur VEGA de l'ESA, les actionneurs électromécaniques remplacent sur les trois étages les vérins hydrauliques permettant ainsi un gain de poids et une meilleure réponse dynamique.

Les déflecteurs mécaniques montés en sortie des tuyères sont aussi utilisés pour dévier le jet et contrôler le vecteur-poussée, par exemple sur les missiles terre-air et air-air.

Une alternative intéressante aux systèmes de contrôle mécanique de la poussée se retrouve dans le contrôle fluidique de l'écoulement à l'intérieur de la tuyère pouvant procurer une simplicité d'utilisation, un gain substantiel de poids et une meilleure réponse dynamique. Un tel système, l'objet de la présente étude utilise le principe de la déviation du jet principal à l'aide de l'injection d'un fluide secondaire dans le divergent de la tuyère. Plusieurs concepts de vectorisation fluidique peuvent être envisagés : la vectorisation par le contrôle de l'onde de choc créée par une injection secondaire, la distorsion de la ligne sonique par l'injection secondaire au voisinage du col, les injections asymétriques pariétales co-courant et contre-courant. Le principe commun aux trois concepts est la création d'un gradient de pression adverse par une injection secondaire dans l'écoulement principal.

Les méthodes de vectorisation de la poussée par incorporation des écoulements co-courant ou contre-courant nécessitent la création d'un conduit parallèle dans le corps de la tuyère comme illustrés à la Figure 1.4(a). Les avantages de cette méthode sont d'une part un très bon rapport de poussées entre les situations non vectorisés et vectorisée et d'autre part un angle important de déviation pour des écoulements faiblement supersonique. Les inconvénients de la méthode sont en revanche une structure complexe de la tuyère donc un regain de masse et un possible ré-attachement de l'écoulement du à l'effet Coanda pour un certain régimes d'écoulement. Par ailleurs, l'effet Coanda est justement mis à contribution pour vectoriser la poussée dans le cas de l'utilisation de la méthode de contre-courant.

La distorsion de la ligne sonique nécessite une injection asymétrique au voisinage du col d'une tuyère convergent-divergent. En déplaçant ainsi la section minimale sonique, l'aérodynamique de l'écoulement de la partie subsonique se retrouve ainsi dissymétrrisée conduisant à une vectorisation de la poussée. L'avantage de cette méthode par rapport à la méthode de contrôle de choc réside dans une moindre perte de poussée conduisant à une vectorisation très efficace pour de

faibles rapports de pression de la tuyère (NPR). En revanche, pour les rapports de pression élevés, cette méthode s'avère moins efficace en terme de l'angle de vectorisation et peut conduire à des situations d'écoulement instables dans le divergent. Cette méthode est suggérée venant en complément de la méthode de contrôle du choc pour une vectorisation multiaxiale.

Le contrôle de la poussée par injection fluidique regroupe un certain nombre de concepts ou la déviation de la poussée est obtenue par injection d'un fluide secondaire, perpendiculaire à l'axe de la tuyère déviant ainsi l'écoulement principal et générant par voie de conséquence une force latérale utile à la vectorisation. Contrairement aux concepts exposés dans le paragraphe précédent, cette méthode a été utilisée avec succès sur un certain nombre de missiles balistiques intercontinentaux comme LGM-30F Minuteman-II ou le missile balistique UGM-27C Polaris A3 et son successeur UGM-73, lancés à partir d'un sous-marin. A noter que pour des engins plus récents utilisant la propulsion liquide, cette méthode de contrôle par injection fluidique a été écartée au profit des méthodes classiques (utilisation de vérins hydraulique).
Cependant, au cours des dernières années, due à l'apparition des moteurs-fusées hybrides et leur utilisation potentielle dans des lanceurs commerciaux à des fins touristiques, on peut noter un regain d'intérêt pour ce type de concept de contrôle de la poussée. A ce propos, on peut rapporter que la société SPG fournisseur de moteur pour le projet SpaceX utilise le concept de contrôle par injection fluidique pour son moteur hybride en utilisant le fluide stocké dans le réservoir d'oxygène liquide.

CONTEXTE DE L'ETUDE

Les avantages attendus de la méthode de vectorisation fluidique (gain de masse, robustesse/simplicité, réponse dynamique rapide) en font un candidat idéal pour les petits lanceurs expérimentaux tels par exemple celui envisagé dans le cadre du programme PERSEUS du CNES.
Le présent travail de thèse se situe dans le cadre du projet PERSEUS du CNES qui a pour but le développement de concepts innovants pour les systèmes de propulsion avancés ou futurs. Le travail ayant pour sujet central la vectorisation par injection fluidique couvre un large spectre d'aspects de ce problème. Bien que

cette méthode de vectorisation soit bien connue, son utilisation dans le contexte de petits lanceurs spatiaux ne possédant pas de réservoirs de stockages additionnels reste à prouver. D'autre part, ayant pour objectif l'applicabilité de la méthode, le périmètre de cette étude a été restreint en limitant le débit secondaire à moins de 5% du débit principal et le rapport des pressions du jet secondaire et du jet principal aux alentours de l'unité.

L'injection transversale dans le divergent d'une tuyère axisymétrique y génère un écoulement complexe impliquant un décollement asymétrique due à un gradient de pression adverse, des interactions et réflexions de chocs diverses et des zones de vortex gouvernant le mélange des flux en aval.
De plus, ces effets sont couplés à la nature confinée de l'écoulement supersonique dans le divergent, ce qui rend don étude particulièrement ardue. A celles-ci s'ajoutent aussi les propriétés et les conditions d'écoulement des fluides primaire et secondaire et l'instationnarité de ces conditions. Pour aborder ce sujet, une triple approche, analytique, numérique et expérimentale a été mise en œuvre. Vue la complexité du problème et la multiplicité des paramètres en jeu, l'analyse intégrant les trois approches était nécessaire pour aborder la problématique de la vectorisation fluidique de la poussée par contrôle de choc dans son ensemble. Les études numérique et expérimentale ont été conduites au laboratoire ICARE du CNRS à Orléans. Pour la partie expérimentale une plateforme d'essais dédiée à cette étude a été développée au cours de cette étude.

ORGANISATION DU DOCUMENT

Ce manuscrit est organisé de la façon suivante :

Après ce premier chapitre introductif, le chapitre 2 décrit les différents aspects et les phénomènes mis en jeu lors de l'injection transversale 2D et 3D respectivement à travers une plaque plane et dans le divergent d'une tuyère. Il s'ensuit la présentation de la conception et les critères de performance d'une tuyère propulsive convergente-divergente. Dans la dernière partie de ce chapitre, on présente les modèles analytiques élaborées pour évaluer les performances de ce type de vectorisation.

Le chapitre 3 décrit le banc et les méthodes expérimentales employés dans cette étude. Les méthodes de diagnostic, qualitative et quantitative sont égale-

ment décrites. Les différents modèles de tuyères sont présentés et leur choix est argumenté.

Le chapitre 4 décrit le travail numérique. Outre, la description du code, il relate la mise en œuvre de la méthode numérique, l'élaboration du maillage. La qualité du maillage et les critères de convergence sont détaillés.

Le chapitre 5 relate particulièrement l'étude de l'influence des paramètres principaux tels le profil de la tuyère primaire, le point d'injection, le rapport des débits et les régimes d'écoulement.

Le chapitre 6 contient l'influence des caractéristiques supplémentaires comme la forme et l'angle de l'injecteur et le nombre de points d'injection.

Le chapitre 7 décrit les études numérique et expérimentale menées sur les l'influence des propriétés des gaz primaire et secondaire. Le chapitre s'étend sur l'étude numérique de la vectorisation fluidique impliquant des gaz multi-espèces non réactives (gaz chauds).

Dans la dernière partie, une synthèse générale sous forme de conclusion ainsi que les perspectives pour la suite de ce travail sont présentées.

C.2 Chapitre 2

Le contenu de ce chapitre est dédié aux fondements théoriques, à l'état de l'art et la modélisation analytique de la vectorisation fluidique d'une tuyère.

La problématique de l'injection secondaire dans le divergent d'une tuyère supersonique peut être reliée au phénomène fondamental, de l'interaction d'un écoulement supersonique avec un jet sonique transversal, à travers une fente (configuration 2D) ou un orifice circulaire (configuration 3D) dans une plaque plane. Du point de vue aérodynamique, le développement du jet injecté dans l'écoulement supersonique principal agit comme un obstacle, autour duquel se forme un choc détaché (Bow shock). L'apparition de cet obstacle et du choc associé induit un gradient de pression adverse dans la couche limite en aval de l'injection. L'augmentation de celui-ci conduit à l'épaississement de la couche limite et éventuellement à la séparation de l'écoulement principal de la plaque plane, générant ainsi un éventail d'ondes qui se focalisent en un choc fort pouvant interagir éventuellement, plus loin en aval, avec le choc détaché (Bow shock). Dans la zone de séparation, une large zone de recirculation est formée comprenant deux tourbillons contrarotatifs, un tourbillon primaire amont (PUV) et un tourbillon secondaire aval (SUV). En aval de l'injecteur et proche de la plaque plane, des tourbillons de sillage sont formés avec ré-attachement de l'écoulement sur la plaque. Dans le cas tridimensionnel d'une injection à travers un orifice circulaire, les tourbillons PUV et SUV peuvent être identifiés comme le tourbillon en forme de fer à cheval (horseshoe) qui envelopperait le jet injecté. Le jet sonique secondaire est largement surdétendu subissant une succession de détente et de recompression à travers des faisceaux de détente et d'ondes de choc respectivement. Ainsi la première séquence de détente et de recompression se termine par un disque de Mach. Les zones de haute pression en amont et de la basse pression en aval du jet provoquent une inclinaison naturelle du jet vers l'aval de l'écoulement. Un mécanisme de mélange des jets dû aux phénomènes complexes d'interaction et de réflexion des chocs avec les tourbillons de sillage se produit en aval du jet.

De manière analogue, la configuration complexe des structures observées lors d'une injection transversale d'un fluide dans un écoulement supersonique peut très bien être transposée dans le cas d'un écoulement confiné. Le cas d'une injection

à travers une fente dans le divergent d'une tuyère 2D ou l'injection à travers un orifice circulaire dans le divergent d'une tuyère 3D axisymétrique représentent l'essentiel des applications dans ce domaine. Les effets de confinement par les parois et la nature non uniforme de l'écoulement dans une section donnée de la tuyère est de nature à rendre la structure de l'interaction et l'évaluation de la distribution des forces s'appuyant sur les parois de la tuyère beaucoup plus complexe.

Les nombreux travaux entrepris dans les années 1960, période ayant vu les premières études significatives menées sur la vectorisation induite par choc (SITVC), ont été largement focalisés sur le développement de modèles analytiques permettant une bonne modélisation de l'interaction d'un jet avec un écoulement supersonique et d'évaluer les charges latérales induites. Dans le modèle bien connu de Zukoski et Spaid, le jet injecté est assimilé à un obstacle solide, dont la hauteur de pénétration est considérée comme le paramètre caractéristique du problème. Partant de là, un modèle analytique, développé pour le cas de l'injection dans une tuyère propulsive, a été adopté et utilisé dans ce travail. Les équations permettant l'évaluation des variables telles que : Pression, frottement pariétal, forces, moments et coefficient de performance, utilisées dans le modèle analytique, sont tirées et présentées dans ce chapitre. Les résultats présentés tout le long de ce manuscrit sont exprimés sous forme de valeurs adimensionnés en termes de coefficients de pression, force, moments et frottement pariétal. Trois coefficients de performance majeurs ont été identifiés : le facteur d'amplification de la vectorisation, le facteur d'amplification de la force globale et le facteur d'amplification de l'impulsion spécifique.

C.3 Chapitre 3

Dans ce chapitre sont décrits, le banc expérimental, les méthodes de mesures et de diagnostic.

Les expériences ont été réalisées dans la soufflerie à rafale EDITH de l'institut ICARE du CNRS d'Orléans. La soufflerie et les équipements de mesure et de diagnostic ainsi que les programmes d'acquisition associés ont été conçus et

élaborés par les auteurs de cette étude. L'installation de la soufflerie est composée, d'un compresseur permettant de stocker de l'air sec et propre à 300 bars dans des bouteilles de 320 litres, d'un réseau de tuyauterie haute pression, d'un régulateur de pression. La chambre de tranquillisation et la tuyère montée sur une balance aérodynamique à 3 axes, sont placées dans un caisson dépressurisé par un groupe de deux pompes à vide de 345 kw de puissance. Le flux secondaire (injecté) est alimenté soit par le réseau d'air comprimé ou bien par des bouteilles sous pression à travers un détendeur secondaire et un convergent via une chambre de tranquillisation secondaire.

Les moyens d'investigation qualitative utilisés dans cette étude reposent sur l'analyse des structures des chocs induits dans l'écoulement aux moyens d'un banc strioscopique de type schlieren monochromatique et à deux couleurs dont l'image est projetée sur l'élément sensible d'une caméra rapide. Les investigations quantitatives reposent quant à elles sur l'utilisation d'une balance aérodynamique pour la mesure des différentes composantes des forces appliquées sur les tuyères étudiées, de capteur de pression et sonde de température pour les conditions d'arrêt et des capteurs de pression stationnaire et instationnaire pour les pressions pariétales. Toutes les mesures ont été enregistrées de façon synchronisée via une interface LabView et post-traitées par Matlab.
Au total, cinq profils de tuyères, conçus et réalisés, ont été testés expérimentalement dans cette étude. Par ailleurs, deux convergents soniques permettant l'adaptation de la chambre secondaire aux différents types d'injecteurs (circulaire et rectangulaire) ont été également conçus et réalisés.

C.4 Chapitre 4

Les méthodes et outils numériques utilisés dans cette thèse sont décrits et présentés en détail dans ce chapitre.

Les calculs numériques réalisés dans cette étude reposent sur le code CPS_C développé par le groupe Bertin en collaboration avec le CNES. Les équations de Navier-Stokes moyennées par la méthode Favre, écrites en formulation volumes finis pour un fluide compressible, sont résolues en utilisant un schéma explicite

et tenant compte pleinement de la viscosité du fluide. Les effets visqueux et la turbulence sont par ailleurs modélisées suivant le modèle standard $k-\varepsilon$ de Jones-Lander et pour certains cas comparés au modèle RNG $k-\varepsilon$.

Un nombre important de cas de vectorisation de tuyères ont été considérés. Les maillages des domaines de calcul parfois très complexes ont été générés en utilisant l'outil Gambit-ANSYS, suivant trois niveaux de raffinement correspondant successivement à 1, 2 et 3.7 millions éléments en considérant la moitié du domaine de calcul pour raison de symétrie. Les calculs ont produit des résultats très proches pour les deux derniers niveaux de raffinement. Par la suite les calculs ont été poursuivis avec le niveau de raffinement intermédiaire. Typiquement le domaine de calcul comprenait le convergent, le divergent, l'injecteur secondaire et le milieu ambiant entourant la sortie de la tuyère. Un niveau de raffinement à la paroi correspondant à Y+ aux environs de 1 a requis 30 éléments de maillage dans la couche limite, par conséquent aucune loi de paroi n'a été nécessaire dans ces calculs. Outre dans la couche limite, les maillages ont été particulièrement resserrés au voisinage des cols des tuyères principale et secondaire, et relâchés vers l'aval et l'extérieur du domaine de calcul.

Dans les chapitres suivants, les résultats des performances de vectorisation sont analysés et présentés en utilisant une approche intégrant à la fois les résultats numériques et expérimentaux.

C.5 Chapitre 5

Dans ce chapitre sont présentées les analyses des performances produites par : La position et le type d'injecteur, le type et les taux de détente des tuyère principale et secondaire.

Le positionnement de l'injecteur dans une section donnée du divergent de la tuyère propulsive a à la fois une influence substantielle sur la topologie complexe résultant de l'interaction des écoulements, et sur les performances de la vectorisation de la tuyère. Dans ce travail deux positions caractéristiques ont été étudiées expérimentalement et numériquement, alors que d'autres points d'injection , si-

tués entre ces deux positions, ont été étudiés par simulation numérique. Un injecteur placé en amont de la section de sorti de la tuyère à la position $x_j/x_t = 0.7$ produit un écoulement très complexe caractérisé par une multitude de réflexion de chocs, un affaissement du jet secondaire, une séparation de l'écoulement principal sur la face opposée à l'injection suivi d'un recollement en aval et un choc caractéristique. Il a été trouvé que cette configuration affecte négativement les

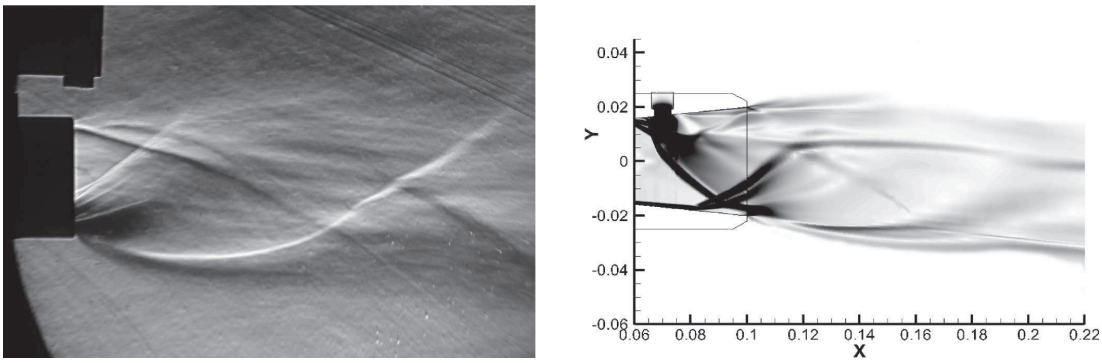

(a) strioscopie expérimentale (b) strioscopie numerique

FIGURE C.1 – Strioscopie de tuyere conique avec l'injection secondaire à $x_j/l_n = 0.7$

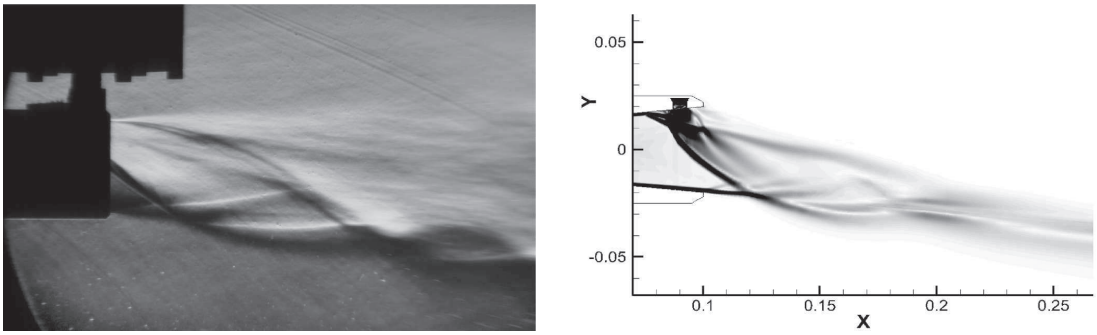

(a) strioscopie expérimentale (b) strioscopie numerique

FIGURE C.2 – Strioscopie de tuyere conique avec l'injection secondaire à $x_j/l_n = 0.9$

performances de la tuyère en plus de potentielles charges latérales instationnaires sur la tuyère. Les structures issues de l'interaction des écoulements sont présentées sous forme d'images strioscopies (schlieren) numériques et expérimentales ainsi

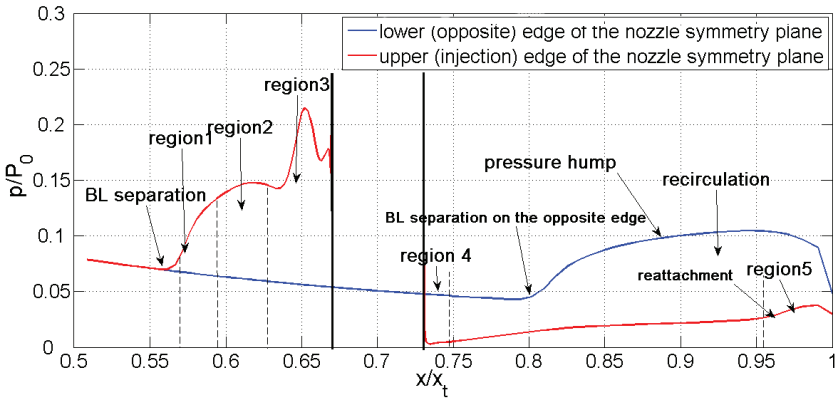

(a) Distribution de la pression pariétale

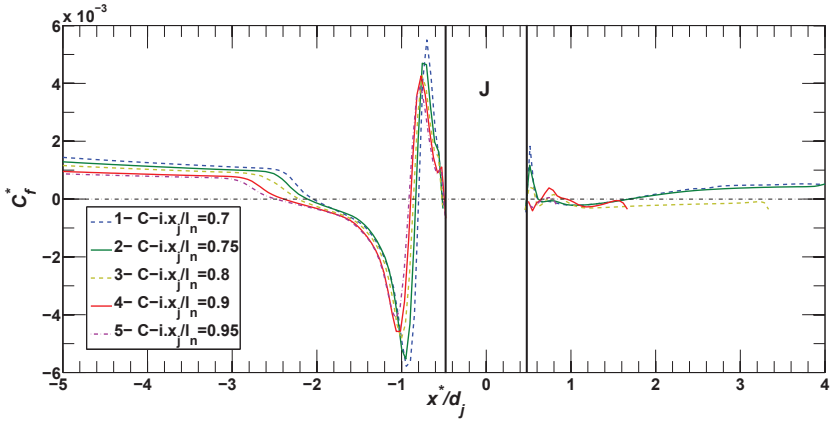

(b) Lignes de frottement de différents cas d'injection

FIGURE C.3 – Distribution de la pression et du frottement pariétal

que sous forme de courbes iso-valeurs. Le positionnement du point d'injection proche de la section de sortie de la tuyère à $x_j/x_t = 0.9$ permet l'élimination des réflexions des chocs et le réattachement de l'écoulement en aval. De plus, l'analyse des pressions pariétales obtenues expérimentalement et numériquement ainsi que les composantes des forces ont montré que les forces appliquées aux parois de la tuyère et les performances de la vectorisation évoluent favorablement et de façon analogue avec le déplacement du point d'injection vers la sortie de la tuyère. Ceci peut être traduit comme une conséquence au déséquilibre, entre la zone de haute pression en amont de l'injecteur et basse pression en aval, qui est positif pour des injections de plus en plus proche de la sortie de la tuyère. Avec l'augmentation du taux de détente de la tuyère, l'enveloppe de l'écoulement à travers le choc dimi-

nue graduellement. Ceci a la même conséquence sur le rapport des composantes pariétale et axiale des forces agissant sur la tuyère qui décroit légèrement pour les tuyères conçues pour des Mach plus élevés. Dans cette étude, deux taux de

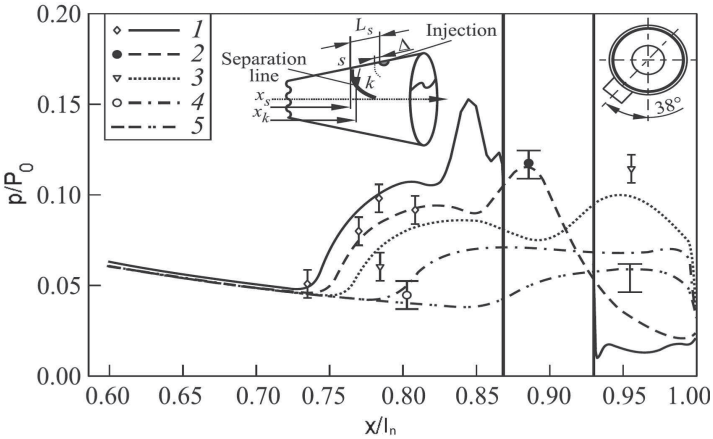

FIGURE C.4 – Répartition de la pression sur différents méridiens de la tuyère et détection de la ligne de séparation : 1 --→ 0°(*symetrie*), 2 --→ 25°, 3 --→ 38°, 4 --→ 60° et 5 --→ 90°.

détentes ont été comparés ; tuyère à Mach 3 et tuyère à Mach 5 avec un rapport de débit fm constant correspondant à un rapport SPR = 1. Outre l'effet du taux de détente de la tuyère, le type de profil de celle-ci a également été étudié. Quatre différents profils de tuyère ont été abordés dans cette étude : Conique, Idéal tronqué (TIC), profil optimisé en poussée (TOC) et le profil à gradient de pression adverse (APG). Contrairement aux deux premiers, les profils TOC (Rao) et APG sont caractérisés par un important choc interne qui explique leur différence avec les tuyères idéales sans choc interne. Les analyses réalisées sur les tuyères à Mach 3 et mach 5 montrent un effet très limité sur les l'écoulement et performances de vectorisation. Cependant, on peut clairement distinguer le choc détaché (bow schock) à travers les différentes régions de l'écoulement. Une analyse rapide sur la vectorisation fluidique (SITVC) d'une tuyère APG montre qu'il y a une légère augmentation de l'angle de vectorisation et de la force pariétale, mais une optimisation supplémentaire est nécessaire pour des performances optimales.

Le taux de pression d'injection secondaire (SPR), qui, dans le cas d'un écoulement d'air froid et sec, peut également être représenté par le rapport du débit

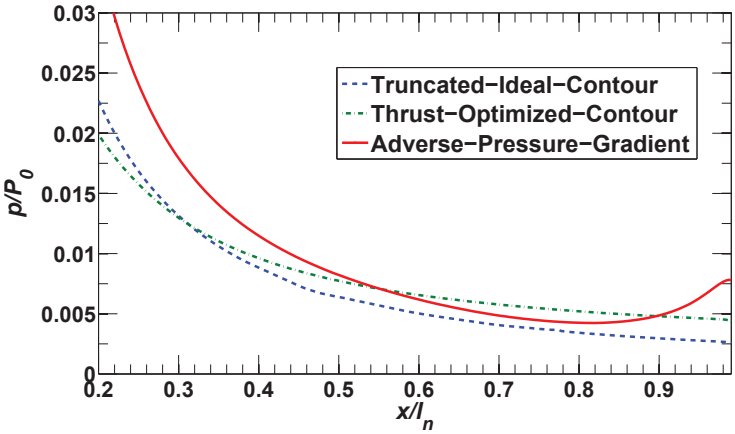

FIGURE C.5 – profils de pression dans le plan de symétrie pour différents types de tuyère

massique secondaire au débit primaire, peut affecter sur le bon fonctionnement de la tuyère. En effet, une pression d'injection élevée, et par conséquent un débit injecté élevé, conduisent à une plus grande hauteur de pénétration du jet, se traduisant par un gradient de pression adverse induit plus important, d'où une zone de séparation plus étendue et un angle de choc de séparation plus important. Cependant une augmentation de la déviation ne varie pas linéairement proportionnelle aux taux d'injection secondaire et par conséquent l'impulsion spécifique globale et les coefficients de vectorisations diminuent quand SPR augmente. Le rapport de détente de la tuyère principale (NPR) influence directement le profil de l'écoulement en sortie de la tuyère et implicitement affecte le développement du jet secondaire. Pour cela, plusieurs cas de fonctionnement en surdétente de la tuyère ont été examinés. Pour des valeurs modérées de NPR, le fonctionnement en surdétente de la tuyère a quelque peu un effet favorable sur la vectorisation, du moment qu'il favorise le rapport de la force pariétale à la force axiale et permet une relaxation de l'écoulement dans la zone d'aspiration en aval de l'orifice d'injection. Une diminution supplémentaire du taux de détente de la tuyère conduirait à la séparation de l'écoulement, non perturbé, au voisinage de la section de sortie de la tuyère, et à un système complexe d'interférence de chocs. Cette configuration affecte de plus en plus la vectorisation de la tuyère avec une limite atteinte lorsque le disque de Mach, résultant de ces interactions arrive au niveau de la

section de l'injecteur.

C.6 Chapitre 6

Les effets de la géométrie de l'injecteur, l'orientation et le type d'injection sont analysés et élaborés dans ce chapitre.

La modification de la géométrie de l'injecteur de sa forme circulaire initiale a des conséquences sur la pénétration du jet secondaire et implicitement sur l'interaction des jets croisés et sur le taux de déviation. Une injection par fente rectangulaire a été réalisée et examinée dans cette étude. La fente rectangulaire est usinée de telle sorte que sa longueur corresponde à un arc de 30° par rapport à l'axe de tuyère principale et sa largeur calculée de façon à avoir la même surface que l'injecteur circulaire. L'injection par fente affecte une région plus grande de l'écoulement principal avec une plus large zone de séparation dans la direction latérale tout en gardant une hauteur de pénétration satisfaisante. Au regard des résultats obtenus dans cette étude, en termes de pressions pariétales et forces aérodynamiques, il a été mis en évidence que le passage de l'injection circulaire à l'injection rectangulaire affecte positivement les performances de la vectorisation.

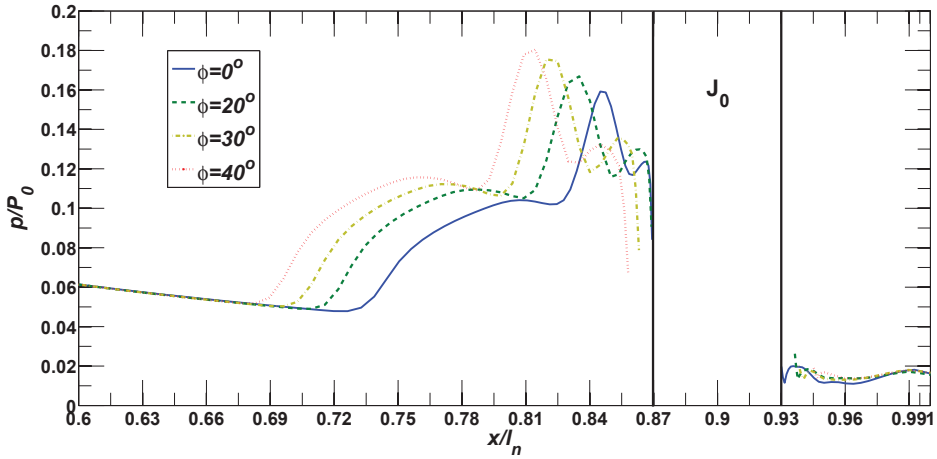

FIGURE C.6 – Distribution de la pression pariétale dans le plan de symétrie de la tuyère conique pour différents angles d'inclinaison, φ

L'orientation du jet, par rapport à la direction de l'écoulement de la tuyère, a un effet encore plus important que celui de la géométrie de l'injecteur. Pour examiner ses influences, une injection circulaire inclinée à 20° vers l'amont de l'écoulement principal a été réalisée et étudiée sur un modèle de tuyère conique. Après une comparaison et validation des résultats expérimentaux et numériques, une large gamme d'angles d'injection a été simulée numériquement. Si une injection inclinée vers l'aval de l'écoulement produit des résultats non escomptés, en termes de déviation et force latérale, l'injection inclinée vers l'amont de l'écoulement (à contre courant) améliore largement ces effets. Ceci est du en grande partie à la poussée exercée sur l'écoulement principal et à l'augmentation du gradient de pression adverse dans la zone séparée. Il a été constaté également un effet négatif sur la composante axiale de la force de poussée qui diminuerait implicitement la poussée globale, ce qui favoriserait le coefficient de vectorisation, avec tout de même un effet négatif sur la force globale et l'impulsion spécifique. Par conséquent, ces effets négatifs et positifs doivent être contrebalancés dans l'optimisation de la méthode de vectorisation (SITVC). Il a été prouvé qu'une inclinaison vers l'amont d'un angle compris entre 20 et 30° donnerait les meilleurs résultats en termes de déviation produite tout en maintenant un niveau satisfaisant pour l'impulsion globale.

En plus du contrôle de la vectorisation par une mono injection sonique, deux autres modes d'injection pour le contrôle de la vectorisation (SITVC) ont été simulés numériquement. Le premier d'entre eux consiste à remplacer l'injecteur sonique par un injecteur supersonique, pour le même SPR et le même taux d'injection. L'objectif étant d'augmenter la force réactive du jet (impulsion du jet). Pour cela, deux injecteurs, conçus pour produire des jets à Mach 1.3 et Mach 1.9 en sortie, ont été testés. Les deux modèles d'injecteurs ont conduit à une amélioration de la composante de la force réactive, mais en même temps à une large détérioration de la composante pariétale.
Le deuxième modèle comporte une injection multiple ,composée de trois orifices répartis sur un angle de 30°, radialement ou suivant une méridienne, et testée sur une tuyère TIC à Mach 5. L'injection multi-orifices produit un écoulement interne et des interactions beaucoup plus complexes. Dans cette étude, il a été trouvé qu'une distribution linéaire des orifices conduit à des résultats négatifs,

alors que l'injection à travers des orifices répartis radialement sur 30° conduit à des résultats similaires voire légèrement améliorés par rapport à une injection mono orifice. Bien qu'il n'y'ait aucun gain direct dans l'utilisation d'une injection multi-orifices, cette méthode pourrait être utilisée pour les ajustements plus fins.

C.7 Chapitre 7

Ce chapitre est divisé en deux partie principales. Dans la première partie, les effets des propriétés physiques du gaz et de l'injection d'espèces multiples ont été étudiés. Dans la seconde partie, des simulations CFD de la vectorisation dans le cas de gaz chauds ont été réalisées puis analysées.

Les propriétés des espèces chimiques affectent considérablement la structure de l'écoulement sur les interactions qui en découlent. Les propriétés thermodynamiques des espèces gazeuses ont été modélisées par Chemkin, en utilisant des polynômes d'ordre 7 pour la capacité calorifique, la conductivité thermique et la viscosité alors que la diffusivité est donnée par le nombre de Schmidt. Dans cette étude les gaz sont considérés comme parfaits. Différents types de gaz ont été utilisés comme gaz d'injection : Hélium, Dioxyde de Carbonne et Argon. Dans ces tests, notre attention s'est focalisée sur les rapports des pressions secondaires SPR et le taux d'injection. Il a été constaté une certaine corrélation entre le produit de la masse molaire par le rapport des chaleurs spécifiques (gamma) et le coefficient de performance. En effet, l'utilisation d'espèces pour lesquelles le produit M.gamma est faible, améliore les courbes de performances. En revanche, la performance est atténuée pour les espèces les plus lourdes.

Pour les applications futures des petits lanceurs pilotés par le programme CNES-Perseus, la vectorisation (SITVC) est simulée numériquement en conditions opératoires réelles. Les fusées Perseus sont prévues pour fonctionner avec un combustible écologique de type éthanol. Dans la présente étude, deux couples de propergol ont été utilisés, $LH_2 - LO_x$ et éthanol-LO_x, à une pression de chambre de 20 bars et une température de combustion de 3200K. Le processus de combustion a été calculé en utilisant le code NASA CEA2 de Gordon-McBride. Un calcul 1D axisymétrique de la tuyère a été réalisé au moyen de GRIMech 2.11 avec un

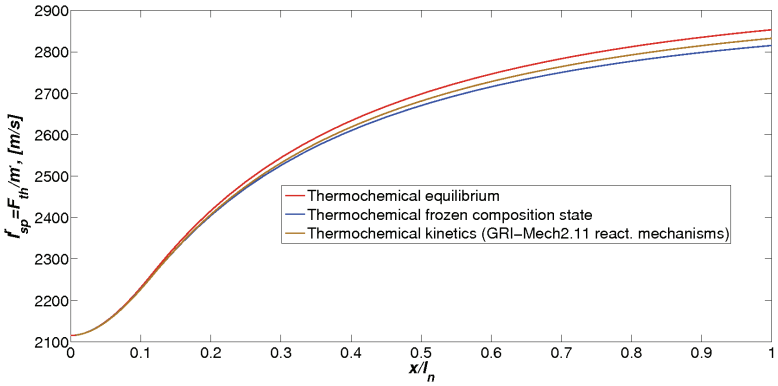

FIGURE C.7 – Evolution de l'impulsion spécifique (calcul 1D) pour le cas du mélange $C_2H_5OH - lO_X$

mécanisme cinétique réduit pour les couples $LH_2 - LO_x$ et éthanol-LO_x, puis comparé avec les calculs à l'équilibre et figé. Des simulations 3D avec le code CPS_C ont été réalisés pour une tuyère vectorisée avec injection secondaire alimentée en gaz chaud, en considérant un écoulement multi-espèces et figé. L'analyse de ces calculs montre que les performances obtenues restent analogues à celles obtenues avec de l'air froid.

C.8 Conclusions

Une analyse détaillée combinant les approches expérimentale, numérique et analytique a été conduite, concernant la vectorisation fluidique de la poussée, objectif assigné à ce travail de thèse et dont les résultats et discussions sont présentés dans les chapitres 5, 6 et 7.

L'étude concernant la position d'injection révèle deux zones d'intérêt distinctes. Lorsque l'injection s'effectue dans la première zone située plus en amont, le choc de décollement est réfléchi par la paroi opposée à l'injection, à l'intérieur de la tuyère, conduisant à une charge latérale induite sur le côté opposé, réduisant ou annulant la vectorisation dans le sens désiré. La seconde zone se situe entre la situation limite ou le choc se réfléchit sur la lèvre de la tuyère et une position d'injection proche de la section de sortie de la tuyère. C'est dans cette seconde zone où la vectorisation est la plus optimale. L'analyse d'un grand nombre de cas

tests montre qu'elle est la conséquence du déséquilibre des pressions entre la zone de haute pression provoquée par un fort choc de décollement située en amont de l'injecteur et une zone de basse pression en aval de celui-ci.

L'influence du taux de détente de la tuyère principale est un autre paramètre dont l'influence est examinée. Notre étude effectuée pour une tuyère avec un nombre de Mach de sortie de 3 et 5 montre que ce paramètre a peu d'influence sur les performances de vectorisation. On montre également que la vectorisation par contrôle de choc peut s'opérer sur plusieurs types de tuyère. L'essai dans les mêmes conditions d'une tuyère avec la présence d'un choc interne due à la non continuité de la pente comme celle de Rao révèle les même performances de vectorisation que celle d'une tuyère idéale sans choc interne. En revanche, ces performances peuvent être davantage augmentées en utilisant une tuyère du type APG (Adverse Pressure Gradient).

L'étude sur les conditions d'injection de l'écoulement secondaire montre une relation directe entre la pression d'injection et la hauteur de pénétration qui détermine en conséquence l'étendue de la zone d'interaction et l'intensité et l'angle de la composante latérale de la poussée. On montre également une diminution du facteur d'amplification d'impulsion qui est le rapport entre les impulsions spécifiques des modes vectorisé et non-vectorisé avec l'augmentation du débit de l'injection secondaire. Il est aussi montré que les faibles sur-détentes de la tuyère favorisent la vectorisation et que cette tendance s'inverse en augmentant davantage la pression ambiante. Cette inversion se produit lorsque le disque de Mach dû à la surdétente atteint la section de la tuyère située au regard de la position d'injection.

Les résultats concernant les paramètres d'injection secondaire montrent que l'angle d'injection (l'angle entre l'axe de l'injecteur et l'axe de la tuyère) est un paramètre déterminant et essentiel affectant grandement les performances de la vectorisation dans le sens où il est déterminant en ce qui concerne l'étendue de la zone de séparation et le taux de déflection du jet primaire par l'obstacle fluidique. Cependant, pour des angles d'inclinaison importants, des instabilités de l'écoulement principal, pouvant affecter la vectorisation, ont été constatées. D'après cette étude, un angle optimal aux alentours de 25° a été trouvé.
De plus, en vue de son optimisation plusieurs types de géométrie de l'injection

secondaire ont été considérés. Il s'est avéré qu'une orifice d'injection secondaire de forme rectangulaire avec son grand axe suivant l'une des circonférences de la tuyère constituait une configuration optimale pour la vectorisation de celle-ci. En revanche, une injection supersonique secondaire assurée par une tuyère convergente-divergente non seulement n'améliorait pas les performances de la vectorisation mais était significativement défavorable à celle-ci.
Il a été également montré qu'une injection secondaire en de multiple points ou "multiport" n'apportait pas d'amélioration significative en terme de performance de vectorisation. De plus, l'injection "multiport" groupés suivant la génératrice de la tuyère était défavorable à la vectorisation alors qu'un groupement des points d'injection suivant la circonférence donnait un résultat identique à celle avec un seul orifice d'injection et ceci pour le même débit injecté. Il est à noter que les interactions potentielles entre les jets issus de différents orifices d'injection étaient hors de champ de cette étude et peuvent être l'objet de futures études.

Afin d'étudier, l'influences des propriétés physique du fluide secondaire, l'injection de différents types de gaz dans l'écoulement principal d'air a été considérée. L'analyse qui s'en est suivie a montré que la pression d'injection du fluide secondaire était déterminante sur la vectorisation plutôt que le débit massique du jet secondaire. Le produit de la masse molaire et le rapport des chaleurs spécifique ($\gamma \cdot M_g$) des gaz primaire et secondaire ont été trouvés inversement proportionnels à l'angle de déviation et l'intensité de la composante latérale de la poussée.

Les simulations numériques de la vectorisation impliquant des gaz chauds non réactifs (produits de la combustion) ont été également réalisées d'une part en considérant un mécanisme réactif utilisant une approche 1D dans la chambre de combustion et ensuite le code CFD prenant le relais pour une simulation 3D complète. Les résultats montrent que dans ces conditions de hautes températures, la vectorisation s'opère et reste pertinente.

Du point de vue de l'auteur, cet ensemble de travaux constitue une contribution et une avancée significative de l'étude de la vectorisation par injection fluidique d'une tuyère. Il a abordé une large spectre de différents aspects de cette méthode de vectorisation comprenant l'optimisation, l'explication physique, étude topologique... En général, des angles de déviation et des forces latérales perti-

nentes ont été obtenus. Le facteur d'amplification de vectorisation dans l'ensemble de cette étude se situait aux alentours de l'unité dans les conditions d'adaptation de la tuyère et ceci pour un rapport des pressions de l'injection secondaire voisin de l'unité et pour une position de l'injection proche de la section de sortie. Ce facteur d'amplification est comparable à celui donné dans la littérature en général.
Les recherches conduites dans ce travail ont été satisfaisantes sous l'angle de certains aspects analysés et leur implication dans la vectorisation par choc d'une tuyère axisymétrique. Cependant, d'autres aspects comme les phénomènes d'instabilité dans la zone de séparation ainsi que les effets des réactions chimiques n'ont pas été abordés dans cette étude. En outre, une étude complète d'une tuyère d'un lanceur est conditionnée par des critères de conception tels que les limites structurales tenant compte des charges latérales de flexion au voisinage du col et les protection thermiques dans les zones d'expansion plus loin en amont.

PERSPECTIVES

Partant de ces remarques, une étude supplémentaire devrait tenir compte d'effets supplémentaires et d'autres approches expérimentales. Même si des instabilités basses fréquences dans le cas d'une vectorisation (SITVC) d'une tuyère par injection proche de la section de sortie sont susceptibles d'être observées en aval de l'injecteur, ce qui d'une importance minime dans ce cas particulier, il n'en demeure pas moins qu'elle peuvent générer des charges latérales pour certains régimes d'écoulement et certains angles d'injection. A la lumière de ça, l'installation expérimentale qui a été développée pour cette étude peut être améliorée en régulant de façon active les paramètres de l'écoulement comme la température, les niveaux de turbulence et en incorporant de nouveaux outils de diagnostic comme la PIV, les huiles à coloration et une anémométrie à fil chaud adaptée au écoulements supersoniques.

Concernant l'approche numérique, l'utilisation des modèles de turbulence LES et DES devrait être envisagée pour réaliser une analyse plus fine des instabilités tout en incorporant un mécanisme réactionnel pour des simulations de cas opérationnels réels. En termes de paramètres de vectorisation par choc (SITVC), le contrôle par activation partielle ou totale des injecteurs opposés dans le cas

d'une injection "multiports", devrait être considéré sur la base des analyses mentionnées plus haut et qui concernent les zones d'instabilités auxquelles on peut s'attendre. Ce travail peut être étendu également à l'étude de la réponse dynamique du système de vectorisation par choc (SITVC) et par un contrôle dans la cas d'une injection "multiports".

Vladeta Zmijanovic

Vectorisation fluidique de la poussée d'une tuyère axisymétrique supersonique par injection secondaire

Résumé :

La vectorisation de la poussée d'une tuyère propulsive supersonique axisymétrique est étudiée par le biais d'une injection fluidique transversale dans sa partie divergente. Cette étude menée dans le cadre du programme *PERSEUS* du CNES a été motivée par la recherche d'une solution alternative au pilotage conventionnel de la poussée par actionneurs mécaniques.

Le travail de la thèse, tout en s'appuyant sur des approches expérimentale et numérique, comprend essentiellement une large étude paramétrique concernant principalement la position de l'injection, la forme de la tuyère, la nature et le débit du fluide injecté.
L'analyse des résultats montre que pour certaines configurations optimales, des angles de déviation pertinents peuvent être obtenus pour des taux d'injections modérés.
L'analyse numérique étendue aux écoulements chauds multi-espèces, plus proches des applications réelles, a montré que la vectorisation fluidique reste très performante lors de l'injection de produits de combustion dans le divergent.

Mots clés : écoulement transversal supersonique, tuyère propulsive, interaction de choc, décollement, force latérale aérodynamique, vectorisation de la poussée

Secondary injection fluidic thrust vectoring of an axisymmetric supersonic nozzle

Abstract :

Secondary injection into the divergent section of a supersonic rocket nozzle is investigated for the fluidic thrust vectoring effects. The study was conducted in the framework of CNES *PERSEUS* program and was motivated by the need for an alternative vectoring solution aimed for a small space launcher.

The thesis work, based on the combined experimental and numerical approaches, essentially comprises of a wide parametric study mainly concerning the position of the injection, the shape of the primary and injection nozzles, flow regime, gas thermophysical properties and injected fluid mass-flow-rate.

The analysis shows that for some optimal configurations, pertinent deflection angles can be obtained using the moderate injection rates.
Furthermore, the study was extended to the hot flow multi-species investigation, simulating a case closer to the real applications. This numerical analysis indicated that the fluidic vectoring method remains effective with injection of combustion products into the divergent section of a propulsive rocket nozzle.

Keywords: supersonic cross-flows, rocket nozzle, shock interaction, flow separation, side loads, thrust vectoring

Laboratoire: ICARE-CNRS
1C Av. de la recherche Scientifique
45071 Orléans cedex2

Centre National d'Études Spatiales
Direction des lanceurs
52, rue Jacques Hillairet
75612 Paris cedex